

# **Additive Manufacturing of Structural and Functional Materials**

Vom Promotionsausschuss der  
Technischen Universität Hamburg  
zur Erlangung des akademischen Grades  
Doktor-Ingenieur (Dr.-Ing.)

genehmigte Dissertation

von  
Sven Drücker

aus  
Hamburg

2023

Vorsitzender des  
Prüfungsausschusses:

Prof. Dr.-Ing. Wolfgang Hintze  
(Technische Universität Hamburg)

Gutachter:

Prof. Dr.-Ing. habil. Bodo Fiedler  
(Technische Universität Hamburg)  
Prof. Dr.-Ing. Benedikt Kriegesmann  
(Technische Universität Hamburg)

Tag der mündlichen Prüfung: 29.03.2023

# Technisch-Wissenschaftliche Schriftenreihe

## Herausgeber:

Prof. Dr.-Ing. habil. Bodo Fiedler

## Anschrift:

Technische Universität Hamburg  
Institut für Kunststoffe und Verbundwerkstoffe  
Denickestraße 15  
21073 Hamburg

## Band 44:

Additive Manufacturing of Structural and Functional Materials  
DOI: <https://doi.org/10.15480/882.5150>

Sven Drücker

 <https://orcid.org/0000-0002-7203-0992>

1. Auflage  
Hamburg 2023

ISSN 2625-6029

Copyright Sven Drücker 2023

Dieses Werk ist lizenziert unter einer Creative Commons Namensnennung 4.0 International Lizenz (<https://creativecommons.org/licenses/by/4.0/>).

## Bibliografische Information der Deutschen Nationalbibliothek:

Die Deutsche Nationalbibliothek verzeichnet diese Publikation in der Deutschen Nationalbibliografie; detaillierte bibliografische Daten sind im Internet über <http://dnb.dnb.de> abrufbar.



# Abstract

Additive manufacturing has attracted great interest in recent years as it shows several advantages over conventional manufacturing techniques. It enables complex parts, reduction of material consumption, individualization, customization, integrated functionality, integrated assembly and economical low volume production as well as the rapid production of prototypes, tools, jigs and fixtures. Despite this potential, many applications are still limited to rapid prototyping. Additive manufacturing is often still prone to imperfections as a robust set of printing parameters is difficult to determine for such a complex process. Hence, extensive post-processing and quality control are required. This study shows two applications of additive manufacturing that go beyond rapid prototyping using structural and functional materials. First, lightweight design with lattice structures is discussed. Second, functional integration is considered with an electrically conductive material that is suited for sensing.

Lattice structures show potential in lightweight design as their mechanical properties can be scaled by the volume fraction of the cells according to the local requirements given by the load paths. In order to use lattice structures in design of structural parts, the mechanical properties and manufacturing imperfections need to be characterized and assessed with respect to performance. Two different materials are considered that are processed with different additive manufacturing techniques: a structural material with the metal alloy Ti-6Al-4V printed by selective laser melting and a low density material with a methacrylate photopolymer printed by stereolithography. Manufacturing imperfections, different volume fractions, building directions and load cases are analyzed for the lattice structures. 3D digital image correlation reveals local strain concentrations and allows to determine true strains and subsequently true stresses. Basic mechanical tests are performed on bulk material to determine the variation of the material properties that are required to calibrate material models for finite element simulations. Finite element simulations of lattice structure models are conducted allowing a better temporal and local resolution of the progressive damage. Depending on the volume fraction, different failure modes can be seen that are captured and explained by finite element simulations. This allows to avoid stress concentrations or undesired buckling in future designs. The evaluation of different load cases is mandatory as a significant difference in tensile and compressive properties is observed. A reliable design process is developed where probabilistic effects of the variation of geometry deviations and material properties need to be captured

with finite element simulations. In order to identify the probability distribution of material properties like strength and fracture strain that are governed by local phenomena, a new model is proposed. It outperforms standard approaches with the central moments. Finally, simulations of lattice structures are compared to computationally inexpensive simulations of unit cells with periodic boundary conditions.

Further applications of additive manufacturing and lattice structures arise in process engineering. Here, they can be utilized as structured packings in reactors to enhance mixing of different phases. Additional process monitoring by integrated sensing can be realized with multi-material 3D printing. Of the four major additive manufacturing techniques only fused filament fabrication offers a facile way to implement this by using several printheads. However, the employment of fused filament fabrication is currently restricted by the anisotropy of the mechanical properties at a low level. These result from limited inter- and intralayer diffusion and entanglement of the usually thermoplastic polymer chains. In this study, a thermosetting polymer for fused filament fabrication printing is developed. The formulation is based on a solid epoxy resin, allowing it to be processed in filament form. A latent curing agent ensures a suitable shelf life, prevents the formulation from curing within the hotend and enables cross-linking over the layers during post-curing. Tensile tests and micrographs of the fracture surfaces prove the mechanical isotropy of the solid epoxy formulation. In addition, the material formulation is modified with single-walled carbon nanotubes to add electrical conductivity and allow functional 3D printing. The electrical conductivity can be adjusted by the filler content, which is low compared to commercial materials due to the favorable high aspect ratio of the nanoparticles. Yet, an electrical anisotropy and a higher percolation threshold compared to established epoxy based nanocomposites is observed. Proof of concept studies show that the functionalized material can be used for temperature and strain sensing applications.

# Kurzfassung

Die additive Fertigung hat in den letzten Jahren großes Interesse geweckt, da sie einige Vorteile gegenüber herkömmlichen Fertigungsverfahren aufweist. Sie ermöglicht komplexe Teile, eine Verringerung des Materialverbrauchs, Individualisierung, kundenspezifische Anpassungen, integrierte Funktionalität, integrierte Montage und wirtschaftliche Kleinserienfertigung sowie die schnelle Herstellung von Prototypen, Werkzeugen, Vorrichtungen und Halterungen. Trotz des Potenzials sind viele Anwendungen immer noch auf das Rapid Prototyping beschränkt. Oftmals ist die additive Fertigung noch anfällig für Imperfektionen, da es schwierig ist robuste Druckparameter für einen derart komplexen Prozess zu bestimmen. Dies zieht eine umfangreiche Nachbearbeitung und Qualitätskontrolle nach sich. In dieser wissenschaftlichen Studie werden zwei Anwendungen der additiven Fertigung vorgestellt, die über das Rapid Prototyping hinausgehen und dabei strukturelle und funktionelle Materialien verwenden. Zuerst wird der Leichtbau mit Gitterstrukturen diskutiert. Zweitens wird die Funktionsintegration mit einem elektrisch leitfähigen Material betrachtet, das sich für die Sensorik eignet.

Gitterstrukturen haben ein großes Potenzial für den Leichtbau, da ihre mechanischen Eigenschaften durch den Volumenanteil der Zellen skaliert werden können, sodass sie den durch die Lastpfade gegebenen lokalen Anforderungen entsprechen. Um Gitterstrukturen bei der Konstruktion von Strukturbauteilen nutzen zu können, müssen die mechanischen Eigenschaften und Herstellungsfehler charakterisiert sowie hinsichtlich der Leistungsfähigkeit bewertet werden. Es werden zwei verschiedene Materialien betrachtet, die mit unterschiedlichen additiven Fertigungstechniken verarbeitet werden: ein Strukturmaterial mit der Metalllegierung Ti-6Al-4V, das durch selektives Laserschmelzen gedruckt wird, und ein Material geringer Dichte mit einem Methacrylat-Photopolymer, das durch Stereolithographie gedruckt wird. Für die Gitterstrukturen werden Herstellungsfehler, unterschiedliche Volumenanteile, Baurichtungen und Lastfälle analysiert. Digitale 3D-Bildkorrelation zeigt lokale Dehnungskonzentrationen und ermöglicht die Bestimmung von wahren Dehnungen sowie nachfolgend wahren Spannungen. Grundlegende mechanische Tests an Vollmaterial werden durchgeführt, um die Variation der Materialeigenschaften zu bestimmen, die zur Kalibrierung von Materialmodellen für Finite-Elemente-Simulationen erforderlich sind. Es werden Finite-Elemente-Simulationen von Gitterstrukturmodellen gemacht, die eine bessere zeitliche und örtliche Auflösung der fortschreitenden Schädigung ermöglichen. Je nach Volumenanteil werden verschiedene Versagensarten beobachtet,

die durch Finite-Elemente-Simulationen erfasst und erklärt werden können. Dies erlaubt es, Spannungskonzentrationen oder unerwünschtes Knicken in zukünftigen Konstruktionen zu vermeiden. Die Untersuchung verschiedener Lastfälle ist zwingend erforderlich, da ein signifikanter Unterschied in den Zug- und Druckeigenschaften zu beobachten ist. Es wird ein zuverlässiger Entwurfsprozess entwickelt, bei dem probabilistische Effekte der Variation von Geometrieabweichungen und Materialeigenschaften mit Finite-Elemente-Simulationen erfasst werden müssen. Zur Ermittlung der Wahrscheinlichkeitsverteilung von Materialeigenschaften wie Festigkeit und Bruchdehnung, die durch lokale Phänomene bestimmt werden, wird ein neues Modell vorgeschlagen. Dieses übertrifft Standardansätze mit zentralen Momenten. Schließlich werden Simulationen von Gitterstrukturen mit vom Rechenaufwand günstigen Simulationen von Einheitszellen mit periodischen Randbedingungen verglichen.

Weitere Anwendungen der additiven Fertigung und der Gitterstrukturen ergeben sich in der Verfahrenstechnik. Hier können sie als strukturierte Packungen in Reaktoren eingesetzt werden, um die Durchmischung verschiedener Phasen zu verbessern. Eine zusätzliche Prozessüberwachung durch integrierte Sensorik kann mittels Multimaterial-3D-Druck realisiert werden. Von den vier wichtigsten additiven Fertigungsverfahren bietet nur die Schmelzschichtung (englisch: fused filament fabrication) eine einfache Möglichkeit, dies umzusetzen, indem mehrere Druckköpfe eingesetzt werden. Der Einsatz von Schmelzschichtung wird jedoch derzeit durch die Anisotropie der mechanischen Eigenschaften auf niedrigem Niveau eingeschränkt. Diese ergibt sich aus der begrenzten Diffusion und Verschlaufung zwischen und innerhalb der Schichten der meist thermoplastischen Polymerketten. In dieser wissenschaftlichen Studie wird ein duroplastisches Polymer für die Schmelzschichtung entwickelt. Die Formulierung basiert auf einem Feststoff-Epoxidharz, das die Verarbeitung in Form von Filamenten ermöglicht. Ein latenter Härter gewährleistet eine angemessene Lagerbeständigkeit, verhindert die Aushärtung innerhalb des Druckkopfes und ermöglicht während der Nachhärtung eine Vernetzung über die Schichten hinaus. Zugversuche und Mikroskopaufnahmen der Bruchflächen belegen die mechanische Isotropie der Feststoff-Epoxidformulierung. Darüber hinaus wird die Materialformulierung mit einwandigen Kohlenstoffnanoröhren (englisch: single-walled carbon nanotubes) modifiziert, um eine elektrische Leitfähigkeit zu ermöglichen und einen funktionellen 3D-Druck zu erlauben. Die elektrische Leitfähigkeit kann über den Füllstoffgehalt eingestellt werden. Dieser ist im Vergleich zu kommerziellen Materialien niedrig aufgrund des günstigen hohen Aspektverhältnisses der Nanopartikel. Dennoch wird eine elektrische Anisotropie und eine höhere Perkolationschwelle im Vergleich zu etablierten Nanokompositen auf Basis von Epoxidharz beobachtet. Machbarkeitsstudien zeigen, dass das funktionalisierte Material für Temperatur- und Dehnungssensoren verwendet werden kann.

# Contents

<b>Abstract</b>	<b>v</b>
<b>Kurzfassung</b>	<b>vii</b>
<b>Acronyms</b>	<b>xiii</b>
<b>1 Introduction</b>	<b>1</b>
1.1 Additive Manufacturing . . . . .	1
1.2 Aim and Objectives . . . . .	9
1.3 Structure of this Dissertation . . . . .	14
<b>2 Additively Manufactured Lattice Structures</b>	<b>15</b>
2.1 State of the Art . . . . .	15
2.2 Materials and Methods . . . . .	19
2.2.1 Titanium and its Alloy Ti-6Al-4V . . . . .	20
2.2.2 Methacrylate Photopolymers . . . . .	22
2.2.3 Sample Preparation . . . . .	26
2.2.4 Microscopy . . . . .	29
2.2.5 Differential Scanning Calorimetry . . . . .	31
2.2.6 Mechanical Testing . . . . .	32
2.2.7 Analytical Formulas for Cubic Lattice Strength and Buckling	35
2.2.8 Random Fields and Variography . . . . .	36
2.2.9 Local Probability Density Function Model . . . . .	37
2.2.10 Finite Element Modeling . . . . .	40
2.3 Results and Discussion . . . . .	44
2.3.1 Quality Control: Porosity, Microstructure and Curing Degree	46
2.3.2 Geometry Characterization . . . . .	48
2.3.3 Mechanical Properties of Bulk Material . . . . .	50
2.3.4 Mechanical Properties of Lattice Structures . . . . .	55
2.3.5 Correlation Length . . . . .	61
2.3.6 Probability Distribution of Local Mechanical Properties . .	64
2.3.7 Comparison of Experiments and Numerical Modeling for Bulk Material . . . . .	66
2.3.8 Comparison of Experiments and Numerical Modeling for Lattice Structures . . . . .	70
2.3.9 Homogenization of Unit Cells . . . . .	82

2.4	Conclusion on Additively Manufactured Lattice Structures . . . . .	84
<b>3</b>	<b>Additive Manufacturing in Process Engineering</b>	<b>91</b>
<b>4</b>	<b>Functional Material Printing</b>	<b>97</b>
4.1	State of the Art . . . . .	97
4.2	Materials and Methods . . . . .	100
4.2.1	Epoxy Resins . . . . .	100
4.2.2	Carbon Nanotubes . . . . .	107
4.2.3	Utilized Commercial Materials . . . . .	115
4.2.4	Functionalization . . . . .	116
4.2.5	Filament Production . . . . .	116
4.2.6	Differential Scanning Calorimetry . . . . .	118
4.2.7	Rheology . . . . .	118
4.2.8	Sample Preparation . . . . .	119
4.2.9	Geometry Characterization . . . . .	121
4.2.10	Mechanical Testing . . . . .	122
4.2.11	Microscopy . . . . .	122
4.2.12	Electrical Characterization . . . . .	122
4.2.13	Sensing Applications . . . . .	123
4.3	Results and Discussion . . . . .	125
4.3.1	Thermokinetic Characteristics, Shelf Life and Stability . . . . .	125
4.3.2	Post-Curing . . . . .	128
4.3.3	Dimensional Stability . . . . .	129
4.3.4	Mechanical Properties . . . . .	130
4.3.5	Fracture Surfaces . . . . .	132
4.3.6	Electrical Properties . . . . .	135
4.3.7	Temperature Sensing . . . . .	139
4.3.8	Strain Sensing . . . . .	141
4.4	Conclusion on Functional Material Printing . . . . .	143
<b>5</b>	<b>Conclusion</b>	<b>147</b>
<b>6</b>	<b>Outlook</b>	<b>151</b>
	<b>Bibliography</b>	<b>155</b>
<b>A</b>	<b>Development of the Solid Epoxy Material Formulation</b>	<b>183</b>
A.1	Prepolymer Development . . . . .	183
A.2	Curing . . . . .	185
A.2.1	Thermokinetic Modeling . . . . .	185
A.2.2	Influence of Final Curing Temperature . . . . .	189

A.3 Photographs of 3D Printed Solid Epoxy Specimens . . . . .	192
<b>Supervised Student Theses and Research Projects</b>	<b>195</b>
<b>Publications</b>	<b>197</b>



# Acronyms

---

Notation	Description
2D	two-dimensional
3D	three-dimensional
ABS	acrylonitrile butadiene styrene
AHEW	amine hydrogen equivalent weight
AM	additive manufacturing
CAD	computer aided design
CB	carbon black
CCC	critical coagulation concentration
CFRP	carbon fiber reinforced polymer
CNT	carbon nanotube
CT	computed tomography
CVD	chemical vapor deposition
DART	Diels-Alder reversible thermoset
DCD	dicyandiamide
DDS	diaminodiphenyl sulfone
DGEBA	diglycidyl ether of bisphenol A
DIC	digital image correlation
DLVO	Derjaguin-Landau-Verwey-Overbeek
DSC	differential scanning calorimetry
DW	direct write
EEW	epoxy equivalent weight
ELI	extra low interstitial
FDM	fused deposition modeling
FEM	finite element method
FFF	fused filament fabrication
FORM	first-order reliability method
FRP	fiber reinforced polymer
GFRP	glass fiber reinforced polymer
HIP	hot isostatic pressing
LCST	lower critical solution temperature
MMA	methyl methacrylate
MWCNT	multi-walled carbon nanotube

---

## Acronyms

---

Notation	Description
NIPAM	<i>N</i> -isopropylacrylamide
NTC	negative temperature coefficient
PA	polyamide
PBC	periodic boundary condition
PC	polycarbonate
PDF	probability density function
PEEK	polyether ether ketone
PEI	polyetherimide
PLA	polylactic acid
PMMA	poly(methyl methacrylate)
POCS	periodic open cellular structure
PP	polypropylene
PTC	positive temperature coefficient
REACH	registration, evaluation, authorisation and restriction of chemicals
SEM	scanning electron microscopy
SENB	single-edge-notch bending
SLA	stereolithography
SLM	selective laser melting
SLS	selective laser sintering
SORM	second-order reliability method
STL	standard triangulation language
SWCNT	single-walled carbon nanotube
TDI	toluene diisocyanate
TPO	diphenyl(2,4,6-trimethylbenzoyl)phosphine oxide
TTT	time-temperature-transformation
UDMA	urethandimethacryate (di-2-methacryloxyethyl 2,2,4-trimethylhexamethylenedicarbamate)
UV	ultraviolet
bcc	body-centered cubic
fmDA	furan-maleimide Diels-Alder
hcp	hexagonal close-packed

---

# 1 Introduction

In this chapter, an introduction to additive manufacturing (AM) is given. Advantages and disadvantages are discussed and the major three-dimensional (3D) printing techniques are described. Furthermore, current challenges of AM are identified. Based on that, the aim and objectives of this study are defined. Finally, the structure of this dissertation is illustrated.

## 1.1 Additive Manufacturing

AM or 3D printing is a manufacturing process where the desired component geometry is reached by joining volume elements of material. The process is usually implemented in the form of successively adding layers of material [1, 2]. It can be associated with a phase transition of the material for instance from liquid or powder to a solid state [3]. Within the scope of DIN 8580 it can be assigned to the group of primary shaping processes [4]. In general, seven basic categories of AM processes are distinguished: (i) binder jetting, (ii) directed energy deposition, (iii) material extrusion, (iv) material jetting, (v) powder bed fusion, (vi) sheet lamination and (vii) vat photopolymerization [5].

The basic concept of AM is that components can be manufactured directly from the model data without any restrictions or intermediate steps [1, 2]. The general workflow however comprises several steps. It starts with the pre-processing. First, a 3D computer aided design (CAD) volume model of the component needs to be created. Then, this model is converted into a standard triangulation language (STL) file consisting of the triangulated surface of the model. This file is imported to the slicer software, where the printing job is prepared. The preparation consists of positioning and orientation of the components, addition of support structures at overhangs, setting of appropriate printing parameters and the slicing of the model in layers. These information can be translated into a file format like G-code that can be interpreted by the printer. Afterwards, the build process is performed where the component is generated by consecutively adding material in layers. This is followed by the post-processing. After printing, larger amounts of excess material need to be removed. Then, the components are taken out of the printer and separated from the build platform. Depending on the process and the later application of the component, further steps might be necessary. Post-curing can be used to increase the cross-linking density of polymers. Heat treatments such as stress relief annealing (before removal from build platform) or

hot isostatic pressing (HIP) can be employed to alter the microstructure of metals. Support structures need to be removed. To ensure a high product quality and to identify manufacturing defects, computed tomography (CT) scans are required. Machining might be necessary for functional surfaces that rely on certain tolerances. Finally, a surface treatment can be applied such as grinding, sand blasting, mechanical, electrical or chemical polishing, pickling or coating. The workflow is presented in Fig. 1.1.

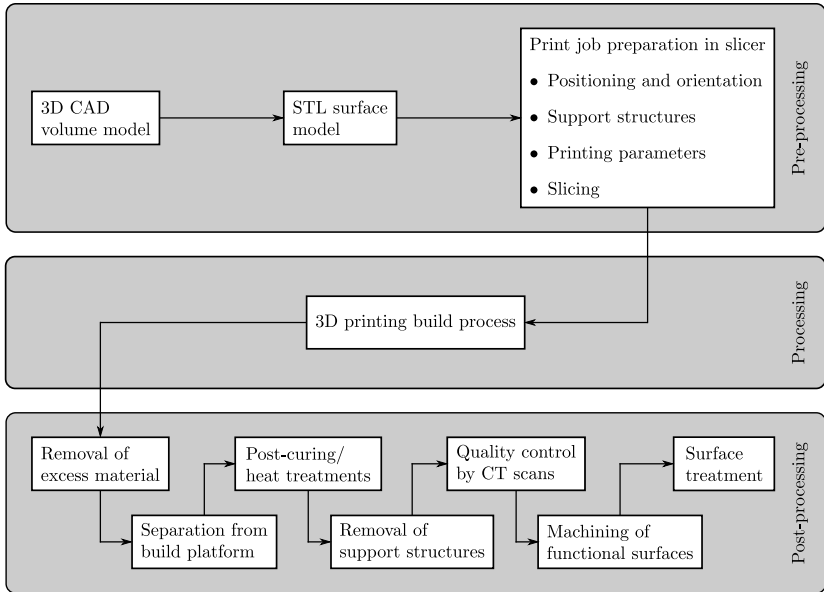


**Figure 1.1:** Workflow of AM.

While AM offers some advantages over conventional manufacturing techniques such as machining, casting, molding or forming, it also exhibits disadvantages. These features are listed in the following:

**Advantages**

- Complex geometries almost without any restrictions
- Individualization and customization
- Reduction of material waste

- No tools needed and thus also no tool wear
- Shorter development cycles due to easier manufacturing of prototypes
- Short production time compared to development of a process with tools
- No storage cost for spare parts by manufacturing on demand
- Simultaneous manufacturing of different parts in one process
- Mobile spare part production in remote locations
- Reduced dependence on suppliers

### Disadvantages

- Long production time
- Small building space
- Low surface quality due to staircase effect
- Support structures deteriorate surface quality
- Limited accuracy due to resolution of the process and thermal residual stresses leading to distortion
- Material properties often lower than for bulk material
- High material cost
- Extensive post-processing
- Limited robustness and reliability of the process
- Certification issues

The advantages of AM can be exploited in applications such as complex and lightweight components, individualization and customization, integrated functionality, integrated assembly and economic low volume production as well as the rapid production of prototypes, tools, jigs and fixtures [1, 2]. The four most widespread techniques are fused filament fabrication (FFF), stereolithography (SLA), selective laser sintering (SLS) and selective laser melting (SLM) [6]. In the following, these processes are shortly introduced with their advantages and disadvantages.

FFF can be assigned to the group of material extrusion processes. The material is provided in the form of a filament. It is continuously conveyed to the heated nozzle by a feeder. Here it is liquefied and then deposited on the build platform. After each layer, the offset between printhead and build platform is increased.

The build platform and the chamber can be heated to achieve better adhesion of the prints and to avoid excessive distortions such as warping. A schematic of the FFF process is presented in Fig. 1.2. In general, most thermoplastic polymers can be processed, ranging from standard thermoplastics such as polylactic acid (PLA) or acrylonitrile butadiene styrene (ABS) over engineering thermoplastics such as polyamide (PA) or polycarbonate (PC) to high-performance thermoplastics such as polyetherimide (PEI) or polyether ether ketone (PEEK). The polymer filaments can also be modified with additives such as fibers, electrically or thermally conductive particles, flame retardants or color pigments. Advantages and disadvantages of FFF are listed below:

### Advantages

- Inexpensive printer
- High build rate
- Inexpensive material
- Large variety of materials
- Feedstock is a solid material yielding a clean process without safety precautions
- Multi-material printing is possible
- Continuous fiber reinforcement is possible

### Disadvantages

- Reduced inter- and intralayer strength due to limited diffusion and entanglement of the polymer chains
- Anisotropic material properties
- Limited resolution
- Rough surface
- Support structures are necessary at overhangs
- Warping (can be reduced with a heated build platform and chamber)

SLA belongs to the category of vat photopolymerization processes. A liquid resin is used as printing material, which is supplied in the form of a resin bath. The resin usually consists of monomers, oligomers and photoinitiators. The resin is cured locally with an ultraviolet (UV) laser at the cross-section of the part

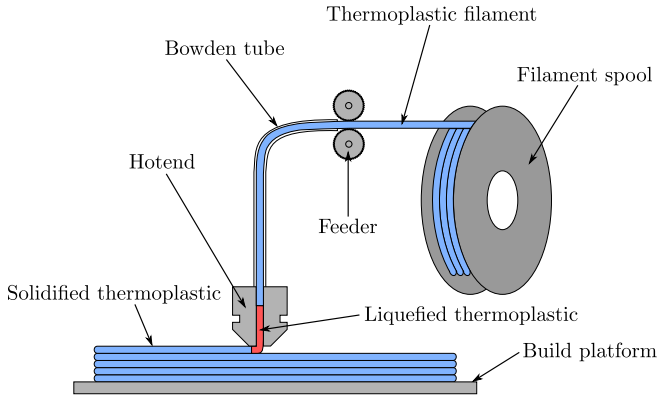


**Figure 1.2:** Schematic of the FFF printing process.

within each layer. Curing can take place either at the resin surface in the regular configuration or at the bottom of the resin bath in the inverted configuration. In the former case, the build platform is lowered in the resin bath after each layer. In the latter case, the build platform raises out of the resin bath and the parts are printed upside down. In both cases liquid resin is supplied after each layer from the resin tank and a wiper ensures a constant top level. The green part needs to be post-cured in a UV oven to ensure full cross-linking. Figure 1.3 shows a schematic of the inverted SLA process. The photopolymerization can be initiated either by free radicals or by cations. In the former case mostly (meth)acrylates are used as monomers and oligomers, while in the latter case usually epoxies are of interest [7, 8]. Acrylate photopolymers have high reaction rates and the reaction stops almost immediately when the light source is removed. However, they show a high level of shrinkage up to 20% that results in dimensional inaccuracies and warping. Contrary, the ring-open reaction of epoxy photopolymers shows low shrinkage of only 1% to 2%. Yet, the reaction rates are too low and uncontrolled dark polymerization continues after removal of the light source. Thus, also epoxy formulations usually contain acrylate resins to increase the reaction rates [2, 9]. Advantages and disadvantages of SLA are listed below:

#### Advantages

- Covalent interlayer bonding due to post-curing
- Isotropic material properties

- High resolution
- Better surface quality than other major AM techniques

### Disadvantages

- Post-curing is necessary
- Photopolymer is expensive and hazardous
- Liquid resin requires elaborate handling
- Prone to contamination of resin bath
- Multi-material printing is difficult
- Support structures are necessary at overhangs
- Material inclusions in internal hollow spaces
- Warping during post-curing due to uneven exposure to UV radiation
- Final parts can still be sensitive to UV exposure
- UV curing characteristics are focus of material development so that mechanical and thermal properties cannot be prioritized
- Modification with additives is restricted by transparency required for UV curing

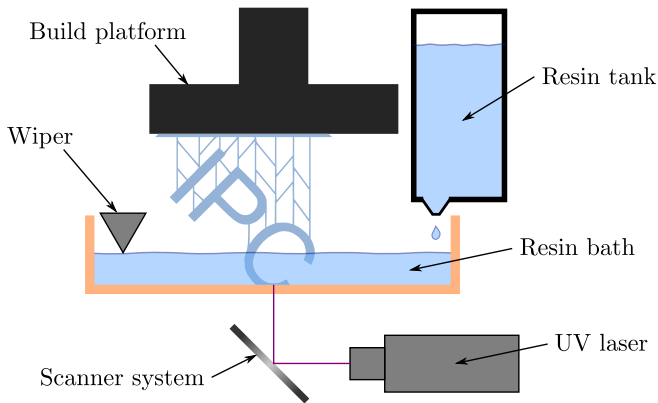


**Figure 1.3:** Schematic of the inverted SLA printing process.

SLM is a powder bed fusion process. The material is supplied in the form of a metal powder with a typical size of 20  $\mu\text{m}$  to 100  $\mu\text{m}$ . In each layer a laser is utilized to melt the powder locally at the cross-section of the part. After each layer, the build platform is lowered in the powder bed and a new layer of powder is transferred on top from the feed chamber by a coater. To avoid oxidation of the material, the process is usually carried out under an inert gas atmosphere such as nitrogen. As the process temperatures for melting a metal are significantly higher than for polymers, support structures are also used for heat transfer to the build platform. A schematic of the SLM process is depicted in Fig. 1.4. Typical materials are aluminum alloys, cobalt alloys, copper alloys, iron alloys, nickel alloys and titanium alloys. Advantages and disadvantages of SLM are listed below:

#### Advantages

- Structural parts possible
- Metallic interlayer bonding due to remelting of lower layers
- Isotropic material properties
- Large variety of materials

#### Disadvantages

- Expensive printer and process
- Powder material is expensive
- Powder material requires elaborate handling (storage, transfer, recycling)
- Thermal residual stresses lead to warping due to high processing temperatures
- Medium surface quality
- Multi-material printing is difficult
- Material inclusions in internal hollow spaces
- Support structures are necessary at overhangs and for heat transfer
- Expensive post-processing (wire eroding from build platform, stress release annealing, support structure removal)

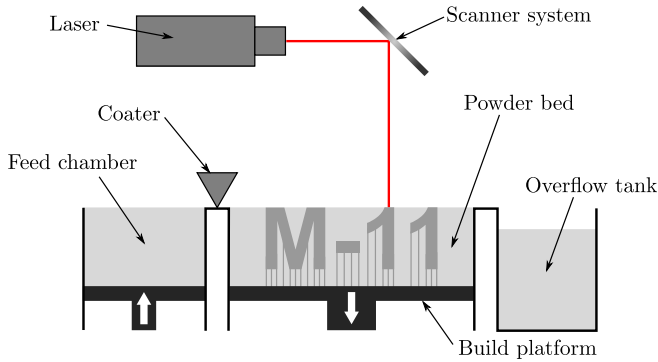


**Figure 1.4:** Schematic of the SLM printing process.

SLS is very similar to SLM except that a thermoplastic polymer powder is processed. In general, amorphous and semi-crystalline polymers can be used as feedstock. However, amorphous thermoplastics soften over a wide temperature range and have a higher viscosity. The former makes it more difficult to liquefy the desired amount of material while the latter results in low sintering rates yielding a higher porosity for the printed parts [10]. In contrast, for some semi-crystalline thermoplastics the supercooling window can be exploited where the crystallization temperature during cooling is below the melting temperature during heating. When the build chamber is heated to this temperature range, the material remains liquid after melting. This allows for diffusion and entanglement of the polymer chains over the layers. Moreover, uncontrolled crystallization accompanied with uneven shrinkage is avoided when the whole print with the surrounding powder is cooled below the crystallization temperature at the end of the process. The desire for a wide supercooling window and an efficient powder production currently limits the material choice basically to PA with approximately 90% of the industrial consumption [11, 12]. Compared to metals, the polymer powders are self supporting and the melting temperatures are lower. Advantages and disadvantages of SLS are listed below:

#### Advantages

- Diffusion and entanglement of polymer chains as build chamber is heated to supercooling window
- Isotropic material properties

- Little warping due to cooling of the entire part at the end of the process
- No support structures necessary

### Disadvantages

- Expensive printer and process
- Material choice is limited
- Powder material is expensive
- Powder material requires elaborate handling (storage, transfer, recycling)
- Medium surface quality
- Multi-material printing is difficult
- Material inclusions in internal hollow spaces
- Long cooling time after print job due to low thermal conductivity

## 1.2 Aim and Objectives

Due to its advantages AM has been booming over the last decade since the expiration of the patent for FFF in 2009. It is established for prototyping and individualized complex parts, however, application for series production is low [13]. Rapid prototyping is especially beneficial as it helps in the early stages of product development where most of the cost of the product life cycle is determined [14, 15]. Despite its potential, the concerns restraint its further deployment. Often AM is still prone to imperfections since a stable set of printing parameters is difficult to determine for such a complex process. Hence, extensive post-processing and quality control are required. This can also be seen in the popular science Gartner hype cycle for emerging technologies where 3D printing appeared in 2007 as a technology trigger [16], reached the peak of inflated expectations in 2012 [17] and fell in the trough of disillusionment in 2015 [18] until it completely disappeared afterwards [19]. The AM users especially seek more reliability and new materials [13, 20]. Hence, this study focuses on these aspects. It shows two applications of AM that go beyond rapid prototyping where its advantages are exploited: (i) lightweight design with lattice structures and (ii) functional integration with an electrically conductive material that is suited for sensing.

In (i) the reliability is of utmost importance as it is a structural application. Thus, two different materials are considered that are processed with different

AM techniques to be able to draw conclusions beyond particular cases. On the one hand, a structural material, the metal alloy Ti-6Al-4V printed with SLM, is investigated. On the other hand, a polymer, a methacrylate resin printed with SLA, is examined. The idea to use lattice structures in lightweight design has a biomimetics background. By definition “biomimetics combine biology and technology with the goal of solving technical problems through the abstraction, transfer, and application of knowledge gained from biological research” [21]. The basic motivation behind biomimetics is that biological structures have been optimized over millions or even billions of years by evolution and have proven to withstand the requirements of the environment. Therefore, it is assumed that they might also be useful in technological developments and that a lot of iterations in the design process can be saved [22, 23]. The process of biomimetics comprises three steps. First, a functional analysis of the biological system is performed. Then, the biological system is abstracted to a model. Finally, the model is transferred and applied to develop a technological solution or product without utilization of the biological system. Two approaches of the biomimetics process need to be distinguished. In a technology pull, a technological challenge is the starting point of the development and biological principles are analyzed that provide a solution or an improvement for an existing product. It is a top-down process. In a biology push, interesting features of a biological system are the origin of the development and they are transferred to a technological product. It is a bottom-up process [24, 25]. Examples of biomimetic developments are products such as velcro and lotus effect paints and methods such as evolutionary optimization algorithms and artificial neural networks. As biomimetic designs often result in complex geometries, the advantages of AM in this regard can be fully exploited [26]. The biological system that is considered as a model for cellular structures is trabecular bone. Figure 1.5 shows trabecular bone in the distal part of a femur. The femur has to withstand very complex loading situations with compression, tension, bending, torsion and impact while being as light as possible. This is realized by the rods of the trabecular bone that follow a trajectory along the various load paths [27]. It can be transferred to lattice structures in lightweight design where the mechanical properties can be scaled by the volume fraction of the unit cells according to the local requirements given by the load paths. Cellular structures are usually classified as open- or closed-cell and periodic or stochastic. Lattice structures can be described as open-cell periodic [28]. In the case of metal AM they are best suited for lightweight design as closed-cell periodic structures cannot be manufactured by SLM without material inclusions. A reliable application of lattice structures in lightweight design requires different load cases to be considered and imperfections to be analyzed. Moreover, the failure behavior needs to be investigated and simulation methods have to be developed that allow a stress analysis in the design process. Finally, probabilistic effects of imperfections (geometric and material) need to be considered due to the current instabilities of AM processes.

With regard to reliability in structural components, the filigree lattice structures push the limits of AM techniques and are therefore chosen as an extreme case. Cellular structures can also be used in various applications such as energy absorption, gas and fluid handling, heat exchangers, thermal insulation, sound control, filters, flame retardance, vibration control, catalytic surfaces, electrical handling, medical implants and buoyancy [28]. As many of these applications are relevant for the field of process engineering, they are also discussed in combination with AM.

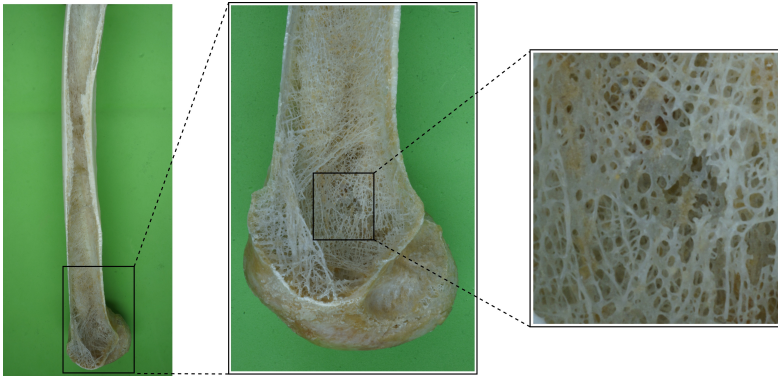


**Figure 1.5:** Trabecular bone in the distal part of a femur as a biological inspiration for cellular structures in a biomimetic design process.

In (ii) the focus is on the development of a new material. Functional integration can either be reached by design or by a combination of materials. The latter requires multi-material printing, which limits the choice of AM processes basically to FFF. Moreover, FFF is the only polymer AM process that allows continuous fiber reinforcement by direct integration into the filament. Hence, it is the only one that is suitable for structural applications. Therefore, a new material is required that solves the anisotropy issue at a low level that is currently limiting a further utilization. The basic idea to overcome this challenge is to use a solid thermoset epoxy resin that can be supplied in the form of a filament. A latent curing agent is needed as a second key constituent of the material formulation allowing a reasonable shelf life and cross-linking over the layers during the post-curing process. In addition, the new material can be modified with carbon nanoparticles to incorporate electrical conductivity and make it suitable for functional applications such as temperature and strain sensing.

The overall aim of this study is formulated in the following research hypothesis.

### Research hypothesis

AM of structural and functional materials has potential beyond rapid prototyping in lightweight design applications with lattice structures as well as in functional applications by multi-material printing.

In order to achieve the aim and to confirm the research hypothesis, the following objectives in the form of working hypotheses are elaborated. Working hypotheses 1 to 4 are concerned with the first application of AM beyond rapid prototyping, namely lightweight design with lattice structures. Working hypotheses 3 to 7 cover the second application with a new material development for functional integration with an electrically conductive material.

### Working hypotheses

1. Additively manufactured lattice structures show potential in lightweight design applications.
2. The evaluation of different load cases is mandatory for the characterization of lattice materials in structural design.
3. The progressive damage behavior of lattice structures can be captured in computationally efficient finite element simulations.
4. A probabilistic analysis of lattice structures incorporating geometrical and material uncertainties is necessary for the robust design of structural components due to insufficient technical maturity of the additive manufacturing process.
5. A solid epoxy thermoset filament based 3D printing material can solve the anisotropy limitations at a low strength level of the current FFF process.
6. Single-walled carbon nanotubes (SWCNTs) can be used as a filler for a functionalized solid epoxy thermoset formulation in the FFF process to incorporate electrical conductivity.
7. The functionalized solid epoxy thermoset filament can be used for 3D printed temperature and strain sensing applications.

A graphical overview of the main content of this study is illustrated in Fig. 1.6.

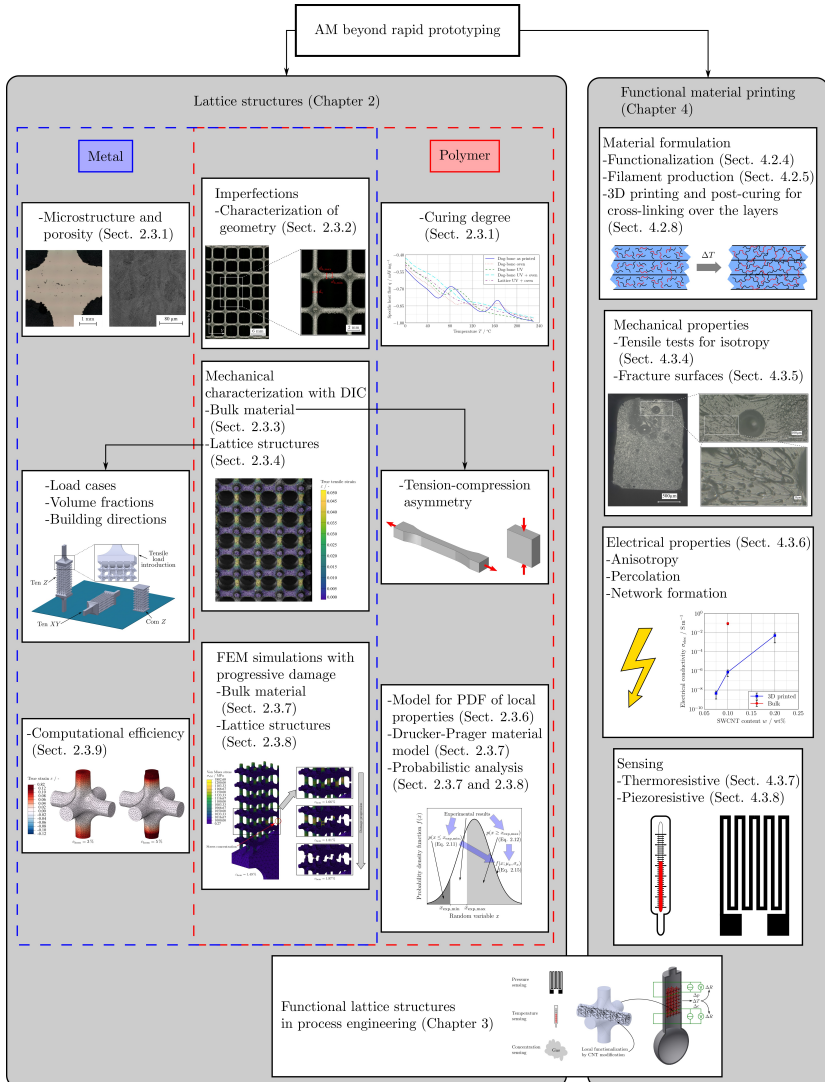


Figure 1.6: Graphical overview of the main content of this study.

### 1.3 Structure of this Dissertation

In Chapter 2, the first application beyond rapid prototyping is presented: lattice structures for lightweight design. At the beginning, the state of the art is summarized. Then, the characteristics of the utilized structural materials are described. This is followed by the experimental and numerical methods for the investigation of lattice structures. Furthermore, the results with regard to imperfections in the printing process and a reliable stress design procedure are discussed. Afterwards, conclusions on the use of additively manufactured lattice structures in mechanical applications are drawn. Parts of this chapter were previously published in [29, 30].

Chapter 3 deals with applications of AM in process engineering. Here, further utilizations of lattice structures are discussed. Also potentials for structure integrated sensing are considered, which leads to the desire for new materials. Parts of this chapter were previously published in [31].

This is followed by Chapter 4, where the second application beyond rapid prototyping is presented: functional integration with an electrically conductive material and the required material development. First, a recap of the state of the art is given. Moreover, the constituents of the new functional material formulation are introduced. Afterwards, the experimental methods utilized to study the properties of the novel material are described. Then, the results with regard to the geometrical, thermal, mechanical, electrical and combined characteristics are discussed. Subsequently, conclusions on the performance of the newly developed material are drawn. Parts of this chapter were previously published in [32].

Finally, conclusions with regard to the research hypothesis are drawn in Chapter 5 and an outlook is given in Chapter 6.

A CRediT author statement is provided in each of the publications [29–32] describing the contributions of the individual authors.

## 2 Additively Manufactured Lattice Structures

This chapter assesses the first application of additive manufacturing (AM) beyond rapid prototyping: lattice structures for lightweight design. The state of the art concerning lattice structures, especially fabricated by AM, is presented in Section 2.1. In Section 2.2 the utilized materials and methods are described. First, the three-dimensional (3D) printed materials, the metal alloy Ti-6Al-4V and the methacrylate photopolymer are introduced and the sample preparation is described. This is followed by an explanation of the experimental methods with microscopy, differential scanning calorimetry (DSC) and mechanical testing. Afterwards, simplified analytical formulas for the prediction of lattice properties are given and random fields as well as variography are discussed. Then, a new model to determine the probability distributions of material properties governed by local phenomena is developed and the finite element method (FEM) modeling approaches are shown. While several steps are similar for both materials and their respective manufacturing processes, for each one a different focus is set. For selective laser melting (SLM) printed Ti-6Al-4V lattice structures the focus is on the influence of different load cases, volume fractions and building directions as well as computationally more efficient homogenized FEM simulations. For stereolithography (SLA) printed methacrylate photopolymer the focus is on a more advanced material model that captures the tension-compression asymmetry and on the probabilistic influence of geometry and material variations. The results are presented and discussed in Section 2.3 starting with the quality control of porosity, microstructure, curing degree and the geometrical accuracy. The mechanical properties of AM fabricated bulk material and lattice structures are shown. Correlation lengths of the parameters are described with variography and probability distributions are determined with the newly proposed model. Then, additional knowledge gained from a comparison of FEM simulations with bulk and lattice experiments is presented. Afterwards, a computationally efficient homogenization approach with lattice unit cells is illustrated. Finally, conclusions on additively manufactured lattice structures are drawn in Section 2.4.

### 2.1 State of the Art

Cellular structures have already been studied extensively in the past [33–35]. Yet, the progress in AM over the past decade has further increased their popularity as AM enables the generation of arbitrary complex structures and by that abolishes

prior manufacturing restrictions. Especially the symbiosis of AM with topology optimization makes cell structures even more interesting [36, 37]. One of the few remaining constraints is the resolution of the prints where filigree cellular structures push the limits. Tailoring unit cells according to the specified requirements by topology optimization takes full advantage of AM [38]. Lattice structures consisting of many unit cells can be seen as metamaterials and are attractive in many applications such as heat conduction [39–41], medical engineering [42, 43], chemical reactors [44–46] or structural design [47] to mention a few.

With regard to the latter, lightweight design has become increasingly important, as it leads to energy savings in the transport sector and thus has ecological as well as economic benefits. Ashby [48] differentiates between two types of cellular materials: bending-dominated and stretch-dominated. While the former are more suited for energy absorbing applications as plastic joints allow for higher deformation, the latter are better for lightweight structural applications due to their higher stiffness and initial collapse strength. As the literature is already vast on lattice structures for energy absorption, in this study a unit cell suited for lightweight structural applications is analyzed. Sigmund [49] reported that closed-wall unit cells perform best with regard to stiffness under triaxial loading, however, these are not suited for many 3D printing applications as material can get entrapped. The surplus material does not support the mechanical behavior but increases weight. Hence, it is not favorable in lightweight design. This is valid for all processes with a powder bed (for instance selective laser sintering (SLS) and SLM) or a resin bath (for example SLA), which are three of the four major techniques in AM. Metals are preferable over unreinforced polymers in lightweight design, due to higher specific stiffness and strength. Thus, in this study the structural material Ti-6Al-4V, manufactured by SLM, is considered. Titanium alloys are especially suited for AM because of the difficulties in processing with conventional manufacturing techniques such as machining [50]. Beyond that, when the focus is on low weight and mechanical properties are of secondary importance, polymers are advantageous. Therefore, also SLA manufactured methacrylate photopolymer is utilized. An optimized open-wall unit cell with regard to stiffness under triaxial loading is composed of struts along the edges of a cube and thus called “cubic” [49, 51]. In addition, a non-uniform parameterization of the individual struts is possible leading to an anisotropic unit cell that shows improvements with regard to compliance minimization in some situations [52]. The cubic unit cell is therefore analyzed in this study. According to Maxwell’s criterion the cubic cell is not statically and kinematically determined and thus a candidate for a bending-dominated unit cell [48, 53]. However, Mazur *et al.* [54] state that the loading direction plays a significant role. Because the struts are aligned with the loading, there is stretch-dominated behavior.

As pointed out by Maconachie *et al.* [55], mechanical testing of lattice structures under compressive load is well established [56–61], however, tensile tests are rarely

found. This might be reasonable for energy absorbing applications, however, for structural lightweight design the tensile performance is equally important and needs to be tested. A reason for this lack of testing could be the more complicated load introduction, often leading to earlier failure due to a jump in stiffness [62]. To the author's knowledge tensile tests were only performed in few studies and either no comparison of the homogenized mechanical properties was done despite the availability of compressive data [63, 64], or only bending-dominated unit cells were analyzed, which are not desired in structural lightweight design [65]. A comparison of tensile and compressive experiments was only performed in one study with a reasonable unit cell for lightweight structural applications [66] and here a direct comparison is only done in terms of failure strain. Hence, one purpose of this study is to investigate the difference of the homogenized mechanical properties in tension and compression for a stretch-dominated unit cell and to gain further insights into the different failure modes depending on the load case.

In order to gain a deeper understanding of the local deformations, digital image correlation (DIC) was successfully used for lattice structure examinations [43, 56, 63, 67–70]. So far, only two-dimensional (2D) DIC was carried out and sometimes not the individual struts but a more diffuse surface was captured. Only for one publication it remains unclear whether 2D or 3D measurements were utilized [66] despite the advantages of 3D measurements. They allow also to investigate struts that are not in one plane and they are less prone to misalignment, tilt and vibrations. Therefore, in this study 3D DIC measurements of lattice structures are conducted.

Even more insights into the deformation, progressive damage and failure process can be gained by the FEM, allowing for a higher temporal and local resolution of the stresses and strains. As yet, different unit cells were analyzed with respect to stress concentrations using linear elastic material models [54, 56, 60, 61]. Also the nonlinear material behavior of lattice structures has been investigated in several studies with elastoplastic models using different definitions of the plastic flow such as von Mises [71–74], Johnson-Cook [75], Gurson-Tvergaard-Needleman [76] or Hill [77]. In contrast, studies with material models capturing progressive damage are rare [76, 78, 79] and only analyzed compressive tests until now, despite the fact that the FEM is especially valuable in understanding failure mechanisms. Regarding the FEM analysis of tensile tests, only one study on stochastic foams is found considering the elastoplastic behavior [80]. Thus, in this study an elastoplastic material model including progressive damage is used and a comparison of tension and compression tests of SLM fabricated Ti-6Al-4V lattice structures is performed. This is essential for lightweight structural applications. Beyond that, a tension-compression asymmetry was not considered in the plasticity models for lattice structures so far, despite the fact that AM is prone to imperfections such as pores, which are dependent on the process parameters [81]. These pores are more severe under tensile loading due to higher stress concentrations resulting

in earlier failure [66]. This is even more critical for polymer materials where the strength differential is naturally inherent even without defects. This might explain the differences in the plastic regime of experiments and simulations Ling *et al.* [73] found. They calibrated the material model with bulk tensile tests and used it in compressive lattice simulations. To account for the tension-compression asymmetry of the SLA fabricated methacrylate photopolymer, a Drucker-Prager yield surface is utilized in this study.

In filigree lattice structures imperfections leave uncertainties in the design, especially when the limits are pushed to small volume fractions. The traditional approach of using safety factors is not desirable in structural lightweight design. Two competing aims need to be satisfied: (i) the safety factor has to be as high as possible to be sure that the structures can withstand the load and (ii) the safety factor should be as small as possible to save weight. As safety factors only depend on past experience, this leaves engineers with a dilemma. In such cases, probabilistic analysis is an approach for more rational decisions [82]. The stochastic FEM is one of the methods frequently used in the past [83]. In this study, the Monte-Carlo simulation framework is applied, where several realizations of the design with random stochastically varying input parameters are analyzed in terms of their varying resulting performance. Generally, the stochastic variation of material properties, geometry and loads can be analyzed [84]. Kriegesmann *et al.* [85] successfully applied probabilistic methods on structures with geometric and loading imperfections. Also for lattice structures stochastic effects have been analyzed for a shape optimized unit cell [86]. On the structural level, only few investigations regarding geometry imperfections and varying material properties allow a comparison of simulated with experimentally observed stochastic distributions [87, 88]. In order to incorporate stochastic variations of the geometry in a lattice structure model, different approaches can be found in the literature. Scanning electron microscopy (SEM) images were analyzed and imperfections of the struts were represented in models by stacked beams with different cross-section diameters [89] or by stacked intersecting spheres [90]. In other studies computed tomography (CT) scans of cellular materials were captured and then directly used as models [72, 91]. As this is usually computationally expensive, Lozanovski *et al.* [74] developed a modeling approach with elliptical cross-sections joined by a loft operation. Input parameters were gathered from slices of CT images and then applied to the model for individual struts and complete lattices. They also determined varying effective strut properties and applied them on straight beam elements in full lattice models [92]. Moreover, geometrical imperfections were modeled by introducing buckling eigenmodes [93]. Also with regard to material property variations different implementations can be found. For honeycomb structures the elastic modulus was varied together with the sheet thickness based on assumed coefficients of variation [94]. Furthermore, a stochastic approach for the elastic properties as well as the geometry was used for foams [95]. In this case, a spatial correlation was

analyzed and applied with random fields. Yet, studies capturing variations in the nonlinear part of the material model (plasticity and failure) are rather rare even outside the field of cellular materials. Ning *et al.* [96] implemented a probabilistic FEM for elastoplastic materials but did not validate it with experiments. Amani *et al.* [76] used the porosity gained from CT scans to vary the plastic material properties of their Gurson-Tvergaard-Needleman model, which needs the porosity as an input. However, they only directly transferred the CT data to the FEM model in one deterministic case without considering several realizations to capture the scatter. Clouston and Lam [97] worked on strand-based wood composites and captured the variation in plastic properties. They included a size effect for the strength when evaluating different specimen volumes. Good results were obtained in validations with experiments under different load cases. Yet, including the size effect in the probability distributions of the plastic properties adds geometric influences to the material, making it impossible to distinguish the individual effects. This shows the challenge in probabilistic analysis of material properties that are governed by localization phenomena like plasticity. However, modeling these phenomena is crucial for a robust design. The linear elastic regime can be considered relatively safe anyway, but especially the nonlinear behavior afterwards needs to be analyzed. Hence, an aim of this study is to implement a probabilistic analysis capturing geometrical imperfections as well as variations of the material properties also beyond the linear elastic limit. This is carried out for the polymer lattice structures. A new model is proposed on how to determine the probability distribution of local mechanical properties like strength and fracture strain.

Due to the complex geometry of lattice structures, FEM simulations of full structures with continuum elements are computationally relatively expensive. In order to reduce the computational cost, studies with beam elements were executed [58, 92, 93, 98]. This comes with reduced resolution of local strains and especially the intersections/nodes need special treatment due to material accumulations. A different approach to reduce computational cost is to use unit cells with periodic boundary conditions (PBCs). This is commonly done for the inverse homogenization problem in topology optimization [49] but only with linear elastic bulk material properties. Only Gavazzoni *et al.* [99] used PBCs for lattice structures with elastoplasticity and were able to predict homogenized stiffness and yield point well whereas they had deviations in the plastic regime. In this study, unit cell simulations with PBCs are carried out with a material model also including progressive damage for SLM manufactured Ti-6Al-4V.

## 2.2 Materials and Methods

In this section, information about titanium and its alloy Ti-6Al-4V as well as methacrylate photopolymers as feedstock materials for AM is given. Then, the

sample preparation is presented, followed by the experimental approach for the characterization of the bulk materials and lattice structures with microscopy, DSC and mechanical testing. Subsequently, analytical formulas for the prediction of lattice structure strength and buckling are described. Afterwards, the use of varlography to generate parameters for random fields of varying specimen properties is introduced. A new model to estimate the probability distribution of local mechanical properties such as strength and fracture strain is proposed. Finally, the FEM models are explained.

### 2.2.1 Titanium and its Alloy Ti-6Al-4V

Titanium and its alloys stand out due to their high specific strength and good corrosion resistance even at elevated temperatures. The specific strength is only surpassed by carbon fiber reinforced polymers (CFRPs), which are however limited to lower operation temperatures [100, 101]. Titanium features an allotropic phase transformation. It shows a hexagonal close-packed (hcp) crystal structure ( $\alpha$  phase) below and a body-centered cubic (bcc) crystal structure ( $\beta$  phase) above the  $\beta$  transus temperature of 882 °C. This crystal structure influences the plastic deformation behavior. While the  $\alpha$  phase has only four independent slip systems, the  $\beta$  phase of titanium has twelve slip systems, which allows homogeneous plastic deformation according to the von Mises criterion. Additionally, the plastic deformation of the  $\beta$  phase is energetically favorable due to the shorter minimum slip path despite the slightly higher packing density of the  $\alpha$  phase slip planes [100].

The mechanical properties of titanium can be influenced by alloying, which changes the  $\beta$  transus temperature. Alloying elements are classified into neutral,  $\alpha$  and  $\beta$  stabilizers. The resulting titanium alloys are then categorized as  $\alpha$ ,  $\alpha + \beta$  and  $\beta$  alloys [101]. The most prominent alloy is Ti-6Al-4V (material number 3.7165), categorized as  $\alpha + \beta$ , because of its balanced properties in terms of strength, ductility and toughness [100]. The chemical composition requirements according to ASTM B 348 [102] and the  $\beta$  transus temperature [101] of Ti-6Al-4V and its extra low interstitial (ELI) elements version are shown in Tab. 2.1. The main alloying elements in Ti-6Al-4V are aluminum and vanadium. Aluminum is an  $\alpha$  stabilizer and increases the strength by substitutional solid solution strengthening. In addition, the strength is further enhanced by interstitial solid solution strengthening with oxygen that also acts as an  $\alpha$  stabilizer. On the other hand, vanadium is used as a  $\beta$  stabilizer allowing to maintain a  $\beta$  phase at room temperature, resulting in higher ductility [101].

An additional increase in strength and also in ductility of  $\alpha + \beta$  alloys can be reached by grain boundary strengthening. Different processing routes and especially cooling rates influence the microstructure. Three different types of microstructures can be obtained: (i) fully lamellar, (ii) bi-modal and (iii) fully

**Table 2.1:** Chemical composition requirements (in wt%) and  $\beta$  transus temperature (in °C) of Ti-6Al-4V and Ti-6Al-4V ELI.

Element	Ti-6Al-4V	Ti-6Al-4V ELI
Aluminum	5.5–6.75	5.5–6.5
Vanadium	3.5–4.5	3.5–4.5
Carbon	$\leq 0.08$	$\leq 0.08$
Oxygen	$\leq 0.2$	$\leq 0.13$
Nitrogen	$\leq 0.05$	$\leq 0.03$
Hydrogen	$\leq 0.015$	$\leq 0.0125$
Iron	$\leq 0.4$	$\leq 0.25$
Others, each	$\leq 0.1$	$\leq 0.1$
Others, total	$\leq 0.4$	$\leq 0.4$
$\beta$ transus temperature	995	975

equiaxed. The latter two require a recrystallization process after cold working. Yet, large deformations of the material after AM are not desired as the geometry is already final. Hence, the focus is on fully lamellar microstructures in the following. At low cooling rates from the  $\beta$  phase into the  $\alpha + \beta$  phase, the  $\alpha$  phase nucleates at the prior  $\beta$  grain boundaries forming a layer. Subsequently,  $\alpha$  lamellae with the same Burgers relationship grow into the  $\beta$  grains in a parallel fashion yielding  $\alpha$  colonies. The  $\alpha$  lamellae are separated by the remaining  $\beta$  phase. At slow cooling rates, the  $\alpha$  lamellae grow until they meet other  $\alpha$  colonies and can thus span half of the prior  $\beta$  grains. With increasing cooling rates,  $\alpha$  colonies also nucleate at other  $\alpha$  colonies leading to a Widmanstätten structure. Hence, the  $\alpha$  colonies and also the thickness of the individual  $\alpha$  lamellae gets smaller leading to the previously mentioned grain boundary strengthening. Very high cooling rates result in fine  $\alpha'$  martensite accompanied by a further increase in strength [101]. Figure 2.1 illustrates the three characteristic microstructures of fully lamellar Ti-6Al-4V depending on the cooling rate obtained by light optical microscopy. The  $\alpha'$  martensite is typical for the SLM process as the heat input is local, the volume of the melt is small and the pre-heating of the build chamber is low, yielding cooling rates of  $1000\text{ }^\circ\text{C s}^{-1}$  to  $10^8\text{ }^\circ\text{C s}^{-1}$  [50]. The  $\alpha'$  martensite can be transformed to a fine lamellar  $\alpha + \beta$  microstructure by annealing in the temperature region of  $700\text{ }^\circ\text{C}$  to  $850\text{ }^\circ\text{C}$  [101]. Finally, also the size of the prior  $\beta$  grains influences the mechanical properties with an increasing strength and ductility for a decreasing grain size [50, 101].

The advantages of titanium are especially exploited in the aerospace and chemical industry as well as the biomedical field where its biocompatibility and bioadhesion are desired in addition. Despite the outstanding properties a wide use of

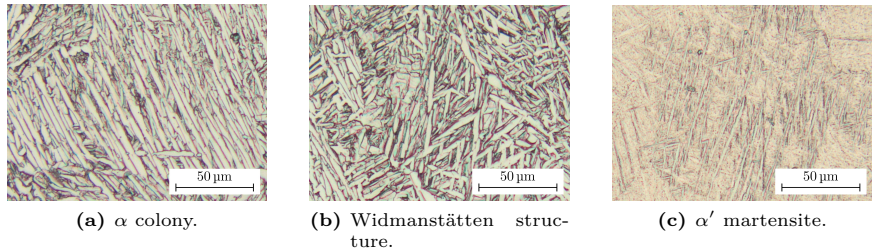


**Figure 2.1:** Characteristic microstructures of fully lamellar Ti-6Al-4V depending on the cooling rate.

titanium and its alloys is hindered due to their relatively high cost compared to other structural materials [101]. In aerospace applications lightweight design is especially important. With conventional subtractive manufacturing techniques such as machining, the buy-to-fly ratio (ratio of the the raw material mass to the final part mass) for typical components is between 10:1 and 20:1 while it can be up to 40:1 [103], which means up to 98 % material waste [104]. Moreover, titanium has a low thermal conductivity reducing the transfer of heat generated at the interface between tool and part. Hence, the tool wear is high so that slow cutting speeds and heavy cutting depths are required [101]. Consequently, the use of AM techniques is of uttermost interest in the production of titanium parts since resources can be saved and the difficulties of machining, leading to high tool costs and long lead times, can be circumvented [50]. Furthermore, topology optimized parts can be produced that are not possible with traditional manufacturing techniques yielding additional lightweight potential. Moreover, AM is attractive for biomedical applications as it enables a high degree of individualization. In summary, industries relying on titanium and its alloys can benefit greatly from AM.

### 2.2.2 Methacrylate Photopolymers

In general, chain polymerization is a chemical reaction where unsaturated monomers add to a growing chain to form large macromolecules: polymers. The reactive double bonds are saturated when links are formed. The chain polymerization reaction is characterized by three steps: chain initiation, chain propagation and chain termination [105]. In the SLA process, photopolymers are utilized. Most photopolymers consist of at least three parts: (i) photoinitiators, (ii) oligomers and (iii) monomers. The photoinitiator is required to obtain an initiating radical. The monomers and oligomers are usually not sensitive to the available light

because of their absorption capabilities [106]. Oligomers reduce the shrinkage compared to monomers [107] and usually dominate the physical and chemical properties of the resulting polymer with their backbone [7, 106]. Smaller monomers are used to adjust the viscosity for easier processing. Moreover, they increase the reaction rate due to their higher mobility. This is especially important at later stages when the movement of larger chains is limited, which results in a higher curing degree [8, 106]. In the case of the methacrylate photopolymer resin used in this study (Clear, Formlabs Inc., Somerville, MA, USA), the constituents are the photoinitiator diphenyl(2,4,6-trimethylbenzoyl)phosphine oxide (TPO), the oligomer urethandimethacrylate (di-2-methacryloxyethyl 2,2,4-trimethylhexamethylenedicarbamate) (UDMA) and a methacrylate monomer, which is proprietary [108]. The molecular structures of the constituents are presented in Fig. 2.2.

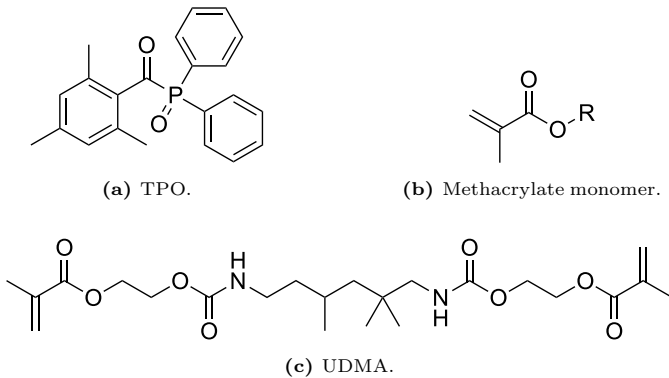


**Figure 2.2:** Constituents of the methacrylate photopolymer resin.

In the case of methacrylate photopolymers, a free-radical polymerization takes place. The reaction relies on the photochemical effect, where a group of atoms (chromophores, e.g. the aromatic carbonyl group in TPO) in a molecule absorbs light. Subsequently, electrons reach an excited state of higher energy. The difference in energy between the ground state and the excited state of the electrons has to correspond to the energy  $E_{\text{photon}}$  of the absorbed photon that is given by

$$E_{\text{photon}} = h_P f, \quad (2.1)$$

where  $h_P$  is Planck's constant and  $f$  is the frequency of the light [7]. The deactivation of the excited state can lead to rapid bond cleavage when the dissociation energy of the bond is lower than the energy from the excited state [106, 109]. This is the case for the C-P bond adjacent to the benzoyl group of TPO [7, 106,

109]. Cleavage of the photoinitiator PI resulting in the formation of two free radicals FR is the starting point of the chain initiation. The decomposition of the photoinitiator is shown schematically in Fig. 2.3.

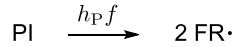


**Figure 2.3:** Scheme of the decomposition of the photoinitiator to form free radicals.

The decomposition of the utilized photoinitiator TPO is illustrated in Fig. 2.4 yielding a benzoyl and a phosphinoyl radical. The phosphinoyl radicals add more efficiently to unsaturated acrylate bonds than the benzoyl radicals due to their pyramidal structure featuring little steric constraints in the addition to double bonds [106, 109]. For many other photoinitiators the benzoyl radical is the major initiating species [2].

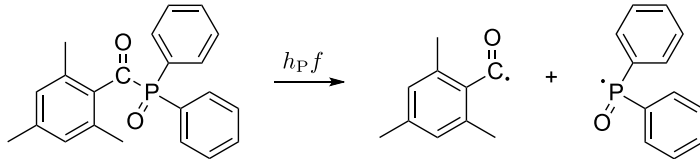


**Figure 2.4:** Decomposition of TPO to form a benzoyl and a phosphinoyl radical.

After the decomposition of the photoinitiator, a free-radical addition upon a monomer takes place forming the starting point of a polymer chain and shifting the active center of the radical to the monomer. Exemplarily, this is depicted for a benzoyl radical upon a methacrylate monomer in Fig. 2.5a. The benzoyl radical attacks the  $\pi$ -bond of the vinyl group of the methacrylate monomer and forms a  $\sigma$ -bond at the  $\beta$ -carbon while the free electron is shifted to the  $\alpha$ -carbon. The addition at the  $\beta$ -carbon is driven by the steric hindrance of the methyl and carboxyl groups close to the  $\alpha$ -carbon. Moreover, the polar nature of the carbonyl group pulls away the electron density of the  $\alpha$ -carbon reducing the electron density compared to the  $\beta$ -carbon [107]. The free-radical addition of the photoinitiator radical upon the first monomer M is again shown schematically in Fig. 2.5b.

The newly formed radical is again capable of attacking another monomer yielding a radical with an even longer chain. The repetition of this process is the chain propagation. It is presented schematically in Fig. 2.6. In the case of monomers with only one unsaturated bond linear chains develop. Two or more functional groups can lead to cross-linked 3D polymer networks [7, 106]. In this case, the

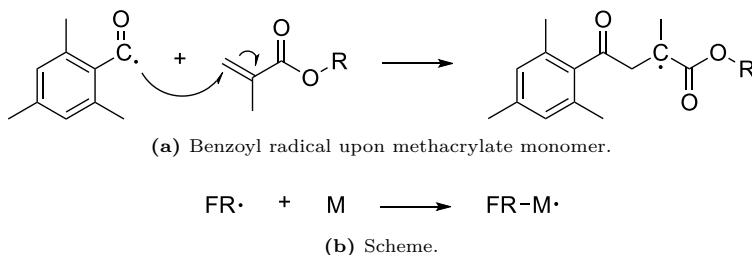


**Figure 2.5:** Free-radical addition of the photoinitiator radical upon the first monomer.

UDMA has two terminating methacrylate groups with unsaturated bonds and also the methacrylate monomer can have further functionalities depending on the group R.

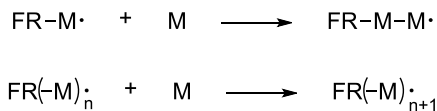


**Figure 2.6:** Scheme of the chain growth propagation.

Chain termination can be caused by three reactions of the polymer networks PN containing a mixture of  $n$  and  $m$  monomers/oligomers. First, termination can take place by recombination where two polymer networks merge by joining the radicals (see Fig. 2.7a). In principal, this can also appear with the free radicals from the photoinitiator in the beginning or with a free radical of a photoinitiator and a polymer network. Second, a hydrogen can be transferred from one polymer network to the other leading to an unsaturated double bond, which is known as disproportionation (see Fig. 2.7b). Finally, a radical can be trapped within a polymer network as the mobility is reduced when the viscosity is increasing at later stages of the curing reaction. This results in occlusion from the reaction (see Fig. 2.7c) [2, 7, 110].

The mobility of the constituents of the resin along the curing reaction leads to characteristic kinetic features. When the polymer chains grow and the viscosity increases abruptly at the gel point, the mobility of the polymer chains with active radicals is reduced drastically. This limits chain termination reactions. However, the diffusion of the smaller monomers is still possible, which leads to the auto-acceleration effect where the polymerization rate increases. When the vitrification point is reached, also the mobility of the monomers is reduced. The

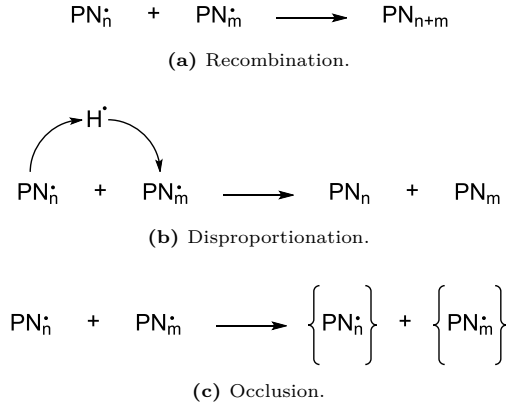


**Figure 2.7:** Scheme of chain termination mechanisms.

polymerization rate drops dramatically, which is called auto-deceleration. In addition, it has to be taken into account that diffusion is a temperature dependent process where higher temperatures lead to more mobility [7, 107].

Applications of acrylate and methacrylate polymers range from coatings and adhesives over poly(methyl methacrylate) (PMMA) as an alternative to glass to dentistry where they are used to fill cavities and for full denture base fabrication [2, 107]. Especially in the field of dentistry the advantages of AM processes can be fully exploited due to the required geometrical complexity and high degree of individualization.

Having introduced the materials utilized for additively manufactured lattice structures in this study, the next sections deal with the experimental approach.

### 2.2.3 Sample Preparation

The metal specimens are manufactured in the SLM process (Concept M2 cusing Dual-Laser, Concept Laser GmbH, Lichtenfels, Germany and SLM500HL, SLM Solutions Group AG, Lübeck, Germany). The process parameters of both machines were optimized with regard to minimum porosity and yield similar results. A Ti-6Al-4V powder (TEKMAT Ti64-53/20, TEKNA Advanced Materials Inc., Quebec, Canada) is processed, where 95 wt% has a diameter of 20  $\mu\text{m}$  to 53  $\mu\text{m}$  and which meets the requirements of ASTM B 348 Grade 23 [102] corresponding to Ti-6Al-4V ELI (see Section 2.2.1). A layer thickness of 30  $\mu\text{m}$  is applied. After the SLM process, the specimens are stress release annealed at 710  $^{\circ}\text{C}$  as residual stresses can effect the integrity of the parts [111]. Finally, they are wire-eroded

from the build platform. For the characterization of the bulk material properties, tensile test specimens according to DIN 50125 Type B [112] with a diameter of 6 mm and a measuring length of 30 mm are used. In order to avoid effects of surface roughness, the specimens are printed with an overmeasure of 2 mm in diameter and machined to the desired geometry by turning.

The analyzed cubic unit cells of the metal lattice structures have a dimension of 6 mm  $\times$  6 mm  $\times$  6 mm and consist of three orthogonal struts with fillets to reduce stress concentrations (see Fig. 2.8a). Volume fractions of 6 %, 13 % and 20 % are considered. The morphological characteristics of the lattice unit cells in computer aided design (CAD) are shown in Tab. 2.2.

**Table 2.2:** Morphological characteristics of the metal unit cells as specified in CAD.

Volume fraction	Strut diameter	Fillet radius
6 %	0.89 mm	0.89 mm
13 %	1.4 mm	1.4 mm
20 %	1.8 mm	1.5 mm

The metal lattice structure specimens are composed of periodically repeated unit cells (five-by-five over the cross-section, eight over the length) to obtain homogenized mechanical properties. The unit cell repetitions are chosen in such a way that the influence of a size effect is small. According to Andrews *et al.* [113], the size effect vanishes with a ratio of five to eight of the specimen size to the unit cell size, depending on whether a closed or open cell foam is considered and whether the stiffness or the strength is analyzed. In contrast to foams, the lattice structures in this study are periodic so the results might not be perfectly transferable. To reduce computational time in the numerical model, a ratio of five is chosen for the cross-section. A ratio of 1.5 to two of specimen length to width is recommended for compressive tests of cellular structures according to DIN 50134 [114] yielding the minimum of eight repetitions over the length. For compressive tests, the load introduction is realized by a rectangular base plate. For tensile tests, a clamping area with a fillet is added as well as a pyramid in the first rows of the lattice structure to reduce the stiffness jump from the bulk base plate to the lattice structure. The tensile load introduction is presented in Fig. 2.8b. The standard process parameters of the bulk material are used and no specific optimization for lattice structures is conducted. In order to analyze the influence of the building orientation [115], tensile specimens are printed in loading direction ( $Z$ ) and perpendicular to it ( $XY$ ). Compressive specimens are only analyzed for aligned building and loading direction ( $Z$ ) (see Fig. 2.8b). The lattice structure specimens are sand blasted to remove excess powder.

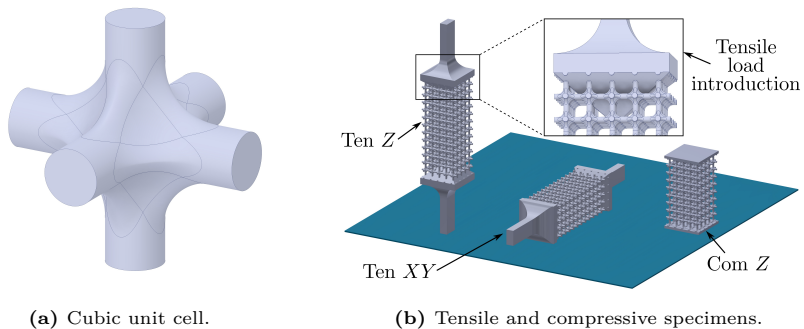


**Figure 2.8:** Cubic unit cell and metal lattice structure specimens for tensile testing with aligned (Ten  $Z$ ) and perpendicular (Ten  $XY$ ) building and loading direction as well as specimens for compressive testing (Com  $Z$ ). Also the pyramid for the load introduction of the tensile specimens is depicted.

To analyze the stochastic variation of dimensional accuracy and the mechanical properties, specimens are manufactured in an SLA process with a 3D printer (Form 2, Formlabs Inc., Somerville, MA, USA) and a methacrylate photopolymer resin (Clear, Formlabs Inc., Somerville, MA, USA). After printing, excess resin is removed in an isopropanol bath. Post-curing is performed in a ultraviolet (UV) radiation oven (Form Cure, Formlabs Inc., Somerville, MA, USA) at  $60^{\circ}\text{C}$  for 4 h. Afterwards, support structures are removed and the contact points are polished with sandpaper. To characterize the bulk material properties, three different specimens are analyzed. Tensile properties are evaluated with dog-bone specimens of type 1BB with a thickness of 3 mm according to DIN EN ISO 527-2 [116]. Compressive tests are performed with rectangular block specimens of type B after DIN EN ISO 604 [117]. The critical strain energy release rate is investigated with single-edge-notch bending (SENB) specimens with dimensions of  $40\text{ mm} \times 8\text{ mm} \times 4\text{ mm}$  in agreement with ASTM D5045 [118]. A notch of 4 mm is introduced by a precision saw (Brillant 220, ATM Qness GmbH, Mammelzen, Germany) with a  $150\text{ }\mu\text{m}$  diamond cut-off wheel followed by initiating the natural crack with a razor blade in a sawing motion. All specimens for the material characterization are printed with a layer height of  $100\text{ }\mu\text{m}$ .

The cubic unit cells (see Fig. 2.8a) of the polymer lattice structures have a dimension of  $4\text{ mm} \times 4\text{ mm} \times 4\text{ mm}$ . The unit cells are periodically repeated five-by-five times over the cross-section and six times over the length to form the lattice structure specimens. The repetitions over the length are further reduced

compared to the metal lattice structures as additional rows are used for the load introduction. The minimum of six repetitions is chosen to still allow an oblique fracture while keeping the specimens small to reduce computational time in the numerical model. The load introduction is realized by a clamping area connected to a base plate with a fillet. Moreover, two rows of cells with a gradient in volume fraction are added in between to reduce the stiffness jump from the bulk clamping area to the lattice structure. This serves as an alternative to the pyramid to prevent early failure [119]. The gradient in volume fraction is realized by an increasing strut diameter towards the base plate. The morphological characteristics of the unit cells with a gradient and in the middle section of the lattice structure specimens, as specified in CAD, are summarized in Tab. 2.3. The diameter of the strut towards the base plate  $d_{bp}$ , the diameter of the strut towards the unit cells  $d_{uc}$  in the middle section, the diameter of the horizontal struts  $d_h$ , the fillet radius  $r_f$  and the resulting volume fraction  $V_f$  are given. The lattice structure specimen with the gradient in volume fraction at the load introduction is presented in Fig. 2.9. As the lattice geometry is more complex, a higher resolution of the layer height with  $25\ \mu\text{m}$  is used. Preliminary experiments with different layer thicknesses only showed minor differences that were within the reproducibility of the printing process of such a low-cost SLA printer. The lattice structure specimens are built as indicated in Fig. 2.9, so that building direction and loading direction coincide.

**Table 2.3:** Morphological characteristics of the polymer unit cells as specified in CAD.

Unit cell	$d_{bp}$ / mm	$d_{uc}$ / mm	$d_h$ / mm	$r_f$ / mm	$V_f$ / %
1st gradient	3.2	2.15	2.68	0.39	65
2nd gradient	2.15	1.1	1.63	0.91	33
Middle section	1.1	1.1	1.1	1.32	20

## 2.2.4 Microscopy

In order to get an impression of the porosity and the microstructure of the additively manufactured Ti-6Al-4V (see Section 2.2.1), exemplary specimens of the bulk material and the lattice structure are cut in half along the building direction ( $Z$ ) by a precision saw (Brillant 220, ATM Qness GmbH, Mammelzen, Germany). Subsequently, they are ground and polished (Saphir 550, ATM Qness GmbH, Mammelzen, Germany). Afterwards, the porosity is captured with digital microscopy (VHX-6000, Keyence Deutschland GmbH, Neu-Isenburg, Germany) and the microstructure is obtained from SEM using the backscattered electron

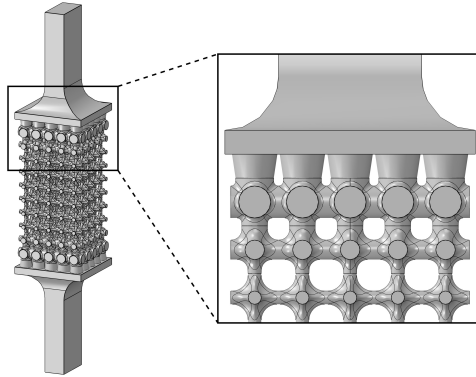


**Figure 2.9:** Polymer lattice structure specimen for tensile testing. Also the gradient in volume fraction at the load introduction is depicted.

detector (Phenom XL Desktop SEM, Thermo Fisher Scientific, Eindhoven, The Netherlands).

The dimensional accuracy of the struts of metal and polymer lattice structures is analyzed with digital microscopy. The smallest diameter of the struts in loading direction is the decisive feature with regard to mechanical properties. Furthermore, also the diameter of the struts perpendicular to the loading direction is important for the transverse contraction behavior. For the metal lattice structures the strut diameters are measured in micrographs of the outer unit cells of three specimens for each volume fraction. Due to the high cost of the metal specimens, they are not cut to evaluate the strut dimensions in the inner part of the lattice because additional specimens would be required for mechanical testing. It is assumed that the outer cells are representative. Instead of analyzing both building directions separately for the tensile tests, the strut diameter is determined in building direction and perpendicular to it for the  $Z$  specimens as illustrated in Fig. 2.10. In building direction ( $Z$ ) the vertical diameter  $d_v$  is measured in the middle of the strut (35 measurements per specimen). In layer plane ( $XY$ ), the struts are fused directly in the powder bed without support material. This leads to two effects: (i) adhesion of additional powder due to heat accumulation because of insufficient heat transfer to the build platform and (ii) notches where the higher density melt sank down in the powder bed and therefore is not bonded to the next layer. Both effects result in a rougher surface and deviations from the desired geometry. Thus, the minimum ( $d_{h,\min}$ ) and maximum horizontal diameter  $d_{h,\max}$  are distinguished for the metal lattice structures (each 24 measurements per specimen).

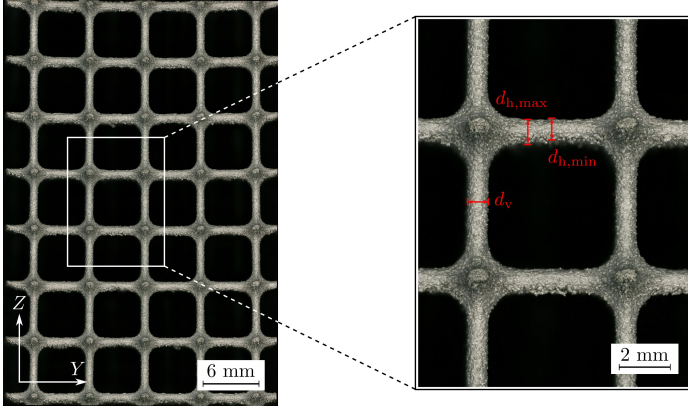


**Figure 2.10:** Micrograph of a metal lattice structure specimen used for the geometry characterization with indicated strut diameter measurements in vertical building direction  $Z$  ( $d_v$ ) as well as in horizontal layer plane  $XY$  ( $d_{h,\min}$ ,  $d_{h,\max}$ ).

Since the manufacturing costs of the polymer lattice structures are lower, also the strut dimensions in the inner part of the lattice are explored to get additional insights. Therefore, the load introduction is removed and the remaining lattice is sliced in five parts by a precision saw as depicted in Fig. 2.11. Then, a micrograph of each slice is taken and the vertical  $d_v$  and horizontal diameters  $d_h$  of the struts are evaluated. As the surface of the horizontal struts of the polymer lattice structures is smooth, both diameters are measured in the middle of the strut. The cut horizontal struts show a non-circular cross-section with material adhesions in the horizontal direction. These stem from insufficient removal of excess resin since the isopropanol flow during washing is only in horizontal direction. Flow in the vertical direction is prevented by the solid base plates. The excess resin has a different appearance (color and opacity) indicating that it is not fully cured. Hence, it is not considered to be load bearing. The excess resin is not considered in the diameter measurements by taking the measurement perpendicular to it. A total of six specimens is analyzed, yielding 150 vertical and 144 horizontal strut diameter measurements.

### 2.2.5 Differential Scanning Calorimetry

Zguris [120] suggests post-curing of the SLA manufactured methacrylate photopolymer at  $60^\circ\text{C}$  for 1 h in a UV oven. However, it remains unclear why this conclusion is drawn as the strength of the material still increases for curing longer

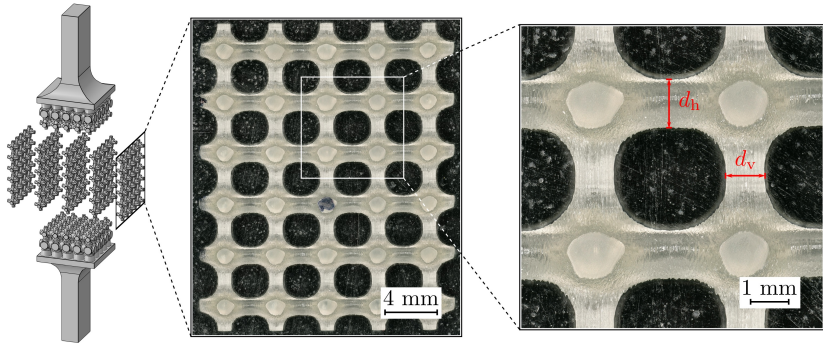


**Figure 2.11:** Cutting of the polymer lattice structure specimens and micrograph analysis for the geometry characterization by strut diameter measurements. The diameter of vertical struts  $d_v$  in loading direction and horizontal struts  $d_h$  perpendicular to it are highlighted.

than 1 h. An own preliminary study showed that stiffness and strength reach a plateau after approximately 4 h. For quality control of the curing degree of the methacrylate photopolymer specimens, a thermal analysis is performed by DSC (DSC 204 F1 Phoenix, NETZSCH-Gerätebau GmbH, Selb, Germany). An exemplary sample of approximately 15 mg is cut from the specimens and analyzed from  $-20\text{ }^\circ\text{C}$  to  $230\text{ }^\circ\text{C}$  with a rate of  $20\text{ K min}^{-1}$  under nitrogen atmosphere. A dog-bone specimen is tested (i) as printed without post-curing, (ii) post-cured only in the oven at  $60\text{ }^\circ\text{C}$  for 2 h and (iii) post-cured only by UV radiation for 2 h as references to investigate the different influences of the the curing mechanisms. Moreover, (iv) a dog-bone specimen and (v) a lattice structure, both post-cured in a UV oven at  $60\text{ }^\circ\text{C}$  for 4 h, are examined. Incomplete curing is visible by residual reaction enthalpy occurring during heating the sample.

### 2.2.6 Mechanical Testing

For the Ti-6Al-4V material characterization 57 uniaxial tensile tests according to DIN EN ISO 6892-1 [121] are performed on a universal testing machine (1484, Zwick, Ulm, Germany) with a strain rate of  $0.00007\text{ s}^{-1}$  for the elastic modulus and  $0.00025\text{ s}^{-1}$  for yield stress, tensile strength and elongation at break. Contacting strain measurements are conducted with an extensometer with sensor arms. Ball and socket joints are utilized at the clamping to guarantee uniaxial loading.

In order to determine the variation of the methacrylate photopolymer material properties, uniaxial tensile tests according to DIN EN ISO 527-1 [122] are

performed on a universal testing machine (Z2.5, ZwickRoell GmbH & Co. KG, Ulm, Germany) with a crosshead speed of  $0.25 \text{ mm min}^{-1}$ . Nine specimens are tested and clamped by screw grips. As polymers often show a tension-compression asymmetry [123], also uniaxial compressive tests conforming with DIN EN ISO 604 [117] are executed. A universal testing machine (Z010, ZwickRoell GmbH & Co. KG, Ulm, Germany) with a crosshead speed of  $1 \text{ mm min}^{-1}$  is utilized to evaluate 15 specimens. Polypropylene (PP) films are placed between the dies and specimens to avoid bulging due to friction during the experiment. The critical strain energy release rate can be used to capture progressive damage in FEM simulations. Therefore, SENB tests in agreement with ASTM D5045 [118] are conducted on a universal testing machine (Z2.5, ZwickRoell GmbH & Co. KG, Ulm, Germany) where the specimens are supported by rollers with a diameter of 6 mm and a spacing of 32 mm. A crosshead speed of  $10 \text{ mm min}^{-1}$  is used to test ten specimens. In order to determine the initial crack length, the fracture surface of the SENB specimens is captured by light optical microscopy (BX51, Olympus Deutschland GmbH, Hamburg, Germany) subsequent to the mechanical tests.

The mechanical characterization of the metal lattice structure specimens is carried out on a universal testing machine (Z400, ZwickRoell GmbH & Co. KG, Ulm, Germany) with a strain rate of  $0.00025 \text{ s}^{-1}$ . For tensile tests wedge clamping jaws are utilized and seven specimens with  $Z$  orientation as well as four specimens with  $XY$  orientation are tested for each volume fraction. Compressive tests are performed between dies and eight specimens are analyzed for each volume fraction. To avoid bulging of the specimens, also here PP films are placed between the dies and the specimens.

The polymer lattice structures are mechanically characterized under tension on a universal testing machine (Z2.5, ZwickRoell GmbH & Co. KG, Ulm, Germany) with a crosshead speed of  $1 \text{ mm min}^{-1}$  and a clamping with screw grips. The analysis consists of 19 specimens. As the performance of lattice structures is often evaluated against bulk material with regard to the weight savings, homogenized properties are desirable. The force  $F$  carried by a cross-section  $A_{\text{hom}}$  of the volume enclosing all unit cells is used to obtain the homogenized engineering stress  $\sigma_{\text{hom}}$  of the metal and polymer lattice structure specimens as depicted in Fig. 2.12.

Strain measurements for all lattice structure specimens, for six metal bulk tensile specimens and for all polymer bulk tensile and compressive specimens are performed with 3D DIC (Aramis 4M, GOM GmbH, Braunschweig, Germany). For this purpose, the specimens are coated with white aerosol paint. After drying, a speckle pattern with black aerosol paint is applied. DIC measurements allow to determine the engineering strain on the tensile and compressive bulk specimens by continuously tracking the distance change between two points, very similar to classical measurements with an extensometer. In that case, the initial measuring distance is chosen to 30 mm for the metal specimens according to DIN 50125 [112]. For the polymer specimens it is chosen to 10 mm according to the standards DIN

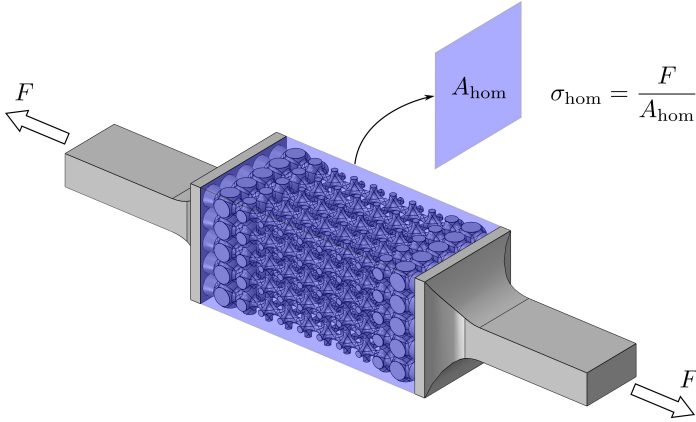


**Figure 2.12:** Determination of the homogenized engineering stress for the lattice structures (exemplarily shown for a polymer lattice structure).

EN ISO 527-2 [116] and DIN EN ISO 604 [117]. Moreover, DIC measurements allow to evaluate the macroscopic homogenized strain of the lattice structures in a similar way without the influence of the load introduction geometry. Here, the homogenized engineering strain  $\varepsilon_{\text{hom}}$  is captured by continuously tracking the distance change  $\Delta L$  between two points on the lattice structures with an initial distance  $L_0$  (see Fig. 2.13). The unit cells in the middle part of the specimen are considered, where no influence of the pyramid or gradient in volume fraction is present.

An even bigger advantage of DIC measurements is that they allow to measure the whole strain field. Hence, higher local strains at the necking of the tensile bulk specimens and in the individual struts of the lattice structure specimens can be visualized. The DIC software (Aramis 2016, GOM GmbH, Braunschweig, Germany) allows the evaluation at a single point of the true strain field. However, these single point measurements often show highly oscillating results, when facets are not recognized well. This is interpreted by the software as artificially large distortions. Instead, to determine the true strain of the tensile bulk specimens, the changing distance  $L$  between two points in the necking region, with an initial distance  $L_0$  of approximately 1 mm, is monitored. The initial distance is chosen in such a way that the highest homogeneous strain in the necking is captured. The true strain  $\varepsilon_{\text{true}}$  is then calculated by integration with

$$\varepsilon_{\text{true}} = \int_{L_0}^L \frac{1}{L} dL = \ln \left( \frac{L}{L_0} \right). \quad (2.2)$$

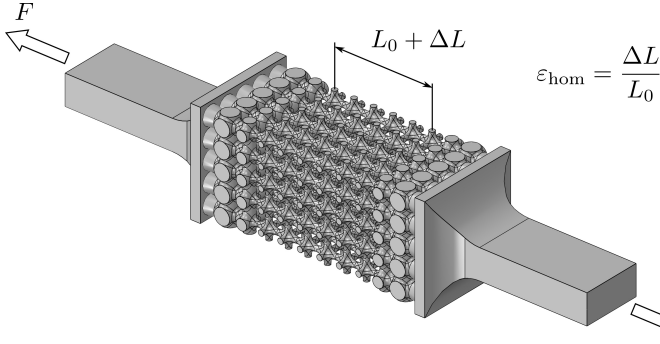


**Figure 2.13:** Determination of the homogenized engineering strain for the lattice structures (exemplarily shown for a polymer lattice structure).

Moreover, the transverse contraction in the necking area of the tensile bulk specimens can be studied by DIC measurements without previously knowing its location as a larger measurement volume can be observed. The transverse strain is recorded by the distance change between two points spanning the width of the specimen in the necking region. Assuming that the material is isotropic, this gives insights in the change in cross-sectional area and thus allows to determine the true stress. True stresses and strains are essential for the material model in the numerical analysis as finite deformations are considered. All of the methacrylate photopolymer bulk tensile specimens are investigated with DIC as the variation of the material properties determined from true strains and stresses shall be captured in the material model. Only six Ti-6Al-4V bulk tensile specimens are examined with DIC since one representative curve is used for material model calibration.

After the description of the experimental procedure, the applied analytical and numerical modeling approaches for lattice structures are presented subsequently.

### 2.2.7 Analytical Formulas for Cubic Lattice Strength and Buckling

Simple analytical formulas can help to predict an approximate failure of cubic lattice structures faster than with FEM simulations. An estimate of the homogenized strength  $\sigma_{\text{m,hom}}$  can be calculated by

$$\sigma_{\text{m,hom}} = \frac{A}{A_{\text{hom}}} \sigma_{\text{m,eng}} = \frac{n_{\text{struts}} \frac{\pi}{4} d^2}{A_{\text{hom}}} \sigma_{\text{m,eng}}, \quad (2.3)$$

where  $A$  is the smallest cross-sectional area of a lattice specimen,  $A_{\text{hom}}$  is the cross-sectional area of the volume enclosing all unit cells (see Fig. 2.12),  $\sigma_{\text{m,eng}}$  is

the nominal tensile strength,  $n_{\text{struts}}$  is the number of struts in the smallest cross-section of a lattice specimen and  $d$  is the average minimum strut diameter ( $d_v$  in the case of structures with aligned building and loading direction and  $d_{h,\min}$  in the case of structures with perpendicular building and loading direction).

In order to evaluate whether microbuckling of individual struts occurs in compression, an estimate with Euler's critical buckling load  $F_{\text{crit}}$  can be made. Loading case 4 with fixed clamping at both ends is assumed as the thicker intersections of the struts prevent rotations. The critical load is given by

$$F_{\text{crit}} = \frac{\pi^2 E_{\text{eng}} I_{\text{circ}}}{(0.5l)^2}, \quad (2.4)$$

with  $E_{\text{eng}}$  being the nominal elastic modulus of the bulk material,  $l$  being the unsupported length of the strut and  $I_{\text{circ}}$  being the area moment of inertia of a circle

$$I_{\text{circ}} = \frac{\pi}{64} d_v^4. \quad (2.5)$$

### 2.2.8 Random Fields and Variography

The variation of properties such as geometry or material parameters is often spatially correlated. The properties at two different spatial points are usually more similar, the closer the points are. The reason for this is the manufacturing process. For instance in the case of the SLA printed methacrylate photopolymer, when there is shadowing in the post-curing process with the UV oven, then not only one tiny spot is affected, but also the regions around this spot see less curing energy due to partial shadowing. Hence, random fields are used to model a spatial correlation between the varying properties in the FEM simulations [124]. A constant trend of the properties, a similar distribution at all spatial points and no directional dependence is assumed, thus resulting in a stationary, homogeneous and isotropic random field. Such a field for a property  $x$  can be generated from an uncorrelated random field by the inverse of the Mahalanobis transformation [125] with

$$\mathbf{x} = \mathbf{\Sigma}^{\frac{1}{2}} \mathbf{z} + \boldsymbol{\mu}_x, \quad (2.6)$$

where  $\mathbf{z}$  is a vector of uncorrelated random numbers with zero mean and a standard deviation of one. The vector  $\boldsymbol{\mu}_x$  contains the mean of  $x$  and  $\mathbf{\Sigma}$  is the covariance matrix of  $x$ . Assuming a stationary random field with variance  $\sigma_x^2$ , the entries of the covariance matrix

$$\mathbf{\Sigma} = r(\Delta\xi) \sigma_x^2 \quad (2.7)$$

can be calculated from the spatial autocorrelation function  $r$  depending on the distance of two points  $\Delta\xi$ . The square root of the covariance matrix can be

calculated via spectral decomposition

$$\Sigma^{\frac{1}{2}} = \mathbf{Q}\mathbf{D}^{\frac{1}{2}}, \quad (2.8)$$

with  $\mathbf{Q}$  being a matrix containing the eigenvectors of  $\Sigma$  and  $\mathbf{D}$  being a diagonal matrix with the eigenvalues of  $\Sigma$  [87]. To save computational time, only eigenvalues that are at least a tenth of the largest eigenvalue are considered. The procedure is similar to the discrete Karhunen–Loève transformation [126].

For determining the appropriate autocorrelation function, a method widely spread in geostatistics is used: variography [127]. A measure for the difference of the property  $x$  at two spatial points with a certain separation distance is determined by the empirical Matheron semivariance

$$\gamma(h \pm \delta) = \frac{1}{2N(h \pm \delta)} \sum_{i,j \in N(h \pm \delta)} (x(\xi_i) - x(\xi_j))^2, \quad (2.9)$$

where  $h$  is the separation distance usually used as a discrete distance within a certain tolerance  $\delta$  where measurements are grouped,  $N$  is the number of point pairs with separation distance  $h$  and  $\xi_i$  as well as  $\xi_j$  are spatial points [128]. Afterwards, a mathematical function to describe the spatial relation is fitted through the variogram. For instance, the spherical model is given by

$$\gamma(h) = \begin{cases} c_0 + c \left( \frac{3h}{2r} - \frac{1}{2} \left( \frac{h}{r} \right)^3 \right) & \text{for } 0 < h \leq r, \\ c_0 + c & \text{for } h > r, \end{cases} \quad (2.10)$$

with  $c_0$  being the nugget,  $c + c_0$  being the sill and  $r$  being the range. The sill is often not easy to recognize because it is reached asymptotically [129]. Hence, the distance where 0.95 of the sill is reached is used as the correlation length  $l_c$ . For higher separation distances, there is only a small further increase in difference of the property  $x$ . To construct the variograms SCIKIT GSTAT is employed [130].

### 2.2.9 Local Probability Density Function Model

Determining the stochastic distributions of the mechanical properties for probabilistic FEM models is straightforward for properties that are affected by the whole specimen such as the stiffness. The distributions can be derived from the central moments and the histograms of the experimental results, which is called the “standard approach” in the following. However, for properties that are dominated by local events like the true strength and local fracture strain, the standard approach is not sufficient. The experiment only shows the weakest part of the specimen or in other words the volume with the biggest flaw, which was already found by Weibull [131]. Testing the remaining parts of the specimens for a second time would lead to a higher strength as the decisive defect in those sections of

the specimen is smaller than in the initial specimen [132]. This also means that the larger the tested volume, the weaker the experimental outcome as the probability to have a critical flaw is higher [133]. Assuming to have the distribution of the property from the sections with the biggest flaw over the whole specimen would lead to an artificially poor performance of the FEM model. However, a reasonable probability distribution is required to model the material variations of the methacrylate photopolymer specimens. Hence, a new method is proposed to determine the probability distribution of true strength and local fracture strain for the methacrylate photopolymer specimens, which is called “local probability density function (PDF) model” hereafter. It is based on the assumption that the specimens consist of sections that have different material properties depending on the flaws within them as depicted in Fig. 2.14a. The flaws are not considered directly but in a continuum mechanical sense as a homogeneous lower value of the property at that section. The basic idea is to find the probability  $p$  of the property  $x$  to be below ( $x \leq x_{\text{exp,min}}$ ) and especially above ( $x \geq x_{\text{exp,max}}$ ) the experimental results. Knowing these, a PDF  $f(x)$  can be determined. The procedure is illustrated in Fig. 2.14b.

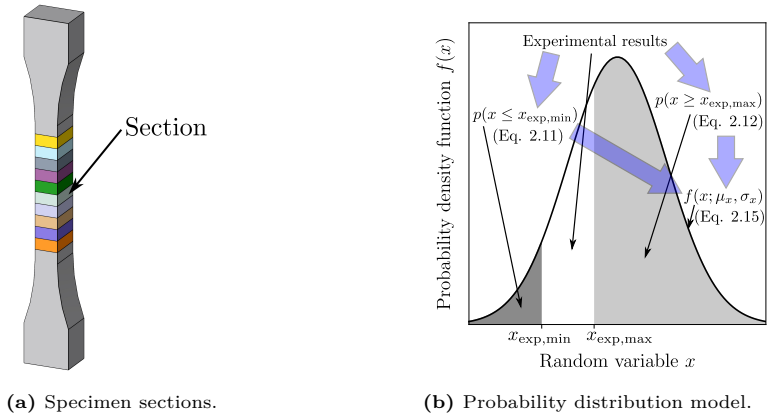


**Figure 2.14:** A dog-bone specimen assumed to consist of sections with different material properties and procedure to determine a model for the probability distribution of local weakest link properties.

First, the part on the left-hand side of the experimental results in the PDF is estimated. From all tested specimens with a specified number of sections only one has the minimal determined property or less. The probability  $p$  of a property

$x$  being below the lowest experimentally measured property  $x_{\text{exp,min}}$  is given by

$$p(x \leq x_{\text{exp,min}}) = \frac{1}{n_{\text{spec}} n_{\text{sec}}}, \quad (2.11)$$

where  $n_{\text{spec}}$  is the number of specimens tested and  $n_{\text{sec}}$  is the number of sections per specimen with homogeneous properties. To estimate the part on the right-hand side of the experimental results in the PDF, a tree diagram helps to visualize the derivation (see Fig. 2.15). Only for one of the tested specimens all the sections are greater or equal to the highest experimental result. The probability  $p$  of a property  $x$  being above the highest experimentally measured property  $x_{\text{exp,max}}$  can be calculated by

$$\begin{aligned} p(x \geq x_{\text{exp,max}})^{n_{\text{sec}}} &= \frac{1}{n_{\text{spec}}} \\ \Leftrightarrow p(x \geq x_{\text{exp,max}}) &= \exp\left(\frac{1}{n_{\text{sec}}} \ln\left(\frac{1}{n_{\text{spec}}}\right)\right). \end{aligned} \quad (2.12)$$

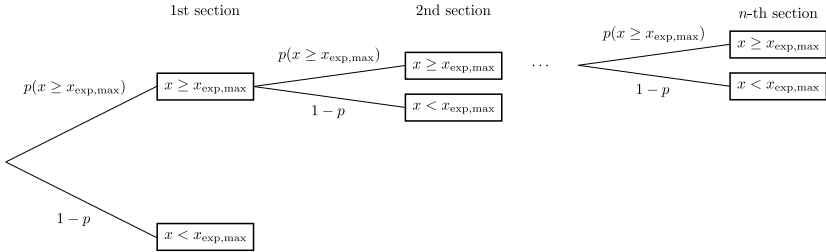


**Figure 2.15:** Tree diagram for the probability of a specimen consisting only of sections with the property  $x$  being above the highest experimentally measured result  $x_{\text{exp,max}}$ , visualizing the derivation of Eq. (2.12).

To strengthen this hypothesis the limiting cases are considered. When an infinite number of specimens is tested, the possibility is close to zero for higher values of the property than found in the experiments

$$\lim_{n_{\text{spec}} \rightarrow \infty} p(x \geq x_{\text{exp,max}}) = 0. \quad (2.13)$$

Testing infinitely long specimens means that there is an infinite number of sections with the property being above the highest value found in the experiments

$$\lim_{n_{\text{sec}} \rightarrow \infty} p(x \geq x_{\text{exp,max}}) = 1. \quad (2.14)$$

In other words, the more specimens are tested, the better the boundaries of the distribution are known. The longer the specimens are, the less is known about the part on the right-hand side of the maximum value that was measured.

Having two fixed points on the PDF, a normal distribution can be fitted by solving a nonlinear system of equations with the unknowns  $\mu_x$  and  $\sigma_x$

$$\begin{bmatrix} \int_{-\infty}^{x_{\text{exp,min}}} f(x; \mu_x, \sigma_x) dx - p(x \leq x_{\text{exp,min}}) \\ \int_{x_{\text{exp,max}}}^{\infty} f(x; \mu_x, \sigma_x) dx - p(x \geq x_{\text{exp,max}}) \end{bmatrix} = \begin{bmatrix} 0 \\ 0 \end{bmatrix}, \quad (2.15)$$

where  $f(x; \mu_x, \sigma_x)$  is the PDF of the experimental property  $x$  depending on the parameters mean  $\mu_x$  and standard deviation  $\sigma_x$ . A normal distribution is used, since the real distribution is unknown and according to the central limit theorem, adding up independent identically distributed random effects, the overall effect tends to the normal distribution for a large number of samples. However, any other distribution with two parameters defining the shape can analogously be applied.

### 2.2.10 Finite Element Modeling

FEM simulations are performed with the commercial FEM code ABAQUS 6.14 for the metal models and ABAQUS 2019 for the polymer models. Finite deformations are considered in all models. Elastoplasticity with continuum damage is employed for both material models in order to capture the progressive failure of the lattice structures. ABAQUS' built-in von Mises plasticity model is used for Ti-6Al-4V in which the yield function  $\Phi$  is given by

$$\Phi = \sigma_{\text{vM}} - \sigma_y \leq 0, \quad (2.16)$$

where  $\sigma_y$  is the yield stress and  $\sigma_{\text{vM}}$  is the von Mises equivalent stress given by

$$\sigma_{\text{vM}} = \sqrt{\frac{3}{2}(\text{dev}(\boldsymbol{\sigma}) : \text{dev}(\boldsymbol{\sigma}))}. \quad (2.17)$$

Here,  $\text{dev}(\boldsymbol{\sigma})$  is the deviator of the Cauchy stress tensor

$$\text{dev}(\boldsymbol{\sigma}) = \boldsymbol{\sigma} + p_{\text{hyd}}\mathbf{1}, \quad (2.18)$$

with  $p_{\text{hyd}}$  being the hydrostatic pressure and  $\mathbf{1}$  being the identity tensor. Associated flow is used and the hardening law is obtained by a multilinear curve of the yield stress depending on the plastic strain from the uniaxial tensile experiments of the bulk material.

In order to account for the differences of tensile and compressive strength of the methacrylate photopolymer, an asymmetric elastoplasticity material model is utilized. A Drucker-Prager model [134, 135] is suggested by Morelle *et al.* [136] as good engineering practice without the need for coding a user defined subroutine for the modeling of thermosetting polymers. Hence, ABAQUS' built-in hyperbolic Drucker-Prager plasticity model is used, where the yield function  $\Phi$  is given by

$$\Phi = \sqrt{(d'_0 - p_{t0} \tan(\beta_f))^2 + \sigma_{vM}^2} - p_{hyd} \tan(\beta_f) - d' \leq 0, \quad (2.19)$$

where  $\beta_f$  is the friction angle (that is the asymptotic slope in the meridional plane),  $p_{t0}$  is the initial hydrostatic tensile strength,  $d'$  is the hardening parameter and  $d'_0$  is the initial value of the hardening parameter. The hardening parameter is obtained by

$$d'(\sigma_{yt}) = \sqrt{(d'_0 - p_{t0} \tan(\beta_f))^2 + \sigma_{yt}^2} + \frac{\sigma_{yt}}{3}, \quad (2.20)$$

where  $\sigma_{yt}$  is a multilinear curve of the yield stress depending on the plastic strain from the uniaxial tensile experiments of the bulk material. For polymers, generally nonassociated flow is assumed [123]. The flow potential is given by

$$\Psi_{flow} = \sqrt{(\epsilon \sigma_{yt0} \tan(\psi))^2 + \sigma_{vM}^2} - p_{hyd} \tan(\psi), \quad (2.21)$$

with  $\sigma_{yt0}$  being the initial tensile yield stress,  $\psi$  being the dilatation angle and  $\epsilon$  being the eccentricity, a parameter determining the bending of the flow potential.

Damage is initiated with ABAQUS' built-in ductile criterion for both, Ti-6Al-4V and the methacrylate photopolymer. Although it is intended for metals it has been previously applied successfully for a thermosetting polymer by Chevalier *et al.* [137]. When the accumulated equivalent plastic strain  $\bar{\epsilon}_p$  reaches the plastic strain at the onset of damage  $\bar{\epsilon}_{p,D}$ , the stress carrying capability of the element is reduced linearly

$$\boldsymbol{\sigma}_D = (1 - D)\boldsymbol{\sigma}, \quad (2.22)$$

where  $\boldsymbol{\sigma}_D$  is the stress tensor of a damaged element and  $D \in [0, 0.95]$  is the damage variable. An energy-based damage evolution is chosen to avoid mesh dependency. The accumulated equivalent plastic strain at failure  $\bar{\epsilon}_{p,f}$  is determined from the critical energy release rate

$$G_{Ic} = \int_{\bar{\epsilon}_{p,D}}^{\bar{\epsilon}_{p,f}} L_{ele} \sigma_y d\bar{\epsilon}_p, \quad (2.23)$$

with  $L_{ele}$  being the characteristic element length. Due to instabilities caused by progressive damage an implicit dynamic time integration method with a backward Euler operator is used, allowing improved convergence behavior [123]. As symmetry of the material Jacobian is lost when the ductile damage evolution model is

utilized, an unsymmetric equation solver is applied [123]. Viscous regularization is employed to further overcome convergence difficulties [123].

The Ti-6Al-4V material model is calibrated with a representative true stress-strain curve obtained from DIC measurements of uniaxial tensile tests on bulk material (see Section 2.2.6). A fine tuning of the material model is performed with a simulation of the bulk material tensile test where a slight variation of the true fracture strain and the true tensile strength is carried out. By this, the necking behavior is adjusted. All three translational degrees of freedom are fixed at one end of the bulk specimen model and a tensile displacement is applied at the other end. For the discretization of all specimen FEM models, ABAQUS' C3D10 tetrahedral 3D continuum elements with quadratic shape functions are utilized. These allow to resolve complex 3D stress fields and are able to capture complex geometries, which is required for the lattice structures. For consistency, they are also applied for metal and polymer bulk tensile specimen models. The metal bulk tensile specimen model is shown in Fig. 2.16a.

The methacrylate photopolymer material model is calibrated with the average true stress-strain curve obtained from DIC measurements of uniaxial tensile tests on dog-bone specimens (see Section 2.2.6). Although polymers show a slight nonlinearity at very small deformations, it is assumed that they behave linear elastic until plastic flow occurs, when 70 % of the yield stress (defined by the horizontal tangent in the stress-strain curve in polymer standards [117, 122]) is reached. Viscous effects are not included as only the quasi-static behavior is analyzed. This reduces computational time and the deviations are small. The tension-compression asymmetry is adjusted with 70 % of the compressive yield stress analogously. Displacement controlled, single element tests on hexahedrons under uniaxial tension and compression are carried out to verify the material model.

Then, methacrylate photopolymer dog-bone specimen models are simulated to validate the probability distribution of the material properties. All three translational degrees of freedom are fixed at one end of the dog-bone model and a tensile displacement is applied at the other end. The elastic modulus as a global material property is homogeneous over the whole specimen model but varies stochastically between the realizations. Local material properties like strength and fracture strain are assigned by random fields in the narrow parallel part of the specimen model. The variation of the strength is realized by shifting the hardening law (see Eq. (2.20)) to higher or lower stresses. The individual sections with homogeneous material properties are chosen to be approximately  $1\text{ mm} \times 1\text{ mm} \times 1\text{ mm}$  corresponding to the length of the homogeneous necking area in the DIC measurements (see Section 2.2.6). Basically, these sections are defined by slicing up the specimen model in cubes and then assigning the same material properties to all elements within one of these cubes. Figure 2.16b illustrates the individual material sections of the methacrylate photopolymer dog-bone specimen model

by different colors. Probability distributions of the material properties with the standard approach are compared with the local PDF model.

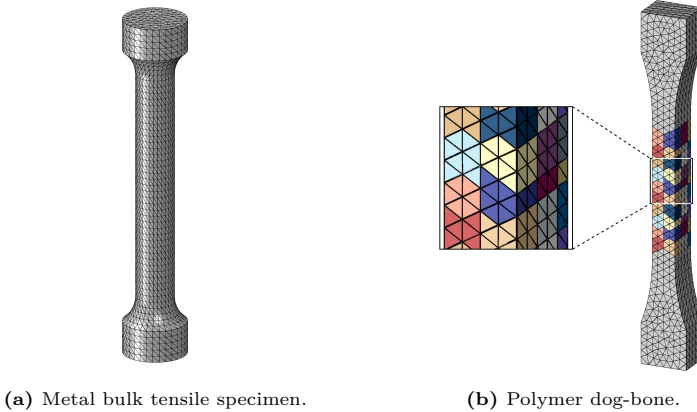


**Figure 2.16:** FEM models of the bulk material tensile test specimens for metal (Ti-6Al-4V) and polymer (methacrylate photopolymer). Individual material sections of the polymer dog-bone model are highlighted by different colors.

Finally, lattice structure specimen models are simulated in order to get further insights into the deformation as well as progressive damage and failure behavior. For the polymer lattice structures also the probability distribution of the combination of varying geometrical and material properties is validated. The geometry of the lattice structures is generated with a PYTHON script, allowing for the automatic construction of parametric models. For polymer lattice structures random fields are utilized to assign individual vertical and horizontal strut diameters on the CAD geometry level. The probability distribution of material properties for the unit cells in the middle with no gradient in volume fraction is realized analogously to the polymer dog-bone specimen models. In order to save computational time, symmetry is used for the simulation of the lattice structures. For the tensile metal lattice structures an eighth of the specimen is modeled, using symmetry in all three Cartesian coordinate directions. For the compressive metal and the tensile polymer lattice structures half of the specimen is modeled and symmetry is only applied in the plane normal to the loading direction. Symmetry in the other two planes is lost when buckling occurs in case of the compressive metal lattice structures. Strictly speaking, for the tensile polymer lattice structures symmetry is lost due to the stochastic variation of the properties. However, by

the approach of using one symmetry plane at least entire loaded cross-sections are modeled while limiting the computational cost. The deformation is displacement controlled at the end of the load introduction for all lattice structure models. Figure 2.17a and Fig. 2.17b depict tensile and compressive metal lattice structure models. A realization of a tensile polymer lattice structure model with individual material sections indicated by different colors is presented in Fig. 2.17c. Realizations with a stochastic variation of only the geometry, only the material and both combined are investigated to get insight in their individual influence.

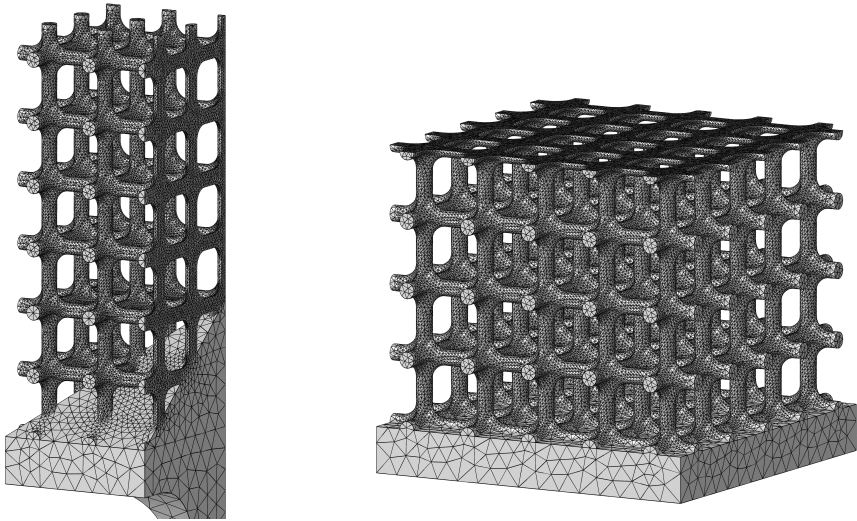
To further reduce computational time, also tensile and compressive tests on metal unit cell models with PBCs are performed. The methacrylate photopolymer is not considered here as the stochastic variation of a lattice structure model (having approximately 750 000 elements and 1 150 000 nodes) cannot be captured by one unit cell. The model size for the metal lattice structures and the periodic unit cells is presented for comparison in Tab. 2.4. The utilization of periodic unit cells results in a significant reduction of the model size. For instance, the 6 % volume fraction unit cell model has less than 2 % of the nodes of the compressive lattice structure model. In addition, the unit cell simulations with PBCs allow to assess whether the utilized specimens in the experiments are suitable to determine homogenized mechanical properties of the lattice structures or if undesired effects of the load introduction influence the results.

**Table 2.4:** Comparison of the model size for metal lattice structures and periodic unit cells.

Model	Volume fraction	Elements	Nodes
Lattice structure tensile	6 %	496 038	785 982
	13 %	346 283	540 731
	20 %	255 058	397 468
Lattice structure compressive	6 %	1 315 320	2 106 087
	13 %	921 786	1 451 546
	20 %	658 712	1 032 485
Unit cell periodic	6 %	23 923	36 628
	13 %	49 101	71 807
	20 %	12 087	18 498

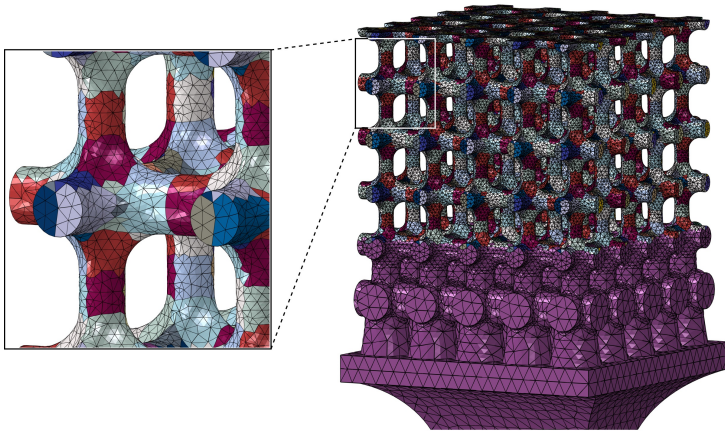
## 2.3 Results and Discussion

This section discusses the results of the study on additively manufactured lattice structures. First, findings of the quality control of porosity and microstructure for Ti-6Al-4V, the curing degree of the methacrylate photopolymer and the geo-



(a) Tensile metal lattice.

(b) Compressive metal lattice.



(c) Tensile polymer lattice.

**Figure 2.17:** FEM models of the lattice structure specimens for metal (Ti-6Al-4V) and polymer (methacrylate photopolymer). The clamping area of the tensile specimens is not shown. Individual material sections of the tensile polymer lattice structure model are highlighted by different colors.

metrical accuracy of lattice structures from both materials are presented. Then, the experimentally determined mechanical properties of the bulk material and lattice structure specimens are shown and discussed with regard to influences of load case, volume fraction, building direction and probabilistic effects. Moreover, the outcome of the procedure to determine the correlation length by variography is depicted and the stochastic variations stemming from the local PDF model are demonstrated. Afterwards, the comparison of FEM simulations and experiments is discussed on the level of the bulk specimens concerning the material model calibration and on the global level of the lattice structure specimens regarding the progressive damage and failure. Finally, a computationally more efficient approach of unit cell simulations with PBCs for homogenization is illustrated also giving insights into the effect of the load introduction.

### 2.3.1 Quality Control: Porosity, Microstructure and Curing Degree

The results for the quality control of the AM process are presented in the following. For SLM manufactured Ti-6Al-4V, the porosity and microstructure is investigated. Figure 2.18 presents micrographs of bulk material and an exemplary lattice structure, showing their porosity and microstructure. In both, bulk material and lattice structure, pores are present. With regard to the microstructure, both SEM images show a combination of  $\alpha'$  martensite and very fine  $\alpha + \beta$  phase inside prior  $\beta$  grains. The  $\alpha'$  martensite develops because of the rapid cooling rates during the SLM process (see Section 2.2.1), while some of it transforms to a fine  $\alpha + \beta$  phase during the stress release annealing [138–140]. A change in microstructure due to heat treatment has also been observed in studies on other SLM alloys [141]. The prior  $\beta$  grains have a columnar shape in building direction. As heat conduction is mostly downward to the build platform, so is their solidification. While heat transfer to the neighboring sides within the bulk material occurs, this is not possible with lattice structures. The thin struts are surrounded by powder that does not have a good heat conductivity and acts like an insulator. Hence, the lattice structures show thinner prior  $\beta$  grains [67, 142, 143].

For SLA manufactured methacrylate photopolymer, the quality of the specimens is analyzed in terms of the curing degree, respectively the residual reaction enthalpy. The results of the thermal analysis by DSC are displayed in Fig. 2.19 with the specific heat flow depending on the temperature. The as printed dog-bone specimen with no post-curing shows two residual reaction enthalpy peaks: one at a temperature of approximately 80 °C and one at 165 °C. Comparing the only oven post-cured sample with the only UV radiation post-cured, it gets evident that both curing mechanisms, temperature and UV radiation, are necessary for complete curing. The first peak vanishes almost completely by oven curing, the second peak vanishes by UV curing. UV radiation is required for the de-

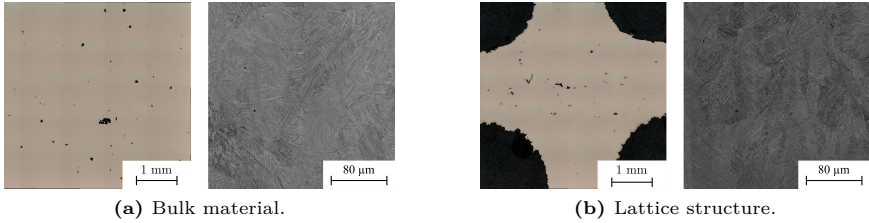


**Figure 2.18:** Micrographs showing the porosity and microstructure of Ti-6Al-4V bulk material and lattice structure.

composition of remaining photoinitiator molecules to form free radicals. Higher temperatures are essential for the mobility of the molecules to avoid occlusion (see Section 2.2.2). For the sample from the dog-bone specimen and that from within the lattice structure, which are both post-cured in the UV oven for 4 h, almost no residual reaction enthalpy is left and the curves match well. They have a similar curing degree and are fully cured. Higher curing temperatures are not recommended since the heat deflection temperature is reached [120].

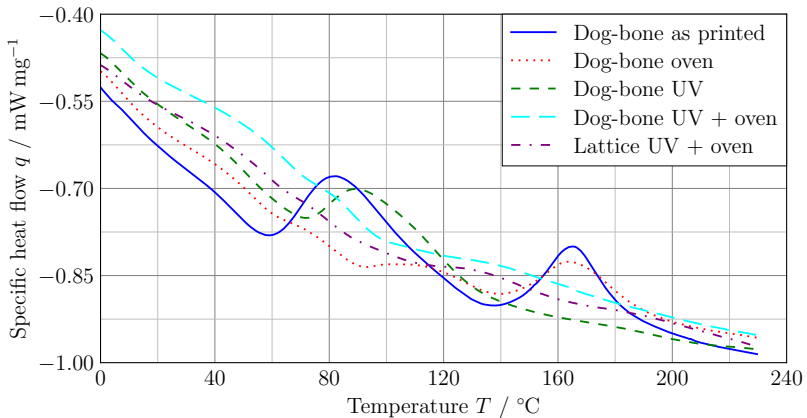


**Figure 2.19:** First heating segment of DSC measurements showing the specific heat flow versus temperature. Exothermal flow is indicated upwards.

### 2.3.2 Geometry Characterization

The results of the geometry characterization of the metal lattice structures are presented in Fig. 2.20. The strut diameter depending on the volume fraction, building direction and loading type is shown as well as a desired reference diameter from the CAD files. For tensile as well as compressive specimens, the strut diameter  $d_v$  in building direction ( $Z$ ) is slightly smaller than the desired CAD diameter. The variation is relatively small (sample coefficient of variation  $v$  smaller than 3%). For tensile specimens, minimum  $d_{h,\min}$  and maximum diameter  $d_{h,\max}$  of the struts in layer plane ( $XY$ ) show a higher variation. Especially, the minimum diameter for lower volume fractions has a significant number of outliers to the lower end. The smaller the diameter, the more volume of the strut is built in the first layer on the powder bed and the narrower the layer. This yields increased probability of notches as the higher density melt can sink down in the powder bed not being fused to the next layer. The average minimum diameter of the struts in layer plane matches the CAD diameter approximately, while the maximum diameter is significantly higher. This can be explained by the powder adhesions that result from fusing directly on the powder bed, which yields significant deviations from the desired diameter (see Section 2.2.4).

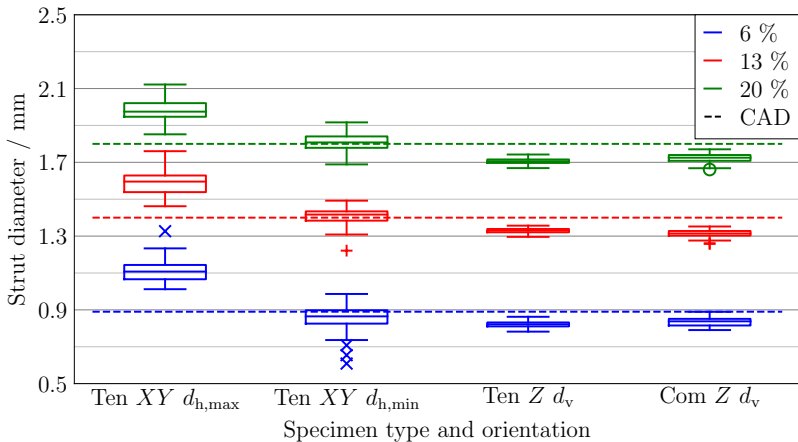


**Figure 2.20:** Strut diameter of the metal lattice structures depending on the volume fraction, building direction and loading type. The desired diameter from the CAD files is given as a reference with dashed lines.

Figure 2.21 shows the results of the geometry measurements of the polymer lattice structures. The smallest strut diameter depending on the strut orientation is shown together with the desired reference diameter from the CAD files. Despite the different manufacturing process and material, the findings are similar to the metal lattice structures. The diameter  $d_v$  of the vertical struts is slightly smaller than the desired CAD diameter. The variation is relatively small (sample coefficient of variation  $v$  approximately 2%). The diameter  $d_h$  of the horizontal struts is significantly larger than the desired CAD diameter and shows a higher variation. Furthermore, there are more outliers, especially towards the larger diameters. This can be explained by the fact that the horizontal struts are printed without a support structure as an overhang. Since the 3D printer Form 2 is an inverted SLA printer, the material at the bottom of the resin bath is cured. At an overhang, also the material on top of the current layer gets residual energy from the UV laser depending on the curing depth. Thus, it is at least partially cured and leads to an increased strut diameter. As a result for modeling the geometrical variation of the strut diameters, two individual random fields are necessary, accounting for the differences in vertical and horizontal diameters. For the vertical struts, a mean of 1.049 mm and a standard deviation of 0.023 mm is used, while for the horizontal struts, a mean of 1.271 mm and a standard deviation 0.04 mm is applied.

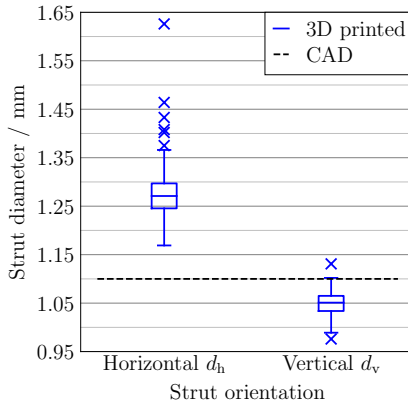


**Figure 2.21:** Strut diameter depending on the strut orientation. The dashed black line is the desired diameter from the CAD files.

### 2.3.3 Mechanical Properties of Bulk Material

The results of the mechanical characterization of the bulk Ti-6Al-4V are shown in Tab. 2.5 including mean  $\mu$ , sample standard deviation  $s$  and sample coefficient of variation  $v$ . All results presented in the table are nominal/engineering properties as they are determined with a contacting extensometer. The variation is relatively small for elastic modulus and especially for yield stress and tensile strength. However, the variation of the elongation at break is relatively high. This cannot be explained by surface roughness since the specimens were machined to the final geometry by turning. A reason for this could be pores within the bulk material (see Section 2.3.1) as there was no hot isostatic pressing (HIP) employed in the post-processing.

**Table 2.5:** Results of the mechanical characterization of the bulk Ti-6Al-4V with the mean  $\mu$ , sample standard deviation  $s$  and sample coefficient of variation  $v$ .

Parameter	$\mu$	$s$	$v$
Elastic modulus $E_{\text{eng}}$	116.12 GPa	11.72 GPa	10.09 %
Yield stress $\sigma_{y,\text{eng}}$	1058.84 MPa	13.80 MPa	1.30 %
Tensile strength $\sigma_{m,\text{eng}}$	1107.30 MPa	12.56 MPa	1.13 %
Elongation at break $\varepsilon_{f,\text{eng}}$	7.80 %	2.91 %	37.25 %

In order to calibrate the material model for the FEM simulations of the metal lattice structures, further properties are necessary. Since necking occurred in the experiments, true stresses and strains cannot be calculated from the nominal values. They are obtained from a DIC measurement where local strains can be observed in the necking region as described in Section 2.2.6. A bulk specimen representative of the overall set of experiments is analyzed. Slightly higher true tensile strength and true fracture strain are determined compared to the nominal/engineering properties. Table 2.6 provides the further parameters for the calibration of the material model along with the sources.

**Table 2.6:** Additional mechanical properties for the Ti-6Al-4V material model.

Parameter	Value	Source
True tensile strength $\sigma_m$	1214 MPa	DIC
True fracture strain $\varepsilon_f$	0.1163	DIC
Poisson's ratio $\nu$	0.34	[144]
Critical energy release rate $G_{Ic}$	7.34 J mm <sup>-2</sup>	[145]

The results of the mechanical characterization of the methacrylate photopolymer bulk material are summarized in Tab. 2.7 with the mean value  $\mu$ , sample standard deviation  $s$  and sample coefficient of variation  $v$ . All values of the tensile and compressive tests are presented in terms of nominal/engineering properties. The tension-compression asymmetry is very pronounced with the compressive yield stress being 67% higher than the tensile yield stress. This underlines the necessity that a material model, such as the Drucker-Prager model, considers this behavior. For the compressive specimens only the yield stress is used in this investigation. For higher deformations significant bulging of the specimens occurs despite the use of PP films to reduce friction. Hence, the deformation is not uniform anymore and a deduction of further properties would be erroneous. In the context of this study, this is not critical as the polymer lattice structures are also primarily loaded in tension and a compressive failure is not expected. Also the Drucker-Prager material model only needs the strength differential as an input from the compressive test.

**Table 2.7:** Results of the mechanical characterization of the methacrylate photopolymer with the number of specimens  $n_{\text{spec}}$ , mean  $\mu$ , sample standard deviation  $s$  and sample coefficient of variation  $v$ .

Experiment	$n_{\text{spec}}$	Parameter	$\mu$	$s$	$v$
Tension	9	Elastic modulus $E_{\text{eng}}$	2200.62 MPa	39.37 MPa	1.79%
		Yield stress $\sigma_{\text{yt,eng}}$	61.65 MPa	0.95 MPa	1.54%
		Elongation at break $\varepsilon_{\text{f,eng}}$	13.24%	2.79%	21.07%
Compression	15	Yield stress $\sigma_{\text{yc,eng}}$	102.92 MPa	2.38 MPa	2.31%
SENB	10	Critical energy release rate $G_{\text{Ic}}$	0.13 N mm <sup>-1</sup>	0.02 N mm <sup>-1</sup>	15.38%

Necking also occurs during the tensile testing of the methacrylate photopolymer dog-bone specimens. Therefore, true stresses and strains for material model calibration are obtained from DIC measurements in the necking region in the same way as for the Ti-6Al-4V specimens (see Section 2.2.6). However, in this case all specimens are considered as the material model is varied on that basis in the numerical models. Thus, a more in-depth analysis is carried out in the following. Figure 2.22 shows the true stress-strain curves of the dog-bone specimens together with the averaged curve. After an almost linear elastic regime, a significant nonlinearity can be observed beyond a strain of 0.02. This is assumed to be the point where plasticity begins within the material model. From a strain of about 0.06 a rather constant stress level is reached followed by a further increase until fracture of the specimen. This can be attributed to large collective molecular movements and subsequent alignment of the molecular network until chain scission [136]. As the level of the constant stress is characteristic for each specimen it is called plateau stress  $\sigma_{\text{pl}}$  in the following and taken at a strain of 0.08. When comparing the true strength  $\sigma_{\text{m}}$  and true fracture strain  $\varepsilon_{\text{f}}$  to their nominal

counterparts, both are significantly higher. This highlights the importance of the evaluation of local stresses and strains for material modeling. The points for the multilinear curve of the yield stress for the hardening law (see Eq. (2.20)) are obtained from the averaged true stress-strain curve. The averaged curve is extrapolated for higher values in order to represent an appropriate hardening until the stochastically varying fracture strain is reached.

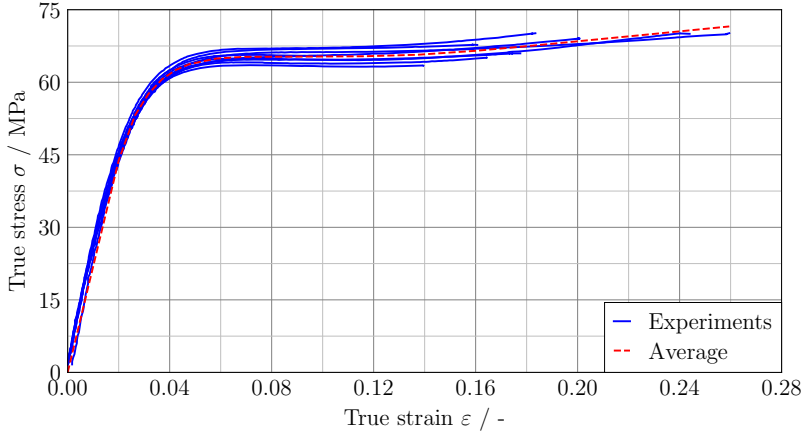


**Figure 2.22:** True stress-strain curves of the dog-bone specimens measured with DIC at the location of the necking. The averaged curve is extrapolated for higher values.

In order to get more insight into the probability distributions of the characteristic true mechanical properties of the methacrylate photopolymer, Kolmogorov-Smirnov tests are carried out. The null hypothesis is that the distribution of the properties follows a normal distribution. A significance level of  $\alpha = 0.05$  is chosen. Table 2.8 summarizes the outcome of the Kolmogorov-Smirnov tests. As the  $p$ -values are all far higher than the significance level, the null hypothesis cannot be rejected. The properties are assumed to be normally distributed.

**Table 2.8:** Kolmogorov-Smirnov tests to check if the characteristic true mechanical properties of the methacrylate photopolymer follow a normal distribution.

	$E$	$\sigma_{pl}$	$\sigma_m$	$\varepsilon_f$
$p$ -value	0.9483	0.9997	0.9204	0.9901

To further explore whether there is a correlation between the characteristic true mechanical properties of the methacrylate photopolymer, they are analyzed in a scatter matrix plot in Fig. 2.23, where the empirical cumulative distribution functions are shown on the diagonal. The results seem to be randomly distributed over the charts with no linear or nonlinear trend visible at a first glance. Only for strength and fracture strain, a linear trend can be recognized. Hence, from the scatter plots, all variables seem to be independent except for strength and fracture strain.

To have a further measure for the independence of the true mechanical properties of the methacrylate photopolymer, the Pearson correlation coefficient is calculated. The findings are presented in Tab. 2.9 together with the corresponding  $p$ -values. The null hypothesis is that the properties are not correlated. Applying a significance level of  $\alpha = 0.05$  for strength and fracture strain, the null hypothesis is rejected. Thus, they are assumed to depend on each other. Having a look at Fig. 2.22 this makes sense: when a high strain is reached, the polymer network is in a state of better alignment, thus leading to a higher strength because the polymer chains are stretched and there is less chain movement remaining. Therefore, the stress increases progressively for higher strains, which results in a positive correlation. Moreover, also for plateau stress  $\sigma_{pl}$  and strength  $\sigma_m$  the  $p$ -value is just below the significance level, also with a slight positive correlation. For all other combinations the null hypothesis cannot be rejected. The properties are assumed to be uncorrelated. Thus, three properties are varied stochastically in the numerical models to perform a probabilistic analysis of the methacrylate photopolymer material properties: (i) the elastic modulus  $E$ , (ii) the plateau stress  $\sigma_{pl}$  and (iii) the fracture strain  $\varepsilon_f$ . The latter two are applied with random fields as they are local properties. The variation in strength is captured implicitly since the whole hardening law is scaled up and down with the plateau stress (see Section 2.2.10) and depending on the fracture strain, the strength is reached earlier or later on that curve.

**Table 2.9:** Pearson correlation coefficient (and  $p$ -value) to check the correlation between the methacrylate photopolymer material properties derived from true strains and stresses.

	$\sigma_{pl}$	$\sigma_m$	$\varepsilon_f$
$E$	-0.0826 (0.8326)	-0.2383 (0.5369)	-0.2726 (0.4779)
$\sigma_{pl}$		0.6908 (0.0394)	0.1801 (0.6429)
$\sigma_m$			0.7664 (0.0160)

The identification of additional properties is needed to apply the hyperbolic Drucker-Prager material model for the methacrylate photopolymer FEM simu-

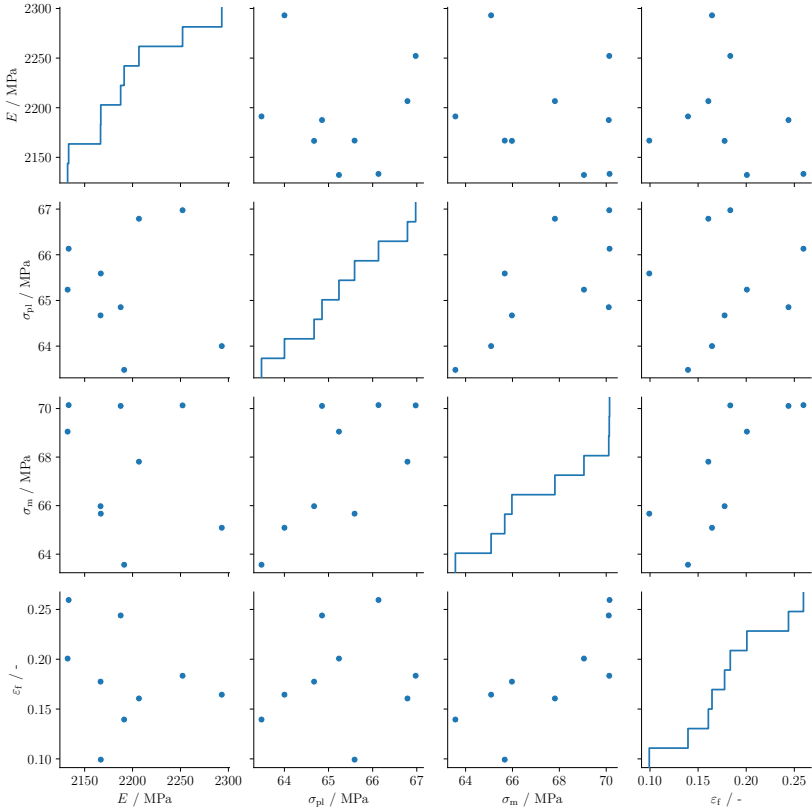


**Figure 2.23:** Scatter matrix plot to check correlation of the experimentally determined methacrylate photopolymer material properties derived from true strains and stresses. Empirical cumulative distribution functions are shown on the diagonal.

lations. These properties are presented in Tab. 2.10. Some of them are derived from the mechanical experiments on bulk material. The Poisson's ratio is calculated from comparisons of the true longitudinal and transverse strains taken from tensile tests in the linear elastic regime. The friction angle and initial hydrostatic tensile strength are determined with Eq. (2.19) based on the strength differential of the yield stress. The dilatation angle is chosen to be relatively small because there is no large volume change detected from the comparison of longitudinal and transverse strain in the plastic regime. In addition, for even smaller dilatation angles, convergence issues occur. Finally, the density is identified by the Archimedes' principle and the eccentricity is left at the default.

**Table 2.10:** Further properties for the methacrylate photopolymer material model.

Parameter	Value
Density $\rho$	1.17 g cm <sup>-3</sup>
Poisson's ratio $\nu$	0.4
Friction angle $\beta_f$	30°
Initial hydrostatic tensile strength $p_{t0}$	44 MPa
Dilatation angle $\psi$	10°
Eccentricity $\epsilon$	0.1

### 2.3.4 Mechanical Properties of Lattice Structures

In the following, the results of the static mechanical characterization of the lattice structures are discussed. Homogenized properties are obtained as described in Section 2.2.6. First, a detailed analysis of the metal lattice structures is presented considering the influence of several factors from design, manufacturing and loading. The investigation of the polymer lattice structures is kept short as no additional influences are considered and the focus is on the probabilistic distribution of the homogenized mechanical properties.

Figure 2.24 shows the homogenized elastic modulus depending on the volume fraction, loading type and building direction for the metal lattice structures. It gets evident that stiffness increases with increasing volume fraction. The stiffness in the tensile test is slightly higher for the  $XY$  specimens. This can be explained by powder adhesion on the bottom surface of the struts in the loading direction due to the overhang during the SLM process. This provides additional material in the loading direction and thus leads to an increased stiffness, which is a global property. With regard to stiffness, there is no significant difference between tensile and compressive loading.

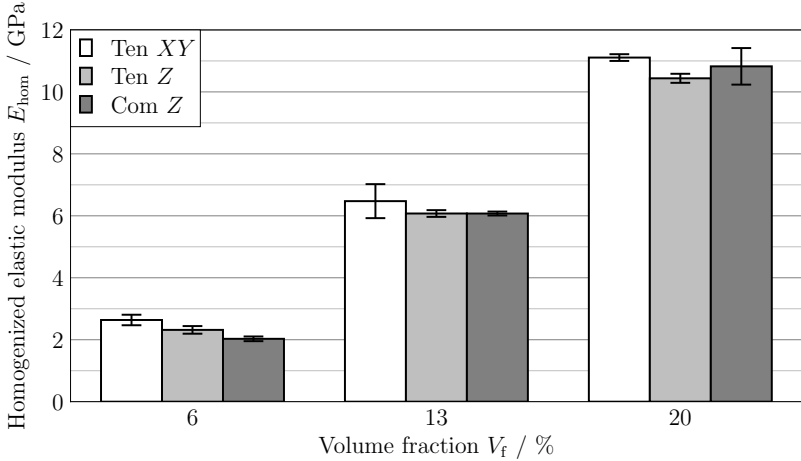


**Figure 2.24:** Homogenized elastic modulus of the metal lattice structures depending on volume fraction, loading type and building direction.

The homogenized strength of the metal lattice structures in the experiments depending on volume fraction, loading type and building direction is illustrated in Fig. 2.25. Additionally, a strength estimate (see Eq. (2.3)) based on the bulk Ti-6Al-4V tensile strength of Tab. 2.5 as well as the idealized CAD dimensions and the measured dimensions of the struts is shown. For the  $Z$  specimens the average vertical strut diameter  $d_v$  is used. For the  $XY$  specimens the average minimum horizontal strut diameter  $d_{h,\min}$  is used as strength is a property local to a plane of struts that has to carry the load. A general trend is that the strength increases with volume fraction. A distinction has to be made for the tensile test specimens depending on the loading direction. For experiments with 6% volume fraction, the  $XY$  specimens have a reduced strength compared to the  $Z$  specimens. At 13% and 20% volume fraction a reverse behavior can be observed. This can again be explained by the struts in the loading direction that are printed directly in the powder bed due to the overhang. There are two effects with regard to strength: (i) more load carrying material is available due to powder adhesions at the bottom surface of the struts and (ii) the notches due to poorly bonded powder and the irregularity of the adhesions lead to stress concentrations. Since the struts of the 6% cells are significantly thinner, the surface has a greater influence. Therefore, the notch effect is dominant leading to earlier failure with a reduced or completely without a plastic regime. The influence of the surface is smaller for 13% and 20% specimens, which is why the additional material

leads to increased strength. A comparison with the estimated tensile strength by the measured dimensions shows good agreement considering the simplicity of the method, especially for specimens with a volume fraction of 13% and below. The deviation of the 6%  $XY$  specimens can be explained by outliers in the minimal measured diameter leading to earlier failure (see Fig. 2.20). For the 20% specimens, the estimated ratio between  $XY$  and  $Z$  specimens matches, however, the strength is slightly higher in the experiments. A reason for this could be the different microstructure of the lattice specimens featuring thinner prior  $\beta$  grains compared to the bulk Ti-6Al-4V material. In addition, the heat accumulation in lattice structures is small compared to bulk material. This results in higher cooling rates, potentially yielding a smaller width of  $\alpha/\alpha'$  lamellae [139, 142, 143, 146]. Such a grain refinement (see Section 2.2.1) leads to increased strength and ductility [100, 101]. Studies that model the microstructure of SLM metals could help in further understanding the influence of the process [147]. When comparing the compressive with the tensile specimens for a volume fraction of 13% and 20%, a higher strength is noticeable. This can be explained by pores in the material that are less severe in compression as the local tensile stress concentration at the pore is much lower [66, 81]. On the contrary, this is not the case for the 6% specimens. Here, microscopic buckling of the individual struts takes place before the final material failure, whereas a shear failure is observed for the higher volume fractions. The buckling of the individual struts yields a reduced macroscopic homogenized strength.

An estimate to evaluate if buckling of the compressive metal lattice structures due to the slenderness of the struts is possible can be made using Eq. (2.4). As there is a rounding at the crossing points of the struts, the unsupported length is not clearly determinable. Instead, the two possible extrema as well as their average are used to have a range within which buckling starts to occur: (i) the completely straight length of the strut without the rounding  $l_{\text{short}}$  and (ii) the complete length of the strut between two of the perpendicular struts  $l_{\text{long}}$ . The estimates of the critical buckling load depending on the volume fraction and the average maximum forces in the experiments are compared in Fig. 2.26. It can be seen that the 6% specimens are a candidate for buckling as the experimental maximum force is higher than the critical buckling load determined with the average unsupported length  $l_{\text{avg}}$ . This corresponds well with the experimental findings. The 13% specimens are at the lower boundary of the estimated buckling load. Since no buckling occurred in the experiments,  $l_{\text{long}}$  is too conservative. The 20% specimens are not prone to buckling. Here, sudden shear failure occurs through one horizontal plane of the lattice cells.

To analyze the unit cell type and to be able to compare it to other unit cells, the normalized elastic modulus and strength depending on volume fraction for tensile metal lattice structure specimens with  $Z$  orientation are shown in Fig. 2.27 together with power law fits based on the Gibson-Ashby model [33]. From the

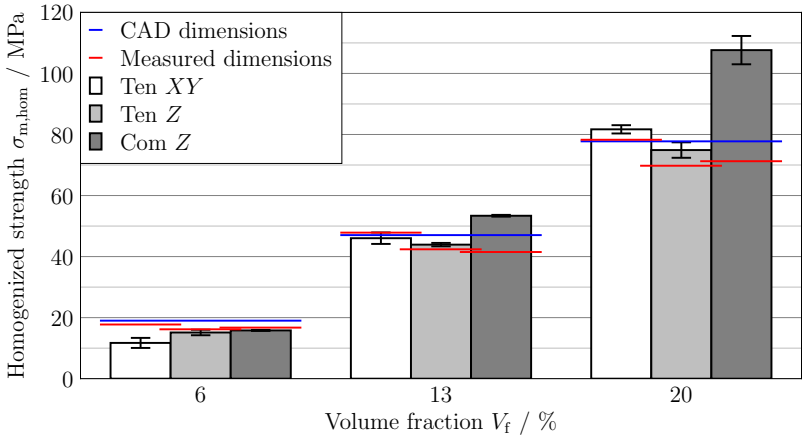


**Figure 2.25:** Homogenized strength of the metal lattice structures depending on volume fraction, loading type and building direction. Comparative strength estimates are calculated with Eq. (2.3) based on the bulk material strength of Tab. 2.5 as well as the idealized CAD dimensions and the measured dimensions in Fig. 2.20.

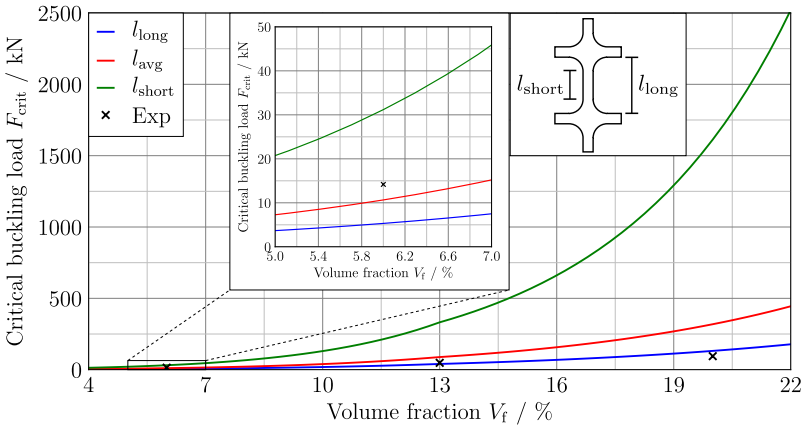


**Figure 2.26:** Estimate of microscopic buckling load of the individual struts based on Euler's critical load for the compressive metal lattice structures. The average maximum forces from the experiments are displayed for comparison.

exponents (1.253 and 1.291), which are close to 1, it can be seen that the analyzed cubic unit cell is stretch-dominated and thus more suited for lightweight structural than energy absorbing applications [48]. A comparison of the obtained fitting parameters to those mentioned for cubic cells in the summary of Maconachie *et al.* [55] shows good agreement, especially with regard to the strength. Compared to the parameters of other unit cells, the superior performance of the cubic cell for lightweight applications can be observed because of the exponent close to 1 and the high linear factor.

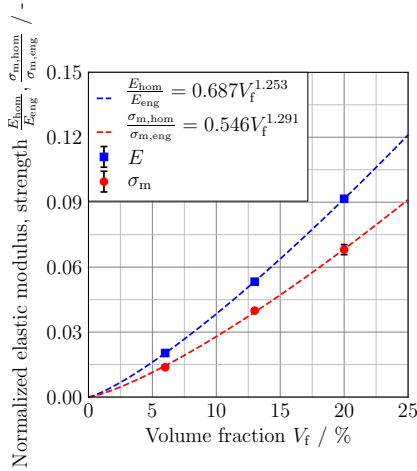


**Figure 2.27:** Normalized elastic modulus and strength depending on volume fraction for tensile metal lattice structures with building orientation  $Z$  as well as Gibson-Ashby power law fits.

Figure 2.28 presents the homogenized fracture strain depending on volume fraction, loading type and building direction for the metal lattice structures. An increasing strain with increasing volume fraction can be observed. A possible explanation for this result is that the surface defects are relatively smaller when the volume fraction increases and are thus less severe. Moreover, the data shows that the  $XY$  oriented specimens in the tensile test are worse than the  $Z$  specimens. This can again be explained by the notch effect of the irregular powder adhesion and poorly bonded powder to load carrying struts at the overhang. Since damage is a local event and always begins at the weakest strut, the notch is the dominant factor here. After the first failure of a strut, the redistribution of the load leads to stress concentrations in the surrounding struts and thus to earlier damage. The

compression tests show a significantly increased fracture strain compared to the tensile tests at a volume fraction of 13% and 20%. This can again be explained by the pores inside the material that have a lower stress concentration factor in compression and are initiation points for failure in tension. It has to be noted that for a significant number of the tensile lattice specimens with  $Z$  orientation, the damage occurs in the cell plane directly above the pyramid.

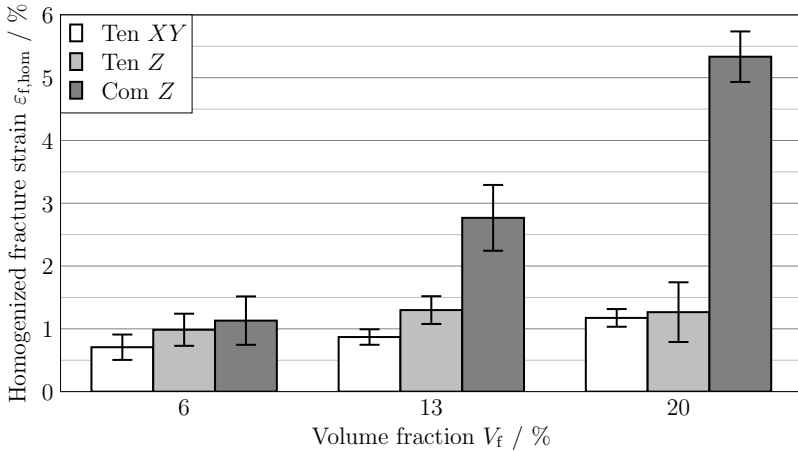


**Figure 2.28:** Homogenized fracture strain depending on volume fraction, loading type and building direction for the metal lattice structures.

### Working hypothesis 2

The evaluation of different load cases is mandatory for the characterization of lattice materials in structural design.

This working hypothesis can be fully confirmed. Due to the instabilities of AM processes, imperfections such as pores can occur, especially when post-processing is simplified without for instance HIP. Pores have a higher stress concentration factor in tension than in compression, thus leading to an earlier failure. While compressive testing might be sufficient for energy absorption applications, in structural design especially tensile load cases are important to prevent an overestimation of the mechanical properties of lattice structures.

The results of the experimental characterization of the polymer lattice structures in terms of homogenized properties are displayed in Tab. 2.11 with mean  $\mu$  and sample standard deviation  $s$ . Also for the polymer lattice structures, a strength estimate with Eq. (2.3) is performed based on the bulk methacrylate photopolymer tensile strength of Tab. 2.7 as well as the idealized CAD dimensions and the measured dimensions in Fig. 2.21. The average vertical strut diameter  $d_v$  is utilized as building and loading direction are aligned. The estimated homogenized strength of 3.66 MPa, based on the CAD strut diameter of 1.1 mm, is slightly higher than the experimentally determined one. An explanation could be the lower measured average vertical strut diameter of 1.049 mm. However, when the homogenized strength estimation is based on the measured strut diameter, a significantly lower value of 3.33 MPa is predicted. This suggests that the bulk methacrylate photopolymer material properties might be slightly different compared to the lattice ones. A reason could be a size effect or a different cross-linking density, which depends on the reaction kinetics of the radical photopolymerization under the influence of the process parameters (see Section 2.2.2). This will be further discussed in Section 2.3.8.

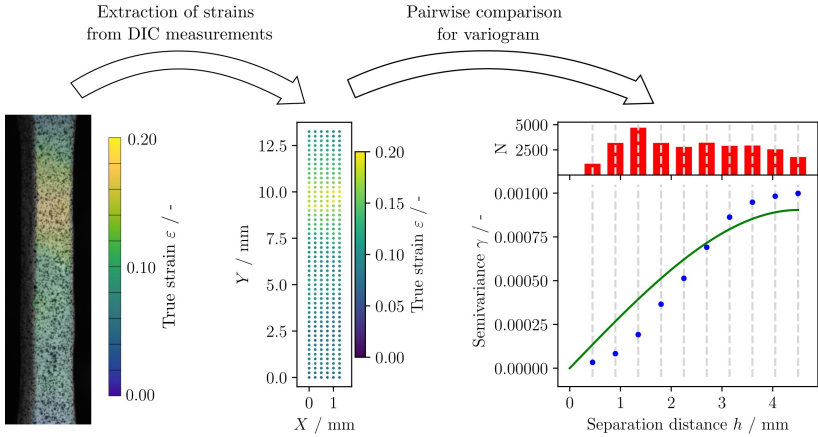
**Table 2.11:** Experimentally determined homogenized mechanical properties of the polymer lattice structures.

Parameter	$\mu$	$s$
Homogenized elastic modulus $E_{\text{hom}}$ / MPa	214.60	6.94
Homogenized strength $\sigma_{\text{m,hom}}$ / MPa	3.59	0.16
Homogenized fracture strain $\varepsilon_{\text{f,hom}}$ / %	3.18	0.75

### 2.3.5 Correlation Length

In order to determine the correlation length for the random fields of material properties and geometry deviations for the probabilistic FEM models of the SLA manufactured methacrylate photopolymer, variography is utilized. With regard to the material properties, it is assumed that strength and fracture strain vary on a similar length scale as they are both localized properties. With the DIC measurements of the bulk tensile polymer specimens, the true strain field can be captured. It is extracted at uniformly spaced discrete points and then the point pairs are compared to generate the variogram. Figure 2.29 illustrates the process for a representative dog-bone specimen and shows the semivariance depending on the separation distance of the points. Moreover, a fit of the spherical model from Eq. (2.10) to the empirical semivariance is depicted. A correlation length of  $l_c = 3.5$  mm for the methacrylate photopolymer material properties is extracted

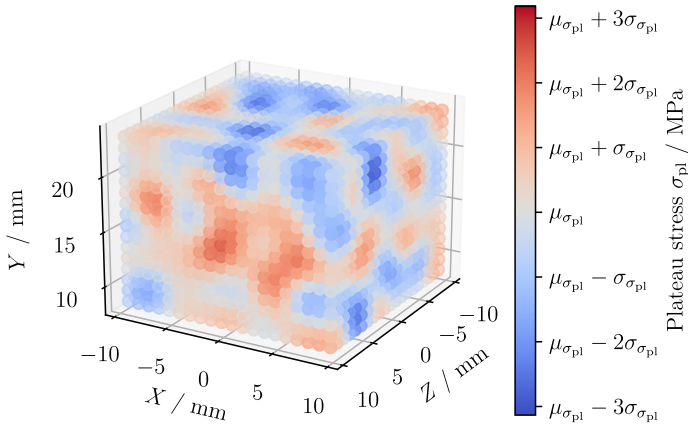
from the variogram. For higher separation distances, there is only a small change in the semivariance.



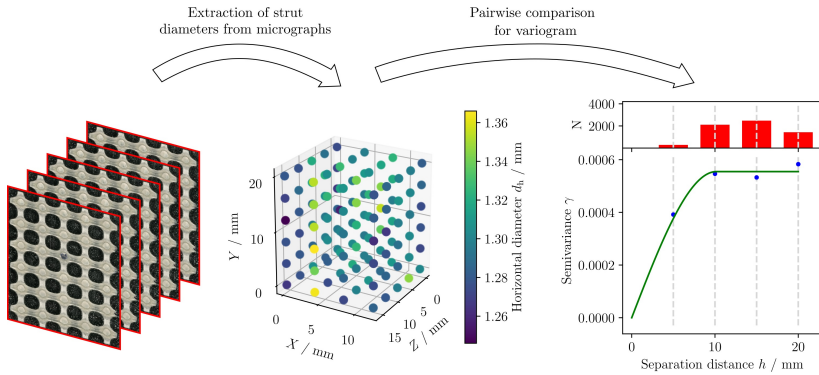
**Figure 2.29:** Determining the correlation length of the local material properties from a variogram of the true strain of a polymer dog-bone specimen. The point pairs are extracted from DIC measurements. The red bars show the number of point pairs at each separation distance, the blue dots depict the empirical semivariance determined with Eq. (2.9) and the green line is a fit of the spherical model according to Eq. (2.10).

A typical realization of a random field of the plateau stress for a polymer lattice structure model with this correlation length is displayed in Fig. 2.30. The plateau stress in terms of standard deviations from the mean is depicted depending on the spatial location within the lattice.

The correlation length for the variation of the strut diameters is identified from the micrographs of the polymer lattice structure slices. By stacking the slices on top of each other, the specimens are recreated. This results in a 3D field of the extracted strut diameters. The point pairs are then again compared to generate the variogram. The procedure together with the semivariance depending on the separation distance for the horizontal strut diameters of an exemplary polymer lattice structure is shown in Fig. 2.31. Again, a fit of the spherical model from Eq. (2.10) to the empirical semivariance is carried out. Here, a correlation length of  $l_c = 8$  mm is obtained from the variogram for the variation of the strut diameters. There is only small change in the semivariance for higher separation distances.



**Figure 2.30:** Typical random field showing the plateau stress in terms of standard deviations from the mean for a polymer lattice structure model.

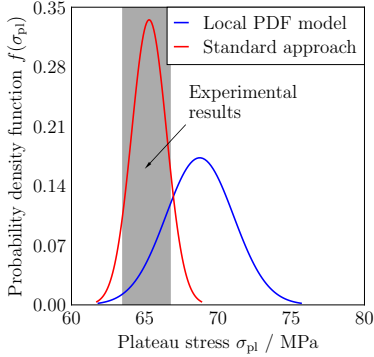
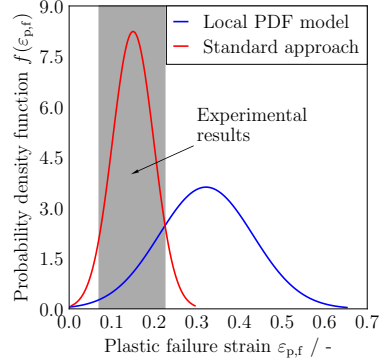
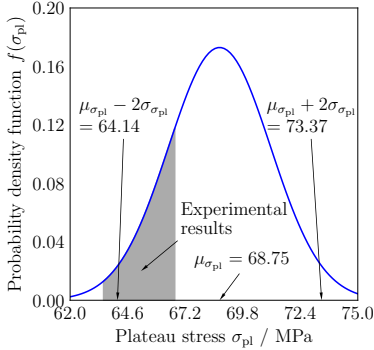
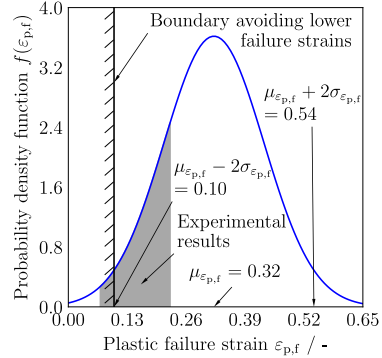


**Figure 2.31:** Determining the correlation length of the strut diameters of the polymer lattice structures from a variogram. The point pairs are extracted from diameter measurements in stacked micrographs of the lattice structure specimen slices. The red bars show the number of point pairs at each separation distance, the blue dots depict the empirical semivariance determined with Eq. (2.9) and the green line is a fit of the spherical model according to Eq. (2.10).

### 2.3.6 Probability Distribution of Local Mechanical Properties

The identification of the probability distribution of the methacrylate photopolymer material properties dominated by local effects poses a challenge for modeling. It is assumed that local defects most likely stem from the manufacturing process. Possible reasons for local defects are manifold and some are listed in the following: (i) bubbles in the resin bath, (ii) printing not perfectly in the focus of the fixed UV laser due to different positions on the build platform, (iii) partial shadowing and curing depth during post-curing, (iv) higher laser absorption of the resin bath in areas where the bottom of the bath degraded because of multiple previous exposures, (v) notches due to the removal of the support structures. Only the volume with the biggest flaw of the specimen is captured by experiments. Hence, a new method, the local PDF model (see Section 2.2.9) is developed and compared to the standard approach where the probability distribution is derived from the central moments of the experimental measurements directly. It is assumed that a polymer dog-bone specimen consists of ten sections with individual homogeneous material properties as the length of the homogeneous necking area in the DIC measurements is approximately 1 mm (see Section 2.2.6) and the parallel measuring length is 10 mm. The PDFs for both approaches (local PDF model and standard approach with central moments) are presented in Fig. 2.32a and Fig. 2.32b for the plateau stress  $\sigma_{pl}$  and the plastic failure strain  $\varepsilon_{p,f}$  of the methacrylate photopolymer respectively. These are the inputs for the random fields in the FEM models. Three standard deviations are shown. For the standard approach, most of the PDF is within the range of the experimental results leaving only small tails outside of it. In case of the local PDF model, a large part of the body of the PDF is outside the range of the experimental results. The mean is shifted to higher values and the curve is flattened leading to a higher standard deviation. The shift to the right for the local PDF model is a result of the length of the polymer dog-bone specimens since there are many sections with a higher property than the ones determined in the experiments. The flattening stems from the relatively small number of specimens tested. This leaves a lot of uncertainty of how much higher the property of the other sections can be, compared to the ones identified by the experiments.

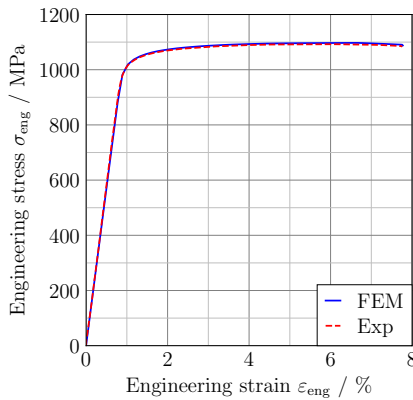
A closer look on the PDFs for the plateau stress  $\sigma_{pl}$  and the plastic failure strain  $\varepsilon_{p,f}$  of the methacrylate photopolymer determined with the local PDF model is displayed in Fig. 2.32c and Fig. 2.32d where the mean and twice the standard deviation are indicated. For the plastic failure strain, negative values could occur in the realizations, which is not possible in reality. Thus, a boundary avoiding very low failure strains is applied at  $\mu_{\varepsilon_{p,f}} - 2\sigma_{\varepsilon_{p,f}}$  leaving a truncated normal distribution.


 (a) Comparison of the  $\sigma_{pl}$  distributions.

 (b) Comparison of the  $\varepsilon_{p,f}$  distributions.

 (c) Probability distribution for  $\sigma_{pl}$ .

 (d) Probability distribution for  $\varepsilon_{p,f}$ .

**Figure 2.32:** Comparison of the probability distributions for the local properties plateau stress  $\sigma_{pl}$  and plastic failure strain  $\varepsilon_{p,f}$  of the methacrylate photopolymer with the standard approach and the local PDF model as well as further insights in the distributions with the proposed local PDF model.

### 2.3.7 Comparison of Experiments and Numerical Modeling for Bulk Material

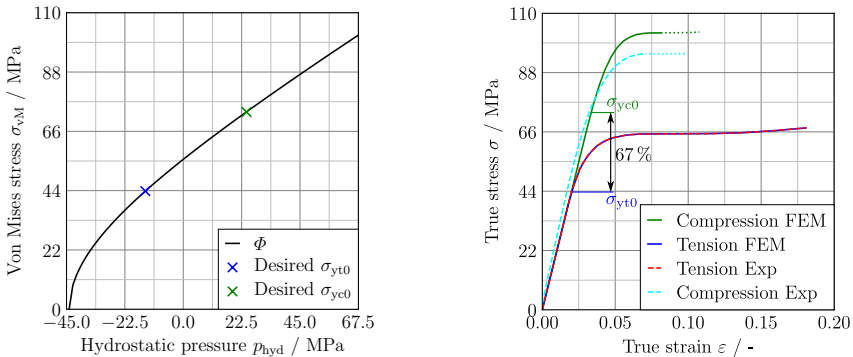
Figure 2.33 presents the engineering stress-strain curve of the FEM simulation of the bulk Ti-6Al-4V tensile test for the calibration of the material model. A comparison to the representative experiment is performed, which was analyzed by DIC in order to determine the true stress-strain curve required for the material model (see Section 2.2.10 and Section 2.3.3). Good agreement is found so that the fine-tuning of the necking behavior on the basis of the DIC data can be considered successful.



**Figure 2.33:** Comparison of the engineering stress-strain curves for a representative experiment and the FEM simulation of the bulk Ti-6Al-4V tensile test.

Also the material model for the methacrylate photopolymer needs to be verified first. This is crucial in order to evaluate whether the proposed probabilistic approach is able to capture the experimentally determined stochastic variation of the lattice structure properties at a later stage. Especially, the ability to represent the tension-compression asymmetry of the methacrylate photopolymer and therefore the material behavior under different load conditions has to be analyzed. Figure 2.34a displays the initial hyperbolic yield surface obtained with the parameters identified in Section 2.3.3. The equivalent von Mises stress at the yield point is shown depending on the hydrostatic pressure. For an increasing hydrostatic pressure, the yield stress also increases. Both, the desired initial yield stress under tension  $\sigma_{yt0}$  and compression  $\sigma_{yc0}$ , are met perfectly.

One element FEM simulations are discussed in the following to examine the differences in the mechanical response to uniaxial tensile and compressive loading. The experimental averages are compared to the one element FEM simulations in terms of the true stress-strain curve in Fig. 2.34b. In the case of tensile loading, the stress-strain response coincides over the whole range: from the elastic regime, yield point and hardening to the fracture strain. Also the difference between the onset of plastic flow in tension and compression is captured well with 67% as found in Section 2.3.2. The compressive curves are only considered up to the yield point since afterwards significant bulging occurs in the experiment. Thus, the stress state is not uniaxial anymore, preventing a comparison. The slight differences between the compressive curves up to that point can also stem from little bulging before the yield point. Since the true cross-section is evaluated in the middle of the compressive specimen, bulging leads to underestimation of the stress. Yet, higher compressive stresses do not occur in the structural simulations of the polymer lattice as the loading is predominantly tensile. Hence, the methacrylate photopolymer material model is considered to be calibrated well and able to exhibit the desired mechanical behavior.

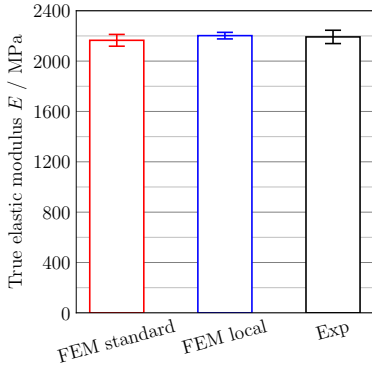


(a) Initial hyperbolic yield surface.

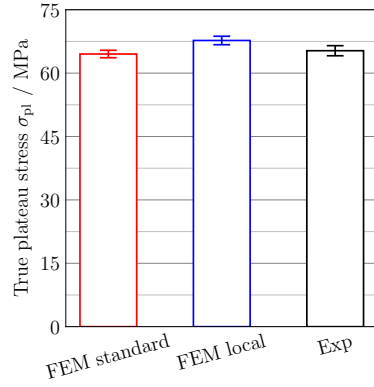
(b) Comparison of experimental average and material model in one element FEM simulations.

**Figure 2.34:** Initial hyperbolic yield surface and comparison of the true stress-strain curves of the experimental average and the calibrated material model of the methacrylate photopolymer in FEM simulations. The compressive curve is not shown completely as the calibration is only for the yield point. However, higher stresses than shown are not present in the simulations later on since the load cases are predominantly tensile.

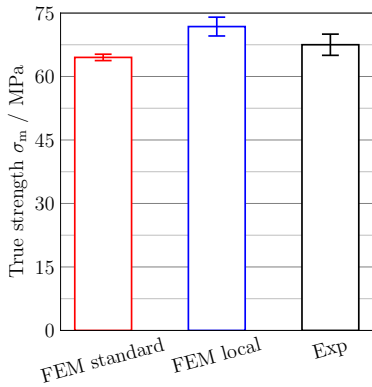
A validation of the spatial correlation and the probability distributions of the methacrylate photopolymer mechanical properties is carried out on the level of dog-bones. The results in terms of the material properties determined from true strains and stresses are shown in Fig. 2.35 with the mean and sample standard deviation. The experimental results are compared with ten realizations of FEM models with probability distributions for the local properties derived from the standard approach (FEM standard) and the local PDF model (FEM local). The true properties in the FEM simulations are captured in a similar way as in the experiments by tracking the distance change between two points in longitudinal and transversal direction in the region of the necking (see Section 2.2.6). With regard to the true elastic modulus, the results are in accordance with each other. The elastic modulus is a global property, hence it is applied exactly the same in both FEM models. Therefore, a difference is not expected. Concerning the true plateau stress and especially the true strength, the FEM standard simulations slightly underestimate and the FEM local simulations slightly overestimate the properties compared to the experiments. In the case of the true strength, the standard deviation of the FEM local simulations is in a similar range as in the experiments, while it is smaller in the FEM standard simulations. The difference of the FEM local simulations can be explained when having a look at the PDF in Section 2.3.6. The number of specimens tested in the experiments together with their length results in a large standard deviation and a higher mean. Since the realizations of the FEM models have a rather small volume where the material properties are varied, the larger mean dominates. Despite the higher standard deviation, not that many low values occur. Testing more specimens in the experiments would reduce the uncertainty in the local PDF approach, thus leading to a smaller part of the body of the PDF being on the right-hand side of the experimentally determined properties. Having a look at the true fracture strain, very similar results are obtained with the FEM local simulations and experiments. In contrast, the FEM standard simulations show significantly smaller fracture strains and also a smaller standard deviation. Here, the inability of the standard approach to capture the probability distribution of the local property gets clearly evident. The probability distribution is obtained based on the property of the worst section of the specimens in the experiments and then distributed over the whole model in the simulation. This results in realizations with artificially low properties. In summary, the FEM simulations with local PDF model show only small deviations from the experiments in strength and capture the fracture strain of the methacrylate photopolymer very well. Hence, the newly proposed model outperforms the standard approach and is used in the following for the polymer lattice structures. With regard to the progression of the plastic deformation, the necking and the fracture, the region with the lowest plateau stress in the random field of a model is decisive. Here, the localization takes place. The fracture strain of the specimen models then depends on the plastic failure strain of that section.



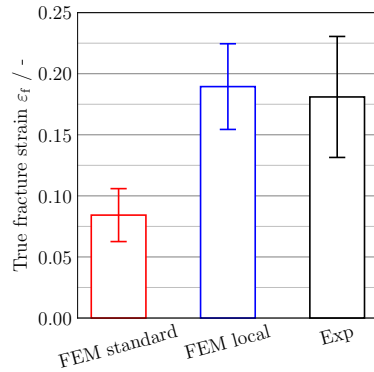
(a) True elastic modulus.



(b) True plateau stress.



(c) True strength.



(d) True fracture strain.

**Figure 2.35:** Comparison of the true mechanical properties for experiments and probabilistic FEM simulations of methacrylate photopolymer dog-bones.

### 2.3.8 Comparison of Experiments and Numerical Modeling for Lattice Structures

A deeper insight into the quasi-static mechanical behavior and failure of the lattice structure specimens is gained from the DIC measurements and the FEM simulations. Figure 2.36 shows the comparison of the absolute homogenized stress-strain curves of the tensile and compressive loading in experiment and simulation for metal lattice structures with different volume fractions. For the simulations, idealized CAD geometries of the metal lattice structures are used. Thus, only specimens with aligned building and loading direction are compared to reduce the influence of powder adhesion and notch effects. The lattice structure specimens are more prone to early failure because of surface defects from the SLM process compared to the bulk specimens that are subsequently machined by turning and used for the Ti-6Al-4V material model calibration. Therefore, a representative experimental lattice structure curve with the highest fracture strain is displayed for the comparison. The stiffness in tension and compression is captured well by the simulations. Also the yield point and strength of the tensile samples can be well represented for all volume fractions. Only slight deviations occur that can be explained by the smaller diameter of the struts in the experiments (see Section 2.3.2). Concerning the fracture strain, two opposing effects occur that cannot be captured by the simulation: (i) a changed microstructure of the smaller struts of the lattice structure (thinner prior  $\beta$  grains, potentially smaller width of  $\alpha/\alpha'$  lamellae) compared to the sample made of bulk Ti-6Al-4V for calibration, which leads to increased strength and fracture strain (see Section 2.2.1) and (ii) the influence of the notches and surface roughness of the SLM manufactured lattice structure specimens that were not machined by turning in contrast to the bulk material specimens. For the 6% specimens, the influence of the surface dominates as the struts are very thin. Therefore, the simulation overestimates the fracture strain. In the case of the 20% specimens, the microstructure effect dominates. Thus, the simulation underestimates the fracture strain. In comparison to tensile metal lattice structure models, a higher homogenized strength and fracture strain is also found in the simulations of the compressive ones. This results from a transverse expansion compared to a contraction in tension. However, the strong difference in strength and fracture strain cannot be captured. The effect of pores being less severe in compression because of a lower local stress concentration is not included in the material model since the calibration is only done with tensile tests. An asymmetric plasticity model as for the methacrylate photopolymer (see Eq. (2.19)) could resolve this. The 6% compressive specimens are represented well in the simulations because they exhibit the early onset of buckling. Very similar deformation modes can be observed compared to DIC measurements (see Fig. 2.37). Also the sudden shear failure mode of the higher volume fraction compressive specimens is captured in the simulations as shown in Fig. 2.38.

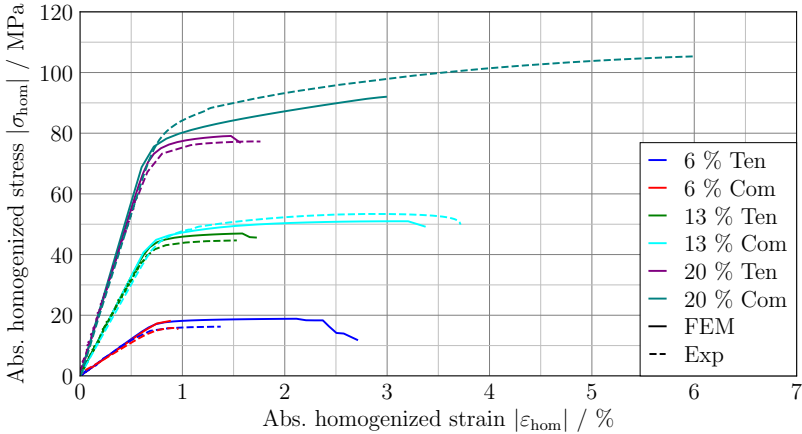


**Figure 2.36:** Comparison of the absolute homogenized engineering stress-strain curves for experiments and FEM simulations of tensile and compressive metal lattice structure specimens with aligned building and loading direction and different volume fractions.

Regarding the fracture strain of the metal lattice structures, the FEM simulations surprisingly show an inverse behavior compared to the experiments: the fracture strain increases with decreasing volume fraction (except for the 6% compressive specimen model where buckling occurs). An explanation can be given based on Fig. 2.39 where contour plots of the von Mises equivalent stress for different volume fractions in tensile tests just before fracture are presented. It can be seen that the stress is more evenly distributed in the 6% model compared to higher volume fractions. Due to more material at the intersection of the struts for higher volume fractions, the loading paths are bending outwards there to use the whole material. Continuing to the thinner struts at the end of the unit cells, they need to bend inside yielding a stress concentration in the middle of the struts. This results in earlier failure.

For the polymer lattice structures probabilistic effects are examined with FEM simulations. A variation of the material properties is conducted. Having seen the ability of the newly proposed local PDF model to capture the probability distribution of the mechanical properties for bulk methacrylate photopolymer dog-bones, a transfer to the more complex lattice structures is carried out. Also the variation in geometrical accuracy is investigated because it plays a role for the more complex lattice structures. Figure 2.40 shows a comparison of the homogenized stress-strain curves of the polymer lattice structures for experiments as

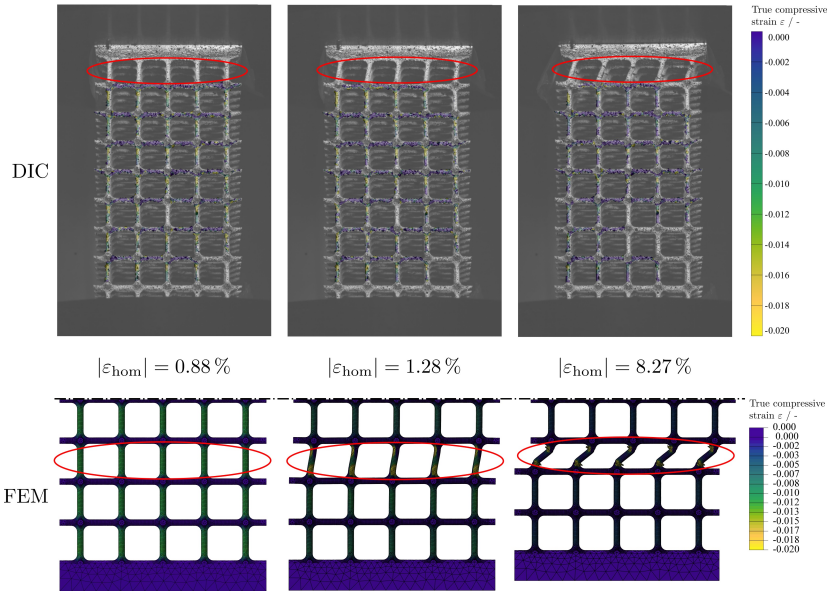


**Figure 2.37:** Sequence of contour plots of the true local strain in loading direction for a compressive metal lattice structure specimen with 6% volume fraction for DIC and FEM showing buckling.

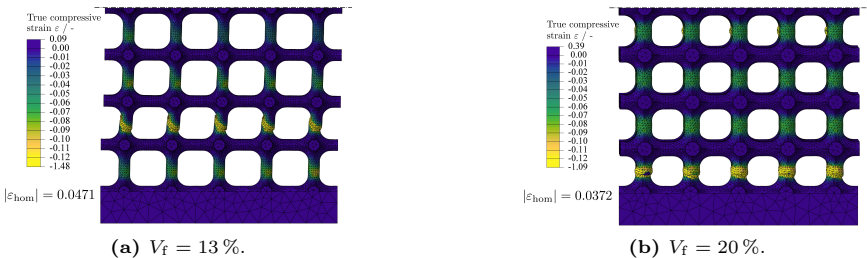


**Figure 2.38:** Contour plots of the true local strain in loading direction for compressive metal lattice structure models with higher volume fraction showing shear damage.

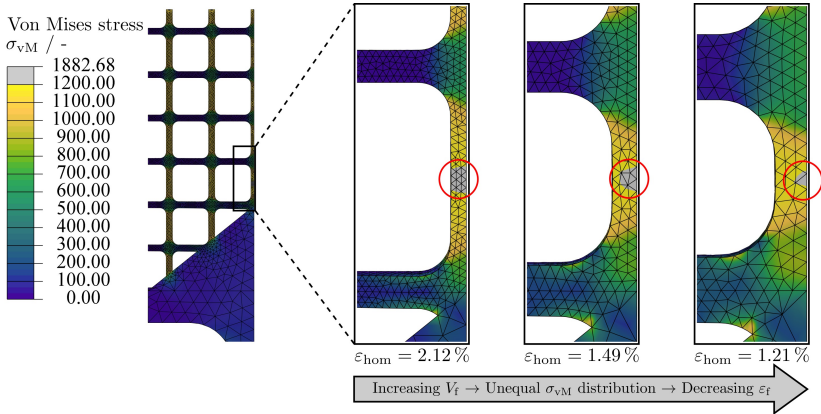


**Figure 2.39:** Contour plots of the von Mises equivalent stress just before fracture showing unequal stress distribution for higher volume fractions of the metal lattice structures.

well as for 20 realizations of FEM models with a stochastic variation of material properties and geometry. Additionally, the homogenized stress-strain response of an FEM model is displayed, where all varying properties are set to the mean  $\mu$ . When comparing the FEM simulations with the experiments, the general trend is represented well. Also a significant amount of the variation can be described. However, the homogenized stiffness in the simulations seems to be slightly underestimated and the homogenized strength and fracture strain are at the lower half of the experimentally determined distributions. Since the homogenized elastic modulus is too low, the material properties can be slightly different in the lattice structure experiments compared to the bulk methacrylate photopolymer as already supposed in Section 2.3.4. A size effect could be responsible, as the individual struts have a smaller volume than the bulk dog-bones. It can as well be a result of the cross-linking density of the methacrylate photopolymer since it develops by a radical reaction mechanism as explained in Section 2.2.2. Thus, the resulting termination speed of the reaction by radical recombination depends on the process parameters. Higher concentrations of radicals due to higher UV intensity can lead to earlier termination [148]. Also depending on the polymer network that has already developed during curing and the ambient temperature, the chain mobility and thus further progress of the reaction is limited [149]. Despite being fully cured as shown by DSC measurements in Section 2.3.1, this can lead to different networks. For instance, the unequal specimen volumes can lead to different heating rates within the post-curing process. Different UV intensities

can occur due to partial shadowing or depending on the curing depth for structures with different volumes. Interestingly, the FEM model with mean properties shows the highest strength and fracture strain. All other FEM simulations are below the mean model. Similar to the dog-bones but with the opposite effect, this can be explained by the local PDF model for the material properties of the methacrylate photopolymer. The volume of the lattice structure specimen models, where the material properties are varied, is large compared to the volume of the dog-bones. Hence, the large standard deviation of the local PDF model due to the limited number of experiments for the calibration dominates. This leads to low values of the property occurring in the larger volume of almost every lattice structure realization. Since the biggest flaw determines the overall behavior of the specimen model for the local mechanical properties, this leads to an inferior performance of most of the realizations compared to the mean FEM model.

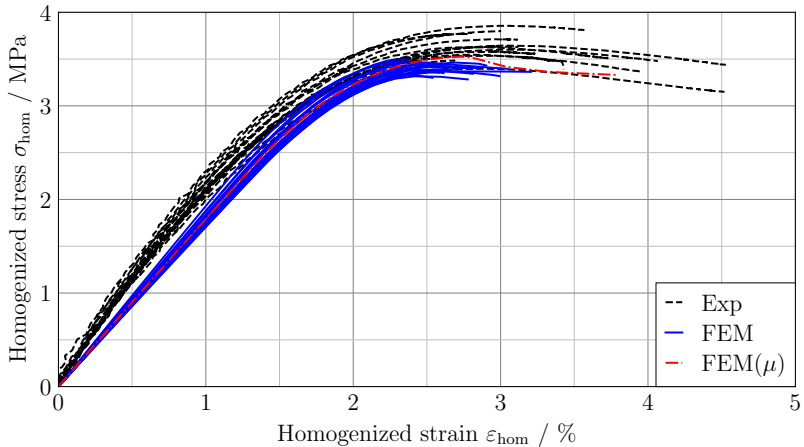


**Figure 2.40:** Comparison of the homogenized stress-strain curves of experiments and FEM simulations of polymer lattice structures incorporating stochastic variations of geometry and material. An FEM simulation with the mean  $\mu$  for all varied parameters is added.

To get deeper insights in the behavior of the polymer lattice structures, the homogenized mechanical properties of the lattice structures are presented in Fig. 2.41 with the mean and the sample standard deviation. The experimental results are separated batch-wise according to each SLA printing process where five lattice structure specimens are manufactured together. However, a certain amount of specimens was not generated correctly so the batches comprise different

numbers of analyzed specimens: three specimens for batch 1 and 3; four specimens for batch 4 and 5; and five specimens for batch 2, respectively. In addition, an advantage of the FEM modeling is exploited: the automatic model generation not only allows to analyze the probabilistic effects of geometry deviations and material properties (Geo+Mat) together, but can also separate the influence of geometry deviations (Geo) and material properties (Mat) from each other. When the probabilistic variation of the geometry deviations is explored, the material is kept constant at the mean and vice versa. For both cases, ten realizations of the model are analyzed. Regarding the experiments, significant differences between the individual batches can be found. For example, the homogenized elastic modulus of batch 3 is significantly lower and the standard deviation of batch 4 is very small compared to the others. In contrast, the standard deviation of the homogenized fracture strain of batch 4 is extremely high, as it includes the three specimen models with the highest strains in the experiments. Differences between the batches indicate that there are additional influences during the polymer specimen preparation that were not considered beforehand. Further effects could be the age of the resin and the resin bath, time between printing and post-curing, time between post-curing and testing as well as moisture absorption. Also the position of the specimen in the SLA printer can influence the mechanical properties because the distance of the fixed UV source is different for the center and the border of the build platform yielding issues with the laser focus.

Concerning the polymer lattice FEM simulations, it can be seen that for a global property like the homogenized elastic modulus the effects of the variation of geometry deviations and material properties are similar. They superimpose when combined leading to a higher standard deviation. The standard deviation is similar compared to the experimental one, although it is on a lower level. For local properties like homogenized strength and fracture strain, one of the influences dominates. In case of the homogenized strength, the geometry deviations dominate as the biggest flaw. The Geo realizations have a similar mean and standard deviation as the combined models. For the homogenized fracture strain, the variation in material properties dominates leading to earlier failure. This yields a similar mean and standard deviation of the Mat realizations and the combined models.

#### Working hypothesis 4

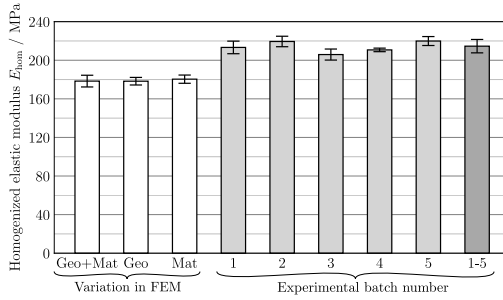
A probabilistic analysis of lattice structures incorporating geometrical and material uncertainties is necessary for the robust design of structural components due to insufficient technical maturity of the additive manufacturing process.

This working hypothesis can be confirmed. AM processes are still prone to geometrical imperfections and varying material properties especially when the limits are pushed with complex lattice structures. These uncertainties can be captured with probabilistic FEM analyses that allow to predict a distribution of the resulting structural mechanical properties. The ability to consider individual effects in numerical models can help to identify the most prominent deficiencies of AM processes and by this ameliorate the reliability.

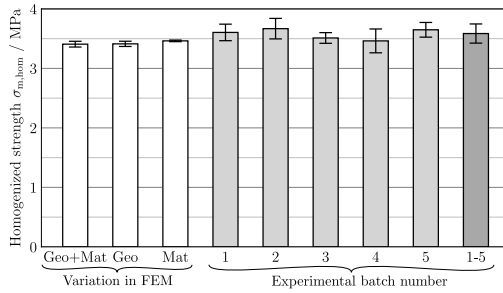
Having a closer look at the tensile metal and polymer lattice structure specimens, the DIC measurements and FEM simulations provide additional insight into the damage progression of the statically tested specimens. Figure 2.42 exemplarily shows the contour plots of the true tensile strain in the DIC measurements and FEM simulations for metal lattice structures with a volume fraction of 20 % at characteristic points of the test (in the elastic regime, at the yield point and at the tensile strength). For the FEM simulations, the structures are mirrored at the vertical axis to have a more similar optical impression compared to the DIC measurements. Local strain concentrations at the minimum diameter of the struts can be clearly seen in the 3D DIC measurements that resolve individual struts. Although DIC and FEM match, it gets evident that the true strain in the struts visible at the outside is significantly lower than that reached in the bulk Ti-6Al-4V samples (see Tab. 2.6).

FEM simulations offer the possibility of a higher spatial resolution, since also cells in the inside of the model can be analyzed. The contour plots of the von Mises stress during damage progression for a tensile metal lattice structure model with 13 % volume fraction are illustrated in Fig. 2.43. Elements with a damage variable  $D > 0.67$  are suppressed for a better visualization of the failure. Due to the slight stiffness jump at the top of the pyramid, there is a stress concentration (and therefore also a higher strain that is comparable to that of the bulk Ti-6Al-4V material) at the strut above. This leads to necking and afterwards to early failure. The consecutive stress redistribution causes all surrounding struts of the plane to fail. This explains that a significantly large number of the experimental tensile metal lattice specimens failed directly above the pyramid as described in Section 2.3.4. Therefore, the simulations also show that there is still potential for improvement at the load introduction when the homogenized properties of the unit cells need to be determined.

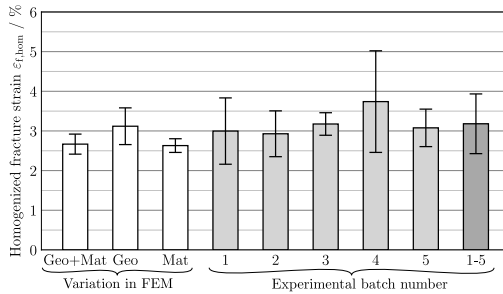
Very similar observations can be made for the polymer lattice structures. Contour plots of the true tensile strain in loading direction of DIC measurements and FEM simulations are illustrated in Fig. 2.44 at the instance, when the homogenized strength is reached. In case of the FEM simulation, the model is mirrored



(a) Elastic modulus.



(b) Strength.



(c) Fracture strain.

**Figure 2.41:** Comparison of the homogenized mechanical properties for experiments and simulations of polymer lattice structures. Experiments are also shown batch-wise. For FEM simulations the variation of geometry and material are shown separately, as well as in combination.

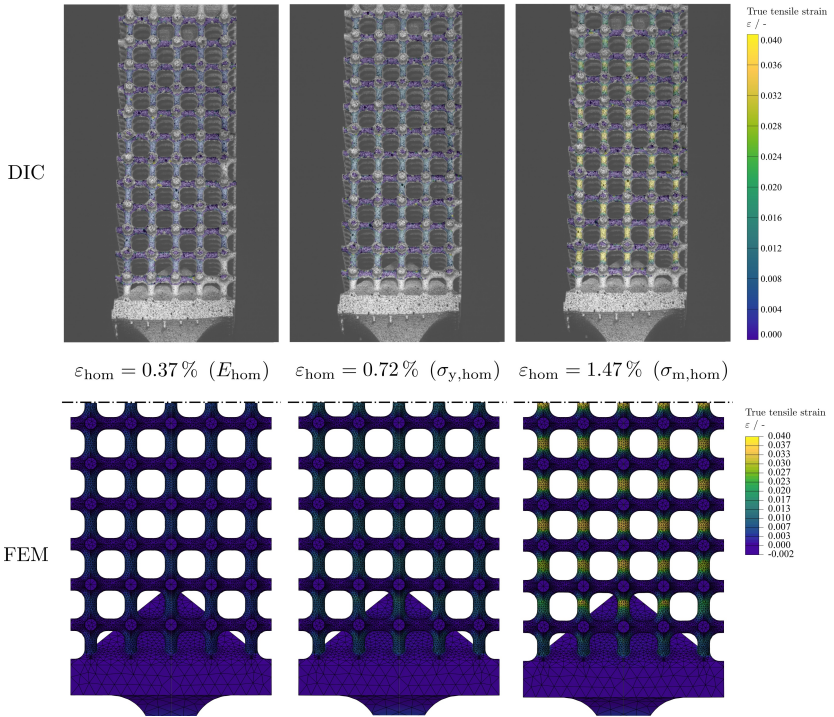


**Figure 2.42:** Comparison of the DIC and FEM contour plots of the true local strain in loading direction for a tensile metal lattice structure specimen with 20% volume fraction at characteristic points of the test (elastic modulus  $E_{\text{hom}}$ , yield stress  $\sigma_{y,\text{hom}}$  and tensile strength  $\sigma_{m,\text{hom}}$ ).

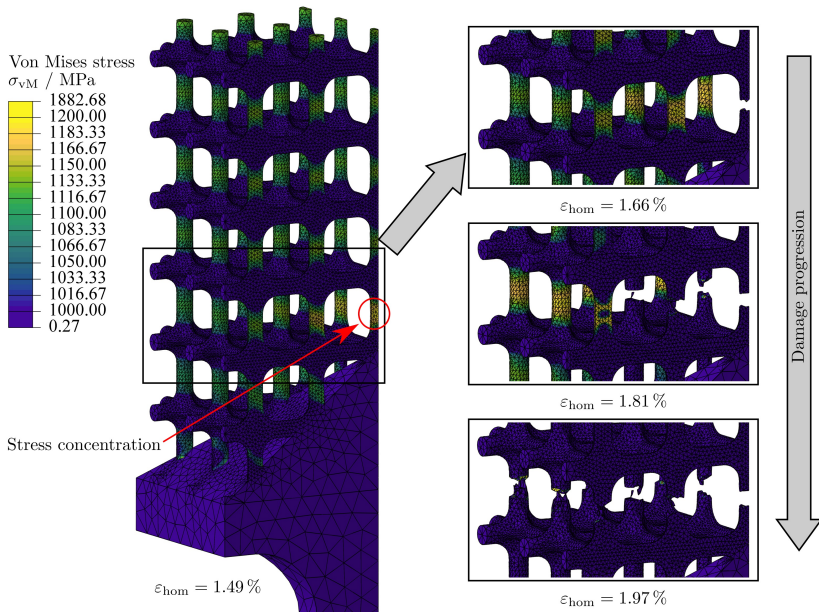


**Figure 2.43:** Contour plots of the von Mises stress for a tensile metal lattice structure model with 13% volume fraction showing the damage progression through the struts at one cross-section.

at the horizontal symmetry plane to have a more similar optical impression. DIC and FEM are in good agreement with local strain concentrations visible at the smallest diameter of the struts in loading direction. Especially for the FEM simulation, slight differences between the strains in the individual struts are visible owing to the geometry and material variations with random fields. However, also here a discrepancy between the true strains reached by the bulk methacrylate photopolymer dog-bone specimens (see Fig. 2.22) and in the individual struts on the outside of the lattice structures can be noticed. FEM simulations can give further insights as also the inner cells can be inspected. Due to the random nature of the geometry and material variations, the initially failing strut can be anywhere in the lattice structure and is not necessarily at the outside that would also be visible by DIC. At this strut similar fracture strains compared to the dog-bone specimens can be found. Yet, they are usually at the lower end of the distribution as the higher lattice specimen model volume increases the probability of a weak section. This also leads to lower overall strains as the load transfer from the already damaged struts to surrounding ones results in a successive failure of the lattice structure.

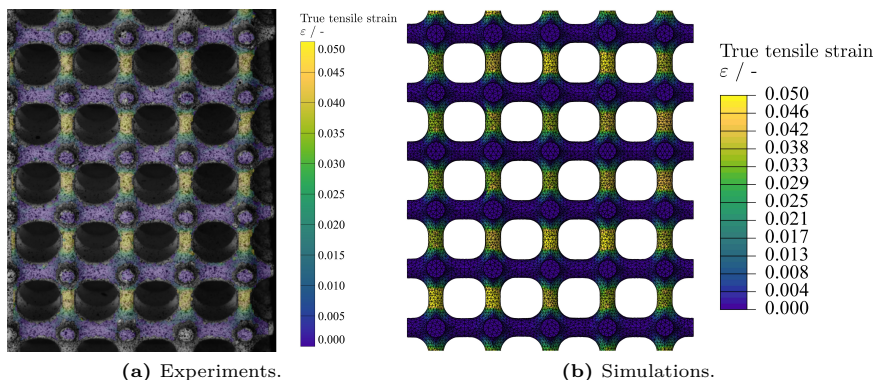
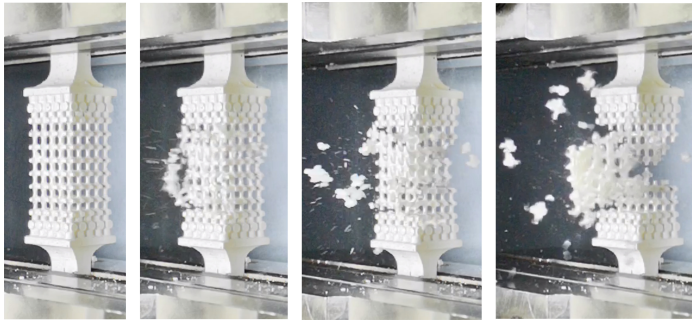


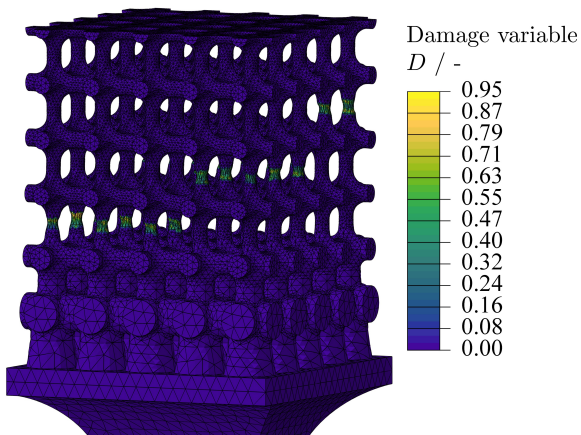
**Figure 2.44:** Comparison of the DIC and FEM contour plots of the true local strain in loading direction for a polymer lattice structure specimen at a homogenized strain of  $\epsilon_{\text{hom}} = 0.023$  appearing approximately at the strength  $\sigma_{\text{m,hom}}$  of the specimen.

FEM simulations also allow to study these failure mechanisms of the polymer lattice structures after the plastic regime. Figure 2.45 shows the damage progression in frames of a slow motion video of the experiment and a contour plot of the damage variable in an exemplary FEM simulation. Due to the probabilistic variation of geometry and material properties, a stochastic failure pattern develops.

The fracture jumps between different planes of the lattice. Hence, experiments and FEM simulations also match well in the last part of the material test. The stochastic nature of the failure pattern further indicates that the gradient at the load introduction serves its purpose and prevents an early failure due to a stiffness jump as for the metal lattice structures and as observed in other studies [62, 65]. Thus, it delivers reliable results in tensile tests of the homogenized mechanical properties of lattice structures.



(a) Experiment.



(b) Simulation.

**Figure 2.45:** Stochastic damage of the polymer lattice structures visible in slow motion video frames of the experiments and in a contour plot of the damage variable in FEM simulations.

### 2.3.9 Homogenization of Unit Cells

Finally, a comparison of FEM simulations of the metal lattice structure models and unit cells with PBCs is conducted. This allows to further evaluate the load introductions and to determine homogenized mechanical properties of the unit cells without the influence of a load introduction. Figure 2.46 shows a comparison of the absolute homogenized engineering stress-strain curves of FEM simulations of metal lattice structure models and unit cells with PBCs for different volume fractions under tension and compression. Elastic modulus and strength are matching in most of the cases. However, especially in the tensile loading case, the unit cells with PBCs show a significantly higher fracture strain and also a slightly higher strength. This can be attributed to the fact that there is no early failure due to a stress concentration at the transition from the pyramidal load introduction to the lattice structure. Also for simulations of unit cells with PBCs similar trends can be observed as for the lattice structure simulations: (i) higher strength and failure strain for compressive compared to tensile tests because of transverse expansion and (ii) increasing failure strain for decreasing volume fraction since the load distribution at the smallest cross-section of the struts is more even. The only significant difference is that for the compressive unit cell with a volume fraction of 6 % a shear damage instead of buckling occurred leading to a massive increase in failure strain.

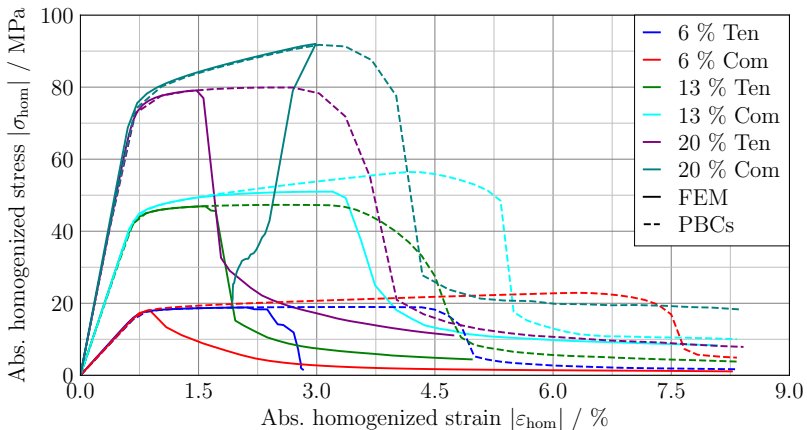


**Figure 2.46:** Comparison of FEM simulations of metal lattice structure models and unit cells with PBCs depending on volume fraction and load case.

The contour plots of the true local strain in loading direction for FEM analysis of metal unit cells with PBCs are illustrated in Fig. 2.47 exemplarily for a volume fraction of 13%. Images just before and after damage occurs are provided to show the failure modes. In tension damage evolves after necking whereas in compression shear damage occurs.

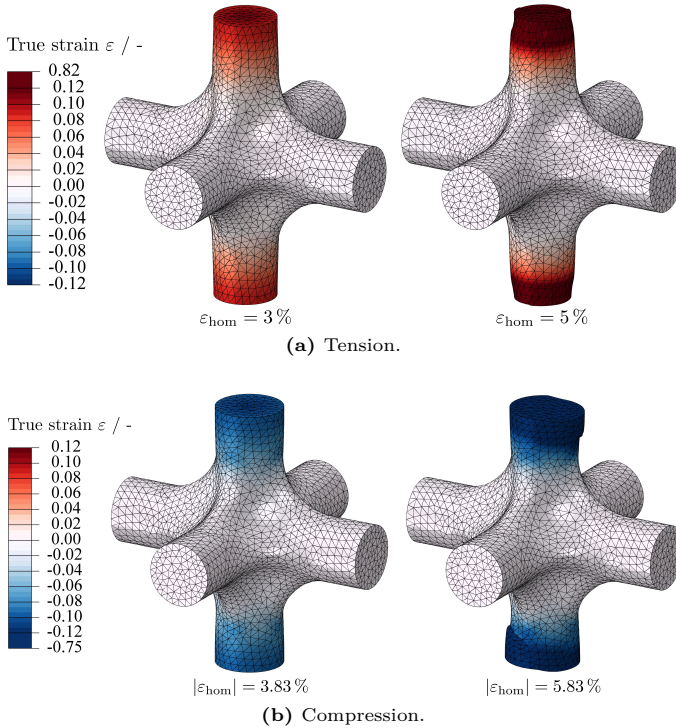


**Figure 2.47:** Contour plots of the true local strain in loading direction for an FEM analysis of metal unit cells with PBCs and a volume fraction of  $V_f = 13\%$ . In tension damage evolves after necking, in compression shear damage occurs.

### Working hypothesis 3

The progressive damage behavior of lattice structures can be captured in computationally efficient finite element simulations.

This working hypothesis can be confirmed. Full lattice structure FEM simulations are able to capture the whole range of a mechanical loading. Reversible elastic deformation, plastic yielding and different failure mechanisms depending on the load case and the volume fraction are in good agreement with experiments. Unit cell simulations with PBCs allow huge savings in computational cost while still delivering reliable results. In addition, they can contribute to a better understanding of further effects such as the load introduction. Deviations for compressive metal lattice structures stem from pores that occur due to manufacturing instabilities. These could either be eliminated by a more elaborate post-processing with HIP and CT quality control or captured with an asymmetric plasticity model.

## 2.4 Conclusion on Additively Manufactured Lattice Structures

In this chapter, a mechanical characterization of additively manufactured lattice structures is performed. SLM fabricated Ti-6Al-4V and SLA fabricated methacrylate photopolymer are considered. Different building directions, load cases and volume fractions are analyzed for Ti-6Al-4V. The probabilistic effects of the variation of geometry deviations and material properties are investigated for a methacrylate photopolymer. The geometrical accuracy of the lattice struts is extracted from micrographs. 3D DIC measurements are used to get further insights about local strain concentrations and for the determination of material properties obtained from true strains and stresses for the material model calibrations. The correlation length of probabilistic effects is determined with variography. In order to identify the probability distribution of local material properties like strength and fracture strain, a new model is developed. FEM simulations of lattice structure models are conducted allowing a better time and local resolution of the progressive damage. Additionally, FEM simulations of unit cells with PBCs are carried out as a computationally more efficient alternative to full lattice structure simulations and for an evaluation of the influence of the load introduction on the determined homogenized mechanical properties.

The experiments on SLM manufactured metal lattice structures have shown a significant difference in tensile and compressive strength. Hence, it is essential to analyze both load cases for stretch-dominated lattice structures applied in

lightweight structural applications. Performing only compressive experiments as frequently in the literature leads to a considerable overestimation of the strength and to uncertainties in the design process. Pores, which are often inherent in the SLM process when no HIP is performed as a post-processing step, are more severe in tension because of a higher local stress concentration leading to earlier failure. This also holds for polymer lattice structures where the tension-compression asymmetry is naturally inherent even without defects.

Even more valuable are insights gained from FEM simulations with material models including progressive damage. Models of lattice structures allow a higher temporal and local resolution than DIC measurements as also hidden struts in the inside of the structure can be analyzed. Hence, they help in understanding the failure process. Build-in material models of commercial FEM codes such as ABAQUS are successfully used to predict failure modes of lattice structures such as necking in tension or shear and buckling in compression. Moreover, the probability distribution of the mechanical properties of lattice structures can be estimated with FEM simulations incorporating stochastic variations of geometry deviations and material properties. Good agreement is found over the whole stress-strain response and the failure progression for the SLA manufactured polymer lattice structures.

With regard to the probability distribution of material properties, global ones like the elastic modulus and properties like strength and fracture strain, which are governed by local effects such as necking, need to be distinguished. While the probability distribution of the elastic modulus can be identified from the central moments of the experimental results of the bulk material characterization specimens, this is not possible for the local properties. Here, the experiments only show the weakest part of the specimens. Distributing these properties over the whole specimen leads to an underestimation in the FEM models. Hence, a new approach, the local PDF model, is developed. It proves to be able to determine the probability distribution of local properties for the SLA printed methacrylate photopolymer well and outperforms the standard approach with the central moments. Slight deviations found during the validation of the model can be explained by the relatively small number of experiments to characterize the material properties. The local PDF model accounts for this by a large standard deviation and a higher mean. This can result in a slight overestimation of the mechanical properties in specimen models with a small volume, while the opposite effect, a slight underestimation, occurs for specimen models with a larger volume. Hence, in future studies a higher number of experiments would be preferable. However, this also shows a feature of the model: the size effect is implicitly integrated. Small deviations can further stem from the SLA manufacturing process. The age of the resin and the resin tank, time between printing and post-curing, time between post-curing and testing as well as moisture absorption and the position of the specimen in the printer might further influence the resulting mechanical properties.

For the characteristic true mechanical properties of the SLA printed methacrylate photopolymer tensile tests (elastic modulus, plateau stress, strength and fracture strain) a hypothetical normal distribution cannot be rejected. Thus, they are assumed to follow a normal distribution. An obvious correlation is found for strength and failure strain. Hence, the probabilistic material models are varied in three properties: elastic modulus, plateau stress and fracture strain. A further finding of the polymer material characterization is the strong tension-compression asymmetry of the methacrylate photopolymer. This is captured well by a hyperbolic Drucker-Prager material model in the FEM simulations. In future works, also compressive tests on other 3D printed bulk materials (for instance also the Ti-6Al-4V utilized in this study) should be considered. In combination with the commonly performed tensile tests they enable the calibration of a material model capturing the tension-compression asymmetry resulting from pores that are currently present in many AM processes. This would allow for a better representation of all load cases necessary for structural design.

In addition, FEM simulations of unit cells with PBCs are established as a computationally inexpensive alternative to determine the homogenized mechanical properties of SLM printed metal lattice structures including failure processes. FEM simulations of unit cells with PBCs in comparison to the lattice structure simulations also show that a non-optimal load introduction leads to earlier failure. A pyramidal load introduction, as for the tensile metal lattice structures, therefore results in an underestimation of the homogenized mechanical properties. Contrary, the gradient in unit cell volume fraction of the polymer lattice structures results in a stochastic failure pattern, indicating that it prevents an early failure due to a stiffness jump. This highlights the importance of the load introduction for lattice structures not only for coupon tests in research facilities but also in the application for larger structural parts.

Further information about local strain concentrations are also gained for the first time from 3D DIC measurements with a resolution of individual struts. They help in identifying critical areas of lattice structures and can be used to improve future designs. DIC measurements also enable the resolution of local phenomena like necking and therefore permit to determine material properties based on true strains and stresses in tensile tests.

Moreover, variography is found to be a valuable tool to determine the correlation length of varying properties. The correlation length allows to determine random fields of the properties for the models. Especially in combination with DIC measurements, the strain fields can be easily evaluated.

With regard to the analysis of the geometry deviations, the vertical struts are slightly smaller than the desired diameter for both, SLM manufactured Ti-6Al-4V and SLA manufactured methacrylate photopolymer. The horizontal struts of the polymer lattice have a smooth surface and are significantly larger. This is a result of the inverted SLA printing process leading to at least partial curing

of additional material at free standing overhangs. The horizontal struts of the metal lattice show surface defects such as powder adhesion and notches from the SLM manufacturing process as they are built directly on the powder bed. They result from adhesion of surrounding powder due to insufficient heat transfer or incorrect fusion because of sinking of the higher density melt. Therefore, the minimum and maximum horizontal diameters of the metal lattice structure struts need to be distinguished. While the minimum horizontal strut diameters approximately match the desired CAD diameters, the maximum horizontal strut diameters are again significantly larger. These imperfections have an influence on the homogenized mechanical properties. For global properties like stiffness, powder adhesion is beneficial, for local properties like fracture strain it leads to earlier failure due to stress concentrations at the rougher surface. Also depending on the volume fraction, the influence differs for the metal lattice structures. For small volume fractions, the influence of a rougher surface is relatively larger than for higher volume fractions leading to less strength. Moreover, deformation modes change depending on the volume fraction of the metal lattice structures. For instance, microscopic buckling of individual struts under compression occurs at very low volume fractions, while sudden shear failure is observed for higher volume fractions. These aspects need to be considered when designing parts with lattice structures.

In addition, a quality control by DSC measurements shows the necessity of temperature and UV radiation in the post-curing process of the SLA manufactured methacrylate photopolymer. Although the measurements indicate that material characterization and lattice structure specimens are both fully cured, a slightly different polymer network can still be present due to the difference in the progression of the radical reaction mechanism. This can explain the remaining differences in the elastic modulus for the lattice structures between experiments and FEM simulations.

Finally, the evaluation of the homogenized lattice strength and buckling of individual struts with analytical formulas are helpful as a quick estimate in the design process. However, a different microstructure or polymer network of the smaller struts compared to the bulk specimens and the amount of defects can lead to slightly varying properties.

This chapter highlights the necessity to investigate different load cases and incorporate probabilistic effects into the design procedure in order to manufacture reliable lattice structures. This applies especially to lightweight design, where high safety factors are not tolerable. It is crucial for manufacturing processes like 3D printing, which are more prone to exhibit imperfections. FEM simulations are advantageous as they allow to distinguish the influence of the variation of individual effects and can help to get deeper insights into the damage progression. The presented approach can be applied to other unit cell types, AM processes and/or materials. Therefore, guidelines for a design engineer to evaluate the potential of

lattice structures for lightweight purposes from a robust design perspective with the proposed modeling approach are summarized in the following:

- Determine the probability distributions and correlation lengths of the relevant input parameters with simple experiments: material properties (especially accounting for a tension-compression asymmetry), geometry, loads
- Generate an FEM model incorporating the varying parameters by random fields
- Validate the model with regard to the simple experiments on the input parameters
- Determine the probability distribution of the performance of the structural components subject to all varying input parameters
- Perform a (weak) validation of the performance of the structural components by a small number of experiments (especially accounting for different load cases)
- Analyze the influence of individual input parameters on the performance of the structure with the model
- Evaluate whether improvements regarding the robustness of the most influential input parameters are possible to enhance the reliability of the performance of the structure
- Compare the probability to be below a certain performance level and the weight savings for lattice structures to conventionally manufactured lightweight components

This procedure could be applied in a multi-scale homogenization framework to determine the effective properties of lattice structures on a micro-scale, which are required for accurate computationally more efficient simulations with nonlinear material models on larger scales.

Some further remarks need to be made here. It can be seen that the proposed design approach with additively manufactured lattice structures is quite tedious. Especially the imperfections due to the current immaturity of AM processes make a reliable design more complicated. Hence, there is some catch-up potential for 3D printer manufacturer and material developer. In addition, it has been recently shown that an optimization with regard to stiffness with isotropic unit cell lattice structures is not beneficial in single point loading scenarios. In more complex loading scenarios such as distributed forces and with anisotropic unit cells (such as the cubic unit cell with different diameters of the individual struts) improvements can be achieved with lattice structures over conventional stiffness based

topology optimization with bulk material. However, manufacturing restrictions such as compatibility of unit cells as well as minimum and maximum dimensions of struts can limit the gains [52]. The use of lattice structures with regard to stiffness optimization can be more beneficial when the unit cells can be individually oriented by rotations instead of an alignment of the whole lattice along specific global axes [150]. Yet, this further complicates the design. Therefore other applications than optimization with regard to stiffness might be more suited for the use of lattice structures fabricated by AM. For instance, additively manufactured cellular structures can have advantages in other structural mechanics applications such as an optimization with regard to an improved buckling load [151]. Closing, there are several other applications where the benefits of cellular structures in combination with the design freedom of AM can be exploited as pointed out in Section 1.2. Since many of them are relevant for process engineering, this is discussed in the following chapter. After confirming working hypotheses 2 to 4, the superordinate working hypothesis 1 on lightweight design with lattice structures can be assessed.

### **Working hypothesis 1**

Additively manufactured lattice structures show potential in lightweight design applications.

This working hypothesis can only be confirmed to some extent. A design process is developed for lattice structures in lightweight applications comprising of an experimental characterization of imperfections and mechanical properties under different load cases as well as a numerical characterization of the failure behavior under probabilistic influences. However, the procedure is cumbersome and there are other applications where the benefits of lattice structures can be exploited more. Many of them also benefit from the mechanical properties that lattice structures provide. The proposed design process helps to use the mechanical features of lattice structures to full capacity in all applications.



### 3 Additive Manufacturing in Process Engineering

Having seen that the benefits of additively manufactured lattice structures in lightweight design are limited compared to the efforts for a reliable design, there is a need to look for further fields where the previously developed methods can be applied. Process engineering is very promising as many of the applications of lattice structures are relevant here. Process engineering focuses on the conversion of substances. The processes are carried out in chemical, physical or biochemical reactors. The aim is usually to gain a high yield and selectivity with a minimal cost of energy and raw materials. For some of those processes, for instance the production of bulk chemicals with more than 10 000 t/a, the consumption of resources (substances and energy) is so high that even improvements of less than 1 % can reduce the cost by several millions [152]. Thus, even slight optimizations have a large potential and are economically and ecologically beneficial.

The main adjustment parameters of chemical reactions are concentrations, temperature and pressure [153]. A homogeneous distribution of the substance concentrations and the temperature is often desirable to have a well defined process and a high reactive surface area between the substances. This applies especially to multi-phase systems and also to non-reactive separation processes such as extraction and absorption. However, in continuously operating plug flow reactors, even with a turbulent flow, very high reactor lengths are required for good mixing of multiple phases. A better homogenization of the substances can be achieved with static mixers or structured packings [152]. They separate, deflect and recombine partial flows to realize a good distributive mixing. Yet, the energy that is required for mixing leads to a pressure drop. The aim is to maximize the distribution of the substances while the pressure drop is minimized.

In this regard, lattice structures produced by additive manufacturing (AM), referred to as periodic open cellular structures (POCSs), are very promising for process intensification. The unit cell topology can be adjusted according to the desired flow properties almost without any manufacturing restrictions. It was shown that POCSs outperform state-of-the-art packings in terms of a homogeneous distribution of the substances [154, 155]. Moreover, several studies analyzed the pressure drop for different unit cell types, cell sizes, volume fractions and orientations in single- and multi-phase flow [44, 156–158].

Another challenge is heat transfer especially for highly exothermic or endothermic reactions in fixed-bed reactors. The often low thermal conductivity of the packed bed can lead to temperature differences that influence the chemical reac-

tion or even to hot-spots, which can result in undesirable byproducts and safety risks. Also here, POCSs can be beneficial to increase heat transfer, particularly when they are manufactured out of metals with high thermal conductivity [159]. The heat transfer was investigated in several studies depending on different unit cell types, cell sizes, volume fractions and orientations showing a higher heat transfer than in commercially available solutions [39, 157, 159]. In addition, it was found that a coupling of the POCS to the reactor wall is advantageous for heat transfer [39, 159]. With AM the wall coupling can be easily realized by integrated functionality in a monolithic printing approach. When a wall coupling is performed, then the POCS can also be utilized as a mechanical support for the reactor wall to withstand the pressure in the reactor, thus allowing to reduce the wall thickness.

While the large and rough surface of lattice structures produced by AM is a hindrance in structural mechanical applications as it is a potential starting point for cracks especially in fatigue, it is a huge upside in POCSs for process engineering applications where it can be used as a catalyst support. Studies successfully deployed this concept in chemical reactors for the hydrogenation of ethene [160] and the oxidation of carbon monoxide [161] as well as in bioreactors for the decarboxylation of ferulic acid with immobilized enzymes [162]. An even higher surface area can be achieved when carbon nanoparticles are utilized as a catalyst support. As shown by Sherbi *et al.* [163], a RuCu catalyst supported on multi-walled carbon nanotubes (MWCNTs) is promising in the hydrogenation of glycerol to 1,2-propanediol. To additionally employ the benefits of POCSs in mixing of the substances in a reactor as well as its own high surface area, carbon nanotubes (CNTs) can be grown on the surface of additively manufactured metal lattice structures by a chemical vapor deposition (CVD) process, which is subject of current research [164]. A Ti-6Al-4V lattice structure with CNTs on its surface is presented in Fig. 3.1.

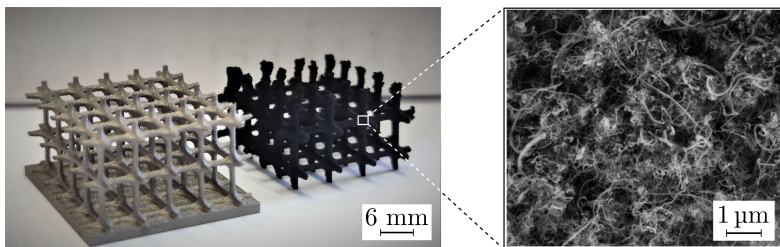


**Figure 3.1:** Additively manufactured Ti-6Al-4V lattice structure with CNTs as a catalyst support on its surface. Images courtesy of Hristiana Velichkova, Institute of Polymers and Composites, Hamburg University of Technology.

One more task of process engineering is the control of the reactors [152]. On the one hand, the reaction conditions need continuous adjustments for the reactor to operate in an optimal state and thus yield a high conversion and selectivity. On the other hand, safety shutdowns need to be implemented for a secure operation of reactors. In a recent study, two interwoven POCSs with a defined offset were used to adjust the flow of the reactive substances by shifting of the POCSs yielding a changed offset [46]. This shows the application of lattice structures as actuators in control. The interpenetrating nature of the POCSs is only possible by AM.

With contributions of this study, further concepts for the control of reactors were developed where the advantages of AM can be exploited. First, a “smart” reactor was developed. The reactor allows self-contained process control by a valve. The valve is made of a stimuli-responsive hydrogel with a lower critical solution temperature (LCST) type behavior. The hydrogel is a copolymer of *N*-isopropylacrylamide (NIPAM) and methyl methacrylate (MMA), which is temperature-responsive. It has a hydrophobic backbone and polar functional groups. At low temperatures the polar groups can form hydrogen bonds resulting in a preferential interaction with water. The large amount of water uptake by the hydrogel leads to an ordered coil structure of the polymer chains, which is very volume filling. Thereby, the flow is blocked meaning that the valve is closed. Above a certain higher temperature (for NIPAM around 32 °C), the hydrogen bonds break up and the hydrophobic backbone leads to a dominantly repulsive interaction with water. Thus, the polymer coil changes conformation to a globuli shaped state to reduce surface with water [165]. The water is expelled resulting in shrinking of the hydrogel and hence an opening of the valve. This transition is reversible. Compressive mechanical tests of the hydrogels show the need for MMA to increase its robustness due to a more rigid network. The hydrogel can be integrated into complex reactor geometries by synthesis within the reactor in a template mold. The water-soluble template can be removed once the polymerization of the hydrogel is finished. This requires multi-material three-dimensional (3D) printing making fused filament fabrication (FFF) the method of choice. To trigger the hydrogel valve, the reactor inlet is realized by helical windings around the valve allowing heat transfer of an exothermic reaction. The production of such complex reactor geometries is facilitated by AM. The functionality of the hydrogel valve is demonstrated in an exothermic emulsion copolymerization. When the initiator feed is stopped, the polymerization is disrupted. This leads to a temperature drop, so that the product outlet is closed and the unreacted substances are guided to the waste outlet. The concept of the “smart” reactor for outlet control by a stimuli-responsive hydrogel valve is depicted in Fig. 3.2. Hu *et al.* [166] extended this approach to stimuli-responsive hydrogel POCSs using digital light processing for the fabrication of such complex geometries. Here, the mass transfer in a multi-phase flow is controlled by the expanded or collapsed state of the hydrogel POCSs. They also show that a change in pH can be used as

a trigger for the phase transition apart from temperature. In addition, AM can help to realize “smart” reactors in terms of flexibility. Reactors can be designed in a modular approach where individual sections can be replaced either by different ones according to the desired reaction or by improved ones that optimize the reaction. These sections can be produced by rapid manufacturing [167].

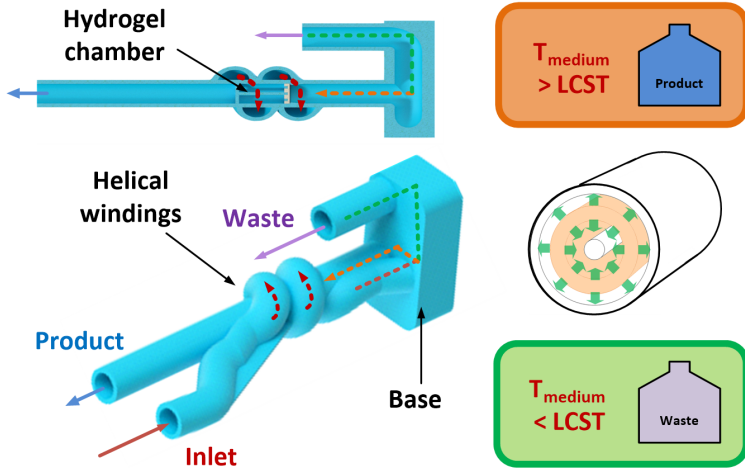


**Figure 3.2:** Concept of a “smart” reactor for self-contained outlet control by a stimuli-responsive hydrogel valve. Image from Hu *et al.* [31].

Having seen that actuation in reactors to adjust the process can be realized by additively manufactured interpenetrating POCSs or integrated hydrogel valves, another aspect of control is the measurement of the process state by sensors to monitor the reaction. Therefore, a second concept of a reactor with integrated sensing is developed. When POCSs are utilized in reactors for improved heat and mass transfer or as a catalyst support, they yield a promising opportunity to integrate sensors as they cover a large volume of the reactor. This allows a simultaneous local and temporal resolution of measurements. AM enables integrated sensing by the selective placement of functional materials such as CNT modified polymer nanocomposites within the lattice structure. Again, multi-material 3D printing is required making FFF the method of choice. CNT modified polymer nanocomposites can be employed in various applications such as strain [168–170], temperature [171–173] and gas sensing [174–176]. Strain sensing relies on the piezoresistive effect. The change in nanoparticle distance due to elongation of the composite leads to a resistance change. Temperature sensing is based on several effects that can also counteract each other. On the one hand, the thermal ex-

pansion of the polymer results in a change in nanoparticle distance similar to the case of strain sensing. On the other hand, the temperature also influences the intrinsic conductivity of the constituents and the tunnel effect. The thermoresistive and piezoresistive behavior of CNT modified polymer nanocomposites is further discussed in Chapter 4. Gas sensing relies on the oxidative/reductive property of the gases. The electron-withdrawing or -donating nature causes a change in the amount of defect electrons in the system, which influences the electrical conductivity of the nanocomposite [177]. Hence, CNT modified polymer nanocomposites are able to monitor all three main parameters of chemical reactions: pressure (in terms of strain), temperature and concentrations (in terms of gas). Furthermore, a locally resolving sensor system enables a tremendous opportunity to get more insights in the reaction process and can unveil potential optimizations without disturbing the flow. The concept of the reactor containing a POCS with integrated sensing is illustrated in Fig. 3.3.

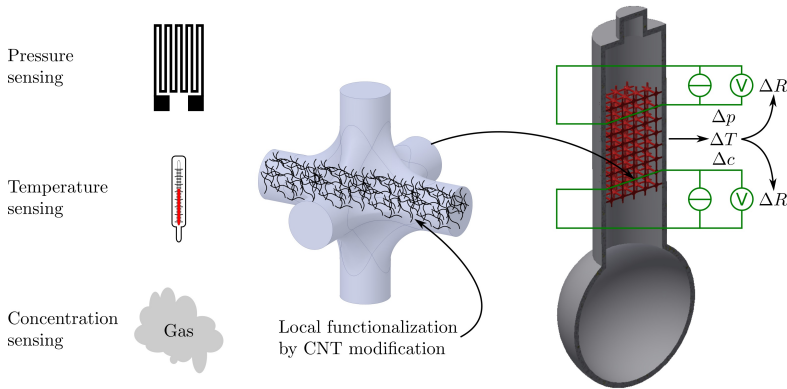


**Figure 3.3:** Concept of a locally resolving sensor system by functional integration in a POCS realized by multi-material printing with a selectively placed functional material such as a CNT modified polymer nanocomposite.

Both newly developed reactor concepts depend on FFF multi-material printing. However, the use of FFF printed structures is currently limited due to the anisotropy issue at a low level. High pressures in reactors require structural integrity. In addition, watertightness can be an issue for FFF printed parts, which is not acceptable in reactors that contain fluids. This highlights the necessity to develop new materials for FFF that solve the anisotropy issue and can be functionalized for integrated sensing applications. It leads to the second application of AM beyond rapid prototyping in this study.



## 4 Functional Material Printing

This chapter is attributed to the second application of additive manufacturing (AM) beyond rapid prototyping: functional integration with an electrically conductive material. Functional integration by a combination of materials requires the possibility of multi-material three-dimensional (3D) printing. Hence, the focus is on a material development for fused filament fabrication (FFF) as it is the only one of the popular AM techniques that allows a facile implementation of multi-material printing. The state of the art regarding FFF printing in general and of functional materials in particular is presented in Section 4.1. In Section 4.2 the utilized materials and methods are described. First, insights into epoxies and carbon nanotubes (CNTs) are given, which are the matrix and filler of the functional nanocomposite for FFF 3D printing. The utilized commercial materials are presented, electrical functionalization is explained and peculiarities of the filament production and sample preparation are elucidated. The measurements for thermal, rheological, geometrical, mechanical, fractographic and electrical characterization are described. The results are presented and discussed in Section 4.3 starting with the thermal properties and the post-curing cycle development. Then, dimensional stability, mechanical properties and fracture surfaces are discussed. Afterwards, electrical properties as well as temperature and strain sensing applications are illustrated. Finally, conclusions on functional material printing are drawn in Section 4.4.

### 4.1 State of the Art

FFF, also known as fused deposition modeling (FDM), is the most widely used AM process [6] and offers several advantages compared to other established techniques utilizing polymers. First, the FFF process offers a very simple way to implement multi-material 3D printing by using several printheads. This makes it the inevitable choice for applications where functional integration is implemented by a combination of materials. Furthermore, the filament is available in solid form, which facilitates handling. Contrary, the liquid ultraviolet (UV) radiation sensitive and often harmful resin (due to cytotoxicity of photoinitiators [178]) in stereolithography (SLA) and the fine powder in selective laser sintering (SLS) require elaborate safety precautions and storage conditions. In addition, a wide range of thermoplastic materials can be used in FFF, while the process limits the material choice to mostly acrylates in SLA and polyamide (PA) in SLS [178, 179].

Compared to SLA, materials can be functionalized by additives such as particles without the restriction of transparency for UV curing. Finally, the acquisition costs for FFF printers are low. Despite these advantages, the FFF process is mainly used for prototyping, simple jigs and fixtures as well as hobby applications. The current deficiency of FFF printing stems from the solidification of the material directly after deposition. This limits diffusion and entanglement of the polymer chains between the layers and between the infill lines within a layer and results in weak interfacial bonding [180]. The anisotropy in mechanical properties at a low level has been shown in several studies considering different materials, load cases, printing parameters and environmental conditions. Dizon *et al.* summarized the major aspects in a review article [179].

In order to circumvent or at least reduce the mechanical anisotropy issue, different approaches are attempted in the literature. First, an optimization of the printing parameters can be performed. For this purpose, the printing speed, nozzle and build platform temperature as well as layer width and height were varied in such a way that the strongest layer bonding is achieved [181]. In addition, the component needs to be oriented in the build space so that the main load path is not perpendicular to the layer interfaces [182]. However, this optimization has to be performed individually for each different component and it restricts the design freedom, which is one of the most persuading features of AM. In other approaches, the material and the fabrication process are modified. CNTs were included in the filament and subsequently excited by microwave irradiation [183]. Thus, heat is introduced into the printed component, which facilitates the diffusion of the polymer chains and improves the adhesion of the layers. Hart *et al.* [184, 185] applied a thermal annealing to amorphous thermoplastics above the glass transition temperature and semi-crystalline thermoplastics above the melting temperature in a specimen specific mold to increase the interlayer fracture toughness. Schaffer *et al.* [186] used gamma radiation to achieve cross-linking across the layers of a copolymer blend. Radiation creates radicals enabling cross-linking. Pretreatment of the individual layers, using plasma, can also improve interlayer bonding [187]. Another method to enhance bonding between the layers is to locally introduce thermal energy by a laser to the previous layer just before depositing the filament [188, 189]. This also allows diffusion across the layers due to the heating. All these possibilities have in common that they require expensive additional devices to improve the bonding. These are either mounted on the FFF printers or are utilized in subsequent processing steps. Despite this effort, in some cases no isotropy is achieved. The approach of Levenhagen and Dadmun [190] only modifies the material. Their idea is to use a bimodal molecular weight blend. The lower molecular weight chains have higher mobility and tend to migrate to an interface and thus enable diffusion and entanglement across layers. They found an increased interlayer adhesion, however, no isotropy could be reached.

An alternative in 3D printing of polymers to achieve isotropy is the utilization of thermosets where cross-linking can span the layer interfaces and lead to improved bonding. The direct write (DW) technique uses inks consisting of liquid resins such as polyurethane [191], epoxy [192–194] or cyanate ester [195] with additives that introduce a shear-thinning behavior such as fumed silica nanoparticles [191, 195] or nanoclay [193, 194]. Similar to FFF the material is extruded in this case either by syringes or dispensing robots. The shear-thinning behavior allows the material to pass through a fine nozzle and maintain its shape after being deposited on the build platform when the shear forces vanish [196]. Post-curing at elevated temperatures or with UV illumination leads to cross-linking and thus isotropic properties. Yet, the market penetration of DW printers is significantly less compared to FFF printers and especially in the case when dispensing robots are used, they are more costly. Similar to DW the Diels-Alder reversible thermoset (DART) 3D printing technology builds on cross-linking to produce isotropic parts [197]. The furan-maleimide Diels-Alder (fmDA) reaction enables reversible cross-linked materials that show thermoset behavior below a certain temperature and are meltable like thermoplastics at elevated temperatures. Although almost isotropic material properties are reached, the process shows some limitations. As with DW, the material is printed with a syringe and thus, it is not available in the form of a filament. In addition, the resolution is half as good as with conventional FFF and the thermal stability is restricted to a temperature of 80 °C.

In this study, for the first time a thermosetting polymer is developed that is provided in the form of a filament and can be printed on a low-cost FFF printer. The cross-linking in a post-curing process solves the mechanical anisotropy issue of FFF that currently restricts the technology. The material formulation is based on a high-molecular weight solid epoxy resin. Liquid epoxy resins with additives can be easily added to the formulation allowing to exploit another advantage of the FFF process: the implementation of multi-material 3D printing is straightforward via several print heads. Hence, local functional properties can be introduced into a component [198]. In recent years, there has been considerable progress in 3D printing of polymer composites as pointed out by Wang *et al.* [178]. Especially, 3D printing of polymers with CNTs to incorporate electrical conductivity is a promising field [199]. While mostly multi-walled carbon nanotubes (MWCNTs) are used as an additive in FFF, single-walled carbon nanotubes (SWCNTs) are rarely found as a filament modifier in the literature [200, 201] despite their superior electrical properties [202, 203]. A reason for this could be that a good dispersion is achieved for MWCNTs more easily [204]. As the nanoparticles can be incorporated in a liquid part of the new material formulation, dispersion can be carried out by three roll milling [205]. This is superior to the techniques for modification of conventional thermoplastic FFF filaments where some degree of inhomogeneity is remaining [206]. Thus, the new material formulation is exemplarily functionalized with SWCNTs. However, different modifications would

also be possible such as flame retardant additives, which enables the new material formulation to be utilized in various applications.

The modification with electrically conductive nanoparticles also allows to employ the new material formulation in sensing applications with FFF printed devices. Piezoresistive sensors that are printed in the FFF process with a thermoplastic polyurethane filament modified with MWCNTs already show potential, yet with relatively high filler contents of 1 wt% to 5 wt% [207, 208]. Conventionally manufactured piezoresistive sensors can be found with significantly lower filler contents of below 0.1 wt% [170]. Reducing the filler content with remaining electrical properties is economically favorable as well as desirable for processability. In addition, CNT nanocomposites can be used for temperature measurements [173]. However, this has not been shown with the FFF printing process despite the possibilities offered by multi-material 3D printing with regard to structural integration of sensors. Therefore, in this research a proof of concept study of the newly developed functionalized material with low SWCNT filler content in strain and temperature sensing applications is performed.

## 4.2 Materials and Methods

In this section, the materials are introduced and the functionalization process by modification with electrically conductive SWCNTs is described. Afterwards, the filament production and its analysis with differential scanning calorimetry (DSC) and oscillatory rheology is presented. Then, the sample preparation is explained. Finally, the characterization of the specimens is elucidated to determine the dimensional stability during curing, the mechanical properties and failure mechanisms as well as electrical and sensing properties.

### 4.2.1 Epoxy Resins

Epoxyes are thermosetting polymers with versatile properties that can be tailored by the formulation. They are used in a variety of fields ranging from automotive, aerospace, marine, civil engineering, electrical and industrial to leisure [209]. Main applications are adhesives, coatings, matrix for fiber reinforced polymers (FRPs) in structural design, flooring and insulation [210]. The most common commercial epoxy resin is diglycidyl ether of bisphenol A (DGEBA), which is produced by a reaction of bisphenol A with epichlorohydrin [209]. The molecular structure of DGEBA is presented in Fig. 4.1. It is also the main constituent of the solid epoxy formulation developed in this study. The outstanding properties of DGEBA can be explained by its molecular structure. Epoxy shows a low shrinkage during curing as the ring-opening reaction preserves the number and types of chemical bonds [2] and no small molecules are liberated during curing. A high reactivity is achieved by the terminal epoxy groups and the hydroxyl groups in

the middle of the molecule. Furthermore, good adhesion and compatibility with many materials is realized with the hydroxyl groups. Moreover, aromatic rings in the backbone lead to high heat and chemical resistance as well as durability. In addition, aliphatic chains and ether linkages result in flexibility. Finally, epoxies show corrosion resistance, electrical insulation and no volatiles are given off during curing [209]. The properties can be adjusted with additives and curing agents that change the viscosity during processing and the resulting polymer network. Also the molecular structure of DGEBA influences the physical properties. The number of repetitions  $n$  determines its molecular weight, which impacts the viscosity and the softening point of the resin. With  $n$  between zero and one, the resin is a liquid, while it moves to a semisolid and then a brittle solid at higher  $n$ , which can be up to 20. With higher  $n$ , the number of epoxy groups per unit mass decreases, leading to a reduced reactivity and cross-linking density resulting in lower heat resistance. Contrary, the number of hydroxyl groups increases, leading to better adhesion. Also the toughness and flexibility increase due to the lower cross-linking density [209]. Even with similar average cross-linking density, mixtures of DGEBA with different bimodal molecular weight distributions influence the environmental resistance and the mechanical properties [211].

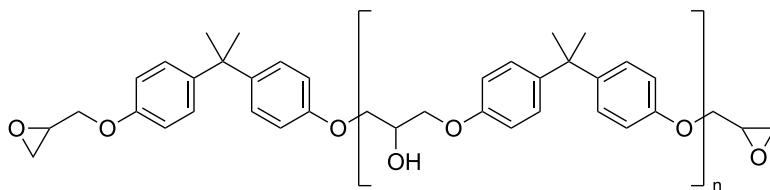


**Figure 4.1:** Molecular structure of DGEBA as the main constituent of the solid epoxy formulation.

In order to obtain a polymer network, DGEBA needs to be combined with a curing agent having more than two reactive functional groups. One of the most important types are nitrogen-containing curing agents such as amines that react via polyaddition. They range from aliphatic amines, which are highly reactive and usually liquid due to their low molecular weight, over cycloaliphatic amines to aromatic amines that are mostly solids and react slower with epoxy groups at elevated temperatures. This allows longer pot lives and the aromatic rings feature good chemical resistance [210]. The reaction of a primary amine with the epoxy group is illustrated in detail in Fig. 4.2. First, a nucleophilic attack of the free electron pair of the amino group takes place to the methylene carbon of the epoxy group. The methylene carbon has a reduced electron density due to the attached oxygen atom and is less sterically hindered than the methanetriyl

carbon. This leads to a positive charge of the nitrogen. The ring opening yields a negative charge of the oxygen. Second, a proton of the nitrogen is transferred to the oxygen resulting in a secondary alcohol and a secondary amine. The high reactivity of the epoxy group compared to normal ethers stems from the ring strain [210].

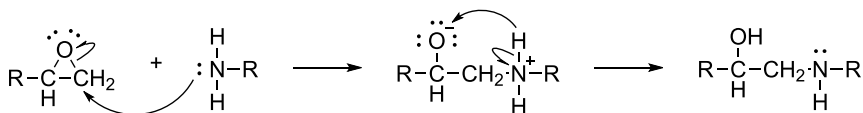
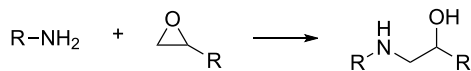


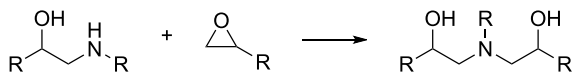
**Figure 4.2:** Nucleophilic attack of the free electron pair of a primary amine on the methylene carbon of the epoxy ring and subsequent formation of a secondary alcohol and secondary amine.

In general, four reaction mechanisms take place during the cure of amines with epoxies [212, 213]. The additions of primary and secondary amine are shown in Fig. 4.3a and Fig. 4.3b. Due to steric effects, the addition of primary amine to epoxy is usually faster than the addition of secondary amine [212]. Hydroxyl groups catalyze the addition reaction of amines to epoxies [212, 214, 215]. On the one hand, these are present in higher molecular weight DGEBA with  $n$  greater 0. On the other hand, additional hydroxyl groups arise from the ring opening reactions of amines with epoxies, which leads to an auto-acceleration effect with increasing degree of curing. As presented in Fig. 4.3c also the hydroxyl groups themselves can react with the epoxy rings by an addition to form ethers. The etherification is significantly slower than the amine additions and usually occurs at higher temperatures or with increasing progress of the curing [212, 213]. It can be further catalyzed by tertiary amines [212]. A fourth reaction mechanism is the homopolymerization displayed in Fig. 4.3d. The presence of tertiary amines leads to a polyetherification. In this case, the tertiary amine causes a ring opening yielding a negatively charged oxygen. This can itself react with an epoxy ring forming a new negatively charged oxygen [210, 216]. Although the reaction of secondary amines with epoxies results in tertiary amines, these are no effective catalysts for etherification and homopolymerization due to steric hindering.

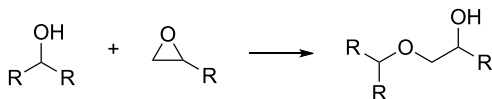
To reach good mechanical properties during curing, the mixing ratio of resin and curing agent has to be balanced. In general, stoichiometric mixing ratios are desirable leaving no unreacted molecules that could influence the surrounding polymer network. The decisive parameter is the number of functional groups of the molecules. Epoxies are characterized by the epoxy equivalent weight (EEW) given by the molecular weight of the epoxy divided by the number of epoxy groups per molecule. Amine curing agents are characterized by the amine hydrogen equivalent weight (AHEW) given by the molecular weight of the amine divided



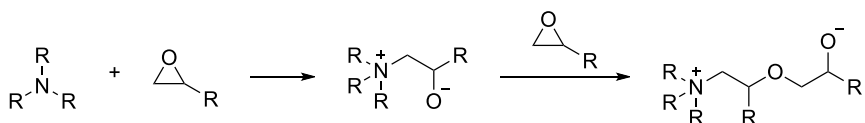
(a) Reaction with primary amine.



(b) Reaction with secondary amine.



(c) Etherification.



(d) Homopolymerization.

**Figure 4.3:** Reaction mechanisms during curing of epoxies with amines.

by the number of active hydrogens per molecule [209]. The stoichiometric mixing ratio can be calculated by

$$\frac{\text{AHEW}}{\text{EEW}} = \frac{m_{ca}}{m_r}, \quad (4.1)$$

where  $m_{ca}$  is the overall mass of the curing agent and  $m_r$  is the overall mass of the epoxy resin. When the formulation includes several different epoxy molecules and curing agents, the characteristic functionality of the mix needs to be calculated. In that case, the EEW is given by

$$\text{EEW} = \frac{m_r}{\sum_i \frac{m_{r,i}}{\text{EEW}_i}} = \frac{1}{\sum_i \frac{w_{r,i}}{\text{EEW}_i}}, \quad (4.2)$$

with  $m_{r,i}$  being the mass of the  $i$ -th epoxy resin component,  $\text{EEW}_i$  being the EEW of the  $i$ -th epoxy resin component and  $w_{r,i}$  being the mass fraction of the  $i$ -th epoxy resin component. Analogously, the AHEW can be determined by

$$\text{AHEW} = \frac{m_{ca}}{\sum_i \frac{m_{ca,i}}{\text{AHEW}_i}} = \frac{1}{\sum_i \frac{w_{ca,i}}{\text{AHEW}_i}}, \quad (4.3)$$

where  $m_{ca,i}$  is the mass of the  $i$ -th curing agent,  $\text{AHEW}_i$  is the AHEW of the  $i$ -th curing agent and  $w_{ca,i}$  being the mass fraction of the  $i$ -th curing agent. Despite stoichiometric ratios being a good starting point, some fine-tuning might be necessary depending on the application as the cross-linking density influences the toughness and heat resistance [209]. Moreover, the functionality might be changed when etherification and homopolymerization occur [212].

The curing process of epoxies with amines has several characteristic stages [210]. In the beginning, small epoxy and amine molecules react with each other forming oligomers. As for many reaction systems, the reaction rate of primary amines is faster than for secondary amines, the molecules grow linearly first [217]. Then, branching starts and the molecular size increases further. When a branched molecule extends throughout the whole structure, the gel point is reached. Here, the mixture contains a gel fraction in addition to a sol fraction for the first time. Prior to the gel point, the mixture is soluble in a solvent whereas afterwards it takes up the solvent and swells. The gel point is usually associated with a rapid increase in viscosity. Afterwards, a highly cross-linked 3D polymer network develops as the sol fraction decreases. In addition to the time, also the temperature plays a major role during curing as the glass transition temperature of the resin increases. When it reaches the curing temperature, vitrification occurs that significantly limits the mobility of molecules. As long as the glass transition temperature is well below the curing temperature, the reaction is controlled by the chemical kinetics. When the glass transition temperature approaches the curing temperature, the reaction becomes diffusion controlled and gets significantly

slower. Curing can still continue very slowly when the glass transition temperature surpasses the curing temperature so that the glass transition temperature is further increased until curing finally stops. To ensure full reaction of all functional groups, often a post-curing at elevated temperatures is performed [210]. The relationship of temperature and time on gelation and vitrification can be illustrated in time-temperature-transformation (TTT) diagrams [218]. Two important features of the curing process of epoxies with amines need to be highlighted, which are used in the formulation of the solid epoxy resin for FFF 3D printing. First, when the curing temperature is significantly below the glass transition temperature, curing essentially stops. This can be exploited by solid epoxies that are in the state of ungelled glass, yielding a long shelf life. Second, when the curing temperature is close to the glass transition temperature curing still continues despite being slowed down. Thus, by a tailored curing temperature profile the glass transition temperature can be increased until the state of a gelled glass is reached. This is possible without changing to an intermediate liquid state where dimensional stability is lost.

In addition, to realize a long shelf life of a solid epoxy filament for an FFF process, a solid latent curing agent is required. In applications with similar demands, such as the prepreg industry, diaminodiphenyl sulfone (DDS) and dicyandiamide (DCD) are often used [219]. The use of DCD is especially favorable since it is inexpensive [212] and very low concentrations are necessary due to an empirical AHEW of only approximately 13 g/eq [220–222] compared to 62 g/eq for DDS [223]. This is advantageous as less particles need to be incorporated in the solid epoxy leading to less embrittlement in the uncured state of the filament. The main reasons of the latency of DCD are the high melting point of 208 °C to 212 °C and the low solubility in epoxy due to the highly polar nature of DCD. However, this also poses a challenge as it can lead to inhomogeneity of the system due to agglomeration causing stoichiometric imbalances and larger particles that remain unreacted. This is usually avoided by very fine milling of the DCD to particle sizes smaller 10  $\mu\text{m}$ . A further challenge of DCD curing is the high reaction temperature of over 150 °C. Together with the highly exothermic reaction, this can lead to heat build up yielding a degradation of the material. Yet, the curing temperature can be reduced by the addition of accelerators such as tertiary amines or substituted ureas [212]. The molecular structures of the curing agent DCD and the utilized uron based accelerator UR 500, which is a toluene diisocyanate (TDI) derivative with isocyanates blocked by dimethylamine, are displayed in Fig. 4.4.

Although the curing mechanism of DCD was analyzed in several studies in the past, the detailed mechanism is not completely understood due to its complex nature [212, 224]. The initial reaction mechanism is the addition of the primary and secondary amines [209, 210]. Also etherification [212] and homopolymerization [209, 210] can appear in the presence of tertiary amines. In addition to the

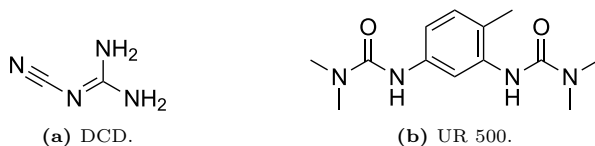


**Figure 4.4:** Molecular structures of the curing agent and accelerator of the solid epoxy formulation developed in this study.

reactions displayed in Fig. 4.3 further mechanisms are proposed. These include the reaction of the cyano group of DCD with hydroxyl groups of higher molecular weight DGEBA and from the ring opening reactions [209, 210, 221, 224, 225] as well as the formation of heterocyclic systems [212, 226]. The complex and numerous reaction mechanisms explain the low empirical AHEW of DCD.

The reaction mechanism of the uron based accelerator is illustrated in Fig. 4.5. In a first step, deblocking of the isocyanate groups occurs as presented in Fig. 4.5a. Deblocking occurs under heat at increased temperatures  $T$  [227] and a synergistic effect with DCD is assumed that activates deblocking *in situ* [209, 210]. Both products of the decomposition, the TDI and the dimethylamine, are capable of reactions with epoxy. As shown in Fig. 4.5b dimethylamine reacts with epoxy to form a tertiary amine. In contrast to the tertiary amines resulting from the amine curing, these are less sterically hindered so that they can act as an accelerator for the reaction of DCD with epoxy. The isocyanate groups of TDI can react with epoxy groups to form oxazolidinones as displayed in Fig. 4.5c. Since TDI has two functional groups additional linkages in the polymer network are formed [210, 220, 224, 227]. Disadvantages of the uron based accelerator are a reduced latency [209, 212] and dangling chains in the polymer network as dimethylamine acts as a chain termination agent. This yields a reduced glass transition temperature [220].

Despite the increased chain length of higher molecular weight DGEBA compared to liquid resins, the chain length is still small compared to thermoplastics. Commercially available 3D printing filaments such as polylactic acid (PLA) can have an approximate weight average molar mass of  $220\,000\text{ g mol}^{-1}$  [190]. Hence, in the uncured state solid epoxies are brittle due to insufficient entanglement of the polymer chains. Polyetheramines can be used as additional curing agents yielding an increased flexibility by incorporating longer chains in the polymer network that reduce the cross-linking density [210]. In addition, the polyether chains are flexible themselves as they are rather linear and the ether linkages require less rotational energy than predominant carbon chains. However, this also reduces the glass transition temperature. Figure 4.6 shows a polyoxypropylene functionally terminated with primary amines. Compared to other aliphatic amine

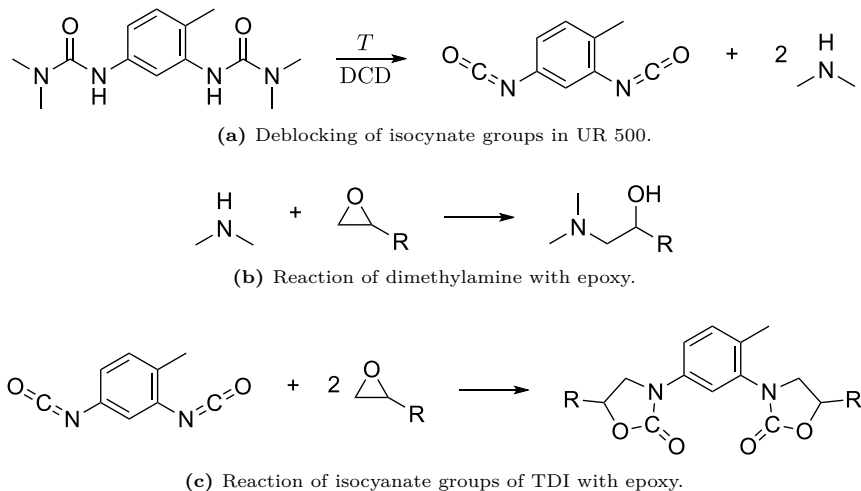


**Figure 4.5:** Reaction mechanisms of UR 500 with epoxies.

curing agents the reactivity is reduced as the amino group is sterically hindered by the neighboring methyl group [228]. The utilized polyetheramine has  $n = 32$  repetitions of the oxypropylene unit.

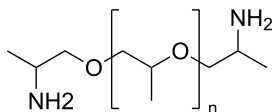


**Figure 4.6:** Molecular structure of a polyetheramine.

### 4.2.2 Carbon Nanotubes

Compared to other material classes like metals or ceramics, polymers have a low density and can be formed and molded at lower temperatures into very complex shapes. Contrary, mechanical properties such as stiffness and strength, thermal stability, as well as electrical and heat conductivity are low. While this is desirable in some applications, it can be a drawback in others. Therefore, polymers are often modified with additives. Especially nanoparticles with one dimension smaller 100 nm are attractive because of the high specific surface area that allows for interactions at the interface and the reduced distance between particles at

similar filler content [229]. Since their rediscovery in 1991 by Iijima *et al.* [230] CNTs have received increased attention because of their high aspect ratio and outstanding properties. CNTs can be thought of as graphene sheets that are rolled up as hollow cylinders. They have a diameter in the range of nanometers and a length up to several millimeters. CNTs are composed almost entirely out of carbon atoms forming  $sp^2$ -hybridized bonds that lead to an ordered hexagonal structure. They can consist of only one atomic layer and are hence called SWCNTs or they can consist of several concentrically stacked layers and are then called MWCNTs [231]. A section of an SWCNT is illustrated schematically in Fig. 4.7.

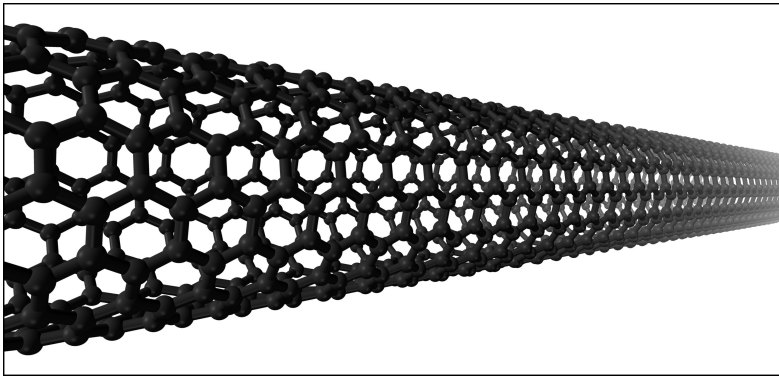


**Figure 4.7:** Schematic illustration of a section of an SWCNT showing the hexagonal arrangement of the carbon atoms.

CNTs have outstanding mechanical properties such as an elastic modulus of 1.28 TPa, which is in the order of diamond [232] and a tensile strength of up to 63 GPa [233] or even 150 GPa [234], which is orders of magnitude higher than that of conventional structural materials such as steel. In addition, they can withstand large bending deformations without damage [234]. Although the incorporation of CNTs in a polymer matrix showed a promising increase in stiffness and fracture toughness even for low filler contents [205], the improvement is far below expectations from rule of mixtures for higher filler contents [235]. Frequently reported issues are: (i) dispersion quality, (ii) interfacial shear strength, (iii) alignment and (iv) waviness [235, 236]. Overcoming these issues is part of current research.

In addition to their mechanical properties, CNTs also offer exceptional thermal properties. They are thermally stable up to 2800 °C in vacuum [231] and a thermal conductivity of  $3000 \text{ W m}^{-1} \text{ K}^{-1}$  was measured [237]. Theoretical studies predict even higher values of up to  $6600 \text{ W m}^{-1} \text{ K}^{-1}$ , which is more than twice as high

as that of diamond [238]. However, these high thermal conductivities cannot be transferred to polymer composites as the phonon mobility is restricted at the interface [235].

Probably the most interesting features of CNTs are their electrical properties. An electrical conductivity of  $2 \times 10^7 \text{ S m}^{-1}$  was measured, which is similar to that of copper and a current carrying capacity of  $6 \times 10^4 \text{ A mm}^{-2}$  was observed, which is orders of magnitude higher [239]. This might enable to overcome the limitations in the silicon-based production of electronic devices [240, 241]. The superior electrical properties of CNTs can be explained by the electronic structure of graphene, which is a zero-gap semiconductor [242]. Depending on the direction of the chiral vector, the CNTs can be either metallic or semiconducting. The chiral vector is the hypothetical roll-up vector connecting two carbon atoms of the graphene sheet so that the head of the vector touches its tail in the tubular CNT shape. The chiral vector can be decomposed into two vectors in the directions of the zigzag carbon bonds of the graphene sheet. The number of steps  $n$  and  $m$  along the base vectors leads to the typical  $(n, m)$  nomenclature [231]. The resulting configurations are called zigzag  $(n, 0)$ , armchair  $(n, n)$  or chiral. Zigzag CNTs are always semiconducting and armchair CNTs are always metallic. Chiral CNTs can be quasi-metallic when the difference of  $n$  and  $m$  is a multiple of three or semiconducting in all other cases. This is an important characteristic when analyzing the temperature dependent resistivity of CNTs as metallic conductors have a positive temperature coefficient (PTC) and semiconductors have a negative temperature coefficient (NTC).

In general, there are three electrical conduction mechanisms that need to be considered in nanocomposites: (i) the intrinsic conductance of the nanoparticle, (ii) the conductance at a direct particle contact and (iii) the conductance between close particles by quantum tunneling [243]. In contrast to thermal conductivity, the excellent electrical conductivity of CNTs can be transferred to polymer composites exploiting the quantum mechanical phenomenon of the tunnel effect. With a small probability electrons can propagate through a potential barrier of certain height and width such as a thin insulating polymer film in a composite. According to Simmons [244] the electrical tunnel current density  $J$  at low applied voltage can be calculated by

$$J = \frac{3\sqrt{2m_e\varphi}}{2s_{\text{film}}} \left(\frac{e}{h_P}\right)^2 V \exp\left(-\frac{4\pi s_{\text{film}}}{h_P} \sqrt{2m_e\varphi}\right), \quad (4.4)$$

with  $m_e$  being the electron rest mass,  $\varphi$  being the height of the potential barrier,  $s_{\text{film}}$  being the thickness of the insulating film,  $e$  being the elementary charge,  $h_P$  being the Planck constant and  $V$  being the voltage across the film. From Eq. (4.4) it can be seen that the tunnel current density strongly depends on the thickness of the insulating film with a higher thickness leading to a smaller current density. This can be exploited in the form of a piezoresistive effect in sensing applications.

In addition, the tunnel current density also depends on the temperature with higher temperatures leading to a higher current density [245].

On a macroscopic scale, an electrical conductivity of a polymer nanocomposite is reached when a particle network forms throughout the component. Hence, the number of conductive paths and the number of particles per path become a factor [246]. The overall electrical conductivity depends on the filler content and usually shows a steep increase at a certain concentration that is known as the percolation threshold. When the filler content increases, the distance between the conductive nanoparticles decreases so that they form larger and larger clusters that finally span the whole component. A further increase in filler content increases the number of conductive paths and the redundancy of the network. Above the percolation threshold, the conductance at a direct particle contact has a dominant role [247]. The electrical conductivity can be predicted with statistical percolation theory [248]. In addition to the filler content also the size and geometry of the filler influence the percolation threshold. With decreasing particle size, the number of particles increases at the same filler content leading to a smaller distance between the particles and thus an increased tunnel current. A high aspect ratio (ratio between largest and smallest dimension) results in a smaller number of particle contacts that are necessary to form a conductive path and a higher probability of particle contacts yielding a higher redundancy of the conductive network [229, 249]. Therefore, CNTs are an ideal candidate for electrical conductivity functionalization. Due to their high aspect ratio, which is typically in the range of 1000, a statistical percolation threshold of 0.1 wt% is predicted [250] in contrast to 16 wt% for spherical particles [251]. The small amount of CNT content to reach electrical conductivity has three advantages: (i) there is no degradation of the mechanical properties due to high filler loadings [249], (ii) further additives can be used that allow for instance an adjustment of the viscosity, flame retardancy or coloring [202] and (iii) the final component cost might be reduced. Hence, many scientific studies regarding the electrical conductivity of CNT polymer composites were already carried out and were summarized by Bauhofer and Kovacs [250]. SWCNTs are especially suited for electrical conductivity modification as their aspect ratio is even higher due to their smaller diameters. The technology established by OCSiAl in 2014 allows industrial scale production volumes of SWCNTs at low cost making them more attractive than before [252]. Furthermore, their SWCNTs gained a registration, evaluation, authorisation and restriction of chemicals (REACH) certification in 2016 allowing the use in a wide range of industries [253, 254].

In addition to the previously mentioned advantages, experiments showed even smaller percolation thresholds for carbon nanoparticles [251, 255]. Sandler *et al.* [256] found a percolation threshold of 0.0025 wt% for MWCNTs, which is significantly below the predicted values from statistical percolation theory. It was deduced that two percolation thresholds coexist in polymer nanocomposites

due to different network forming mechanisms: (i) the higher statistical percolation threshold where particles get close enough to form a conductive network due to filler loading and (ii) the lower kinetic percolation threshold where a conductive network develops due to aggregation of the particles [257]. To explain the kinetic percolation threshold of CNTs, colloid science needs to be considered [256, 258].

Colloids usually consist of a discontinuous phase that is uniformly distributed in a finely divided state in a continuous phase. The discontinuous phase has one dimension in the range of 1 nm to 1  $\mu\text{m}$  [259]. Within the scope of this study, the discontinuous phase are particles and the continuous phase is a solvent, however, in principle also other combinations in the state of matter are possible. The dimensions of the particles lead to a high surface-to-volume ratio. As the molecules at the interface of the particle to the solvent have different properties than in the bulk phases, their contributions to the system behavior need to be considered. Here, effects of surface chemistry become crucial [259]. To understand the circumstances at which a conductive network of nanoparticles forms throughout the polymer, the attractive and repulsive forces between the particles need to be considered. In general there are four forces each [260]. The attractive forces are: (i) electrostatic forces between positively and negatively charged particles, (ii) van der Waals forces, (iii) chemical and physical adsorption forces where a molecule with multiple functional groups bridges several particles and (iv) interface forces during coalescence of particles with a solvation shell that is immiscible with the dispersant and allows bridging of particles. The repulsive forces are: (i) electrostatic forces between like-charged particles, (ii) Born repulsion, (iii) entropic repulsion where hindrance of the mobility of molecules adsorbed to the particle's surface leads to a loss in entropy at close contact and (iv) short range lyosphere repulsion where a lyosphere shell of the dispersant needs to be desorbed to allow coagulation of the particles. The most important forces are the attractive van der Waals forces and the repulsive electrostatic Coulomb forces between like-charged particles.

The stability of colloidal dispersions can be analyzed with Derjaguin-Landau-Verwey-Overbeek (DLVO) theory combining these two main factors [261, 262]. While the van der Waals potential for individual molecules is inversely proportional to the sixth power of the distance, for particles the forces between all pairs of molecules in the particles need to be summed up [263]. This leads to an inverse proportionality of the potential between two parallel half-spaces to the squared distance for small ranges and to the cubed distance for greater ranges due to a retardation effect [259, 264]. In the case of a close approach of two spherical particles, the potential is inversely proportional to the distance. The surface charges of the particles, which are required for the repulsive electrostatic forces, can arise by a variety of mechanisms: (i) ionization of surface groups, (ii) preferential solution of one species of ions from sparingly soluble crystals, (iii) isomorphous substitution where an ion of a particle is replaced by one with

a different charge, (iv) charged crystal surfaces at fracture planes and (v) adsorption of surfactant ions [259, 265]. In the case of CNTs, there are only few reactive surface groups as they mainly consist of carbon. However, catalytic impurity atoms from production and surface oxides from storage can be found [266]. In organic dispersants such as epoxy resin, the interaction can be described as an acid-base equilibrium [267]. A proton transfer of the reactive surface groups to adsorbed dispersant molecules with subsequent desorption of the proton-carrying dispersant molecules leaves a negatively charged surface as in mechanism (i) [268]. The charged surface attracts counterions resulting in the formation of an electrical double layer. According to the Stern model it consists of an inner layer of ions that adhere to the particle's surface. Here, the potential drops linearly from the surface potential  $\Psi_0$  to the Stern potential  $\Psi_\delta$  at the outer Helmholtz plane, which is defined at the center of the adhered ions. The inner layer is followed by a diffuse layer where the ion concentration decreases with increasing distance. Here, the potential drops further exponentially [265, 269]. The characteristic distance at which the Stern potential has dropped to  $1/e$  is given by the Debye length  $1/\kappa$  and can be calculated by

$$\kappa = \sqrt{\frac{e^2 \sum_i n_i z_i^2}{\varepsilon_r \varepsilon_0 k_B T}} = \sqrt{\frac{2N_A e^2 I}{\varepsilon_r \varepsilon_0 k_B T}}, \quad (4.5)$$

where  $e$  is the elementary charge,  $n_i$  is the number density of ion  $i$ ,  $z_i$  is the charge number of ion  $i$ ,  $\varepsilon_r$  is the relative permittivity,  $\varepsilon_0$  is the vacuum permittivity,  $k_B$  is the Boltzmann constant,  $T$  is the thermodynamic temperature,  $N_A$  is the Avogadro constant and  $I$  is the ionic strength. The ionic strength is defined by

$$I = \frac{1}{2} \sum_i c_i z_i^2, \quad (4.6)$$

with  $c_i$  being the molar concentration of ion  $i$ . The Debye length is also referred to as the diffuse layer thickness [259, 265]. It can be seen that the Debye length depends on the charge number of the ions as well as the molar concentration. The lower the charge number and the molar concentration of the ions, the higher the thickness of the diffuse layer and hence the more far-reaching is the repulsive electrostatic potential [265, 269]. Another characteristic of the electrical double layer is the electrostatic potential. However, it is not possible to measure it directly. Instead, the electrokinetic potential  $\zeta$  is determined. It is the potential at the shear plane between the effective solid-liquid interface, which develops when a charged particle is moved in the dispersant. In that case, the adhered ions and also a part of the diffuse layer form an envelop that remains in contact with the particle so that the interface is not directly at the surface. The zeta potential can be experimentally determined with electrokinetic experiments such as streaming current and streaming potential measurements, electro-osmotic, electrophoretic

or electroacoustic investigations. It is often assumed that the zeta potential is approximately equal to the Stern potential. The higher the zeta potential, the higher the repulsive potential [264, 265]. The electrical double layer with its characteristic attributes according to the Stern model is displayed in Fig. 4.8.

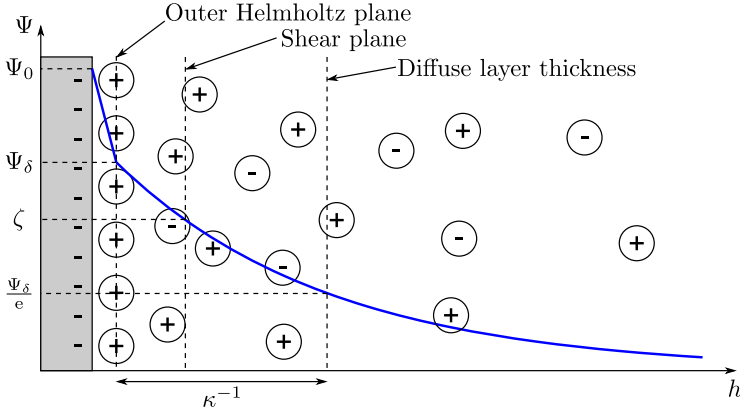


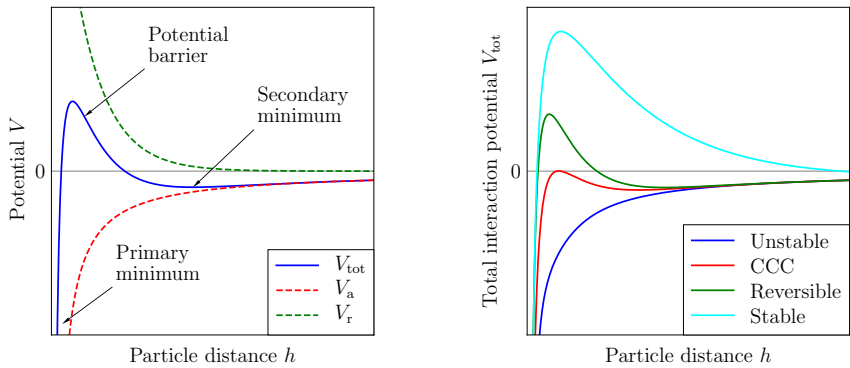
**Figure 4.8:** Electrical double layer according to the Stern model (following [265, 269]). The blue line shows the potential  $\Psi$  depending on the distance from the particle  $h$ .

According to DLVO theory the attractive van der Waals potential  $V_a$  and the repulsive electrostatic Coulomb potential  $V_r$  can be combined by linear addition to form the total interaction potential

$$V_{\text{tot}} = V_a + V_r. \quad (4.7)$$

This leads to the typical curve displayed in Fig. 4.9a that can be used to explain the stability of colloidal dispersions. At short and large distances the attractive potential dominates, while at intermediate distances the repulsive potential can dominate depending on the electrical double layer. In the secondary minimum, the particles are loosely coagulated and the potential barrier can prevent the system from further approach and the formation of aggregates. However, due to Brownian motion and diffusion some particles can still overcome the potential barrier. Hence, higher temperatures can lead to aggregation as the kinetic energy of the particles and thus the Brownian motion increase [259, 269]. In addition, the stability of a colloidal dispersion is strongly dependent on the height of the potential barrier and thus on the charge number and molar concentration of the ions in the dispersant as shown in Fig. 4.9b. At low ion concentrations, the potential barrier is high and the system stable so that no coagulation occurs (cyan

line). At slightly higher ion concentrations, the typical shape with a primary and a secondary minimum occurs with the previously mentioned properties (green line). The loose coagulation in the secondary minimum is reversible and can be eliminated for instance by shear forces. With further increasing ion concentration, at some point the height of the potential barrier is at  $V_{\text{tot}} = 0 \text{ J}$  and the critical coagulation concentration (CCC) is reached (red line). Finally, at high ion concentrations the attractive potential dominates at all particle distances and rapid aggregation takes place so that the system is unstable (blue line) [260, 265, 269, 270].



(a) Additive combination of attractive and repulsive potential.

(b) Various shapes of the total interaction potential.

**Figure 4.9:** Additive combination of the attractive van der Waals potential  $V_a$  and the repulsive electrostatic Coulomb potential  $V_r$  yielding the total interaction potential  $V_{\text{tot}}$  according to DLVO theory. Different shapes of the total interaction potential depend on the electrical double layer (following [270]).

The previously mentioned influences on overcoming the potential barrier and thus the formation of conductive networks in colloidal dispersions according to DLVO theory have been analyzed for CNTs in epoxy. Faiella *et al.* [271] showed that an increased temperature during composite curing leads to faster network formation. First, the Brownian motion of particles is favored leading to perikinetic coagulation. In addition, the viscosity of the epoxy resin is reduced, which increases the mobility of the particles. Inam and Peijs [272] found that the presence of the curing agent yields faster aggregation as the ion concentration is increased. This reduces the repulsive potential barrier. Moreover, Kovacs *et al.* [257] state that the introduction of shear forces influences the particle aggregation and

conductive network formation. The process of orthokinetic coagulation can be described with a stability diagram. In a system that is initially loosely coagulated in the secondary minimum, low shear forces eliminate the coagulation and stabilize the system. Higher shear forces allow to overcome the potential barrier and lead to the formation of aggregates in the primary minimum. At very high shear forces these aggregates are broken up and the system is stable again with separated particles [258, 273, 274]. These considerations have to be taken into account when analyzing the electrical conductivity of CNT modified epoxies.

### 4.2.3 Utilized Commercial Materials

To realize a thermoset filament that can be printed with a standard, low-cost FFF printer, a solid epoxy resin (Epilox A 50-02, LEUNA-Harze GmbH, Leuna, Germany) is used as the main constituent. As solid epoxies are brittle, a polyetheramine (Jeffamine D-2000, Huntsman Corporation, The Woodlands, TX, USA) is added as a curing agent for the production of a prepolymer. To ensure long shelf life, latent solid DCD is employed as the main curing agent. It is added in the form of a paste (IsoQure DCD LER 50, Isochem Kautschuk-GmbH, Udenheim, Germany) with liquid epoxy resin to facilitate mixing and avoid agglomerates. To reduce the curing temperature, a solid uron based accelerator (IsoQure UR 500 LER 50, Isochem Kautschuk-GmbH, Udenheim, Germany) is utilized, also in the form of a paste with liquid epoxy resin. For electrical functionalization SWCNTs (TUBALL, OCSiAl Europe S.a.r.l, Leudelange, Luxembourg) are used in the form of a masterbatch dispersed (see Section 4.2.4 for details) in liquid epoxy resin (EPIKOTE Resin MGS RIMR 135, Hexion Inc., Columbus, OH, USA). In addition, a pre-dispersed concentrate of SWCNTs (TUBALL MATRIX 301, OCSiAl Europe S.a.r.l, Leudelange, Luxembourg) is employed. A summary of the EEW and AHEW of the constituents of the newly developed material formulation is presented in Tab. 4.1. They are needed to determine stoichiometric mixing ratios with Eq. (4.1) to Eq. (4.3). To benchmark the newly developed material, a comparison with commercial thermoplastic filaments is carried out. A PLA filament (PrimaValue PLA, PrimaCreator, Malmö, Sweden) is analyzed for a comparison of the mechanical properties. Two further filaments are considered for a comparison of the electrical properties: (i) carbon black (CB) filled PLA filament (Conductive PLA, Protoplant Inc., Vancouver, WA, USA) and (ii) MWCNT filled acrylonitrile butadiene styrene (ABS) filament (3DXSTAT ESD-ABS, 3DXTECH, Grand Rapids, MI, USA) [275]. The PLA/CB filament has a CB content smaller than 21.43 wt% [276] and the ABS/MWCNT filament has a carbon additives content of less than 10 wt% [277].

**Table 4.1:** Summary of the EEW and AHEW of the utilized commercial materials.

Material	EEW	AHEW	Source
Epilox A 50-02	475 g/eq		[278]
Liquid epoxy resin <sup>1</sup>	189 g/eq		[279]
EPIKOTE Resin MGS RIMR 135	176 g/eq		[280]
Jeffamine D-2000		514 g/eq	[228]
IsoQure DCD		13 g/eq	[220–222]

<sup>1</sup> The exact chemistry of the liquid epoxy utilized in the pastes with DCD and the uron based accelerator remains unclear, so a standard epoxy (EPON Resin 828, Hexion Inc., Columbus, OH, USA) is assumed.

#### 4.2.4 Functionalization

For electrical functionalization SWCNTs are dispersed in liquid epoxy resin by a three roll mill (120E-250, EXAKT Advanced Technologies GmbH, Norderstedt, Germany) that allows to apply the required higher shear forces to break up aggregates (see Section 4.2.2). A masterbatch with a concentration of 2 wt% is produced. A dispersion in the solid epoxy resin would be desirable, however, its viscosity is too high for the three roll milling process. Three roll milling leads to superior dispersion qualities compared to ultrasonication [281] due to the high shear amplitudes that are necessary to separate the agglomerates [282]. In addition, three roll milling avoids fracture [205], while ultrasonication can damage the SWCNTs yielding a reduction in length [271]. The rollers are heated to a temperature of 25 °C and a seven step process with decreasing gaps is applied [283]. The process parameters are listed in Tab. 4.2 with gap widths and rotational speeds  $\omega_{cyc}$ .

**Table 4.2:** Parameters of the three roll milling process.

Step	Gap 1	Gap 2	$\omega_{cyc,1}$	$\omega_{cyc,2}$	$\omega_{cyc,3}$
1	120 $\mu\text{m}$	40 $\mu\text{m}$	33 rpm	100 rpm	300 rpm
2	40 $\mu\text{m}$	13 $\mu\text{m}$	33 rpm	100 rpm	300 rpm
3 - 7	13 $\mu\text{m}$	5 $\mu\text{m}$	33 rpm	100 rpm	300 rpm

#### 4.2.5 Filament Production

To reduce pores, the solid epoxy resin is degassed in a vacuum oven (VO400, Memmert GmbH & Co. KG, Schwabach, Germany) at a temperature of 100 °C

and a pressure of 10 mbar before further processing. Since the solid epoxy resin is too brittle to be used as a filament in the FFF process, a prepolymer with the polyetheramine curing agent is prepared. The solid epoxy resin is heated to a temperature of 100 °C in an oven (UF30plus, Memmert GmbH & Co. KG, Schwabach, Germany) to reach a liquid state and the polyetheramine is added substoichiometrically with a mass fraction of 6:19 of polyetheramine:solid epoxy (the proper stoichiometry is a mass fraction of 13:12). The utilized mixing ratio was determined in preliminary rheology measurements to obtain a formulation where the gel point is just not reached (see Appendix A.1). Thus, longer and flexible prepolymer molecules are gained while the mixing with further components is still possible as full curing is avoided (see Section 4.2.1). After stirring with a spatula for premixing, the material is homogenized in a dual asymmetric centrifuge (Speedmixer DAC 150.1 FVZ, Hauschild GmbH & Co. KG, Hamm, Germany). The prepolymer is cured at a temperature of 80 °C for 2.5 h. Then, the prepolymer is added to solid epoxy resin with a mass fraction of 3:17 of prepolymer:solid epoxy. In case of the functionalized filament, the SWCNT masterbatch is added according to the desired final SWCNT concentration. For a final SWCNT content of 0.05 wt%, 0.075 wt% and 0.1 wt% the in-house masterbatch (see Section 4.2.4) is used, where an exceptional dispersion quality is known from previous works [284]. However, with an increasing amount of masterbatch also the amount of liquid epoxy in the filament increases yielding a filament that loses structural integrity. Significantly higher filler concentrations in the masterbatch are difficult to reach with the process described in Section 4.2.4. Hence, the commercial pre-dispersed concentrate of SWCNTs with 10 wt% is used for a final SWCNT content of 0.2 wt%. Furthermore, a stoichiometric amount of the DCD paste is added. The components are heated to a temperature of 120 °C, premixed with a spatula and homogenized in a dual asymmetric centrifuge. In a last mixing step, the uron based accelerator paste is added with a mass fraction of 1:2 of uron based accelerator paste:DCD paste. A final homogenization is again carried out with a dual asymmetric centrifuge. Then, the material is filled in a syringe, reheated again and extruded as a filament with a slightly larger than desired diameter. To reach the final diameter of  $1.75 \pm 0.10$  mm for FFF printing, the filament is rolled on a heating plate with a spatula at a temperature of approximately 50 °C. Filaments with a length of 5 cm to 12 cm are produced. The steps of the filament production process are illustrated in Fig. 4.10. This kind of filament production process is used instead of a professional extrusion as it allows flexible adjustments of the material formulations with small amounts of material and without cleaning of the extruder.

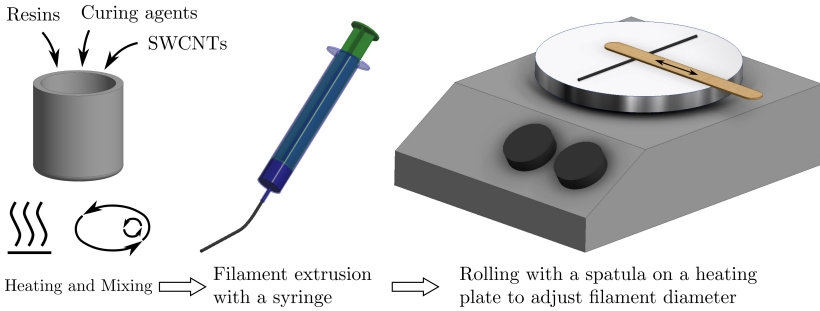


**Figure 4.10:** Filament production process for the solid epoxy formulation.

#### 4.2.6 Differential Scanning Calorimetry

A thermal analysis of the newly developed solid epoxy formulation is performed by DSC (DSC 204 F1 Phoenix, NETZSCH-Gerätebau GmbH, Selb, Germany). All measurements are carried out with a rate of  $10 \text{ K min}^{-1}$  under nitrogen atmosphere. Representative samples with a mass of approximately 15 mg are cut from the specimens. The uncured material formulation is investigated from temperatures of  $-50^\circ\text{C}$  to  $250^\circ\text{C}$ . On the one hand, the glass transition temperature  $T_g$  is determined where softening starts. On the other hand, the onset temperature of the exothermal curing peak  $T_{c,on}$  is analyzed, which acts as a limit for the processing temperature. Moreover, the shelf life of the uncured material is examined by determining the specific residual reaction enthalpy of the curing peak. For this purpose, the material is stored at room temperature  $T_r = 23^\circ\text{C}$  and in a freezer at a temperature of  $-28^\circ\text{C}$ . Measurements are performed after 1 week, 1 month, 3 months and 6 months. In addition, the thermal stability of cured dog-bones of the unmodified solid epoxy formulation and the one with 0.2 wt% SWCNT modification is investigated in terms of the glass transition temperature. The shelf life and thermal stability measurements are conducted from temperatures of  $23^\circ\text{C}$  to  $250^\circ\text{C}$ . For comparison of the thermal stability, also the PLA filament is examined from temperatures of  $-20^\circ\text{C}$  to  $230^\circ\text{C}$ .

#### 4.2.7 Rheology

In oscillatory rheology, the shear stress  $\sigma_{12}$  depending on the time  $t$  is given by

$$\sigma_{12}(t) = \underbrace{G' \gamma_0 \sin(\omega t)}_{\text{elastic part}} + \underbrace{G'' \gamma_0 \cos(\omega t)}_{\text{viscous part}}, \quad (4.8)$$

where  $\gamma_0$  is the shear strain amplitude,  $\omega$  is the angular frequency,  $G'$  is the storage modulus and  $G''$  is the loss modulus [285]. For visco-elastic materials, a phase shift  $\delta$  between strain and stress can be observed and the loss factor  $\tan(\delta)$  is determined with

$$\tan(\delta) = \frac{G''}{G'}. \quad (4.9)$$

It can be used to characterize whether the material behavior is predominantly solid ( $G' > G''$ ) or fluid ( $G' < G''$ ) [286]. At  $\tan(\delta) = 1$ , the solid to fluid crossover point is reached. To ensure dimensional stability during curing, a predominantly solid behavior is necessary. Oscillatory measurements with a rheometer (ARES RDA-III 28, TA Instruments, New Castle, PA, USA) are carried out in parallel plate configuration. A plate diameter of 40 mm and a gap size of 0.5 mm is used. Time sweeps are performed at increasing temperature levels with a frequency of 1 Hz and a strain amplitude of 1%. The measurement parameters are inside the linear visco-elastic region determined from preliminary experiments. The temperature is increased in such a way that the material remains below the solid to liquid crossover point. As curing progresses, the glass transition temperature increases allowing higher curing temperatures subsequently until the material is fully cured (see Section 4.2.1).

### 4.2.8 Sample Preparation

To characterize the solid epoxy formulation, specimens are prepared with an FFF 3D printer (Ender-5 Pro, Shenzhen Creality 3D Technology Co., Ltd, Shenzhen, China). As the filament is not available on spools due to the production process, the printing process needs to be adjusted. The bowden tube is removed at the feeder and filament pieces are filled in the bowden tube. Then, the bowden tube is reattached to the feeder and a thermoplastic filament on a spool is used to push the solid epoxy forward to the hotend by the feeder. The adjusted printing process is shown in Fig. 4.11. A 0.4 mm diameter nozzle is used. The build platform is not heated and printing is performed on a paper sheet that provides good adhesion during printing and is easy to peel off afterwards. All solid epoxy specimens are post-cured in an oven according to a temperature program developed by rheology measurements as presented in Section 4.2.7, ensuring dimensional stability. The temperature is held at 40 °C for 72 h, at 45 °C for 72 h, at 55 °C for 36 h, at 70 °C for 6 h, at 100 °C for 1 h and at 140 °C for 80 min. The temperature ramps in between are conducted with a rate of 1 K min<sup>-1</sup>. The temperature program is very conservative in terms of the time spans at the individual temperature steps as the current filament production method is very cumbersome. A loss of specimens is not acceptable. The benchmark thermoplastic filaments for comparison of the mechanical and electrical properties are printed in a regular setup on a heated glass build platform. For the ABS/MWCNT material, adhe-

sive (PrimaFIX, PrimaCreator, Malmö, Sweden) is applied on the glass plate. All prints are carried out with a layer height of 0.2 mm, a line width of 0.4 mm, a line distance of 0.4 mm and 100 % infill density. Printing and build platform temperatures as well as printing speeds are presented in Tab. 4.3.

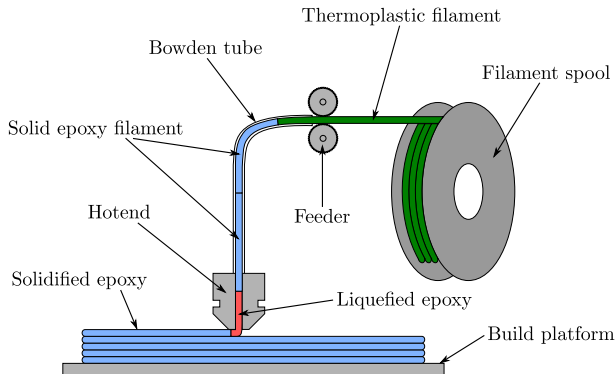


**Figure 4.11:** FFF printing process with the solid epoxy formulation.

**Table 4.3:** Printing  $T_p$  and build platform  $T_{bp}$  temperatures as well as printing  $v_p$  and initial layer  $v_{p,ini}$  speeds for the different materials.

Material	$T_p$	$T_{bp}$	$v_p$	$v_{p,ini}$
Solid epoxy	120 °C	23 °C	20 mm s <sup>-1</sup>	10 mm s <sup>-1</sup>
Solid epoxy/SWCNT 0.05 wt%	110 °C	23 °C	20 mm s <sup>-1</sup>	10 mm s <sup>-1</sup>
Solid epoxy/SWCNT 0.075 wt%	100 °C	23 °C	20 mm s <sup>-1</sup>	10 mm s <sup>-1</sup>
Solid epoxy/SWCNT 0.1 wt%	80 °C	23 °C	20 mm s <sup>-1</sup>	10 mm s <sup>-1</sup>
Solid epoxy/SWCNT 0.2 wt%	95 °C	23 °C	20 mm s <sup>-1</sup>	10 mm s <sup>-1</sup>
PLA	220 °C	60 °C	80 mm s <sup>-1</sup>	20 mm s <sup>-1</sup>
PLA/CB	215 °C	60 °C	35 mm s <sup>-1</sup>	20 mm s <sup>-1</sup>
ABS/MWCNT	230 °C	105 °C	50 mm s <sup>-1</sup>	20 mm s <sup>-1</sup>

In order to evaluate the mechanical anisotropy, tensile dog-bone specimens of type 1BB are printed with a thickness of 2 mm according to DIN EN ISO 527-2 [116]. The specimens are oriented either with a 0° or a 90° infill. To avoid premature failure due to a rough surface, one wall line is printed around the infill. Strictly speaking, further experiments with intermediate infill directions and also specimens successively tilted to the upright are necessary to ensure isotropy. However, it is assumed that infills parallel and perpendicular to the loading di-

rection are the extreme cases and no mechanical values outside their range are expected for other orientations. The different infill orientations to analyze the anisotropy are schematically shown in Fig. 4.12. In addition,  $0^\circ$  dog-bones with the functionalized solid epoxy formulation are printed to evaluate the thermo- and piezoresistive behavior of the newly developed material. For a characterization of the electrical volume conductivity, cubes having a volume of  $5\text{ mm} \times 5\text{ mm} \times 5\text{ mm}$  are printed with the functionalized solid epoxy formulation consisting only of  $0^\circ$  infill (along the  $X$ -axis). Photographs of the 3D printed and post-cured mechanical, electrical and sensing specimens are shown in Appendix A.3.

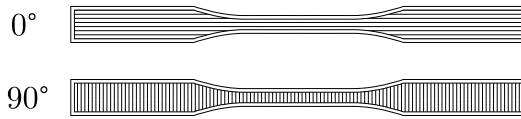


**Figure 4.12:** Different orientations of the infill to analyze the mechanical anisotropy of 3D printed dog-bones.

Also bulk material specimens of the solid epoxy formulation are produced to compare the 3D printed material to conventional manufacturing techniques. Dog-bones with the non-functionalized solid epoxy formulation are used as a mechanical reference. Cubes of the functionalized solid epoxy formulation with 0.1 wt% SWCNT content are utilized as an electrical reference. For this purpose, the material is casted in an aluminum cup after the last mixing step with the accelerator and cured in an oven at a temperature of  $140^\circ\text{C}$  for 80 min. After demolding, the plates are face milled (EuroMod 30, isel Germany AG, Eichenzell, Germany) to the desired thickness. For the mechanical characterization specimens, the surface quality is further improved with an automatic grinder (Saphir 550, ATM Qness GmbH, Mammelzen, Germany) using 320, 600, 1200 and 2500 grit sandpaper. Afterwards, contour milling is carried out to obtain the dog-bone and cube specimens from the plates. For the dog-bones also the contours' surfaces are finished by grinding with 2500 grit sandpaper.

### 4.2.9 Geometry Characterization

The dimensional change of the 3D printed solid epoxy formulation during post-curing is analyzed for the dog-bone specimens depending on the infill direction. Measurements are taken with a caliper on three specimens each before and after post-curing. The width and thickness are measured at three points: at the two shoulders for clamping and at the narrow parallel part in the middle. Furthermore, the length of the specimens is determined. The locations of the measurements are depicted in Fig. 4.19.

### 4.2.10 Mechanical Testing

The mechanical properties are characterized in uniaxial tensile tests according to DIN EN ISO 527-1 [122]. A universal testing machine (Z2.5, ZwickRoell GmbH & Co. KG, Ulm, Germany) is utilized to test five specimens in each configuration with a crosshead speed of  $0.25 \text{ mm min}^{-1}$ . The dog-bones are clamped by screw grips and the strain is measured with a non-contact video extensometer (videoXtens, ZwickRoell GmbH & Co. KG, Ulm, Germany).

### 4.2.11 Microscopy

In order to gain information on failure mechanisms and the homogeneity of the material, the fracture surfaces are investigated. Micrographs are recorded with a digital microscope (VHX-6000, Keyence Deutschland GmbH, Neu-Isenburg, Germany).

### 4.2.12 Electrical Characterization

For the characterization of the electrical volume conductivity, the cubes are ground with 600 grit sandpaper to remove the polymer rich surface [168]. Afterwards, the surface is cleaned with isopropanol and opposite sides are contacted with conductive silver paint. Measurements are carried out in  $X$ -,  $Y$ - and  $Z$ -direction with three specimens each to determine the anisotropy of electrical volume conductivity. The solid epoxy formulation with 0.2 wt% SWCNTs and the commercial reference materials PLA/CB and ABS/MWCNT are compared. The electrical resistance is measured with a source measure unit (2601A SYSTEM SourceMeter, Keithley Instruments Inc., Cleveland, OH, USA) in the four-wire sensing setup. A voltage of 100 mV is applied to avoid Joule heating. Moreover, the percolation curve is analyzed for the SWCNT functionalized solid epoxy formulation with three specimens each in  $X$ -direction. For the solid epoxy formulation with 0.05 wt% and 0.075 wt% SWCNT content a higher voltage of 5 V is applied as the measurement resolution limit is reached. Also a comparison with the casted and milled bulk functionalized solid epoxy formulation is carried out with three specimens to assess the influence of the manufacturing technique.

To evaluate the formation of a conductive network of SWCNTs (as discussed in Section 4.2.2) due to attractive forces of the nanoparticles according to colloid theory [251, 255, 256], the electrical volume conductivity is observed during the curing process. The functionalized solid epoxy formulation with 0.1 wt% SWCNTs is filled in a polypropylene (PP) tube after the last mixing step with the accelerator. The tube has a diameter of 15.8 mm and a filling height of 15 mm is used. The material is contacted at both ends with copper electrodes that are mounted on pistons compressing the material and holding it in place. A similar setup was used by Meeuw *et al.* [283]. The electrical resistance is continuously

measured throughout the curing process with a source measure unit in a two-wire sensing setup at a voltage of 1 V and a frequency of 2 Hz. The wires are soldered to the copper electrodes. The setup is placed in an oven at a temperature of 140 °C analogously to the casted material. Figure 4.13 shows the experimental setup.

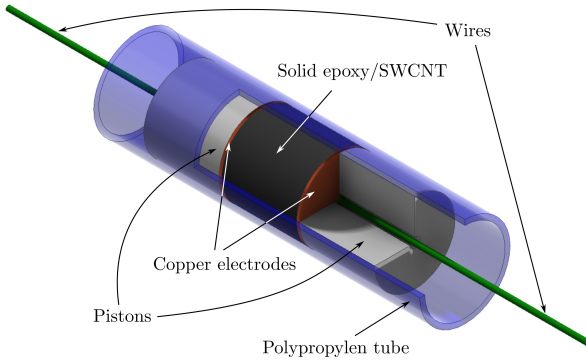


**Figure 4.13:** Experimental setup to continuously measure the conductivity of the solid epoxy formulation with SWCNTs during curing.

### 4.2.13 Sensing Applications

In a proof of concept study, the thermoresistive and piezoresistive material behavior of the functionalized formulation is tested with a 3D printed dog-bone of the solid epoxy formulation with 0.2 wt% SWCNTs. By exploiting the physical nature of the material, the application as a temperature and a strain sensor is analyzed. Just like the conductivity cubes, the dog-bone is ground with 600 grit sandpaper to remove the polymer rich surface and the surface is cleaned with isopropanol afterwards. Similar to Wichmann *et al.* [168], the dog-bone is contacted with two ring electrodes of conductive silver paint. They are applied with a length of 5 mm and a spacing of 10 mm in between, corresponding to the measurement length in DIN EN ISO 527-2 [116]. The wires are connected to the ring electrodes by conductive silver paint. The sensing specimen is illustrated schematically in Fig. 4.14. The electrical resistance is measured with a source measure unit in a two-wire sensing setup at a voltage of 40 V.

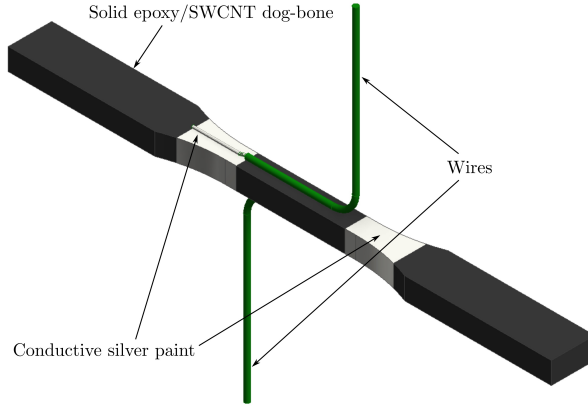


**Figure 4.14:** Preparation of the solid epoxy/SWCNT dog-bone specimen for the characterization in sensing applications.

### Thermoresistive Characterization

In order to investigate the temperature sensing capabilities, a temperature data logger (SD200, Extech Instruments, Nashua, NH, USA) with a type K thermocouple is placed next to the specimen as a temperature reference. The resistance is measured at room temperature ( $T_r = 23^\circ\text{C}$ ), in a freezer at a temperature of  $-29^\circ\text{C}$  and in an oven at temperatures of  $40^\circ\text{C}$ ,  $60^\circ\text{C}$ ,  $80^\circ\text{C}$ ,  $100^\circ\text{C}$  and  $120^\circ\text{C}$ . The resistance is measured for 1 min at a frequency of 1 Hz. The resistance is then averaged and plotted against the corresponding temperature. To determine the temperature coefficient of resistance  $\alpha_T$  as a measure for the sensitivity, an exponential law is fitted to the resistance  $R$  depending on the temperature  $T$  with

$$R = R(T_0) \exp(\alpha_T(T - T_0)), \quad (4.10)$$

where  $R(T_0)$  is the resistance at the reference temperature  $T_0$ , in this case  $23^\circ\text{C}$ . Furthermore, the signal-to-noise ratio is determined

$$\text{SNR} = \frac{\mu}{s}, \quad (4.11)$$

with  $\mu$  being the mean of the resistance during the 1 min measurement and  $s$  being the sample standard deviation. As a measure for the response time, the time constant  $\tau$  of a first order linear time invariant system of the resistance  $R$  depending on the time  $t$  can be determined with

$$R = (R_2 - R_1) \left( 1 - \exp\left(-\frac{t}{\tau}\right) \right) + R_1, \quad (4.12)$$

where  $R_2$  is the resistance at the end of a step input and  $R_1$  is the resistance at the beginning of a step input. In order to determine the time constant of the dog-bone temperature sensor, the step input is applied by placing the specimen being at room temperature in an oven at a temperature of  $100^\circ\text{C}$ . The resistance is measured over time with a frequency of 1 Hz.

### Piezoresistive Characterization

The strain sensing capabilities are evaluated by a cyclic tensile test with increasing loading steps similar to Meeuw *et al.* [170]. A universal testing machine with a crosshead speed of  $0.25\text{ mm min}^{-1}$  is utilized to reach forces of 40 N, 80 N, 120 N, 160 N and 200 N with subsequent unloading in between. Afterwards, a final loading step until failure is performed. The displacement is kept constant for 10 s at each loading direction change to capture viscous effects. The dog-bone is clamped by screw grips and the displacement is measured by the crosshead. To insulate the specimen from the load frame, sandpaper is placed between the specimen and the clamps, which additionally ensures that no slipping occurs. During the cyclic tensile test, the resistance is measured with a source measure unit at a frequency of 2 Hz.

## 4.3 Results and Discussion

This section discusses the results of the study on functional material printing. First, the thermokinetic characteristics, shelf life and thermal stability of the new solid epoxy material for FFF printing are presented. Then, the determination of a post-curing cycle with rheology is described and results of the dimensional stability during curing are shown. Afterwards, the mechanical properties from tensile tests are discussed together with failure mechanisms obtained from fractography. Moreover, the electrical properties of the functionalized material are explained. Finally, the temperature and strain sensing capabilities are presented.

### 4.3.1 Thermokinetic Characteristics, Shelf Life and Stability

A representative DSC measurement of the uncured solid epoxy formulation showing the characteristics of the newly developed material is given in Fig. 4.15. The uncured material has a glass transition temperature of  $T_g = 32.5^\circ\text{C}$  determined at the inflection point. The onset temperature of the curing peak is reached at  $T_{c,on} = 128^\circ\text{C}$ . However, curing already starts slowly beforehand. The important characteristic of the solid epoxy material formulation is that the  $T_g$  is above room temperature  $T_r$  avoiding softening before the filament is printed. In addition, the processing temperature  $T_p$  is below  $T_{c,on}$  preventing significant curing during the

short times of the mixing process and the printing. The thermokinetic behavior is further characterized in Appendix A.2.1.

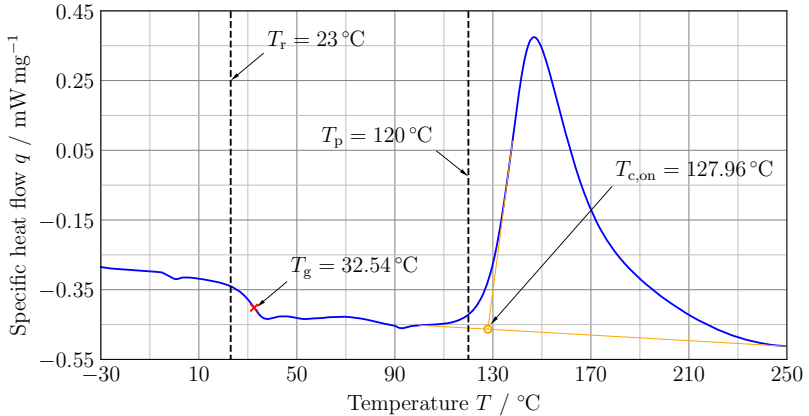


**Figure 4.15:** DSC measurement of the uncured solid epoxy formulation showing the characteristics of the new material. The glass transition temperature  $T_g$  and onset temperature of the curing peak  $T_{c,on}$  are set in context with room temperature  $T_r$  and processing temperature  $T_p$ .

In order to estimate the shelf life of the uncured solid epoxy formulation, the specific reaction enthalpy of DSC measurements depending on the storage time and temperature is illustrated in Fig. 4.16. When stored at room temperature, the specific residual reaction enthalpy drops by approximately 5% within the first month and remains almost constant afterwards. This could be a result of the reaction of the uron based accelerator with epoxy at lower temperatures [287]. In a freezer, the solid epoxy formulation shows no significant decrease in specific residual reaction enthalpy in the first 6 months. Slight deviations are within the measurement accuracy of the DSC. As no significant curing takes place under either storage condition, the material has at least a shelf life of 6 months making it suitable for commercial applications. A reason for the interruption of curing could be that the glass transition temperature  $T_g$  of the uncured material formulation is above the storage temperature. Hence, the reaction is diffusion controlled and the mobility of the molecules is limited (see Section 4.2.1). Furthermore, the high molecular weight solid epoxy resin has a lower number of reactive groups decreasing the probability of reactions. Contrary, for liquid epoxy resins a progression of the curing reaction can sometimes be observed.

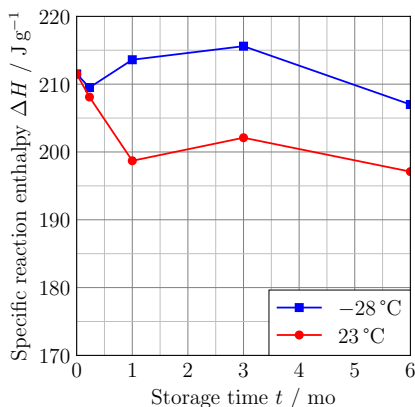
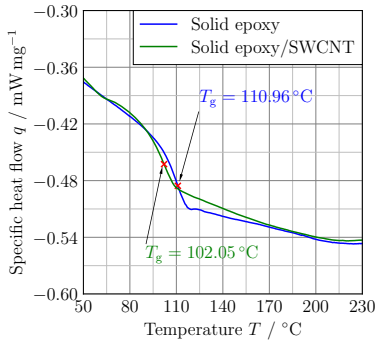
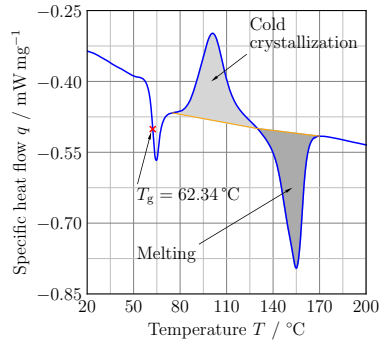


**Figure 4.16:** DSC measurements of the specific residual reaction enthalpy of the uncured solid epoxy formulation over storage time at different storage temperatures as an indicator for the shelf life.

Figure 4.17a depicts DSC measurements to determine the thermal stability of the cured solid epoxy and the cured functionalized solid epoxy with 0.2 wt% SWCNTs. The  $T_g$  at the inflection point is used as a measure for thermal stability. With  $102\text{ }^\circ\text{C}$ , the  $T_g$  of the functionalized material is slightly lower compared to  $111\text{ }^\circ\text{C}$  for the non-functionalized material. This can be explained by the matrix of the masterbatch, which is added to the formulation. The liquid epoxy of the in-house masterbatch contains the reactive diluent 1,6-hexanediol diglycidyl ether [215, 288], the commercial pre-dispersed SWCNT concentrate contains ethoxylated alcohol [289]. Both are linear molecules that reduce the rigidity of the network, yielding a lower  $T_g$ . Compared to standard liquid epoxy resin formulations with amine curing agents, the  $T_g$  of the new solid epoxy material formulations is slightly higher due to the DCD enabling a high cross-linking density [210]. However, compared to high  $T_g$  epoxy systems the thermal stability is rather low because of the lower cross-linking density due to the longer solid epoxy molecules. To benchmark the cured solid epoxy, a DSC measurement of the commercial PLA is shown in Fig. 4.17b. With a  $T_g = 62\text{ }^\circ\text{C}$  at the inflection point, the thermal stability is significantly lower. In addition, at a temperature of approximately  $80\text{ }^\circ\text{C}$  cold crystallization takes place resulting in shrinkage and subsequently warping.



(a) Cured solid epoxy formulations.



(b) Commercial PLA.

**Figure 4.17:** DSC measurements to determine the thermal stability by the  $T_g$  of dog-bone specimens printed with the solid epoxy (post-cured) and PLA. Further phase transitions are also visible for PLA.

### 4.3.2 Post-Curing

The loss factor over time and the corresponding temperature during the oscillatory rheological measurement are presented in Fig. 4.18. It can be seen that the loss factor is always below  $\tan(\delta) = 1$  showing the predominantly solid behavior of the solid epoxy formulation, resulting in dimensional stability during post-curing. In a previous temperature ramp it was found that the solid to fluid crossover point is reached at a temperature of  $50^\circ\text{C}$ . Hence, the measurement is started at a temperature of  $40^\circ\text{C}$  to have a certain gap. During the first 51 h the loss factor is almost constant. Then, the temperature is increased to  $45^\circ\text{C}$  and the loss factor increases to just below  $\tan(\delta) = 1$ . Subsequently, the loss factor decreases over the next 40 h and is then again almost constant over another 29 h. Afterwards, the temperature is increased to  $55^\circ\text{C}$  so that the loss factor increases to just below  $\tan(\delta) = 1$ . This is followed by a decreasing loss factor over the next 26 h. Thereafter, the temperature is increased to  $70^\circ\text{C}$  so that the loss factor increases to just below  $\tan(\delta) = 1$  again. Consecutively, the loss factor decreases quickly over the next 6 h and is almost constant afterwards for another 17 h. Finally, the temperature can be increased up to the melting point of DCD at  $210^\circ\text{C}$  without any further significant increase in loss factor. The decreasing loss factor is an indicator for polymer network formation. The uron based accelerator itself can act as a curing agent at lower temperatures without the involvement of DCD [287]. The successive constant phases at a given temperature can be explained by hindered mobility of the molecules when

the current curing temperature is too far below the  $T_g$ , which increases during the network formation (see Section 4.2.1). Thus, the temperature needs to be increased further to continue the network formation [105, 209]. To ensure the dimensional stability during post-curing, the temperature program used in this study is chosen slightly more conservative as explained in Section 4.2.8. The temperature is kept constant slightly longer for the individual stages except for the 70 °C stage. Here, after the 6 h with decreasing loss modulus an additional step at a temperature of 100 °C is inserted. Due to the uron based accelerator, a temperature of 140 °C is sufficient for full curing (see Appendix A.2.2 for further details). In the future, less conservative post-curing should be analyzed to achieve shorter curing cycles. At least the time spans where the loss factor remains constant can be eliminated as curing is not progressing significantly. This alone would reduce the post-curing time drastically. Even further reductions of the time spans at the individual temperature steps could be possible as long as the loss factor stays below  $\tan(\delta) = 1$ , resulting in predominantly solid behavior and leading to dimensional stability.

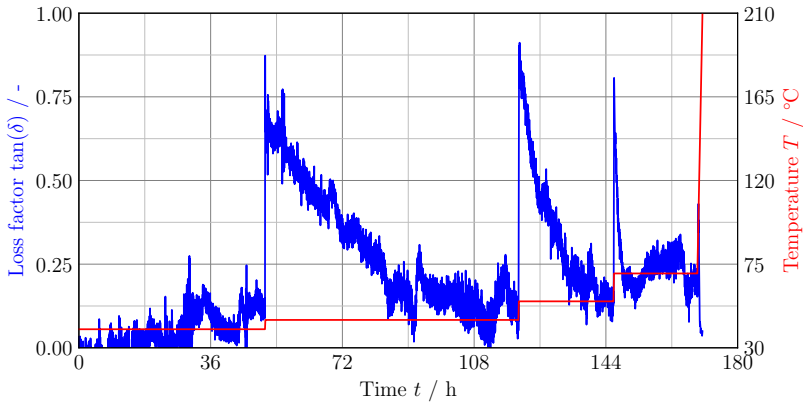


**Figure 4.18:** Loss factor over time during a temperature profile in a rheology measurement of the solid epoxy formulation showing the predominantly solid behavior.

### 4.3.3 Dimensional Stability

The relative dimensional change of the 3D printed solid epoxy dog-bones during post-curing depending on the measurement location and infill orientation is shown in Fig. 4.19. Overall, the relative dimensional change is small with less than

4%. For width measurements in  $Y$ -direction, a more pronounced decrease can be seen for the  $90^\circ$  infill specimens. For length measurements in  $X$ -direction, a more pronounced decrease can be seen for the  $0^\circ$  infill specimens. For both types of specimens, the thickness in  $Z$ -direction increases. A reason for this can be relaxation processes of the polymer molecules, which are stretched and oriented during deposition on the build platform. Hence, shrinking can be seen in infill direction, while an expansion is observed perpendicular to it. In the uncured state the material could be slightly anisotropic due to the stretched and oriented polymer molecules. However, the relaxation during post-curing resolves this issue. In addition, chemical shrinkage takes place due to the cross-linking of the epoxy, which decreases the free volume. This leads to a slight overall decrease in dimensions and is superimposed to the relaxation effect. It explains why the increase in thickness is not always as high as the decrease in infill direction.

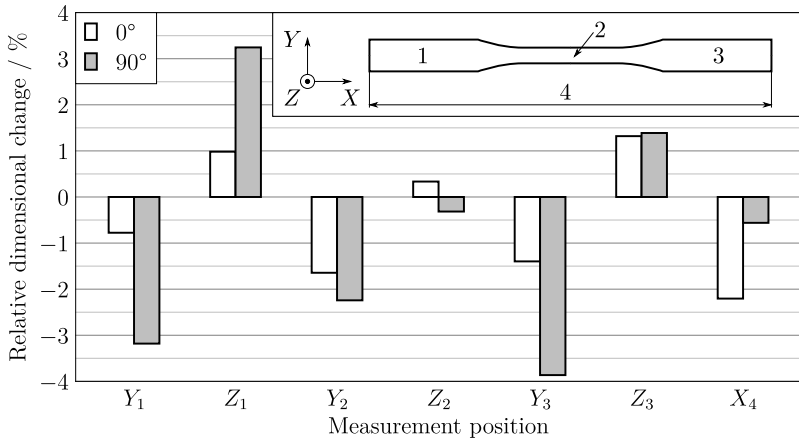


**Figure 4.19:** Relative dimensional change of the 3D printed solid epoxy dog-bones during post-curing depending on measurement location and infill orientation.

#### 4.3.4 Mechanical Properties

In the following, the results of the static mechanical characterization of the 3D printed solid epoxy formulation with tensile tests are discussed. The influence of the infill direction is analyzed. It is an indicator if the new material formulation can be a solution for the anisotropy issue at a low level in FFF printing that

currently prevents it from being used in more challenging applications. To investigate the influence of the manufacturing technique, a comparison with casted and milled bulk specimens is performed. As a benchmark, the 3D printed solid epoxy formulation is compared to 3D printed commercial PLA. The results are presented in terms of nominal/engineering properties and in the form of bar charts with standard deviations and a scatter plot of all observations.

Figure 4.20a shows the results for the elastic modulus. Both, 3D printed solid epoxy and PLA, show no significant difference depending on the infill direction. The 3D printed solid epoxy specimens have a slightly lower stiffness than the bulk ones. This can be explained by the cross-section, which is perfectly rectangular for the casted and subsequently milled specimens, while it has slight roundings for the 3D printed specimens (see Section 4.3.5). As the cross-section is determined with a caliper and assumed to be rectangular, it is overestimated for the 3D printed specimens. Overall, the PLA specimens have a higher stiffness, however, both materials are within the commonly known range.

With regard to strength (see Fig. 4.20b) no difference can be observed for the 3D printed solid epoxy depending on the infill direction, while the strength of the  $90^\circ$  PLA specimens is significantly lower than that of the  $0^\circ$  specimens. There is only very little diffusion and entanglement of the polymer chains between the infill lines of the thermoplastic PLA as the material solidifies immediately after deposition. This results in weak bonding, which is typical for FFF. Contrary, cross-linking during the post-curing eliminates this issue for the thermosetting solid epoxy formulation. In addition, the overall strength of the cured solid epoxy is higher than that of PLA. Also compared to the bulk specimens, the 3D printed solid epoxy dog-bones reach a similar strength. Slight deviations can again be explained by the overestimated cross-section. Yet, the scatter of the 3D printed specimens is higher. This can be a result of the filament production process and adjusted printing process, which are more prone to manufacturing errors than casting and milling. Variations in the filament diameter and pores can be reduced for instance with a professional filament extrusion process.

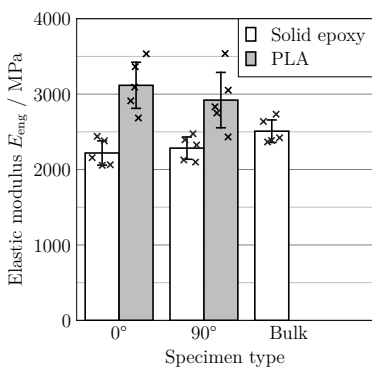
The results for the elongation at break are depicted in Fig. 4.20c. Just as in case of the strength, no difference is visible for the 3D printed solid epoxy depending on the infill direction. In addition, a comparison to the bulk specimens shows a very similar elongation at break of the 3D printed solid epoxy dog-bones. This shows that the cross-linking during post-curing spans the interface between the infill lines and results in isotropic mechanical properties. Slight deviations can be explained by the more error prone simplified filament production process and adjusted printing process compared to casting and milling. In contrast, the elongation at break of the  $90^\circ$  PLA specimens is drastically lower compared to the  $0^\circ$  specimens. This can again be explained by the weak bonding being typical for FFF. Overall, the  $0^\circ$  PLA specimens show a higher plastic deformation compared to the solid epoxy specimens. For thermoplastics, polymer chain movement allows

higher plastic deformations, while the deformation is limited for thermosets due to cross-linking [105].

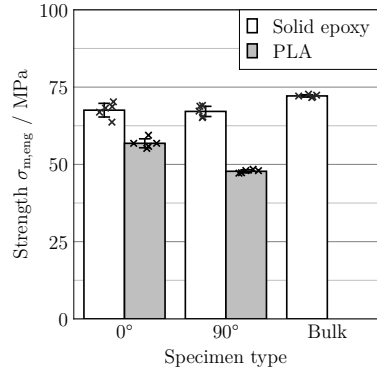
### 4.3.5 Fracture Surfaces

Further insights about the new solid epoxy formulation and its failure mechanisms can be gained from the fracture surfaces presented in Fig. 4.21. It can be seen that the fracture surface is homogeneous and the individual infill lines are not visible anymore for both infill directions. This underlines that the material is isotropic. When looking at the cross-section of the 3D printed dog-bones, slight roundings at the upper edges are recognized that lead to an overestimation of the area when assuming it to be rectangular. In comparison, the casted and milled dog-bones show a perfectly rectangular cross-section. This might explain the minor difference in elastic modulus and strength. For the 3D printed specimens, large pores can be identified as the origin of the failure. A smoother region can be observed surrounding the pore where the crack accelerates, which is additionally shown in the magnifications. In this region parabolic markings can be seen. They are an indicator for an interaction of the primary crack with secondary cracks that nucleate at inhomogeneities [290, 291]. Small particles with a size less than  $10\ \mu\text{m}$  can be observed at the parabolic markings. The residual fracture surface is rough. In contrast, the fracture surface of the bulk specimens is significantly smoother. Smaller pores can be identified as the origin of the failure. Again, a smooth region surrounding the origin can be observed with only very few parabolic markings nucleated at pores. The residual fracture surface is slightly rougher. The significantly rougher fracture surface of the 3D printed specimens results from the particles. The particle size suggests that it is remaining DCD. The uron based accelerator can act as a curing agent itself (see Section 4.2.1) and allows curing at lower temperatures than with DCD [287]. As the post-curing cycle for the 3D printed specimens remains for a long time at low temperatures, curing starts without an involvement of the DCD. In the later stages of the curing cycle with higher temperatures, a reaction with DCD takes place. Yet, this leaves some remaining DCD. Contrary, for the casted specimens curing takes place at elevated temperatures throughout the process so that an accelerated DCD reaction occurs from the beginning on. Further investigations with regard to a higher final curing temperature above the melting point of DCD are presented in Appendix A.2.2. However, neither an improvement of the mechanical properties is observed, nor the issue of remaining DCD can be solved.

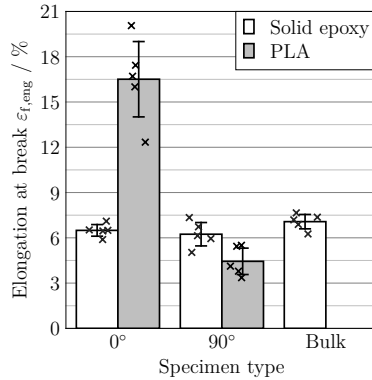
Having a look at the fracture surfaces of the 3D printed PLA dog-bones in Fig. 4.22, the individual wall and infill lines are clearly visible. Also pores between the lines can be seen. This inhomogeneity shows the lack of diffusion and entanglement of the polymer chains over the interfaces between the lines. It leads to the anisotropy issue in FFF printing. The fractography results correspond well



(a) Elastic modulus.

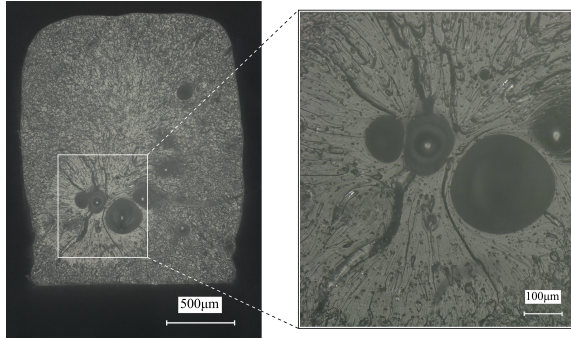


(b) Strength.

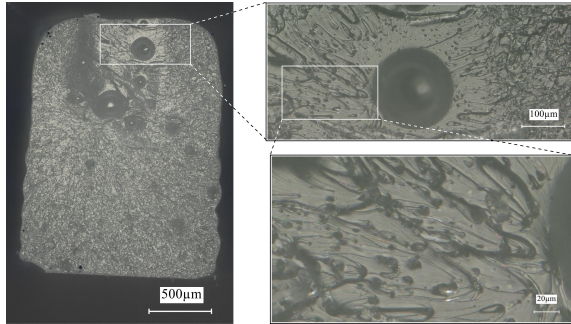


(c) Elongation at break.

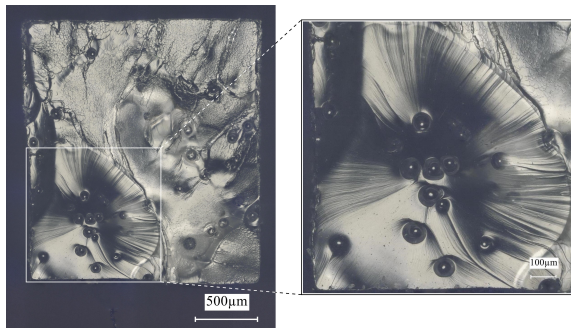
**Figure 4.20:** Comparison of the mechanical properties of 3D printed specimens with different infill orientations and bulk specimens for the developed solid epoxy formulation and a commercial PLA filament.



(a) Solid epoxy with 0° infill.



(b) Solid epoxy with 90° infill.



(c) Solid epoxy casted and milled.

**Figure 4.21:** Fracture surfaces of the 3D printed as well as casted and milled dog-bones with the solid epoxy formulation.

with the mechanical results where the  $90^\circ$  specimens underperform as the interfaces are perpendicular to the loading direction. An origin of failure is difficult to identify because of the inhomogeneity.

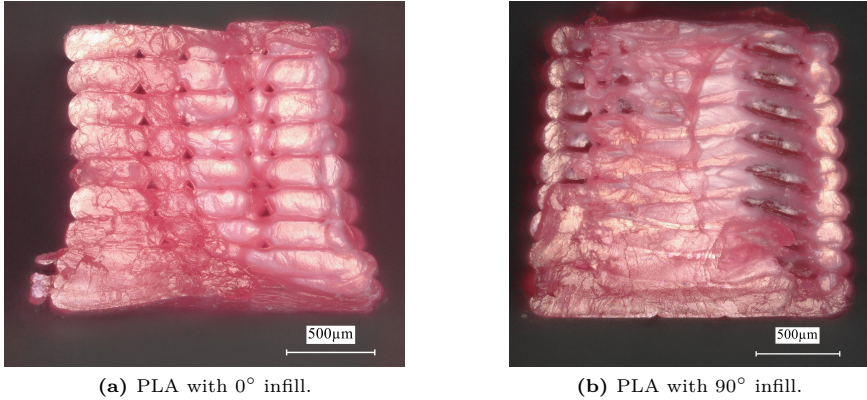


**Figure 4.22:** Fracture surfaces of the 3D printed dog-bones with commercial PLA filament.

#### Working hypothesis 5

A solid epoxy thermoset filament based 3D printing material can solve the anisotropy limitations at a low strength level of the current FFF process.

This working hypothesis can be fully confirmed. The mechanical characterization of 3D printed dog-bones shows isotropic material properties in terms of elastic modulus, strength and elongation at break. The successful cross-linking over the layers is reassured by the fact that even similar material properties compared to casted and milled bulk specimens are reached. Moreover, the fracture surfaces show that a homogeneous material is obtained without the visibility of individual infill lines.

#### 4.3.6 Electrical Properties

A comparison of the electrical volume conductivity depending on the direction to determine the electrical anisotropy is shown in the bar chart with sample standard deviations in Fig. 4.23. The 3D printed solid epoxy formulation with

0.2 wt% SWCNTs and two commercial filaments with different carbon fillers are investigated. All materials show the highest conductivity in the  $X$ -direction of the infill lines. Lower conductivity is found in  $Y$ - and  $Z$ -direction. For the solid epoxy/SWCNT the conductivity perpendicular to the lines is approximately four orders of magnitude lower and similar in both directions. The ABS/MWCNT has a similar conductivity as the solid epoxy/SWCNT in  $X$ -direction and approximately one order of magnitude lower in  $Y$ - and two orders of magnitude lower in  $Z$ -direction. The PLA/CB has a conductivity that is approximately three orders of magnitude higher than that of solid epoxy/SWCNT in  $X$ -direction. The conductivity in  $Y$ - and  $Z$ -direction is only slightly lower. The differences can be explained by nanoparticle morphology, filler content and manufacturing technique. The high aspect ratio over 3000 for the SWCNTs [292] allows to reach a similar conductivity for the solid epoxy/SWCNT material in  $X$ -direction as for the ABS/MWCNT despite having only a filler content of 0.2 wt% compared to 10 wt%. However, an even higher conductivity is reached in the PLA/CB with a filler content of over 20 wt%. Here, the filler content is so high that also the electrical anisotropy almost vanishes. Contrary, the electrical anisotropy of the other two materials can be explained by the FFF technique. The material is deposited in lines and solidifies quickly afterwards. Each interface between the lines can be seen as a barrier for electrical conductivity since a polymer rich surface is usually found in nanocomposites. Thus, the conductivity is lower in the directions perpendicular to the infill lines. The effect is even worse for the 3D printed solid epoxy with the extremely low filler content. This reduces the probability of conductive paths during nanoparticle network formation according to percolation theory. Despite the cross-linking during post-curing that spans the interface between the infill lines, the nanoparticle mobility is limited due to the predominantly solid behavior [271] shown in Section 4.3.2.

In order to be able to adjust the electrical conductivity of the functionalized solid epoxy formulation to the application, the percolation behavior is examined. Figure 4.24a shows the electrical volume conductivity of the solid epoxy/SWCNT depending on the filler content. Error bars display the sample standard deviation. The 3D printed specimens are measured in infill direction  $X$  and a comparison with casted and milled bulk specimens is presented. No electrical conductivity is measured with an SWCNT content of 0.05 wt%. With increasing SWCNT content the whole range from static dissipative to conductive can be covered where the percolation threshold of  $1 \times 10^{-6} \text{ S m}^{-1}$  [293] is reached at an SWCNT content of approximately 0.1 wt%. This actually corresponds to the predicted statistical percolation threshold of CNT fillers [250]. A comparison of the bulk to the 3D printed specimens with a similar filler content of 0.1 wt% shows a significantly higher conductivity of approximately five orders of magnitude for the bulk specimens. This can be explained by two effects. First, the casted and milled specimens consist of homogeneous bulk material with no polymer rich sections at

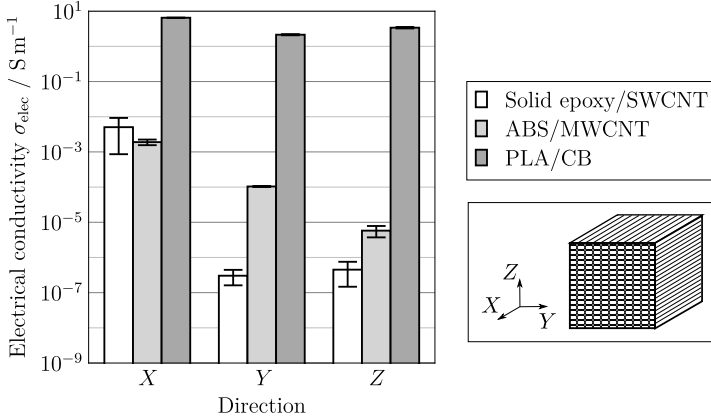
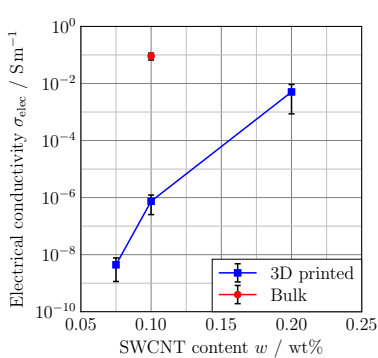


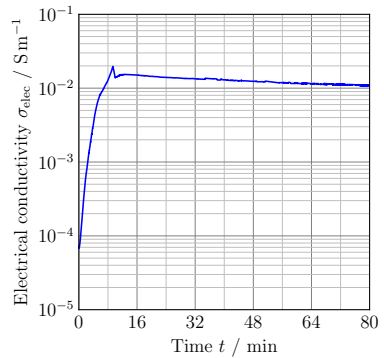
**Figure 4.23:** Comparison of the electrical conductivity depending on the direction for the 3D printed solid epoxy formulation with 0.2 wt% SWCNTs and two commercial filaments.

the interfaces of the infill lines. This allows conductive paths to form through the whole volume of the specimens, while they are limited to the individual infill lines for the 3D printed specimens. Therefore, the probability to have conductive paths is increased for the bulk specimens according to percolation theory because of a lower length to diameter ratio [294]. The conductive paths are sensitive to interruptions. Having a larger cross-section allows redundancies in conductive paths. Second, the different curing procedures of the 3D printed and casted specimens influence the conductivity. In the case of the 3D printed specimens, the material is in a predominantly solid state (see Section 4.3.2), which limits the mobility of the SWCNTs [271]. In addition, the DCD curing agent remains in particle form with low solubility in the early phases of the post-curing process. Therefore, the ion concentration remains low so that repulsive electrostatic forces dominate at intermediate distances of the total interaction potential for colloidal dispersions according to DLVO theory (see Section 4.2.2). The potential barrier cannot be overcome. Hence, agglomeration after thorough dispersion is suppressed. Yet, this is essential in building electrically conductive paths during network formation when being below the statistical percolation threshold and relying on the kinetic percolation threshold [257]. In contrast, curing of the casted material at elevated temperatures allows the agglomeration of the SWCNTs and the formation of an electrically conductive network as depicted in Fig. 4.24b. In this case, the electrical conductivity is shown over time during curing of the casted material

in the oven at a temperature of 140 °C. During the first 10 min the conductivity increases significantly over two orders of magnitude. A higher conductivity can already be observed in the beginning of the measurement compared to the 3D printed specimens. It can be explained by the time it took to close the tube with the pistons and attach the wires to the source measure unit during which an agglomeration can already take place. In addition, more conductive paths can form through the larger homogeneous volume according to percolation theory. The slightly lower final conductivity compared to the bulk cube specimens can be explained by the different specimen dimensions. The length of the material volume used to observe the electrical conductivity during curing is larger compared to the bulk cubes. This increases the probability to have an interruption of conductive paths.



(a) Percolation curve.



(b) Conductivity during curing of casted material.

**Figure 4.24:** Electrical conductivity depending on the SWCNT content in the solid epoxy formulation and the manufacturing process. The 3D printed specimens are measured in infill direction X. The discrepancy between 3D printed and bulk material can be explained when looking at the electrical conductivity over time during curing of the casted material.

### Working hypothesis 6

SWCNTs can be used as a filler for a functionalized solid epoxy thermoset formulation in the FFF process to incorporate electrical conductivity.

This working hypothesis can be confirmed. Depending on the filler content, the whole range of electrical properties can be obtained from static dissipative to conductive. Due to the functionalization with high aspect ratio SWCNTs, significantly lower filler loadings are sufficient compared to commercial alternatives. However, compared to nanocomposites with liquid epoxy resins a higher percolation threshold is observed, which corresponds to the theoretical statistical one. This is caused by a limitation of the nanoparticle mobility during curing in a predominantly solid state. Thus, a conductive network formation is suppressed. Hence, a kinetic percolation threshold is not observed. In contrast to the mechanical properties, the electrical conductivity is anisotropic. This is a result of the polymer rich surface of the individual infill lines acting as a barrier.

#### 4.3.7 Temperature Sensing

Exploiting the thermoresistive properties of the 3D printed nanocomposite, a proof of concept study of the application as a temperature sensor is carried out. A characteristic curve of the resistance depending on the temperature for the 3D printed solid epoxy formulation with 0.2 wt% SWCNT content is shown in Fig. 4.25. The curve is bijective within the considered range. The resistance decreases with increasing temperature. Fitting the exponential law of Eq. (4.10) to the experimentally determined data points yields a temperature coefficient of resistance of  $\alpha_T = -0.0158 \text{ }^\circ\text{C}^{-1}$ . Different effects counteract each other in case of the resistance depending on the temperature for an SWCNT nanocomposite. Depending on whether the SWCNTs are in zigzag, armchair or chiral configuration, they are either semiconducting or metallic (see Section 4.2.2). However, usually all configurations can be found with two thirds semiconducting and one third metallic [295]. The SWCNTs used in this study also consist of both types [296]. They can be separated [297], yet such processes damage or contaminate the SWCNTs and the efficiency is low [295]. In addition, the tunnel effect is depending on the distance between two conducting particles and the temperature [244, 245]. A higher temperature leads to thermal expansion of the polymer matrix. This results in an increased distance between the nanoparticles, which reduces the tunnel current. Yet, an increased temperature also raises the energy level of the electrons, which increases the tunnel current. The NTC suggests that the raised energy level of the electrons is the dominant effect. Tunneling resistance plays the dominant role in nanocomposites when the filler content is low and dispersion is good [298]. The relatively high resistance in the range of several  $\text{G}\Omega$  can be explained by the electrical anisotropy of the 3D printed specimens and the contacting with ring electrodes. Due to the barrier of the polymer rich surface

of the individual infill lines, current only flows through the outer layer. Thus, the conductive cross-section is reduced. The measured current is close to but still within the limits of the utilized source measure unit. However, such a high resistance might be problematic for other data acquisition systems.

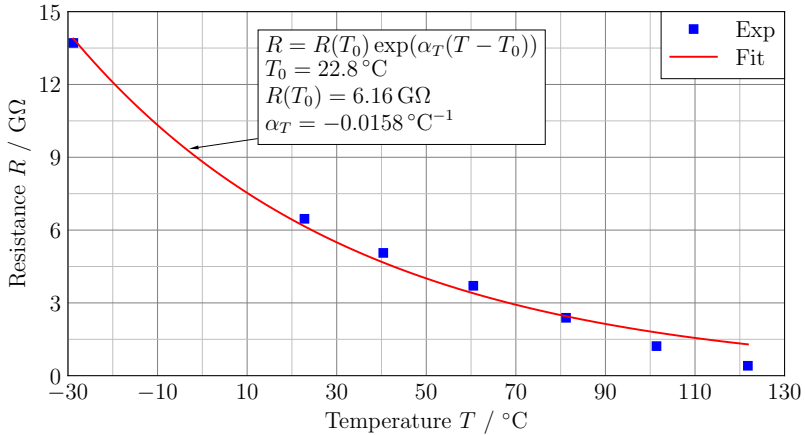


**Figure 4.25:** Characteristic curve of the resistance depending on the temperature for the 3D printed solid epoxy formulation with 0.2 wt% SWCNT modification. A fit to determine the temperature coefficient of resistance  $\alpha_T$  is included.

Figure 4.26a shows the signal-to-noise ratio depending on the temperature for the 3D printed solid epoxy formulation with 0.2 wt% SWCNT content. Two factors influence the signal-to-noise ratio. First, the lower the temperature, the higher the mean of the resistance measurement. Second, the higher the temperature, the better the resolution of the source measure unit as the resistance decreases. Hence, the standard deviation of the resistance measurement is reduced. Both effects lead to a higher signal-to-noise ratio and are counteracting each other. At a temperature of  $-29^\circ\text{C}$  a high signal-to-noise ratio is observed because the high mean of the resistance measurement dominates. From temperatures of  $23^\circ\text{C}$  to  $81^\circ\text{C}$  the signal-to-noise ratio increases as the reduced standard deviation of the resistance measurement dominates. Above a temperature of  $81^\circ\text{C}$  the signal-to-noise ratio decreases as the decreasing mean of the resistance measurement dominates. With the signal-to-noise ratio always above 50 the signal can be clearly distinguished from the noise over the whole temperature range.

For an estimate of the response time of the temperature sensing specimen, the relative resistance change over time when placed from room temperature

in an oven at a temperature of  $100\text{ }^{\circ}\text{C}$  is depicted in Fig. 4.26b. The corresponding temperature measured with a thermocouple is presented as well. The relative resistance change approaches approximately  $-80\%$  asymptotically after an initial step decrease due to the temperature step input to a higher level. A time constant of  $\tau = 19.51\text{ s}$  is determined with a fit of Eq. (4.12) for the solid epoxy/SWCNT dog-bone specimen. In comparison, the commercial thermocouple has a time constant that is half as big. The difference can be explained by the poor thermal conductivity of epoxy resin and the larger volume and mass of the solid epoxy/SWCNT sensing specimen.

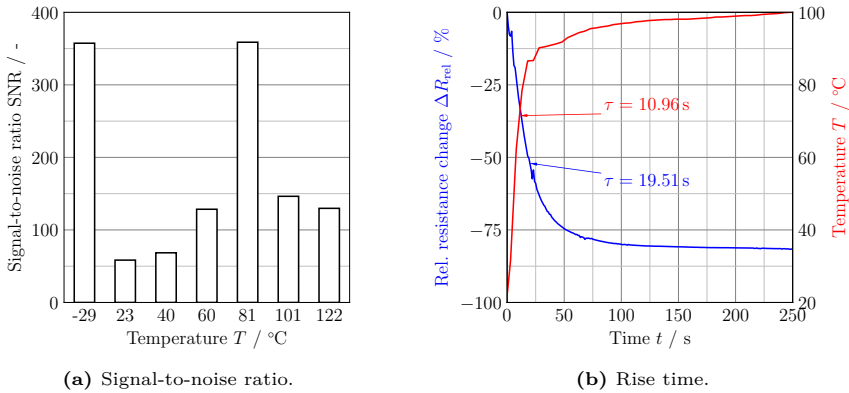


**Figure 4.26:** Signal-to-noise ratio depending on the temperature and time constant  $\tau$  when placing the 3D printed sensing specimen in an oven at a temperature of  $100\text{ }^{\circ}\text{C}$ . The relative resistance change is shown for the solid epoxy formulation with 0.2 wt% SWCNT modification together with the temperature from a thermocouple.

### 4.3.8 Strain Sensing

The results of the proof of concept study for the application of the 3D printed solid epoxy/SWCNT material as a strain sensor are shown in Fig. 4.27. Relative resistance change, displacement and force are shown over time during a cyclic tensile test with increasing loading steps. With increasing displacement, the resistance increases. This piezoresistive phenomenon can be explained by the tunnel effect (see Section 4.2.2). Due to the straining of the material, the distance between the nanoparticles increases leading to a reduced tunnel current. The plastic deformation of the dog-bone specimen indicated by the remaining

displacement in the unloaded state is also captured by a remaining increase in resistance. When the displacement of the previous cycle is exceeded, the relative resistance changes with a steeper slope than beforehand especially for the later cycles. After maximum loading of a cycle, the resistance is decreasing with a delay. These two phenomena can be explained by the complex visco-elasto-plastic material behavior of polymers. Until the previous maximum loading is reached, the material behaves predominantly elastic where the nanoparticle distance changes only slightly. Hence, the slope of the relative resistance change is less steep. Afterwards, especially in the higher loading cycles the plastic behavior leads to material flow and increases the nanoparticle distance more drastically. Thus, the slope of the relative resistance change is steeper. At the maximum loading of the cycles, a relaxation in the force is visible. Therefore, the polymer network is still in motion and thus also the nanoparticle distances are still changing. This viscous effect is still present in the beginning of the unloading and leads to a delayed response of the relative resistance change. Finally, the failure of the functionalized dog-bone specimen is registered by a sudden loss of electrical conductivity.

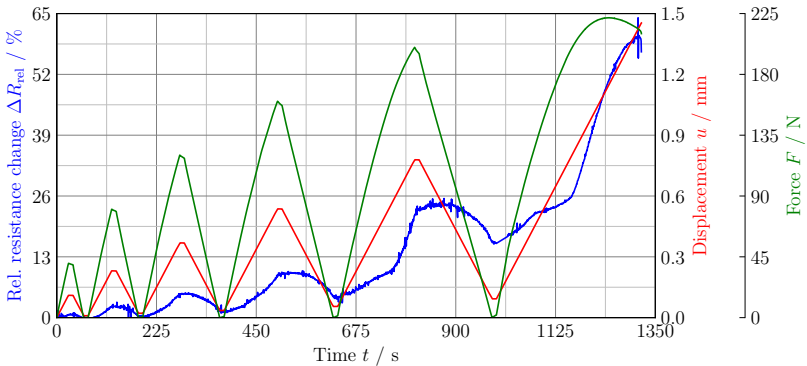


**Figure 4.27:** Strain sensing with a 3D printed dog-bone specimen of the solid epoxy formulation with 0.2 wt% SWCNT modification. The relative resistance change is shown together with the displacement and the force depending on the time.

**Working hypothesis 7**

The functionalized solid epoxy thermoset filament can be used for 3D printed temperature and strain sensing applications.

This working hypothesis can be confirmed. The proof of concept studies show that the SWCNT modified solid epoxy thermoset filament can be used for functional integration by FFF 3D printing in terms of sensing. The temperature sensing specimen has a distinct signal, is sufficiently fast and bijective in the analyzed range. The strain sensing specimen can trace loading and unloading in cyclic experiments and further indicates failure by a loss of conductivity.

## 4.4 Conclusion on Functional Material Printing

In this chapter, a new material for FFF 3D printing is presented that solves the mechanical anisotropy issue at a low level and is suitable for functional applications by means of a nanoparticle modification. The key constituents of the material formulation are a solid thermoset epoxy resin and a latent curing agent allowing a cross-linking during the post-curing process. The material formulation is explained and thermal as well as rheological measurements are conducted to show basic properties. The geometry changes during post-curing are investigated to ensure dimensional stability. Static tensile tests are carried out to show the isotropy of the 3D printed material and fracture surfaces are inspected to gain more insights into the failure mechanisms. In addition, the new material is modified with SWCNTs to incorporate electrical conductivity and make it suitable for functional 3D printing. The electrical properties are characterized with regard to anisotropy, percolation and conductive network formation. To benchmark the new material, a comparison with specimens from commercial thermoplastic filaments and with casted and milled bulk specimens is performed. Finally, the capabilities of the functionalized new material in temperature and strain sensing applications is shown in a proof of concept study.

Tensile tests on 3D printed dog-bones of the developed solid epoxy formulation with an infill in loading direction and perpendicular to it show the isotropic nature of the new material with regard to elastic modulus, strength and elongation at break. Also compared to bulk specimens only insignificant differences can be found. In contrast, the commercial PLA exhibits the well known anisotropy in strength and elongation at break. The superior properties of the solid epoxy formulation are reached by cross-linking during post-curing that spans the interface between the infill lines. Contrary, diffusion and entanglement of the polymer

chains for commercial thermoplastic filaments are limited as the material solidifies immediately after deposition. Also the fracture surfaces underline the findings of the mechanical experiments. A homogeneous fracture surface is observed for the 3D printed solid epoxy formulation, while the individual infill lines are still visible for the commercial PLA. Compared to the casted and milled specimens, the 3D printed solid epoxy specimens show slight roundings at the upper edges and larger pores that are the origin of the failure. These can be attributed to the simplified filament production process and adjusted printing process, which are more prone to manufacturing errors. Variations in the filament diameter and pores should be reduced for instance with a professional filament extrusion process in the future. A filament extrusion process is also needed to enable a continuous FFF printing process from a spool. In addition, the fracture surfaces of the 3D printed specimens show remaining DCD particles. They are a result of the post-curing process that starts at low temperatures where the uron based accelerator itself acts as a curing agent and consumes functional epoxy groups. However, this neither affects the mechanical properties nor the thermal stability.

DSC measurements of the uncured newly developed material show its characteristics: the glass transition temperature is above room temperature allowing to feed it as a solid filament to the FFF printer and the onset temperature of the curing peak is above the processing temperature preventing significant curing during mixing and printing. During storage of the uncured solid epoxy formulation at room temperature or in the freezer no significant decrease in residual reaction enthalpy is found within the first 6 months. With a  $T_g$  over  $100\text{ }^\circ\text{C}$  of the post-cured solid epoxy formulation (with and without SWCNT modification), the thermal stability outperforms the commercial PLA. A slow post-curing temperature program is developed with oscillatory rheological measurements by keeping the material below the solid to fluid crossover point. This ensures dimensional stability, which is shown in geometrical measurements. The relative dimensional change due to relaxation and chemical shrinkage is below 4%. The current post-curing process is very conservative and should be optimized in the future to reach more reasonable production times.

With regard to electrical volume conductivity, an anisotropic material behavior is detected for the 3D printed functionalized solid epoxy formulation with the highest conductivity found in the direction of the infill lines. The interfaces between the infill lines can be seen as a barrier for electrical conductivity because of the polymer rich surface typically found in nanocomposites. Hence, a lower conductivity is found perpendicular to the infill lines. The high aspect ratio of SWCNTs as a conductive modifier allows to reach the percolation threshold with only 0.1 wt% filler content in infill direction. With 0.2 wt% filler content, a similar conductivity is reached compared to commercial ABS/MWCNT material with a carbon additives content of 10 wt%. Higher conductivities are reached with the commercial PLA/CB material that also displays a less pro-

nounced anisotropy. However, here a significantly higher filler content of over 20 wt% is utilized. Compared to bulk specimens of the functionalized solid epoxy formulation, the 3D printed ones show a significantly lower electrical conductivity. This results from the 3D printed solid epoxy being in a predominantly solid state during post-curing. This limits the mobility of the SWCNTs and thus suppresses agglomeration after thorough dispersion, which is essential in the formation of a conductive network. Contrary, the curing of the casted specimens directly at elevated temperatures in a liquid state allows this agglomeration.

The proof of concept studies show the capabilities of the newly developed electrically modified material in functional 3D printed sensing applications. In temperature sensing applications a bijective characteristic curve is found for the resistance depending on the temperature in the analyzed range from  $-30\text{ }^{\circ}\text{C}$  to  $120\text{ }^{\circ}\text{C}$ . An NTC of resistance of  $\alpha_T = -0.0158\text{ }^{\circ}\text{C}^{-1}$  is observed. It can be explained by the raised energy level of the electrons due to the higher temperatures, which increases the tunnel current. With a signal-to-noise ratio greater than 50 over the investigated temperature range, the signal can be clearly distinguished from the noise. The time constant of approximately 20 s, determined from a step input from room temperature to  $100\text{ }^{\circ}\text{C}$ , is sufficiently fast for many applications. In strain sensing applications, the 3D printed functionalized solid epoxy is able to follow loading and unloading cycles with increasing and decreasing resistance. Material failure is captured by a loss of conductivity.



## 5 Conclusion

In this study two applications of additive manufacturing (AM) are shown that go beyond rapid prototyping and exploit its advantages. The applications are chosen based on the demands of AM users seeking more reliability and new materials. As a first application, reliable lightweight design with lattice structures is considered for two materials, which are printed by different AM techniques. The structural material Ti-6Al-4V fabricated by selective laser melting (SLM) and a methacrylate photopolymer fabricated by stereolithography (SLA) are investigated. The influence of different load cases, volume fractions and building directions on the mechanical properties of the lattice structures are analyzed. The mechanical properties of the three-dimensional (3D) printed bulk material are explored to be able to calibrate material models for finite element method (FEM) simulations that are essential in a structural design process. Moreover, the variation of material properties and geometrical accuracy are examined and also incorporated in FEM models. Digital image correlation (DIC) measurements and FEM simulations are performed to investigate the deformation and progressive damage process as well as failure modes. A probability distribution of the homogenized mechanical properties of the lattice structures is obtained. Such a probabilistic analysis can be used in a reliable design process, avoiding high safety factors that interfere with lightweight design. Also computationally more efficient FEM simulations of unit cells with periodic boundary conditions (PBCs) are conducted in a homogenization approach. In addition, further applications of lattice structures and AM in process engineering are presented and new concepts are developed. This also leads to the second application of AM beyond rapid prototyping where functional integration is considered. It is implemented with an electrically conductive material that is suited for sensing. Functional integration by a combination of materials is usually based on fused filament fabrication (FFF) printing that is currently limited by the anisotropy issue at a low level due to insufficient inter- and intralayer strength of commercial thermoplastic polymers. Here, the demand for new materials is met. The newly developed material is based on a thermosetting solid epoxy resin and a latent curing agent. This allows a supply of the material in the form of a filament for use in low-cost FFF printers as well as cross-linking in a post-curing process leading to isotropic mechanical properties. The mechanical and thermal properties of the new material formulation are analyzed. Further, it is functionalized by single-walled carbon nanotubes (SWCNTs) to introduce electrical conductivity. The electrical properties are in-

vestigated. Finally, the modification with nanoparticles allows the employment as temperature and strain sensors, which is explored in proof of concept studies.

The following conclusions can be drawn from this study concerning the hypotheses presented in Section 1.2.

### Research hypothesis

AM of structural and functional materials has potential beyond rapid prototyping in lightweight design applications with lattice structures as well as in functional applications by multi-material printing.

The research hypothesis can be confirmed. Despite being cumbersome, a reliable design process is developed for lattice structures to be used in lightweight applications. It requires a probabilistic approach and the consideration of different load cases. In addition, other applications are presented that can profit from additively manufactured lattice structures. Even more promising is the newly developed solid epoxy material formulation for FFF multi-material printing. It shows isotropic mechanical properties and can be used in functional applications such as temperature and strain sensing by a modification with SWCNTs that introduces electrical conductivity.

With regard to the additively manufactured lattice structures in lightweight design, an evaluation of different load cases is mandatory. Manufacturing imperfections such as pores are often present in the currently immature AM techniques. They yield a different material behavior in tension and compression. On the one hand, analyzing only compressive specimens leads to an overestimation of the strength that could result in an earlier failure than expected. On the other hand, exploring only tensile specimens yields an underestimation of the strength so that lightweight potential is being wasted.

Moreover, it is shown that the progressive damage behavior of lattice structures can be captured with FEM simulations. They have a higher local and temporal resolution than experiments and thus help to get additional insights. Here, the choice of the material model is of importance. For 3D printed materials, a tension-compression asymmetry can often be observed. It is either naturally inherent in the case of polymers or stems from manufacturing imperfections such as pores. This needs to be included in advanced material models such as Drucker-Prager to obtain reliable numerical results. Beyond that, FEM simulations on unit cells with PBCs are computationally less expensive while still delivering feasible results. They also contribute to a better understanding of the influence of the load introduction.

Furthermore, a probabilistic design process for lattice structures is developed. It incorporates the geometrical and material uncertainties that stem from instabilities of current AM processes and materials. Considering these influences is important for a reliable lightweight design with lattice structures. This allows to avoid high safety factors that still leave some uncertainty due to their empirical nature and result in higher weights. Special attention needs to be paid regarding the determination of the probability distribution of mechanical properties that are governed by local effects such as strength and fracture strain. The proposed local probability density function (PDF) model seems to be a promising approach to estimate them accurately.

Finally, the potential of additively manufactured lattice structures in lightweight design applications is left to further discussions. While advantages can be seen especially in complex loading situations and with additional degrees of freedom by free rotation of the unit cells, the design process is very elaborate. In contrast, other fields could exploit the benefits of AM and lattice structures more easily and extensively. Especially the application in process engineering could contribute to an increasing conversion of substances and a higher selectivity in reactors. Hence, raw material and energy can be saved, which is economically and ecologically beneficial. To withstand the high pressures in reactors it still makes sense to exploit the mechanical properties that lattice structures provide. Here, the proposed design process helps to use the mechanical features of lattice structures to full capacity.

Concerning the newly developed thermoset material for FFF printing, very promising results are obtained. The solid epoxy basis allows to supply the material in the form of a filament. The latent curing agent permits an appropriate shelf life and circumvents curing during filament production or in the hotend. Yet, it allows cross-linking over the layers in a specially developed post-curing temperature program while dimensional stability is ensured. A mechanical characterization of the 3D printed material shows that the anisotropy issue at a low strength level of the current FFF process is solved. The material properties are not only isotropic, they are in a similar range as those of casted and milled bulk material. These findings could revolutionize FFF printing.

In addition, it is shown that the solid epoxy thermoset can be functionalized with SWCNTs to incorporate electrical conductivity. However, the electrical properties are anisotropic as the polymer rich surface of the infill lines acts like a barrier for electrical conductivity. Moreover, a significantly lower electrical conductivity than for casted bulk material and for liquid epoxies in other state of the art nanocomposites is observed. This can be explained by the predominantly solid state of the 3D printed material during curing that prevents the formation of a conductive network by agglomeration. Therefore, kinetic percolation cannot be reached and the higher statistical percolation threshold seems to be valid. Overall, the electrical conductivity can be adjusted by the filler content and the use of

SWCNTs still allows electrical conductivity at very low filler loadings compared to commercial filaments.

Lastly, proof of concept studies demonstrate that the functionalized solid epoxy thermoset filament can be used for 3D printed temperature and strain sensing applications. The temperature sensing specimen exhibits a bijective characteristic curve in the analyzed range and has a sufficiently high signal-to-noise ratio as well as a sufficiently low time constant. The strain sensing specimen is capable to follow the loading and unloading in cyclic experiments and can detect failure. Hence, the newly developed material can be utilized for functional integration by multi-material 3D printing.

To summarize, AM is most probably not going to be the universal manufacturing technique that will replace all the others. However, there are promising applications beyond rapid prototyping where AM is clearly advantageous and thus it will coexist along with other manufacturing technologies. As AM is relatively young compared to traditional manufacturing techniques, the current immaturities could be overcome in the future, so that the processes are getting more reliable and the choice of materials is getting bigger. This dissertation is a contribution in that direction.

## 6 Outlook

This study has shown that additive manufacturing (AM) of structural and functional materials has potential beyond rapid prototyping in applications with lattice structures as well as in functional applications by multi-material printing. Nevertheless, further research is necessary to gain deeper insights and several extensions are possible to capitalize on the findings made so far.

With regard to the newly developed functional material, an upscaling of the filament production needs to be carried out by a transfer to a professional extrusion process. This reduces pores and variations in the filament diameter. Moreover, it enables continuous fused filament fabrication (FFF) printing of larger parts from a spool. Several investigations are necessary for a scale up of the filament production with an extruder:

- Differential scanning calorimetry (DSC) measurements, so that the material does not cure during the extrusion process and jam the extruder
- Rheology measurements to find a suitable viscosity for extrusion
- Analysis of the haptics/handling of the filament, such as flexibility to be rolled on a spool, tackiness to avoid sticking together and abrasiveness of the feeder
- Development of an air-cooling track as water uptake could negatively influence the material properties
- Determination of extrusion parameters for a constant thickness and a round cross-section

Slight adjustments of the material formulation might be necessary to cope with the higher requirements of continuous printing such as smaller bending radii and the abrasive effect of the feeder. The flexibility and toughness of the filament could be improved by a thermoplastic additive with longer polymer chains such as phenoxy, which is compatible with epoxies. Also an elastomer modification such as rubber could be an option. When continuous printing is enabled, further investigations are necessary with regard to printing and curing of tall parts as dimensional stability is only proved for flat objects so far. Also the post-curing needs amelioration to achieve shorter cycles. Currently, most of the time is spent at low curing temperatures where the reactivity of the material system is low.

This is necessary to secure dimensional stability since the initial curing degree is low. Using higher printing temperatures or longer filament processing times could slightly increase the initial curing degree. Hence, post-curing can start at higher temperatures and by that save tremendous amounts of time. However, this is a delicate topic because higher printing temperatures also increase the probability of cured material inside the print head and clogging of the nozzle. Thus, some fine tuning is necessary. Also the amount of remaining functional groups should be considered, which are required for cross-linking over the interfaces. In addition, the mechanical properties of the functionalized material and a combination of functionalized and non-functionalized material in a multi-material printing approach needs to be investigated. Especially the interfacial strength is of interest to ensure that there are no further weaknesses in functionally integrated parts. However, studies on structure integrated epoxy/carbon nanotube (CNT) strain sensor films in glass fiber reinforced polymer (GFRP) showed no significant loss in mechanical properties when the films are not fully cured and a co-curing process with the laminate is carried out [299]. Similarly, no significant loss in the mechanical properties at the interface of the multi-material print is expected because the remaining reactive groups can form cross-links in the post-curing process. Furthermore, the issue of a lower electrical conductivity of the three-dimensional (3D) printed functionalized solid epoxy compared to casted specimens could be addressed. Here, the predominantly solid state during post-curing suppresses the formation of a conductive network due to limited nanoparticle mobility. In the case of functionalized paths that are completely surrounded by non-functionalized material this challenge could be overcome by a reduced amount of accelerator, a slower accelerator or no accelerator at all in the functionalized material. In that case, the functionalized material liquefies during the post-curing process allowing for a conductive network formation while still being bounded and held in shape by the solid non-functionalized material. The functionalized material can then be cured at a higher temperature. Also the proof of concept studies with regard to temperature and strain sensing need to be extended. The repeatability and the influence of electrical anisotropy on the sensing capabilities have to be investigated. In addition, the sensitivity, signal-to-noise ratio and response time has to be analyzed for different single-walled carbon nanotube (SWCNT) filler contents. Moreover, the influence of the visco-elasto-plastic material behavior in strain sensing needs further examinations. Finally, the new material formulation could be used in combination with continuous fiber reinforcements allowing 3D printed structural polymer parts without the current weak interfaces. Applications in topology optimized lightweight design are very promising as additional degrees of freedom with regard to fiber orientation are available compared to conventional fiber reinforced polymer (FRP) manufacturing processes.

Concerning the lattice structure applications, especially the probabilistic analysis needs further investigation as reliability is essential for AM users. More exper-

iments could be performed to statistically support the results. Also the number of finite element method (FEM) simulations needs to be increased for a numerical Monte-Carlo analysis. As the computational cost is extremely high, surrogate modeling could be carried out to gain additional data. Furthermore, first-order reliability methods (FORMs) and second-order reliability methods (SORMs) could be applied for a stochastic moment approximation of the joint probability density function (PDF) of the random variables. However, the number of random variables is high as geometry and material deviations are applied as random fields. Hence, these methods also demand a high computational effort. Computationally more efficient calculations such as the unit cell analyses with periodic boundary conditions (PBCs) could be integrated in the stochastic design process. In addition, the newly developed local PDF model for estimating the probability distribution of local properties such as strength and fracture strain needs further assessment as it seems very promising. In this study, it became evident that the stereolithography (SLA) process with the Form 2 and a photopolymer is very sensitive to the process parameters and the environment as well as the condition of the material and the machine leading to variations in the mechanical properties. The cause is difficult to identify due to the high number of influencing factors. Thus, it might be interesting to apply the local PDF model to a more stable AM process in order to analyze if the small deviations between experiments and simulations disappear. Moreover, the application of the local PDF model in the probabilistic analysis of other material systems and manufacturing processes with localization phenomena could be investigated. Currently, studies capturing variations in the nonlinear part of the material model are rare despite their importance in a reliable design process.

Finally, further applications of additively manufactured lattice structures could be investigated. In the field of process engineering, a combination with the newly developed material could be interesting for periodic open cellular structures (POCSs) with optimized topology for process intensification and integrated temperature sensing for process monitoring. In the field of electronics, additively manufactured heat sinks show potential [300], where also lattice structures could be considered due to their large surface area.



## Bibliography

- [1] A. Gebhardt. *Generative Fertigungsverfahren: Additive Manufacturing und 3D Drucken für Prototyping - Tooling - Produktion*. Carl Hanser Verlag, 2013.
- [2] I. Gibson, D. Rosen, and B. Stucker. *Additive Manufacturing Technologies*. Springer, 2015.
- [3] VDI Association of German Engineers. *Additive manufacturing processes, rapid manufacturing – Basics, definitions, processes*. 2014.
- [4] German Institute for Standardization. *Manufacturing processes – Terms and definitions, division*. 2020.
- [5] German Institute for Standardization. *Additive manufacturing – General principles – Terminology (ISO/ASTM 52900:2015)*. 2017.
- [6] Sculpteo. *The State of 3D Printing*. 2018.
- [7] A. Ravve. *Light-Associated Reactions of Synthetic Polymers*. Springer, 2006.
- [8] P. J. Bártolo. *Stereolithography: Materials, Processes and Applications*. Springer Science & Business Media, 2011.
- [9] J. Eschl. “Die mechanischen Eigenschaften von Stereolithographiematerialien während der Aushärtung”. PhD thesis. Universität Stuttgart, 2002.
- [10] R. Brighenti, M. P. Cosma, L. Marsavina, A. Spagnoli, and M. Terzano. “Laser-based additively manufactured polymers: a review on processes and mechanical models”. In: *Journal of Materials Science* 56.2 (2021), pp. 961–998. DOI: 10.1007/s10853-020-05254-6.
- [11] M. Schmid. *Selektives Lasersintern (SLS) mit Kunststoffen: Technologie, Prozesse und Werkstoffe*. Carl Hanser Verlag, 2015.
- [12] M. Schmid, A. Amado, and K. Wegener. “Polymer powders for selective laser sintering (SLS)”. In: *30th International Conference of the Polymer Processing Society*. Vol. 1664. AIP Conference Proceedings. Cleveland, Ohio, USA, 2015, p. 160009. DOI: 10.1063/1.4918516.
- [13] Medacom GmbH. *MakerBot 3D Printing Trends Report 2020*. 2020.
- [14] VDI Association of German Engineers. *Economical decisions during design engineering process – Methods and equipment*. 1987.

- [15] K. Ehrlenspiel, A. Kiewert, U. Lindemann, and M. Mörtl. *Kostengünstig Entwickeln und Konstruieren*. Springer, 2014.
- [16] Gartner Inc. *Hype Cycle for Emerging Technologies*. 2007.
- [17] Gartner Inc. *Hype Cycle for Emerging Technologies*. 2012.
- [18] Gartner Inc. *Hype Cycle for Emerging Technologies*. 2015.
- [19] Gartner Inc. *Hype Cycle for Emerging Technologies*. 2016.
- [20] Sculpteo. *The State of 3D Printing - 2020 Edition*. 2020.
- [21] VDI Association of German Engineers. *Biomimetics – Biomimetic materials, structures and components*. 2013.
- [22] C. Mattheck. *Design in Nature*. Springer, 1998.
- [23] VDI Association of German Engineers. *Biomimetics – Integrated product development process for biomimetic optimisation*. 2017.
- [24] German Institute for Standardization. *Biomimetics – Terminology, concepts and methodology (ISO 18458:2015)*. 2016.
- [25] VDI Association of German Engineers. *Biomimetics – Fundamentals, conception, and strategy*. 2021.
- [26] M. Gralow, F. Weigand, D. Herzog, T. Wischeropp, and C. Emmelmann. “Biomimetic design and laser additive manufacturing – A perfect symbiosis?” In: *Journal of Laser Applications* 32.2 (2020), p. 021201. DOI: 10.2351/1.5131642.
- [27] G. O. Hofmann. *Medizin für Ingenieure: Grundwissen für Entwickler, Techniker und Wissenschaftler*. Carl Hanser Verlag, 2021.
- [28] O. Rehme. “Cellular Design for Laser Freeform Fabrication”. PhD thesis. Hamburg University of Technology, 2009.
- [29] S. Drücker, M. Schulze, H. Ipsen, L. Bandegani, H. Hoch, M. Kluge, and B. Fiedler. “Experimental and numerical mechanical characterization of additively manufactured Ti6Al4V lattice structures considering progressive damage”. In: *International Journal of Mechanical Sciences* 189 (2021), p. 105986. DOI: 10.1016/j.ijmecsci.2020.105986.
- [30] S. Drücker, J. K. Lüdeker, M. Blecken, A. Kurt, K. Betz, B. Kriegesmann, and B. Fiedler. “Probabilistic analysis of additively manufactured polymer lattice structures”. In: *Materials & Design* 213 (2022), p. 110300. DOI: 10.1016/j.matdes.2021.110300.

- 
- [31] X. Hu, J. Karnetzke, M. Fassbender, S. Drücker, S. Bettermann, B. Schroeter, W. Pauer, H.-U. Moritz, B. Fiedler, G. Luinstra, and I. Smirnova. “Smart reactors – Combining stimuli-responsive hydrogels and 3D printing”. In: *Chemical Engineering Journal* 387 (2020), p. 123413. DOI: 10.1016/j.cej.2019.123413.
- [32] S. Drücker, H. Voormann, K.-P. von Berg, M. W. H. Ahrens, V. K. Wisniewski, E. Schröder, A. Kehne, S. Detjen, S. Kaysser, C.-A. Keun, and B. Fiedler. “Solid epoxy for functional 3D printing with isotropic mechanical properties by material extrusion”. In: *Additive Manufacturing* 55 (2022), p. 102797. DOI: 10.1016/j.addma.2022.102797.
- [33] L. J. Gibson and M. F. Ashby. *Cellular Solids: Structure and Properties*. Cambridge University Press, 1997.
- [34] M. F. Ashby, A. G. Evans, N. A. Fleck, L. J. Gibson, J. W. Hutchinson, and H. N. G. Wadley. *Metal Foams: A Design Guide*. Butterworth-Heinemann, 2000.
- [35] N. A. Fleck, V. S. Deshpande, and M. F. Ashby. “Micro-architected materials: past, present and future”. In: *Proceedings of the Royal Society A: Mathematical, Physical and Engineering Sciences* 466 (2010), pp. 2495–2516. DOI: 10.1098/rspa.2010.0215.
- [36] M. Osanov and J. K. Guest. “Topology Optimization for Architected Materials Design”. In: *Annual Review of Materials Research* 46.1 (2016), pp. 211–233. DOI: 10.1146/annurev-matsci-070115-031826.
- [37] J. Liu, A. T. Gaynor, S. Chen, Z. Kang, K. Suresh, A. Takezawa, L. Li, J. Kato, J. Tang, C. C. L. Wang, L. Cheng, X. Liang, and A. C. To. “Current and future trends in topology optimization for additive manufacturing”. In: *Structural and Multidisciplinary Optimization* 57.6 (2018), pp. 2457–2483. DOI: 10.1007/s00158-018-1994-3.
- [38] O. Sigmund. “Materials with prescribed constitutive parameters: An inverse homogenization problem”. In: *International Journal of Solids and Structures* 31.17 (1994), pp. 2313–2329. DOI: 10.1016/0020-7683(94)90154-6.
- [39] C. Hutter, D. Büchi, V. Zuber, and P. R. von Rohr. “Heat transfer in metal foams and designed porous media”. In: *Chemical Engineering Science* 66.17 (2011), pp. 3806–3814. DOI: 10.1016/j.ces.2011.05.005.
- [40] T. Wu, K. Liu, and A. Tovar. “Multiphase topology optimization of lattice injection molds”. In: *Computers & Structures* 192 (2017), pp. 71–82. DOI: 10.1016/j.compstruc.2017.07.007.

- [41] H. Zhou, X. Zhang, H. Zeng, H. Yang, H. Lei, X. Li, and Y. Wang. “Light-weight structure of a phase-change thermal controller based on lattice cells manufactured by SLM”. In: *Chinese Journal of Aeronautics* 32.7 (2019), pp. 1727–1732. DOI: 10.1016/j.cja.2018.08.017.
- [42] S. Arabnejad Khanoki and D. Pasini. “Fatigue design of a mechanically biocompatible lattice for a proof-of-concept femoral stem”. In: *Journal of the Mechanical Behavior of Biomedical Materials* 22 (2013), pp. 65–83. DOI: 10.1016/j.jmbbm.2013.03.002.
- [43] W.-M. Chen, Y. M. Xie, G. Imbalzano, J. Shen, S. Xu, S.-J. Lee, and P. V. S. Lee. “Lattice Ti structures with low rigidity but compatible mechanical strength: Design of implant materials for trabecular bone”. In: *International Journal of Precision Engineering and Manufacturing* 17.6 (2016), pp. 793–799. DOI: 10.1007/s12541-016-0097-6.
- [44] M. Klumpp, A. Inayat, J. Schwerdtfeger, C. Körner, R. F. Singer, H. Freund, and W. Schwieger. “Periodic open cellular structures with ideal cubic cell geometry: Effect of porosity and cell orientation on pressure drop behavior”. In: *Chemical Engineering Journal* 242 (2014), pp. 364–378. DOI: 10.1016/j.cej.2013.12.060.
- [45] A. Olenberg, W. Reschetnik, G. Kullmer, and E. Y. Kenig. “Optimization of structured packings using twisted tape inserts”. In: *Chemical Engineering Research and Design* 132 (2018), pp. 1–8. DOI: 10.1016/j.cherd.2017.12.036.
- [46] G. Do, M. Geißelbrecht, W. Schwieger, and H. Freund. “Additive manufacturing of interpenetrating periodic open cellular structures (interPOCS) with in operando adjustable flow characteristics”. In: *Chemical Engineering and Processing - Process Intensification* 148 (2020), p. 107786. DOI: 10.1016/j.cep.2019.107786.
- [47] M. Bici, S. Brischetto, F. Campana, C. G. Ferro, C. Seclì, S. Varetto, P. Maggiore, and A. Mazza. “Development of a multifunctional panel for aerospace use through SLM additive manufacturing”. In: *Procedia CIRP* 67 (2018), pp. 215–220. DOI: 10.1016/j.procir.2017.12.202.
- [48] M. Ashby. “The properties of foams and lattices”. In: *Philosophical Transactions of the Royal Society A: Mathematical, Physical and Engineering Sciences* 364 (2006), pp. 15–30. DOI: 10.1098/rsta.2005.1678.
- [49] O. Sigmund. “On the Optimality of Bone Microstructure”. In: *IUTAM Symposium on Synthesis in Bio Solid Mechanics*. Ed. by P. Pedersen and M. P. Bendsøe. Kluwer Academic Publishers, 1999, pp. 221–234. DOI: 10.1007/0-306-46939-1\_20.

- 
- [50] D. Herzog, V. Seyda, E. Wycisk, and C. Emmelmann. “Additive manufacturing of metals”. In: *Acta Materialia* 117 (2016), pp. 371–392. DOI: 10.1016/j.actamat.2016.07.019.
- [51] Z. Xiao, Y. Yang, R. Xiao, Y. Bai, C. Song, and D. Wang. “Evaluation of topology-optimized lattice structures manufactured via selective laser melting”. In: *Materials & Design* 143 (2018), pp. 27–37. DOI: 10.1016/j.matdes.2018.01.023.
- [52] B. N. Vu, F. Wein, and M. Stingl. “Two-Scale Optimization and Generation of Anisotropic Cellular Designs in the Context of Additive Manufacturing”. In: *Computer-Aided Design* 140 (2021), p. 103073. DOI: 10.1016/j.cad.2021.103073.
- [53] V. S. Deshpande, M. F. Ashby, and N. A. Fleck. “Foam topology: bending versus stretching dominated architectures”. In: *Acta Materialia* 49.6 (2001), pp. 1035–1040. DOI: 10.1016/S1359-6454(00)00379-7.
- [54] M. Mazur, M. Leary, S. Sun, M. Vcelka, D. Shidid, and M. Brandt. “Deformation and failure behaviour of Ti-6Al-4V lattice structures manufactured by selective laser melting (SLM)”. In: *The International Journal of Advanced Manufacturing Technology* 84 (2016), pp. 1391–1411. DOI: 10.1007/s00170-015-7655-4.
- [55] T. Maconachie, M. Leary, B. Lozanovski, X. Zhang, M. Qian, O. Faruque, and M. Brandt. “SLM lattice structures: Properties, performance, applications and challenges”. In: *Materials & Design* 183 (2019), p. 108137. DOI: 10.1016/j.matdes.2019.108137.
- [56] B. Gorny, T. Niendorf, J. Lackmann, M. Thoene, T. Troester, and H. Maier. “In situ characterization of the deformation and failure behavior of non-stochastic porous structures processed by selective laser melting”. In: *Materials Science and Engineering: A* 528.27 (2011), pp. 7962–7967. DOI: 10.1016/j.msea.2011.07.026.
- [57] C. Yan, L. Hao, A. Hussein, and D. Raymont. “Evaluations of cellular lattice structures manufactured using selective laser melting”. In: *International Journal of Machine Tools and Manufacture* 62 (2012), pp. 32–38. DOI: 10.1016/j.ijmactools.2012.06.002.
- [58] R. Gümürük and R. Mines. “Compressive behaviour of stainless steel micro-lattice structures”. In: *International Journal of Mechanical Sciences* 68 (2013), pp. 125–139. DOI: 10.1016/j.ijmecsci.2013.01.006.

- [59] S. Ahmadi, S. Yavari, R. Wauthle, B. Pouran, J. Schrooten, H. Weinans, and A. Zadpoor. “Additively Manufactured Open-Cell Porous Biomaterials Made from Six Different Space-Filling Unit Cells: The Mechanical and Morphological Properties”. In: *Materials* 8.4 (2015), pp. 1871–1896. DOI: 10.3390/ma8041871.
- [60] M. Leary, M. Mazur, J. Elambasseril, M. McMillan, T. Chirent, Y. Sun, M. Qian, M. Easton, and M. Brandt. “Selective laser melting (SLM) of AlSi12Mg lattice structures”. In: *Materials & Design* 98 (2016), pp. 344–357. DOI: 10.1016/j.matdes.2016.02.127.
- [61] M. Leary, M. Mazur, H. Williams, E. Yang, A. Alghamdi, B. Lozanovski, X. Zhang, D. Shidid, L. Farahbod-Sternahl, G. Witt, I. Kelbassa, P. Choong, M. Qian, and M. Brandt. “Inconel 625 lattice structures manufactured by selective laser melting (SLM): Mechanical properties, deformation and failure modes”. In: *Materials & Design* 157 (2018), pp. 179–199. DOI: 10.1016/j.matdes.2018.06.010.
- [62] H. Alsalla, L. Hao, and C. Smith. “Fracture toughness and tensile strength of 316L stainless steel cellular lattice structures manufactured using the selective laser melting technique”. In: *Materials Science and Engineering: A* 669 (2016), pp. 1–6. DOI: 10.1016/j.msea.2016.05.075.
- [63] F. Brenne, T. Niendorf, and H. Maier. “Additively manufactured cellular structures: Impact of microstructure and local strains on the monotonic and cyclic behavior under uniaxial and bending load”. In: *Journal of Materials Processing Technology* 213.9 (2013), pp. 1558–1564. DOI: 10.1016/j.jmatprotec.2013.03.013.
- [64] S. Merkt. “Qualifizierung von generativ gefertigten Gitterstrukturen für maßgeschneiderte Bauteilfunktionen”. PhD thesis. Rheinisch-Westfälische Technische Hochschule Aachen, 2015.
- [65] R. Gümruk, R. Mines, and S. Karadeniz. “Static mechanical behaviours of stainless steel micro-lattice structures under different loading conditions”. In: *Materials Science and Engineering: A* 586 (2013), pp. 392–406. DOI: 10.1016/j.msea.2013.07.070.
- [66] P. Köhnen, C. Haase, J. Bültmann, S. Ziegler, J. H. Schleifenbaum, and W. Bleck. “Mechanical properties and deformation behavior of additively manufactured lattice structures of stainless steel”. In: *Materials & Design* 145 (2018), pp. 205–217. DOI: 10.1016/j.matdes.2018.02.062.
- [67] T. Niendorf, F. Brenne, and M. Schaper. “Lattice Structures Manufactured by SLM: On the Effect of Geometrical Dimensions on Microstructure Evolution During Processing”. In: *Metallurgical and Materials Transactions B* 45.4 (2014), pp. 1181–1185. DOI: 10.1007/s11663-014-0086-z.

- 
- [68] T. Voiconi, E. Linul, L. Marşavina, T. Sadowski, and M. Kneć. “Determination of Flexural Properties of Rigid PUR Foams Using Digital Image Correlation”. In: *Advanced Materials and Structures V*. Vol. 216. Solid State Phenomena. Trans Tech Publications Ltd, 2014, pp. 116–121. DOI: 10.4028/www.scientific.net/SSP.216.116.
- [69] N. Vanderesse, A. Richter, N. Nuño, and P. Bocher. “Measurement of deformation heterogeneities in additive manufactured lattice materials by Digital Image Correlation: Strain maps analysis and reliability assessment”. In: *Journal of the Mechanical Behavior of Biomedical Materials* 86 (2018), pp. 397–408. DOI: 10.1016/j.jmbbm.2018.07.010.
- [70] W. Hao, Y. Liu, T. Wang, G. Guo, H. Chen, and D. Fang. “Failure analysis of 3D printed glass fiber/PA12 composite lattice structures using DIC”. In: *Composite Structures* 225 (2019), p. 111192. DOI: 10.1016/j.compstruct.2019.111192.
- [71] P. Li, Z. Wang, N. Petrinic, and C. Siviour. “Deformation behaviour of stainless steel microlattice structures by selective laser melting”. In: *Materials Science and Engineering: A* 614 (2014), pp. 116–121. DOI: 10.1016/j.msea.2014.07.015.
- [72] L. Boniotti, S. Beretta, L. Patriarca, L. Rigoni, and S. Foletti. “Experimental and numerical investigation on compressive fatigue strength of lattice structures of AlSi7Mg manufactured by SLM”. In: *International Journal of Fatigue* 128 (2019), p. 105181. DOI: 10.1016/j.ijfatigue.2019.06.041.
- [73] C. Ling, A. Cernicchi, M. D. Gilchrist, and P. Cardiff. “Mechanical behaviour of additively-manufactured polymeric octet-truss lattice structures under quasi-static and dynamic compressive loading”. In: *Materials & Design* 162 (2019), pp. 106–118. DOI: 10.1016/j.matdes.2018.11.035.
- [74] B. Lozanovski, M. Leary, P. Tran, D. Shidid, M. Qian, P. Choong, and M. Brandt. “Computational modelling of strut defects in SLM manufactured lattice structures”. In: *Materials & Design* 171 (2019), p. 107671. DOI: 10.1016/j.matdes.2019.107671.
- [75] P. Li. “Constitutive and failure behaviour in selective laser melted stainless steel for microlattice structures”. In: *Materials Science and Engineering: A* 622 (2015), pp. 114–120. DOI: 10.1016/j.msea.2014.11.028.
- [76] Y. Amani, S. Dancette, P. Delroisse, A. Simar, and E. Maire. “Compression behavior of lattice structures produced by selective laser melting: X-ray tomography based experimental and finite element approaches”. In: *Acta Materialia* 159 (2018), pp. 395–407. DOI: 10.1016/j.actamat.2018.08.030.

- [77] V. S. Deshpande, N. A. Fleck, and M. F. Ashby. “Effective properties of the octet-truss lattice material”. In: *Journal of the Mechanics and Physics of Solids* 49.8 (2001), pp. 1747–1769. DOI: 10.1016/S0022-5096(01)00010-2.
- [78] Z. Wang and P. Li. “Characterisation and constitutive model of tensile properties of selective laser melted Ti-6Al-4V struts for microlattice structures”. In: *Materials Science and Engineering: A* 725 (2018), pp. 350–358. DOI: 10.1016/j.msea.2018.04.006.
- [79] P. Baranowski, P. Płatek, A. Antolak-Dudka, M. Sarzyński, M. Kuciewicz, T. Durejko, J. Małachowski, J. Janiszewski, and T. Czujko. “Deformation of honeycomb cellular structures manufactured with Laser Engineered Net Shaping (LENS) technology under quasi-static loading: Experimental testing and simulation”. In: *Additive Manufacturing* 25 (2019), pp. 307–316. DOI: 10.1016/j.addma.2018.11.018.
- [80] N. Michailidis, F. Stergioudi, H. Omar, D. Papadopoulos, and D. Tsipas. “Experimental and FEM analysis of the material response of porous metals imposed to mechanical loading”. In: *Colloids and Surfaces A: Physicochemical and Engineering Aspects* 382.1 (2011), pp. 124–131. DOI: 10.1016/j.colsurfa.2010.12.017.
- [81] J. P. Oliveira, A. D. LaLonde, and J. Ma. “Processing parameters in laser powder bed fusion metal additive manufacturing”. In: *Materials & Design* 193 (2020), p. 108762. DOI: 10.1016/j.matdes.2020.108762.
- [82] A. Haldar and S. Mahadevan. *Probability, Reliability and Statistical Methods in Engineering Design*. John Wiley & Sons, 2000.
- [83] G. Stefanou. “The stochastic finite element method: Past, present and future”. In: *Computer Methods in Applied Mechanics and Engineering* 198.9 (2009), pp. 1031–1051. DOI: 10.1016/j.cma.2008.11.007.
- [84] J. D. Arregui-Mena, L. Margetts, and P. M. Mummery. “Practical Application of the Stochastic Finite Element Method”. In: *Archives of Computational Methods in Engineering* 23.1 (2014), pp. 171–190. DOI: 10.1007/s11831-014-9139-3.
- [85] B. Kriegesmann, R. Rolfes, C. Hühne, J. Teßmer, and J. Arbocz. “Probabilistic design of axially compressed composite cylinders with geometric and loading imperfections”. In: *International Journal of Structural Stability and Dynamics* 10.4 (2010), pp. 623–644. DOI: 10.1142/S0219455410003658.
- [86] J. K. Lüdeker, O. Sigmund, and B. Kriegesmann. “Inverse homogenization using isogeometric shape optimization”. In: *Computer Methods in Applied Mechanics and Engineering* 368 (2020), p. 113170. DOI: 10.1016/j.cma.2020.113170.

- 
- [87] B. Kriegesmann, R. Rolfes, C. Hühne, and A. Kling. “Fast probabilistic design procedure for axially compressed composite cylinders”. In: *Composite Structures* 93.12 (2011), pp. 3140–3149. DOI: 10.1016/j.compstruct.2011.06.017.
- [88] C. Schillo, B. Kriegesmann, and D. Krause. “Reliability based calibration of safety factors for unstiffened cylindrical composite shells”. In: *Composite Structures* 168 (2017), pp. 798–812. DOI: 10.1016/j.compstruct.2017.02.082.
- [89] G. Campoli, M. Borleffs, S. A. Yavari, R. Wauthle, H. Weinans, and A. Zadpoor. “Mechanical properties of open-cell metallic biomaterials manufactured using additive manufacturing”. In: *Materials & Design* 49 (2013), pp. 957–965. DOI: 10.1016/j.matdes.2013.01.071.
- [90] M. R. Karamooz Ravari and M. Kadkhodaei. “A Computationally Efficient Modeling Approach for Predicting Mechanical Behavior of Cellular Lattice Structures”. In: *Journal of Materials Engineering and Performance* 24 (2015), pp. 245–252. DOI: 10.1007/s11665-014-1281-4.
- [91] E. Verhulp, B. van Rietbergen, R. Müller, and R. Huiskes. “Indirect determination of trabecular bone effective tissue failure properties using micro-finite element simulations”. In: *Journal of Biomechanics* 41.7 (2008), pp. 1479–1485. DOI: 10.1016/j.jbiomech.2008.02.032.
- [92] B. Lozanovski, D. Downing, P. Tran, D. Shidid, M. Qian, P. Choong, M. Brandt, and M. Leary. “A Monte Carlo simulation-based approach to realistic modelling of additively manufactured lattice structures”. In: *Additive Manufacturing* 32 (2020), p. 101092. DOI: 10.1016/j.addma.2020.101092.
- [93] M. Smith, Z. Guan, and W. Cantwell. “Finite element modelling of the compressive response of lattice structures manufactured using the selective laser melting technique”. In: *International Journal of Mechanical Sciences* 67 (2013), pp. 28–41. DOI: 10.1016/j.ijmecsci.2012.12.004.
- [94] D. Asprone, F. Auricchio, C. Menna, S. Morganti, A. Prota, and A. Reali. “Statistical finite element analysis of the buckling behavior of honeycomb structures”. In: *Composite Structures* 105 (2013), pp. 240–255. DOI: 10.1016/j.compstruct.2013.05.014.
- [95] M. Geißendörfer, A. Liebscher, C. Proppe, C. Redenbach, and D. Schwarzer. “Stochastic multiscale modeling of metal foams”. In: *Probabilistic Engineering Mechanics* 37 (2014), pp. 132–137. DOI: 10.1016/j.probengmech.2014.06.006.

- [96] L. Ning, T. Wilson H, and Z. Jiashou. “Reliability of elasto-plastic structure using finite element method”. In: *Acta Mechanica Sinica* 18.1 (2002), pp. 66–81. DOI: 10.1007/BF02487525.
- [97] P. L. Clouston and F. Lam. “A stochastic plasticity approach to strength modeling of strand-based wood composites”. In: *Composites Science and Technology* 62.10 (2002), pp. 1381–1395. DOI: 10.1016/S0266-3538(02)00086-6.
- [98] L. Xiao and W. Song. “Additively-manufactured functionally graded Ti-6Al-4V lattice structures with high strength under static and dynamic loading: Experiments”. In: *International Journal of Impact Engineering* 111 (2018), pp. 255–272. DOI: 10.1016/j.ijimpeng.2017.09.018.
- [99] M. Gavazzoni, L. Boniotti, and S. Foletti. “Influence of specimen size on the mechanical properties of microlattices obtained by selective laser melting”. In: *Proceedings of the Institution of Mechanical Engineers, Part C: Journal of Mechanical Engineering Science* 235.10 (2019), pp. 1774–1787. DOI: 10.1177/0954406219869741.
- [100] C. Leyens and M. Peters. *Titanium and Titanium Alloys: Fundamentals and Applications*. John Wiley & Sons, 2003.
- [101] G. Lütjering and J. C. Williams. *Titanium*. Springer Science & Business Media, 2007.
- [102] ASTM International. *Standard Specification for Titanium and Titanium Alloy Bars and Billets*. 2009.
- [103] B. Dutta and F. H. Froes. *Additive Manufacturing of Titanium Alloys*. Butterworth-Heinemann, 2016.
- [104] I. Uckelmann. *Buy-to-Fly Ratio*. Materialise NV, 2017.
- [105] G. W. Ehrenstein. *Polymer Werkstoffe*. Carl Hanser Verlag, 2011.
- [106] J. P. Fouassier and J. Lalevée. *Photoinitiators for Polymer Synthesis*. John Wiley & Sons, 2012.
- [107] B. W. Darvell. *Materials Science for Dentistry*. Woodhead publishing, 2018.
- [108] Formlabs Inc. *Clear Resin (Safety Data Sheet)*. Feb. 25, 2020.
- [109] W. Schnabel. *Polymers and Light*. John Wiley & Sons, 2007.
- [110] H. Becker. “Polymerisationsinhibierung von (Meth-)Acrylaten”. PhD thesis. Technische Universität Darmstadt, 2003.
- [111] A. Salmi and E. Atzeni. “Residual stress analysis of thin AlSi10Mg parts produced by Laser Powder Bed Fusion”. In: *Virtual and Physical Prototyping* 15.1 (2019), pp. 49–61. DOI: 10.1080/17452759.2019.1650237.

- 
- [112] German Institute for Standardization. *Testing of metallic materials – Tensile test pieces*. 2016.
- [113] E. W. Andrews, G. Gioux, P. Onck, and L. J. Gibson. “Size effects in ductile cellular solids. Part II: experimental results”. In: *International Journal of Mechanical Sciences* 43.3 (2001), pp. 701–713. DOI: 10.1016/S0020-7403(00)00043-6.
- [114] German Institute for Standardization. *Testing of metallic materials – Compression test of metallic cellular materials*. 2008.
- [115] R. Wauthle, B. Vrancken, B. Beynaerts, K. Jorissen, J. Schrooten, J.-P. Kruth, and J. V. Humbeeck. “Effects of build orientation and heat treatment on the microstructure and mechanical properties of selective laser melted Ti6Al4V lattice structures”. In: *Additive Manufacturing* 5 (2015), pp. 77–84. DOI: 10.1016/j.addma.2014.12.008.
- [116] German Institute for Standardization. *Plastics – Determination of tensile properties – Part 2: Test conditions for moulding and extrusion plastics (ISO 527-2:2012)*. 2012.
- [117] German Institute for Standardization. *Plastics – Determination of compressive properties (ISO 604:2002)*. 2003.
- [118] ASTM International. *Standard Test Methods for Plane-Strain Fracture Toughness and Strain Energy Release Rate of Plastic Materials*. 2014.
- [119] S. Drücker, S. Inman, and B. Fiedler. “Simulation and optimization of the load introduction geometry of additively manufactured lattice structure specimens”. In: *ECCM 2018 - 18th European Conference on Composite Materials*. Athens/Greece, June 25, 2018, pp. 1–8. ISBN: 978-151089693-2.
- [120] Z. Zguris. *How Mechanical Properties of Stereolithography 3D Prints are Affected by UV Curing*. Somerville, MA, USA: Formlabs Inc., 2016.
- [121] German Institute for Standardization. *Metallic materials – Tensile testing – Part 1: Method of test at room temperature (ISO 6892-1:2016)*. 2017.
- [122] German Institute for Standardization. *Plastics – Determination of tensile properties – Part 1: General principles (ISO 527-1:2012)*. 2012.
- [123] Dassault Systèmes Simulia Corp. *Abaqus 6.14 Analysis User’s Guide*. 2014.
- [124] E. Vanmarcke. *Random Fields: Analysis and Synthesis*. World Scientific, 2010.
- [125] W. K. Härdle and L. Simar. *Applied Multivariate Statistical Analysis*. Springer-Verlag, 2015.
- [126] B. Kriegesmann. “Probabilistic Design of Thin-Walled Fiber Composite Structures”. PhD thesis. Leibniz University Hannover, 2012.

- [127] G. Matheron. “Principles of geostatistics”. In: *Economic Geology* 58.8 (1963), pp. 1246–1266. DOI: [10.2113/gsecongeo.58.8.1246](https://doi.org/10.2113/gsecongeo.58.8.1246).
- [128] N. A. C. Cressie. *Statistics for Spatial Data*. John Wiley & Sons, 1993.
- [129] T. M. Burgess and R. Webster. “Optimal interpolation and isarithmic mapping of soil properties”. In: *Journal of Soil Science* 31.2 (1980), pp. 315–331. DOI: [10.1111/j.1365-2389.1980.tb02084.x](https://doi.org/10.1111/j.1365-2389.1980.tb02084.x).
- [130] M. Mälícke and H. D. Schneider. *Scikit-GStat 0.2.6: A scipy flavoured geostatistical analysis toolbox written in Python*. Version v0.2.6. Nov. 7, 2019. DOI: [10.5281/zenodo.3531816](https://doi.org/10.5281/zenodo.3531816).
- [131] W. Weibull. “A Statistical Theory of the Strength of Materials”. In: *Proceedings of the Royal Swedish Institute for Engineering Research* 151 (1939), pp. 1–45.
- [132] W. V. Liebig, C. Leopold, T. Hobbiebrunken, and B. Fiedler. “New test approach to determine the transverse tensile strength of CFRP with regard to the size effect”. In: *Composites Communications* 1 (2016), pp. 54–59. DOI: [10.1016/j.coco.2016.09.003](https://doi.org/10.1016/j.coco.2016.09.003).
- [133] W. Weibull. “Zur Abhängigkeit der Festigkeit von der Probengröße”. In: *Ingenieur-Archiv* 28.1 (1959), pp. 360–362. DOI: [10.1007/BF00536130](https://doi.org/10.1007/BF00536130).
- [134] D. C. Drucker and W. Prager. “Soil mechanics and plastic analysis or limit design”. In: *Quarterly of Applied Mathematics* 10.2 (1952), pp. 157–165. DOI: [10.1090/qam/48291](https://doi.org/10.1090/qam/48291).
- [135] D. Drucker. “Plasticity theory strength-differential (SD) phenomenon, and volume expansion in metals and plastics”. In: *Metallurgical Transactions* 4.3 (1973), pp. 667–673. DOI: [10.1007/BF02643073](https://doi.org/10.1007/BF02643073).
- [136] X. P. Morelle, J. Chevalier, C. Bailly, T. Pardoën, and F. Lani. “Mechanical characterization and modeling of the deformation and failure of the highly crosslinked RTM6 epoxy resin”. In: *Mechanics of Time-Dependent Materials* 21.3 (2017), pp. 419–454. DOI: [10.1007/s11043-016-9336-6](https://doi.org/10.1007/s11043-016-9336-6).
- [137] J. Chevalier, P. P. Camanho, F. Lani, and T. Pardoën. “Multi-scale characterization and modelling of the transverse compression response of uni-directional carbon fiber reinforced epoxy”. In: *Composite Structures* 209 (2019), pp. 160–176. DOI: [10.1016/j.compstruct.2018.10.076](https://doi.org/10.1016/j.compstruct.2018.10.076).
- [138] T. Vilaro, C. Colin, and J.-D. Bartout. “As-fabricated and heat-treated microstructures of the Ti-6Al-4V alloy processed by selective laser melting”. In: *Metallurgical and Materials Transactions A* 42.10 (2011), pp. 3190–3199. DOI: [10.1007/s11661-011-0731-y](https://doi.org/10.1007/s11661-011-0731-y).

- [139] M. Simonelli, Y. Y. Tse, and C. Tuck. “Effect of the build orientation on the mechanical properties and fracture modes of SLM Ti-6Al-4V”. In: *Materials Science and Engineering: A* 616 (2014), pp. 1–11. DOI: 10.1016/j.msea.2014.07.086.
- [140] E. Wycisk, S. Siddique, D. Herzog, F. Walther, and C. Emmelmann. “Fatigue Performance of Laser Additive Manufactured Ti-6Al-4V in Very High Cycle Fatigue Regime up to  $10^9$  Cycles”. In: *Frontiers in Materials* 2 (2015), pp. 1–8. DOI: 10.3389/fmats.2015.00072.
- [141] S. L. Sing, S. Huang, and W. Y. Yeong. “Effect of solution heat treatment on microstructure and mechanical properties of laser powder bed fusion produced cobalt-28chromium-6molybdenum”. In: *Materials Science and Engineering: A* 769 (2020), p. 138511. DOI: 10.1016/j.msea.2019.138511.
- [142] X. Gong, J. Lydon, K. Cooper, and K. Chou. “Beam speed effects on Ti-6Al-4V microstructures in electron beam additive manufacturing”. In: *Journal of Materials Research* 29.17 (2014), pp. 1951–1959. DOI: 10.1557/jmr.2014.125.
- [143] U. Prisco, A. Astarita, A. E. Hassanin, and S. Franchitti. “Influence of processing parameters on microstructure and roughness of electron beam melted Ti-6Al-4V titanium alloy”. In: *Materials and Manufacturing Processes* 34.15 (2019), pp. 1753–1760. DOI: 10.1080/10426914.2019.1683576.
- [144] ASM Aerospace Specification Metals Inc. *Titanium Ti-6Al-4V (Grade 5), Annealed*. Mar. 19, 2018. URL: <http://asm.matweb.com/search/SpecificMaterial.asp?bassnum=mtp641> (visited on 03/19/2018).
- [145] E. Wycisk. *Ermüdungseigenschaften der laseradditiv gefertigten Titanlegierung TiAl6V4*. Springer, 2017.
- [146] X. Zhao, S. Li, M. Zhang, Y. Liu, T. B. Sercombe, S. Wang, Y. Hao, R. Yang, and L. E. Murr. “Comparison of the microstructures and mechanical properties of Ti-6Al-4V fabricated by selective laser melting and electron beam melting”. In: *Materials & Design* 95 (2016), pp. 21–31. DOI: 10.1016/j.matdes.2015.12.135.
- [147] J. H. K. Tan, S. L. Sing, and W. Y. Yeong. “Microstructure modelling for metallic additive manufacturing: a review”. In: *Virtual and Physical Prototyping* 15.1 (2019), pp. 87–105. DOI: 10.1080/17452759.2019.1677345.
- [148] C. Decker. “Kinetic Study and New Applications of UV Radiation Curing”. In: *Macromolecular Rapid Communications* 23.18 (2002), pp. 1067–1093. DOI: 10.1002/marc.200290014.

- [149] J. G. Kloosterboer. “Network formation by chain crosslinking photopolymerization and its applications in electronics”. In: *Electronic Applications* (1988), pp. 1–61. DOI: 10.1007/BFb0025902.
- [150] P. Geoffroy-Donders, G. Allaire, and O. Pantz. “3-d topology optimization of modulated and oriented periodic microstructures by the homogenization method”. In: *Journal of Computational Physics* 401 (2020), p. 108994. DOI: 10.1016/j.jcp.2019.108994.
- [151] A. Clausen, N. Aage, and O. Sigmund. “Exploiting Additive Manufacturing Infill in Topology Optimization for Improved Buckling Load”. In: *Engineering* 2.2 (2016), pp. 250–257. DOI: 10.1016/j.eng.2016.02.006.
- [152] W. Reschetilowski. *Handbuch Chemische Reaktoren*. Springer, 2020.
- [153] G. Emig and E. Klemm. *Chemische Reaktionstechnik*. Springer, 2017.
- [154] M. Lämmermann, W. Schwieger, and H. Freund. “Experimental investigation of gas-liquid distribution in periodic open cellular structures as potential catalyst supports”. In: *Catalysis Today* 273 (2016), pp. 161–171. DOI: 10.1016/j.cattod.2016.02.049.
- [155] C. Spille, A. Lyberis, M. I. Maiwald, D. Herzog, M. Hoffmann, C. Emmelmann, and M. Schlüter. “SMART-Reactors: Tailoring Gas Holdup Distribution by Additively Manufactured Lattice Structures”. In: *Chemical Engineering & Technology* 43.10 (2020), pp. 2053–2061. DOI: 10.1002/ceat.202000211.
- [156] A. Inayat, J. Schwerdtfeger, H. Freund, C. Körner, R. F. Singer, and W. Schwieger. “Periodic open-cell foams: Pressure drop measurements and modeling of an ideal tetrakaidecahedra packing”. In: *Chemical Engineering Science* 66.12 (2011), pp. 2758–2763. DOI: 10.1016/j.ces.2011.03.031.
- [157] N. F. Bastos Rebelo, K. A. Andreassen, L. I. Suarez Ríos, J. C. Piquero Cambor, H.-J. Zander, and C. A. Grande. “Pressure drop and heat transfer properties of cubic iso-reticular foams”. In: *Chemical Engineering and Processing - Process Intensification* 127 (2018), pp. 36–42. DOI: 10.1016/j.cep.2018.03.008.
- [158] M. Lämmermann, G. Horak, W. Schwieger, and H. Freund. “Periodic open cellular structures (POCS) for intensification of multiphase reactors: Liquid holdup and two-phase pressure drop”. In: *Chemical Engineering and Processing - Process Intensification* 126 (2018), pp. 178–189. DOI: 10.1016/j.cep.2018.02.027.

- [159] C. Busse, H. Freund, and W. Schwieger. “Intensification of heat transfer in catalytic reactors by additively manufactured periodic open cellular structures (POCS)”. In: *Chemical Engineering and Processing - Process Intensification* 124 (2018), pp. 199–214. DOI: 10.1016/j.cep.2018.01.023.
- [160] T. Knorr, P. Heinl, J. Schwerdtfeger, C. Körner, R. F. Singer, and B. J. Etzold. “Process specific catalyst supports—Selective electron beam melted cellular metal structures coated with microporous carbon”. In: *Chemical Engineering Journal* 181–182 (2012), pp. 725–733. DOI: 10.1016/j.cej.2011.10.009.
- [161] R. Balzarotti, M. Ambrosetti, M. Arnesano, A. Anglani, G. Groppi, and E. Tronconi. “Periodic open cellular structures (POCS) as enhanced catalyst supports: Optimization of the coating procedure and analysis of mass transport”. In: *Applied Catalysis B: Environmental* 283 (2021), p. 119651. DOI: 10.1016/j.apcatb.2020.119651.
- [162] N. Büscher, C. Spille, J. K. Kracht, G. V. Sayoga, A. W. H. Dawood, M. I. Maiwald, D. Herzog, M. Schlüter, and A. Liese. “Countercurrently Operated Reactive Extractor with an Additively Manufactured Enzyme Carrier Structure”. In: *Organic Process Research & Development* 24.9 (2020), pp. 1621–1628. DOI: 10.1021/acs.oprd.0c00205.
- [163] M. Sherbi, A. Wesner, V. K. Wisniewski, A. Bukowski, H. Velichkova, B. Fiedler, and J. Albert. “Superior CNT-supported bimetallic RuCu catalyst for the highly selective hydrogenolysis of glycerol to 1,2-propanediol”. In: *Catalysis Science & Technology* 11.20 (2021), pp. 6649–6653. DOI: 10.1039/d1cy01518d.
- [164] M. Schlüter and I. Smirnova. *SMART Reactors (Draft for Collective Research Center)*. 2021.
- [165] D. Szopinski. “Viscoelastic Properties of Aqueous Guar Gum Derivative Solutions and their Stimuli-Responsive Hydrogels”. PhD thesis. University of Hamburg, 2016.
- [166] X. Hu, C. Spille, M. Schlüter, and I. Smirnova. “Smart Structures—Additive Manufacturing of Stimuli-Responsive Hydrogels for Adaptive Packings”. In: *Industrial & Engineering Chemistry Research* 59.43 (2020), pp. 19458–19464. DOI: 10.1021/acs.iecr.0c03137.
- [167] S. Bettermann, B. Schroeter, H.-U. Moritz, W. Pauer, M. Fassbender, and G. A. Luinstra. “Continuous emulsion copolymerization processes at mild conditions in a 3D-printed tubular bended reactor”. In: *Chemical Engineering Journal* 338 (2018), pp. 311–322. DOI: 10.1016/j.cej.2018.01.038.

- [168] M. H. Wichmann, S. T. Buschhorn, J. Gehrmann, and K. Schulte. “Piezoresistive response of epoxy composites with carbon nanoparticles under tensile load”. In: *Physical Review B* 80.24 (2009), p. 245437. DOI: 10.1103/PhysRevB.80.245437.
- [169] W. Obityayo and T. Liu. “A Review: Carbon Nanotube-Based Piezoresistive Strain Sensors”. In: *Journal of Sensors* 2012 (2012), p. 652438. DOI: 10.1155/2012/652438.
- [170] H. Meeuw, C. Viets, W. Liebig, K. Schulte, and B. Fiedler. “Morphological influence of carbon nanofillers on the piezoresistive response of carbon nanoparticle/epoxy composites under mechanical load”. In: *European Polymer Journal* 85 (2016), pp. 198–210. DOI: 10.1016/j.eurpolymj.2016.10.027.
- [171] H. C. Neitzert, L. Vertuccio, and A. Sorrentino. “Epoxy/MWCNT Composite as Temperature Sensor and Electrical Heating Element”. In: *IEEE Transactions on Nanotechnology* 10.4 (2011), pp. 688–693. DOI: 10.1109/TNANO.2010.2068307.
- [172] J. T. Shen, S. T. Buschhorn, J. T. M. De Hosson, K. Schulte, and B. Fiedler. “Pressure and temperature induced electrical resistance change in nano-carbon/epoxy composites”. In: *Composites Science and Technology* 115 (2015), pp. 1–8. DOI: 10.1016/j.compscitech.2015.04.016.
- [173] B. F. Monea, E. I. Ionete, S. I. Spiridon, D. Ion-Ebrasu, and E. Petre. “Carbon Nanotubes and Carbon Nanotube Structures Used for Temperature Measurement”. In: *Sensors* 19.11 (2019), p. 2464. DOI: 10.3390/s19112464.
- [174] B. Philip, J. K. Abraham, A. Chandrasekhar, and V. K. Varadan. “Carbon nanotube/PMMA composite thin films for gas-sensing applications”. In: *Smart Materials and Structures* 12.6 (2003), pp. 935–939. DOI: 10.1088/0964-1726/12/6/010.
- [175] D. R. Kauffman and A. Star. “Carbon Nanotube Gas and Vapor Sensors”. In: *Angewandte Chemie International Edition* 47.35 (2008), pp. 6550–6570. DOI: 10.1002/anie.200704488.
- [176] S. Srivastava, S. S. Sharma, S. Kumar, S. Agrawal, M. Singh, and Y. K. Vijay. “Characterization of gas sensing behavior of multi walled carbon nanotube polyaniline composite films”. In: *International Journal of Hydrogen Energy* 34.19 (2009), pp. 8444–8450. DOI: 10.1016/j.ijhydene.2009.08.017.

- 
- [177] O. Lupan, V. Postica, M. Mecklenburg, K. Schulte, Y. K. Mishra, B. Fiedler, and R. Adelung. “Low powered, tunable and ultra-light aerographite sensor for climate relevant gas monitoring”. In: *Journal of Materials Chemistry A* 4.42 (2016), pp. 16723–16730. DOI: 10.1039/c6ta05347e.
- [178] X. Wang, M. Jiang, Z. Zhou, J. Gou, and D. Hui. “3D printing of polymer matrix composites: A review and prospective”. In: *Composites Part B: Engineering* 110 (2017), pp. 442–458. DOI: 10.1016/j.compositesb.2016.11.034.
- [179] J. R. C. Dizon, A. H. Espera, Q. Chen, and R. C. Advincula. “Mechanical characterization of 3D-printed polymers”. In: *Additive Manufacturing* 20 (2018), pp. 44–67. DOI: 10.1016/j.addma.2017.12.002.
- [180] C. Bellehumeur, L. Li, Q. Sun, and P. Gu. “Modeling of Bond Formation Between Polymer Filaments in the Fused Deposition Modeling Process”. In: *Journal of Manufacturing Processes* 6.2 (2004), pp. 170–178. DOI: 10.1016/S1526-6125(04)70071-7.
- [181] T. J. Coogan and D. O. Kazmer. “Bond and part strength in fused deposition modeling”. In: *Rapid Prototyping Journal* 23.2 (2017), pp. 414–422. DOI: 10.1108/RPJ-03-2016-0050.
- [182] J. Steuben, D. L. Van Bossuyt, and C. Turner. “Design for fused filament fabrication additive manufacturing”. In: *Proceedings of the ASME 2015 International Design Engineering Technical Conferences & Computers and Information in Engineering Conference*. American Society of Mechanical Engineers, Boston, USA, Aug. 2, 2015, pp. 1–14. DOI: 10.1115/DETC2015-46355.
- [183] M. Zhang, X. Song, W. Grove, E. Hull, Z. J. Pei, F. Ning, and W. Cong. “Carbon Nanotube Reinforced Fused Deposition Modeling Using Microwave Irradiation”. In: *Proceedings of the ASME 2016 International Manufacturing Science and Engineering Conference*. Blacksburg, Virginia, USA, June 27, 2016, pp. 1–7. DOI: 10.1115/MSEC2016-8790.
- [184] K. R. Hart, R. M. Dunn, J. M. Sietins, C. M. Hofmeister Mock, M. E. Mackay, and E. D. Wetzel. “Increased fracture toughness of additively manufactured amorphous thermoplastics via thermal annealing”. In: *Polymer* 144 (2018), pp. 192–204. DOI: 10.1016/j.polymer.2018.04.024.
- [185] K. R. Hart, R. M. Dunn, and E. D. Wetzel. “Increased fracture toughness of additively manufactured semi-crystalline thermoplastics via thermal annealing”. In: *Polymer* 211 (2020), p. 123091. DOI: 10.1016/j.polymer.2020.123091.

- [186] S. Shaffer, K. Yang, J. Vargas, M. A. D. Prima, and W. Voit. “On reducing anisotropy in 3D printed polymers via ionizing radiation”. In: *Polymer* 55.23 (2014), pp. 5969–5979. DOI: 10.1016/j.polymer.2014.07.054.
- [187] C.-C. Shih, M. Burnette, D. Staack, J. Wang, and B. L. Tai. “Effects of cold plasma treatment on interlayer bonding strength in FFF process”. In: *Additive Manufacturing* 25 (2019), pp. 104–111. DOI: 10.1016/j.addma.2018.11.005.
- [188] A. K. Ravi, A. Deshpande, and K. H. Hsu. “An in-process laser localized pre-deposition heating approach to inter-layer bond strengthening in extrusion based polymer additive manufacturing”. In: *Journal of Manufacturing Processes* 24 (2016), pp. 179–185. DOI: 10.1016/j.jmapro.2016.08.007.
- [189] A. Deshpande, A. Ravi, S. Kusel, R. Churchwell, and K. Hsu. “Interlayer thermal history modification for interface strength in fused filament fabricated parts”. In: *Progress in Additive Manufacturing* 4.1 (2019), pp. 63–70. DOI: 10.1007/s40964-018-0063-1.
- [190] N. P. Levenhagen and M. D. Dadmun. “Bimodal molecular weight samples improve the isotropy of 3D printed polymeric samples”. In: *Polymer* 122 (2017), pp. 232–241. DOI: 10.1016/j.polymer.2017.06.057.
- [191] L. Laberge-Lebel, B. Aissa, M. A. El Khakani, and D. Therriault. “Ultraviolet-Assisted Direct-Write Fabrication of Carbon Nanotube/Polymer Nanocomposite Microcoils”. In: *Advanced Materials* 22.5 (2010), pp. 592–596. DOI: 10.1002/adma.200902192.
- [192] R. D. Farahani, H. Dalir, V. Le Borgne, L. A. Gautier, M. A. El Khakani, M. Lévesque, and D. Therriault. “Direct-write fabrication of freestanding nanocomposite strain sensors”. In: *Nanotechnology* 23.8 (2012), p. 085502. DOI: 10.1088/0957-4484/23/8/085502.
- [193] B. G. Compton and J. A. Lewis. “3D-Printing of Lightweight Cellular Composites”. In: *Advanced Materials* 26.34 (2014), pp. 5930–5935. DOI: 10.1002/adma.201401804.
- [194] N. S. Hmeidat, J. W. Kemp, and B. G. Compton. “High-strength epoxy nanocomposites for 3D printing”. In: *Composites Science and Technology* 160 (2018), pp. 9–20. DOI: 10.1016/j.compscitech.2018.03.008.
- [195] S. Chandrasekaran, E. B. Duoss, M. A. Worsley, and J. P. Lewicki. “3D printing of high performance cyanate ester thermoset polymers”. In: *Journal of Materials Chemistry A* 6.3 (2018), pp. 853–858. DOI: 10.1039/c7ta09466c.

- 
- [196] R. D. Farahani, M. Dubé, and D. Therriault. “Three-Dimensional Printing of Multifunctional Nanocomposites: Manufacturing Techniques and Applications”. In: *Advanced Materials* 28.28 (2016), pp. 5794–5821. DOI: 10.1002/adma.201506215.
- [197] K. Yang, J. C. Grant, P. Lamey, A. Joshi-Imre, B. R. Lund, R. A. Smaldone, and W. Voit. “Diels–Alder Reversible Thermoset 3D Printing: Isotropic Thermoset Polymers via Fused Filament Fabrication”. In: *Advanced Functional Materials* 27.24 (2017), p. 1700318. DOI: 10.1002/adfm.20170318.
- [198] P. F. Flowers, C. Reyes, S. Ye, M. J. Kim, and B. J. Wiley. “3D printing electronic components and circuits with conductive thermoplastic filament”. In: *Additive Manufacturing* 18 (2017), pp. 156–163. DOI: 10.1016/j.addma.2017.10.002.
- [199] S. Agarwala, G. L. Goh, G. D. Goh, V. Dikshit, and W. Y. Yeong. “3D and 4D printing of polymer/CNTs-based conductive composites”. In: *3D and 4D Printing of Polymer Nanocomposite Materials*. Ed. by K. K. Sadasivuni, K. Deshmukh, and M. A. Almaadeed. Elsevier, 2020, pp. 297–324. DOI: 10.1016/b978-0-12-816805-9.00010-7.
- [200] T. T. Nguyen and J. Kim. “4D-Printing – Fused Deposition Modeling Printing and PolyJet Printing with Shape Memory Polymers Composite”. In: *Fibers and Polymers* 21.10 (2020), pp. 2364–2372. DOI: 10.1007/s12221-020-9882-z.
- [201] B. J. A. Gutierrez, S. Dul, A. Pegoretti, J. Alvarez-Quintana, and L. Fambri. “Investigation of the Effects of Multi-Wall and Single-Wall Carbon Nanotubes Concentration on the Properties of ABS Nanocomposites”. In: *C* 7.2 (2021), p. 33. DOI: 10.3390/c7020033.
- [202] H. Meeuw, M. Radek, and B. Fiedler. “Development of a colored GFRP with antistatic properties”. In: *AIP Conference Proceedings*. Vol. 2055. 1. AIP Publishing LLC, 2019, p. 090007. DOI: 10.1063/1.5084885.
- [203] H. Meeuw, J. Körbelin, V. K. Wisniewski, A. S. Nia, A. R. Vázquez, M. R. Lohe, X. Feng, and B. Fiedler. “Carbon Nanoparticles’ Impact on Processability and Physical Properties of Epoxy Resins—A Comprehensive Study Covering Rheological, Electrical, Thermo-Mechanical, and Fracture Properties (Mode I and II)”. In: *Polymers* 11.2 (2019), p. 231. DOI: 10.3390/polym11020231.
- [204] B. Fiedler, F. H. Gojny, M. H. Wichmann, M. C. Nolte, and K. Schulte. “Fundamental aspects of nano-reinforced composites”. In: *Composites Science and Technology* 66.16 (2006), pp. 3115–3125. DOI: 10.1016/j.compscitech.2005.01.014.

- [205] F. H. Gojny, M. H. G. Wichmann, U. Köpke, B. Fiedler, and K. Schulte. “Carbon nanotube-reinforced epoxy-composites: enhanced stiffness and fracture toughness at low nanotube content”. In: *Composites Science and Technology* 64.15 (2004), pp. 2363–2371. DOI: 10.1016/j.compscitech.2004.04.002.
- [206] K. Gnanasekaran, T. Heijmans, S. van Bennekom, H. Woldhuis, S. Wijnia, G. de With, and H. Friedrich. “3D printing of CNT- and graphene-based conductive polymer nanocomposites by fused deposition modeling”. In: *Applied Materials Today* 9 (2017), pp. 21–28. DOI: 10.1016/j.apmt.2017.04.003.
- [207] J. F. Christ, N. Aliheidari, A. Ameli, and P. Pötschke. “3D printed highly elastic strain sensors of multiwalled carbon nanotube/thermoplastic polyurethane nanocomposites”. In: *Materials & Design* 131 (2017), pp. 394–401. DOI: 10.1016/j.matdes.2017.06.011.
- [208] K. Kim, J. Park, J.-h. Suh, M. Kim, Y. Jeong, and I. Park. “3D printing of multiaxial force sensors using carbon nanotube (CNT)/thermoplastic polyurethane (TPU) filaments”. In: *Sensors and Actuators A: Physical* 263 (2017), pp. 493–500. DOI: 10.1016/j.sna.2017.07.020.
- [209] E. M. Petrie. *Epoxy Adhesive Formulations*. McGraw Hill Professional, 2006.
- [210] B. Ellis. *Chemistry and technology of epoxy resins*. Springer, 1993.
- [211] H. Kishi, T. Naitou, S. Matsuda, A. Murakami, Y. Muraji, and Y. Nakagawa. “Mechanical properties and inhomogeneous nanostructures of dicyandiamide-cured epoxy resins”. In: *Journal of Polymer Science Part B: Polymer Physics* 45.12 (2007), pp. 1425–1434. DOI: 10.1002/polb.21170.
- [212] M. D. Gilbert. “Mechanism and Kinetics of the Dicyandiamide Cure of Epoxy Resins”. PhD thesis. University of Massachusetts Amherst, 1988.
- [213] E. Dümichen. “Einsatz neuer thermoanalytischer Verfahren zur Untersuchung thermischer und thermo-oxidativer Degradationsmechanismen sowie dem Netzwerkaufbau von Polymeren”. PhD thesis. Freie Universität Berlin, 2015.
- [214] I. T. Smith. “The mechanism of the crosslinking of epoxide resins by amines”. In: *Polymer* 2 (1961), pp. 95–108. DOI: 10.1016/0032-3861(61)90010-6.
- [215] E. Dümichen, M. Javdanitehran, M. Erdmann, V. Trappe, H. Sturm, U. Braun, and G. Ziegmann. “Analyzing the network formation and curing kinetics of epoxy resins by in situ near-infrared measurements with variable heating rates”. In: *Thermochimica Acta* 616 (2015), pp. 49–60. DOI: 10.1016/j.tca.2015.08.008.

- [216] L. Guadagno, L. Vertuccio, A. Sorrentino, M. Raimondo, C. Naddeo, V. Vittoria, G. Iannuzzo, E. Calvi, and S. Russo. “Mechanical and barrier properties of epoxy resin filled with multi-walled carbon nanotubes”. In: *Carbon* 47.10 (2009), pp. 2419–2430. DOI: 10.1016/j.carbon.2009.04.035.
- [217] J. Mijovic, A. Fishbain, and J. Wijaya. “Mechanistic Modeling of Epoxy-Amine Kinetics. 1. Model Compound Study”. In: *Macromolecules* 25.2 (1992), pp. 979–985. DOI: 10.1021/ma00028a072.
- [218] J. B. Enns and J. K. Gillham. “Time–Temperature–Transformation (TTT) Cure Diagram: Modeling the Cure Behavior of Thermosets”. In: *Journal of Applied Polymer Science* 28.8 (1983), pp. 2567–2591. DOI: 10.1002/app.1983.070280810.
- [219] H. Lengsfeld, F. Wolff-Fabris, J. Krämer, J. Lacalle, and V. Altstädt. *Faserverbundwerkstoffe: Prepregs und ihre Verarbeitung*. Carl Hanser Verlag, 2015.
- [220] N. Poisson, A. Maazouz, H. Sautereau, M. Taha, and X. Gambert. “Curing of dicyandiamide epoxy resins accelerated with substituted ureas”. In: *Journal of Applied Polymer Science* 69.12 (1998), pp. 2487–2497. DOI: 10.1002/(SICI)1097-4628(19980919)69:12<2487::AID-APP20>3.0.CO;2-T.
- [221] M. Hayaty, H. Honarkar, and M. H. Beheshty. “Curing behavior of dicyandiamide/epoxy resin system using different accelerators”. In: *Iranian Polymer Journal* 22.8 (2013), pp. 591–598. DOI: 10.1007/s13726-013-0158-y.
- [222] Kautschuk-Group. *IsoQure DCD LER 50 (Technical Data Sheet)*. Oct. 27, 2020.
- [223] Hexion Inc. *EPIKURE Curing Agent 962 (Technical Data Sheet)*. Jan. 27, 2015.
- [224] L. V. Chursova, A. I. Tkachuk, N. N. Panina, Y. M. Gurevich, A. N. Babin, and G. V. Malkov. “A Study of the Mechanism of Curing of the Dicyandiamide-Epoxydiane Oligomer System in the Presence of Asymmetrical Urea”. In: *Polymer Science Series D* 8.2 (2015), pp. 153–162. DOI: 10.1134/S1995421215020057.
- [225] T. F. Saunders, M. F. Levy, and J. F. Serino. “Mechanism of the Tertiary Amine-Catalyzed Dicyandiamide Cure of Epoxy Resins”. In: *Journal of Polymer Science Part A-1: Polymer Chemistry* 5.7 (1967), pp. 1609–1617. DOI: 10.1002/pol.1967.150050711.
- [226] Kautschuk-Group. *IsoQure UR 500 (Technical Data Sheet)*. Sept. 23, 2020.

- [227] Kautschuk-Group. *IsoQure DCD 100 ETS (Technical Data Sheet)*. Sept. 23, 2020.
- [228] B. Burton, D. Alexander, H. Klein, A. Garibay-Vasquez, A. Pekarik, and C. Henkee. *Epoxy formulations using Jeffamine polyetheramines*. The Woodlands, TX, USA: Huntsman Corporation, Apr. 27, 2005.
- [229] K. Hilarius. “Elektrische und rheologische Eigenschaften von kohlenstoffbasierten Füllstoffnetzwerken in Polymeren”. PhD thesis. Technische Universität Darmstadt, 2014.
- [230] S. Iijima. “Helical microtubules of graphitic carbon”. In: *Nature* 354.6348 (1991), pp. 56–58. DOI: 10.1038/354056a0.
- [231] E. T. Thostenson, Z. Ren, and T.-W. Chou. “Advances in the science and technology of carbon nanotubes and their composites: a review”. In: *Composites Science and Technology* 61.13 (2001), pp. 1899–1912. DOI: 10.1016/S0266-3538(01)00094-X.
- [232] E. W. Wong, P. E. Sheehan, and C. M. Lieber. “Nanobeam Mechanics: Elasticity, Strength, and Toughness of Nanorods and Nanotubes”. In: *Science* 277.5334 (1997), pp. 1971–1975. DOI: 10.1126/science.277.5334.1971.
- [233] M.-F. Yu, O. Lourie, M. J. Dyer, K. Moloni, T. F. Kelly, and R. S. Ruoff. “Strength and Breaking Mechanism of Multiwalled Carbon Nanotubes Under Tensile Load”. In: *Science* 287.5453 (2000), pp. 637–640. DOI: 10.1126/science.287.5453.637.
- [234] B. G. Demczyk, Y. M. Wang, J. Cumings, M. Hetman, W. Han, A. Zettl, and R. O. Ritchie. “Direct mechanical measurement of the tensile strength and elastic modulus of multiwalled carbon nanotubes”. In: *Materials Science and Engineering: A* 334.1 (2002), pp. 173–178. DOI: 10.1016/S0921-5093(01)01807-X.
- [235] P. S. Goh, A. F. Ismail, and B. C. Ng. “Directional alignment of carbon nanotubes in polymer matrices: Contemporary approaches and future advances”. In: *Composites Part A: Applied Science and Manufacturing* 56 (2014), pp. 103–126. DOI: 10.1016/j.compositesa.2013.10.001.
- [236] S. Drücker, J. Wilmers, and S. Bargmann. “Influence of the microstructure on effective mechanical properties of carbon nanotube composites”. In: *Coupled Systems Mechanics* 6.1 (2017), pp. 1–15. DOI: 10.12989/csm.2017.6.1.001.
- [237] P. Kim, L. Shi, A. Majumdar, and P. L. McEuen. “Thermal Transport Measurements of Individual Multiwalled Nanotubes”. In: *Physical Review Letters* 87.21 (2001), p. 215502. DOI: 10.1103/PhysRevLett.87.215502.

- [238] S. Berber, Y.-K. Kwon, and D. Tománek. “Unusually High Thermal Conductivity of Carbon Nanotubes”. In: *Physical Review Letters* 84.20 (2000), pp. 4613–4616. DOI: 10.1103/PhysRevLett.84.4613.
- [239] T. W. Ebbesen, H. J. Lezec, H. Hiura, J. W. Bennett, H. F. Ghaemi, and T. Thio. “Electrical conductivity of individual carbon nanotubes”. In: *Nature* 382.6586 (1996), pp. 54–56. DOI: 10.1038/382054a0.
- [240] M. Taghioskoui. “Trends in graphene research”. In: *Materials Today* 12.10 (2009), pp. 34–37. DOI: 10.1016/S1369-7021(09)70274-3.
- [241] A. Hirsch. “The era of carbon allotropes”. In: *Nature Materials* 9.11 (2010), pp. 868–871. DOI: 10.1038/nmat2885.
- [242] M. Kaempgen. “Eigenschaften und Anwendungen von Netzwerken aus Kohlenstoff-Nanoröhren”. PhD thesis. Universität Stuttgart, 2006.
- [243] W. S. Bao, S. A. Meguid, Z. H. Zhu, and G. J. Weng. “Tunneling resistance and its effect on the electrical conductivity of carbon nanotube nanocomposites”. In: *Journal of Applied Physics* 111.9 (2012), p. 093726. DOI: 10.1063/1.4716010.
- [244] J. G. Simmons. “Generalized Formula for the Electric Tunnel Effect between Similar Electrodes Separated by a Thin Insulating Film”. In: *Journal of Applied Physics* 34.6 (1963), pp. 1793–1803. DOI: 10.1063/1.1702682.
- [245] J. G. Simmons. “Generalized Thermal J-V Characteristic for the Electric Tunnel Effect”. In: *Journal of Applied Physics* 35.9 (1964), pp. 2655–2658. DOI: 10.1063/1.1713820.
- [246] X.-W. Zhang, Y. Pan, Q. Zheng, and X.-S. Yi. “Time dependence of piezoresistance for the conductor-filled polymer composites”. In: *Journal of Polymer Science Part B: Polymer Physics* 38.21 (2000), pp. 2739–2749. DOI: 10.1002/1099-0488(20001101)38:21<2739::AID-POLB40>3.0.CO;2-0.
- [247] C. Li, E. T. Thostenson, and T.-W. Chou. “Sensors and actuators based on carbon nanotubes and their composites: A review”. In: *Composites Science and Technology* 68.6 (2008), pp. 1227–1249. DOI: 10.1016/j.compscitech.2008.01.006.
- [248] S. Kirkpatrick. “Percolation and Conduction”. In: *Reviews of Modern Physics* 45.4 (1973), pp. 574–588. DOI: 10.1103/RevModPhys.45.574.
- [249] C. Viets. “Piezoresistive Polymere und Glasfaser-Kunststoff-Verbunde auf Basis von Kohlenstoffnanopartikeln”. PhD thesis. Technische Universität Hamburg-Harburg, 2014.

- [250] W. Bauhofer and J. Z. Kovacs. “A review and analysis of electrical percolation in carbon nanotube polymer composites”. In: *Composites Science and Technology* 69.10 (2009), pp. 1486–1498. DOI: 10.1016/j.compscitech.2008.06.018.
- [251] R. Schueler, J. Petermann, K. Schulte, and H.-P. Wentzel. “Agglomeration and electrical percolation behavior of carbon black dispersed in epoxy resin”. In: *Journal of Applied Polymer Science* 63.13 (1997), pp. 1741–1746. DOI: 10.1002/(SICI)1097-4628(19970328)63:13<1741::AID-APP5>3.0.CO;2-G.
- [252] M. Predtechensky and Y. Koropachinsky. *Low-cost scalable production and applications of single-walled carbon nanotubes*. Monthly Lunch Presentation. Santa Clara, CA, USA: IEEE San Francisco Bay Area Nanotechnology Council, May 20, 2014.
- [253] OCSiAl Europe S.a.r.l. *TUBALL (Safety Data Sheet)*. Dec. 22, 2016.
- [254] G. Van Kerckhove. *TUBALL Nanotubes: Health, Safety & Environmental Status*. Workshop: Governance of emerging nano-risk in the semiconductor industry. Brussels, Belgium: OCSiAl Europe S.a.r.l, Apr. 26, 2018.
- [255] R. Schueler, J. Petermann, K. Schulte, and H.-P. Wentzel. “Percolation in carbon black filled epoxy resin”. In: *Macromolecular Symposia* 104.1 (1996), pp. 261–268. DOI: 10.1002/masy.19961040122.
- [256] J. K. W. Sandler, J. E. Kirk, I. A. Kinloch, M. S. P. Shaffer, and A. H. Windle. “Ultra-low electrical percolation threshold in carbon-nanotube-epoxy composites”. In: *Polymer* 44.19 (2003), pp. 5893–5899. DOI: 10.1016/S0032-3861(03)00539-1.
- [257] J. Z. Kovacs, B. S. Velagala, K. Schulte, and W. Bauhofer. “Two percolation thresholds in carbon nanotube epoxy composites”. In: *Composites Science and Technology* 67.5 (2007), pp. 922–928. DOI: 10.1016/j.compscitech.2006.02.037.
- [258] R. Schüler. “Entwicklung polymerer Verbundwerkstoffe mit elektrischer Leitfähigkeit”. PhD thesis. Technische Universität Hamburg-Harburg, 1994.
- [259] D. H. Everett. *Basic Principles of Colloid Science*. The Royal Society of Chemistry, 1988.
- [260] G. Brezesinski and H.-J. Mögel. *Grenzflächen und Kolloide*. Spektrum Akademischer Verlag, 1993.

- [261] B. V. Derjaguin and L. Landau. “Theory of the Stability of Strongly Charged Lyophobic Sols and of the Adhesion of Strongly Charged Particles in Solutions of Electrolytes”. In: *Acta Physicochimica URSS* 14 (1941), pp. 633–662.
- [262] E. J. W. Verwey and J. T. G. Overbeek. *Theory of the stability of lyophobic colloids*. Elsevier Publishing Company, 1948.
- [263] H. C. Hamaker. “The London—van der Waals attraction between spherical particles”. In: *Physica* 4.10 (1937), pp. 1058–1072. DOI: 10.1016/S0031-8914(37)80203-7.
- [264] R. J. Hunter. *Foundations of Colloid Science*. Oxford University Press, 2001.
- [265] T. Cosgrove. *Colloid Science*. John Wiley & Sons, 2005.
- [266] H. P. Boehm. “Some aspects of the surface chemistry of carbon blacks and other carbons”. In: *Carbon* 32.5 (1994), pp. 759–769. DOI: 10.1016/0008-6223(94)90031-0.
- [267] M.-K. Schwarz. “Elektrisch leitfähige Füllstoffnetzwerke in Duroplasten auf der Basis von Kohlenstoff-Nanopartikeln, -Nanofasern und -Nanotubes”. PhD thesis. Technische Universität Hamburg-Harburg, 2006.
- [268] F. M. Fowkes, H. Jinnai, M. A. Mostafa, F. W. Anderson, and R. J. Moore. “Mechanism of Electric Charging of Particles in Nonaqueous Liquids”. In: *Colloids and Surfaces in Reprographic Technology*. Ed. by M. Hair and M. D. Croucher. ACS Publications, 1982, pp. 307–324. DOI: 10.1021/bk-1982-0200.ch015.
- [269] G. J. Lauth and J. Kowalczyk. *Einführung in die Physik und Chemie der Grenzflächen und Kolloide*. Springer, 2016.
- [270] J. N. Israelachvili. *Intermolecular and Surface Forces*. Academic Press, 2011.
- [271] G. Faiella, V. Antonucci, S. T. Buschhorn, L. A. Prado, K. Schulte, and M. Giordano. “Tailoring the electrical properties of MWCNT/epoxy composites controlling processing conditions”. In: *Composites Part A: Applied Science and Manufacturing* 43.9 (2012), pp. 1441–1447. DOI: 10.1016/j.compositesa.2012.04.002.
- [272] F. Inam and T. Peijs. “Re-agglomeration of Carbon nanotubes in two-part epoxy system; Influence of the concentration”. In: *5th International Bhurban Conference on Applied Science and Technology (IBCAST 2007)*. Islamabad, Pakistan, 2007.

- [273] G. R. Zeichner and W. R. Schowalter. “Use of trajectory analysis to study stability of colloidal dispersions in flow fields”. In: *AIChE Journal* 23.3 (1977), pp. 243–254. DOI: 10.1002/aic.690230306.
- [274] S. C. Heintz. “Über die Auswirkung von Scherbelastung auf das rheologische und elektrische Verhalten von Kohlenstoffnanoröhrchen/Epoxid Suspensionen”. PhD thesis. Technische Universität Hamburg-Harburg, 2012.
- [275] 3DXTECH. *3DXSTAT ESD ABS*. June 24, 2021. URL: <https://www.3dxtech.com/product/3dxstat-esd-abs/> (visited on 06/24/2021).
- [276] Protoplant Inc. *Composite Conductive Fiber PLA (Safety Data Sheet)*. Oct. 5, 2018.
- [277] 3DXTECH. *3DXSTAT ESD-ABS (Safety Data Sheet)*. Aug. 1, 2017.
- [278] LEUNA-Harze GmbH. *Epilox A 50-02 (Technical Data Sheet)*. Apr. 1, 2015.
- [279] Hexion Inc. *EPON Resin 828 (Technical Data Sheet)*. June 11, 2018.
- [280] Hexion Inc. *EPIKOTE Resin MGS RIMR 135 (Technical Data Sheet)*. Mar. 23, 2015.
- [281] S. Schulz, G. Faiella, S. Buschhorn, L. Prado, M. Giordano, K. Schulte, and W. Bauhofer. “Combined electrical and rheological properties of shear induced multiwall carbon nanotube agglomerates in epoxy suspensions”. In: *European Polymer Journal* 47.11 (2011), pp. 2069–2077. DOI: 10.1016/j.eurpolymj.2011.07.022.
- [282] H. Meeuw, V. Wisniewski, and B. Fiedler. “Frequency or Amplitude?—Rheo-Electrical Characterization of Carbon Nanoparticle Filled Epoxy Systems”. In: *Polymers* 10.9 (2018), p. 999. DOI: 10.3390/polym10090999.
- [283] H. Meeuw, J. Körbelin, D. von Bernstorff, T. Augustin, W. Liebig, and B. Fiedler. “Smart dispersion: Validation of OCT and impedance spectroscopy as solutions for in-situ dispersion analysis of CNP/EP-composites”. In: *Materialia* 1 (2018), pp. 185–197. DOI: 10.1016/j.mtla.2018.06.002.
- [284] H. Meeuw, V. K. Wisniewski, U. Köpke, A. S. Nia, A. R. Vázquez, M. R. Lohe, X. Feng, and B. Fiedler. “In-line monitoring of carbon nanoparticle epoxy dispersion processes”. In: *Production Engineering* 13.3 (2019), pp. 373–390. DOI: 10.1007/s11740-019-00884-5.
- [285] T. Schröder. *Rheologie der Kunststoffe*. Carl Hanser Verlag, 2018.
- [286] T. G. Mezger. *Applied Rheology*. Anton Paar GmbH, 2014.

- [287] F. Hübner, J. Meuchelböck, F. Wolff-Fabris, M. Mühlbach, V. Altstädt, and H. Ruckdäschel. “Fast curing unidirectional carbon epoxy prepregs based on a semi-latent hardener: The influence of ambient aging on the prepregs Tg0, processing behavior and thus derived interlaminar performance of the composite”. In: *Composites Science and Technology* 216 (2021), p. 109047. DOI: 10.1016/j.compscitech.2021.109047.
- [288] Hexion Inc. *EPIKOTE Resin MGS RIMR 135 (Safety Data Sheet)*. June 22, 2017.
- [289] OCSiAl Europe S.a.r.l. *TUBALL MATRIX 301 (Technical Data Sheet)*. May 21, 2019.
- [290] W. Cantwell, A. Roulin-Moloney, and T. Kaiser. “Fractography of unfilled and particulate-filled epoxy resins”. In: *Journal of Materials Science* 23.5 (1988), pp. 1615–1631. DOI: 10.1007/BF01115700.
- [291] M. D. Hayes, D. B. Edwards, and A. R. Shah. *Fractography in Failure Analysis of Polymers*. William Andrew, 2015.
- [292] OCSiAl Europe S.a.r.l. *TUBALL (Technical Data Sheet)*. Sept. 18, 2020.
- [293] F. H. Gojny, M. H. Wichmann, B. Fiedler, I. A. Kinloch, W. Bauhofer, A. H. Windle, and K. Schulte. “Evaluation and identification of electrical and thermal conduction mechanisms in carbon nanotube/epoxy composites”. In: *Polymer* 47.6 (2006), pp. 2036–2045. DOI: 10.1016/j.polymer.2006.01.029.
- [294] C. Leopold, T. Augustin, T. Schwebler, J. Lehmann, W. V. Liebig, and B. Fiedler. “Influence of carbon nanoparticle modification on the mechanical and electrical properties of epoxy in small volumes”. In: *Journal of Colloid and Interface Science* 506 (2017), pp. 620–632. DOI: 10.1016/j.jcis.2017.07.085.
- [295] C. Liu and H.-M. Cheng. “Controlled Growth of Semiconducting and Metallic Single-Wall Carbon Nanotubes”. In: *Journal of the American Chemical Society* 138.21 (2016), pp. 6690–6698. DOI: 10.1021/jacs.6b00838.
- [296] V. I. Kleshch, V. A. Eremina, P. Serbun, A. S. Orekhov, D. Lützenkirchen-Hecht, E. D. Obraztsova, and A. N. Obraztsov. “A Comparative Study of Field Emission From Semiconducting and Metallic Single-Walled Carbon Nanotube Planar Emitters”. In: *physica status solidi (b)* 255.1 (2017), p. 1700268. DOI: 10.1002/pssb.201700268.
- [297] T. Tanaka, H. Jin, Y. Miyata, S. Fujii, H. Suga, Y. Naitoh, T. Minari, T. Miyadera, K. Tsukagoshi, and H. Kataura. “Simple and Scalable Gel-Based Separation of Metallic and Semiconducting Carbon Nanotubes”. In: *Nano Letters* 9.4 (2009), pp. 1497–1500. DOI: 10.1021/nl8034866.

- [298] Y. Yu, G. Song, and L. Sun. “Determinant role of tunneling resistance in electrical conductivity of polymer composites reinforced by well dispersed carbon nanotubes”. In: *Journal of Applied Physics* 108.8 (2010), p. 084319. DOI: 10.1063/1.3499628.
- [299] C. Buggisch, D. GIBhardt, N. Felmet, Y. Tetzner, and B. Fiedler. “Strain sensing in GFRP via fully integrated carbon nanotube epoxy film sensors”. In: *Composites Part C: Open Access* 6 (2021), p. 100191. DOI: 10.1016/j.jcomc.2021.100191.
- [300] A. Struve. *Generatives Design zur Optimierung additiv gefertigter Kühlkörper*. Springer, 2021.
- [301] S. Vyazovkin. “Model-free kinetics: Staying free of multiplying entities without necessity”. In: *Journal of Thermal Analysis and Calorimetry* 83.1 (2006), pp. 45–51. DOI: 10.1007/s10973-005-7044-6.
- [302] M. Hayaty, M. H. Beheshty, and M. Esfandeh. “Cure kinetics of a glass/epoxy prepreg by dynamic differential scanning calorimetry”. In: *Journal of Applied Polymer Science* 120.1 (2011), pp. 62–69. DOI: 10.1002/app.32982.
- [303] S. Vyazovkin. “Computational aspects of kinetic analysis. Part C. The ICTAC Kinetics Project – the light at the end of the tunnel?” In: *Thermochimica Acta* 355.1 (2000), pp. 155–163. DOI: 10.1016/S0040-6031(00)00445-7.
- [304] NETZSCH-Gerätebau GmbH. *Model-Free (Isoconversional) Analysis Methods in Kinetics Neo*. Jan. 28, 2022. URL: <https://kinetics.netzsch.com/de/features/modelfree/> (visited on 01/28/2022).
- [305] E. Moukhina and T. Rampke. *Netzsch Kinetics Neo Software Demonstration*. Sisseln, Switzerland: NETZSCH-Gerätebau GmbH, Jan. 24, 2019.
- [306] H. L. Friedman. “Kinetics of Thermal Degradation of Char-Forming Plastics from Thermogravimetry. Application to a Phenolic Plastic”. In: *Journal of Polymer Science Part C: Polymer Symposia* 6.1 (1964), pp. 183–195. DOI: 10.1002/polc.5070060121.
- [307] NETZSCH-Gerätebau GmbH. *Friedman Analysis*. Jan. 28, 2022. URL: <https://kinetics.netzsch.com/de/features/modelfree/> (visited on 01/28/2022).

# A Development of the Solid Epoxy Material Formulation

In this appendix further insights into the development of the solid epoxy material formulation are given. First, the prepolymer development is described. Afterwards, the curing of the material formulation is further analyzed. A thermokinetic model is constructed and the influence of the final curing temperature on the mechanical properties is examined. Finally, photographs of the three-dimensional (3D) printed solid epoxy specimens are presented.

## A.1 Prepolymer Development

To reduce the brittleness of the uncured solid epoxy, a prepolymer is developed that is added to the material formulation. The idea is that longer oligomer chains could act like thermoplastic polymer chains and allow some entanglement. The prepolymer is based on the solid epoxy resin to not add further components to the formulation. For increased flexibility, a polyetheramine curing agent is used. A substoichiometric curing is needed for the prepolymer to allow mixing with the other components in further steps. On the one hand, the curing degree should be as high as possible to have long oligomer chains. On the other hand, the gel point should not be reached as this would not allow a homogeneous distribution in further mixing steps. The aim is to determine the amount of polyetheramine curing agent where the gel point is just not reached. Here, the fluid to solid crossover point in oscillatory rheology at  $\tan(\delta) = 1$  is used as the definition for the gel point [286]. In order to find a suitable prepolymer, different formulations with increasing amount of polyetheramine curing agent are analyzed by oscillatory rheology. A polyetheramine content of 14 wt% to 52 wt% is investigated where the latter corresponds to the stoichiometric amount of curing agent for the solid epoxy resin. The preparation of the prepolymer formulations is carried out as presented in Section 4.2.5. The prepolymer formulations are investigated with oscillatory rheology using the same setup and parameters as in Section 4.2.7. Time sweeps are performed at a temperature of 80 °C.

Figure A.1a shows an exemplary rheology measurement of the prepolymer formulation with a polyetheramine content of 24 wt%. This is the prepolymer being utilized in the material formulation for the filament in Section 4.2.5. The storage and loss modulus as well as the loss factor are displayed depending on the time

during the curing reaction at a temperature of  $80^\circ\text{C}$ . Storage modulus and loss modulus both increase with advancing time as curing of the material progresses until an equilibrium is reached. The storage modulus approaches the loss modulus. This can also be observed by the decreasing loss factor that approaches a value slightly higher than  $\tan(\delta) = 1$  in the final equilibrium state when all functional groups of the curing agent are consumed. After approximately 2.5 h no significant change is observed anymore, so this is employed as the curing time for the prepolymer in Section 4.2.5. The results of the examination of the prepolymer formulations by oscillatory rheology are presented in Fig. A.1b. The loss factor in the equilibrium state at the end of the curing reaction is depicted over the amount of polyetheramine curing agent in the formulation. With increasing amount of polyetheramine the final loss factor decreases as the material can be further cured. The gel point is reached with a polyetheramine content between 26 wt% and 28 wt%. To ensure that the gel point is not reached, a slightly lower polyetheramine content of 24 wt% is employed for the prepolymer in the filament.

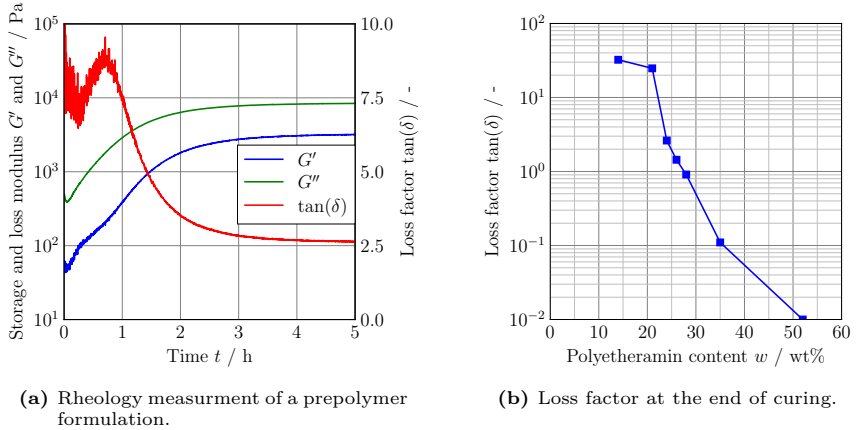


**Figure A.1:** Results of the oscillatory rheology measurements of the prepolymer formulations. An exemplary measurement of the finally utilized prepolymer formulation with a polyetheramine content of 24 wt% is shown as well as the loss factor at the end of curing over the amount of polyetheramine curing agent.

## A.2 Curing

This appendix section deals with the curing of the solid epoxy material formulation. A thermokinetic model is constructed by Friedman analysis. The mechanical properties depending on the final curing temperature are investigated to evaluate whether higher curing temperatures are beneficial.

### A.2.1 Thermokinetic Modeling

The curing reaction of thermosets can influence their final properties. Therefore, the reaction kinetics need to be analyzed. A thermokinetic model allows prediction of the progress of the reaction and can also be used to optimize the curing process to achieve the desired material properties. The progress of the curing reaction over time  $t$  can be characterized by the degree of conversion  $\alpha_c$ . It is given by

$$\alpha_c(t) = \frac{\Delta H(t)}{\Delta H}, \quad (\text{A.1})$$

where  $\Delta H(t)$  is the specific reaction enthalpy reached up to the point in time  $t$  and  $\Delta H$  is the specific reaction enthalpy of the entire curing process. The kinetic equation to determine the conversion rate can be expressed by

$$\frac{d\alpha_c}{dt} = k(T)f(\alpha_c), \quad (\text{A.2})$$

with  $k(T)$  being the reaction rate constant at temperature  $T$  and  $f(\alpha_c)$  being the reaction model. Arrhenius behavior is assumed for the reaction rate constant with

$$k(T) = A \exp\left(\frac{-E_a}{R_{\text{gas}}T}\right), \quad (\text{A.3})$$

where  $A$  is the pre-exponential factor,  $E_a$  is the activation energy and  $R_{\text{gas}}$  is the universal gas constant. Activation energy, pre-exponential factor and reaction model are often referred to as the kinetic triplet [301]. A similar material formulation to the one in this study has been analyzed by Hayaty *et al.* [302] with a diglycidyl ether of bisphenol A (DGEBA) resin, a dicyandiamide (DCD) curing agent and a uron based accelerator. They assumed an autocatalytic reaction model

$$f(\alpha_c) = \alpha_c^m (1 - \alpha_c)^n, \quad (\text{A.4})$$

with  $n$  and  $m$  being independent reaction orders. A slightly different approach is considered here with a model-free kinetic method.

The basic idea behind model-free analysis methods is that in reality most reactions do not occur in a single step. Contrary, there are usually several concurrent and competing reactions in multiple steps that contribute to an overall conversion rate. Hence, it is not possible to describe this with one reaction model on

a physical basis. Also the activation energy and the pre-exponential factor are not identical throughout the reaction and independent of the temperature profile [303]. As the kinetic triplet cannot be determined in a meaningful way anyway, model-free analyses do not rely on a reaction model. Instead, it is assumed that all constituents of the kinetic triplet  $E_a(\alpha_c)$ ,  $A(\alpha_c)$  and  $f(\alpha_c)$  depend on the degree of conversion. The second assumption is that the conversion rate at a specific degree of conversion is only depending on the temperature [304]. Then, inserting Eq. (A.3) in Eq. (A.2) yields one kinetic equation that describes the reaction by

$$\frac{d\alpha_c}{dt} = A(\alpha_c)f(\alpha_c) \exp\left(\frac{-E_a(\alpha_c)}{R_{\text{gas}}T}\right). \quad (\text{A.5})$$

While for model-based analyses the kinetic equation (or equations in case of multiple known reaction steps) should hold throughout the entire region of temperatures and degrees of conversion, model-free analysis virtually uses multiple kinetic equations that are only valid for a specific temperature and degree of conversion [301]. These model-free methods are called isoconversional approach. Model-free methods are not applicable, when the heating rate influences the reaction and when the kinetic mechanism changes at a different conversion [305].

In this study the Friedman analysis is employed [306, 307]. It is a differential model-free method as the conversion rate itself is analyzed that usually needs to be determined by numerical differentiation of experimental data. Taking natural logarithms of Eq. (A.5) yields

$$\ln\left(\frac{d\alpha_c}{dt}\right) = \ln(A(\alpha_c)f(\alpha_c)) - \frac{E_a(\alpha_c)}{R_{\text{gas}}} \frac{1}{T}, \quad (\text{A.6})$$

which is a linear equation in  $1/T$ , where  $\ln(A(\alpha_c)f(\alpha_c))$  is the intercept and  $E_a(\alpha_c)/R_{\text{gas}}$  is the slope. For experiments at different temperature conditions, straight lines can be obtained by a least squares fit through the isoconversional points in a plot of  $\ln(d\alpha_c/dt)$  versus  $1/T$ . Then, the activation energy depending on the degree of conversion can be directly obtained from the slope of the isoconversional lines without the assumption of a reaction model. When a reaction model is assumed, also the pre-exponential factor depending on the degree of conversion can be determined by the intercept of the isoconversional lines.

To obtain a thermokinetic model, the solid epoxy material formulation (prepared as presented in Section 4.2.5) is analyzed by differential scanning calorimetry (DSC) (DSC 204 F1 Phoenix, NETZSCH-Gerätebau GmbH, Selb, Germany) under nitrogen atmosphere. The different temperature conditions are realized in four dynamic experiments with various heating rates of  $1 \text{ K min}^{-1}$ ,  $2 \text{ K min}^{-1}$ ,  $5 \text{ K min}^{-1}$  and  $10 \text{ K min}^{-1}$ . Samples with a mass of approximately 15 mg are utilized. A temperature ramp from  $25^\circ\text{C}$  to  $250^\circ\text{C}$  is investigated to capture the

entire curing peak. The thermokinetic analysis is performed with the commercial software KINETICS NEO (NETZSCH-Gerätebau GmbH, Selb, Germany).

The results of the DSC measurements in terms of specific heat flow over temperature depending on the heating rate are presented in Fig. A.2a. A baseline correction is carried out for better comparability. For increasing heating rates a higher specific heat flow can be observed as well as a peak maximum at higher temperatures. With increasing heating rates, high temperatures are reached faster so that the conversion rate is increasing leading to a higher specific heat flow. Also the peak maximums are shifted as the material is not heated uniformly anymore at higher rates and the conversion rate might lag behind the heating rate. Figure A.2b shows the corresponding degree of conversion over temperature depending on the heating rate. The characteristic S-shaped curves can be seen. Similar to the specific heat flow peaks also the degree of conversion is shifted to higher temperatures for increasing heating rates. In addition, the slope at the inflection point is lower for increasing heating rates, meaning that the reaction takes place over a larger temperature range.

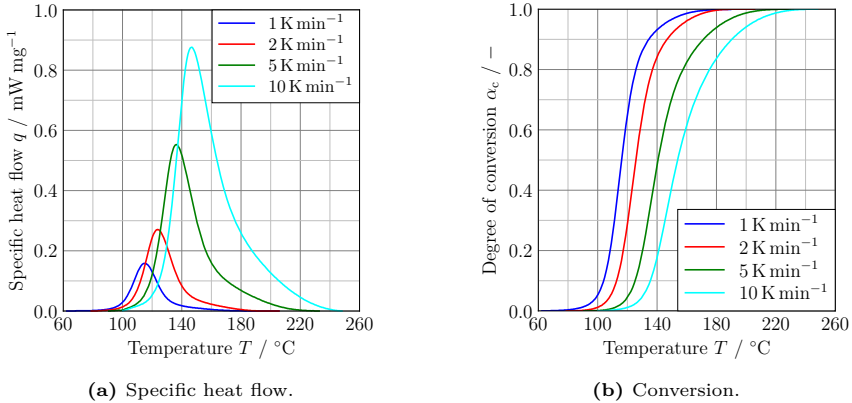


**Figure A.2:** Specific heat flow and conversion over temperature from DSC measurements of the solid epoxy material formulation depending on the heating rate.

The characteristic plot of the Friedman analysis is depicted in Fig. A.3 with the logarithm of the conversion rate over the reciprocal temperature for different heating rates. The isoconversional lines at specific degrees of conversion, which are necessary to determine the activation energy, are presented with a parula/viridis colormap.

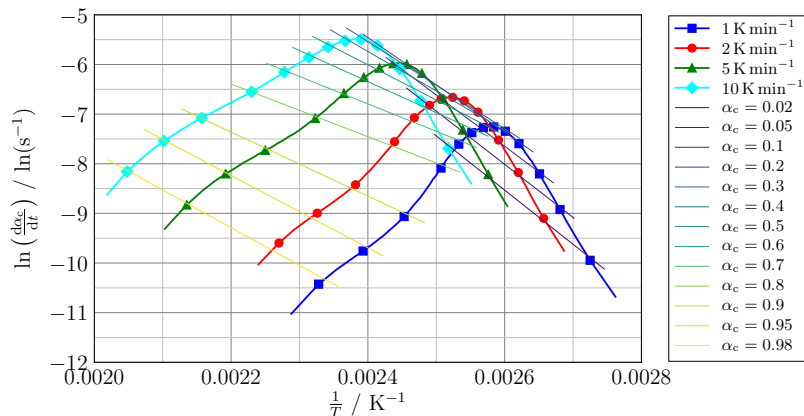


**Figure A.3:** Characteristic plot of the Friedman analysis for the solid epoxy material formulation.

Figure A.4a shows the activation energy depending on the degree of conversion according to the Friedman analysis together with the probable error based on the fit. It can be seen that the activation energy is higher at low degrees of conversion and then decreases until a degree of conversion of approximately  $\alpha_c = 0.8$ . Afterwards, it rises again. A reason for this could be that the contribution of the individual steps to the overall reaction rate of a multi-step reaction change with the degree of conversion and the temperature [301]. As described in Section 4.2.1, the initial reaction mechanism of DCD with DGEBA is the addition of the primary and secondary amines. Later on etherification, homopolymerization, a reaction of the cyano group of DCD with hydroxyl groups of DGEBA as well as the formation of heterocyclic systems can occur. The thermokinetic model obtained from Friedman analysis can be utilized to predict the curing reaction of the solid epoxy material formulation. The prediction of the degree of conversion over time depending on the isothermal curing temperature is displayed in Fig. A.4b. Temperatures below  $110^\circ\text{C}$  are not examined as they would be below the final glass transition temperature so that the reaction becomes diffusion controlled. This means a change in mechanism, making the model-free analysis invalid. With increasing curing temperature the predicted time to reach full conversion is decreasing. Two isothermal predictions are especially interesting in the following. Isothermal curing at  $210^\circ\text{C}$  is considered as it is above the melting point of DCD and could therefore prevent unreacted particles. Yet, this is  $100^\circ\text{C}$  above the final glass transition temperature and therefore thermal degra-

dation could be an issue. Hence, lower temperature isothermal curing at  $140^\circ\text{C}$  is of interest, which is far enough above the final glass transition temperature for the reaction to be controlled by the chemical kinetics. For isothermal curing at  $140^\circ\text{C}$  the predicted time to reach a full conversion is approximately 80 min. For isothermal curing at  $210^\circ\text{C}$  the predicted time to reach a full conversion is below 10 min. In the following the influence of the final curing temperature on the mechanical properties is investigated.

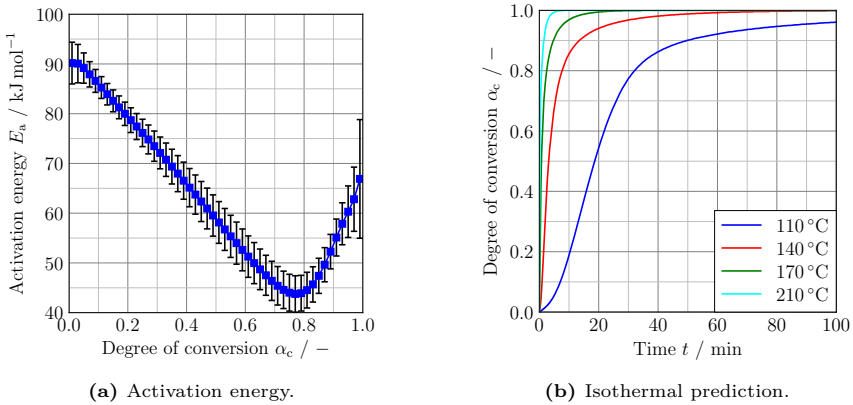


**Figure A.4:** Activation energy over degree of conversion and prediction of isothermal curing time depending on the temperature according to the Friedman analysis of the solid epoxy material formulation.

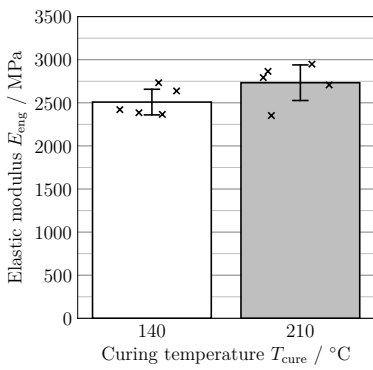
## A.2.2 Influence of Final Curing Temperature

In order to examine the influence of the final curing temperature on the mechanical properties of the solid epoxy material formulation, uniaxial tensile tests with casted and milled bulk material dog-bone specimens are performed. Bulk material specimens are utilized here as the focus is on the pure material properties. Contrary, for 3D printed specimens material property differences due to the final curing temperature might be covered by larger influences of the additive manufacturing (AM) process. In addition, the preparation is less elaborate compared to 3D printed specimens. The specimen preparation is carried out as described in Section 4.2.8 except that a different final curing temperature of  $210^\circ\text{C}$  for 10 min is employed. The mechanical testing is conducted with the same setup and parameters as in Section 4.2.10.

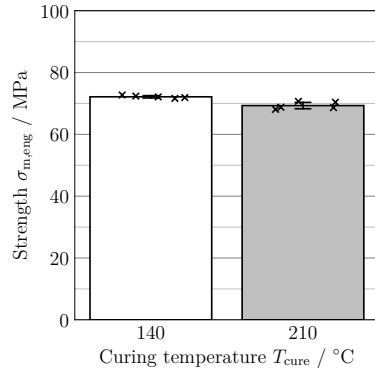
A comparison of the mechanical properties of casted and milled bulk specimens for the solid epoxy material formulation depending on the curing temperature  $T_{\text{cure}}$  is shown in Fig. A.5. The results are presented in terms of nominal/engineering properties and in the form of bar charts with standard deviations and a scatter plot of all observations. A slightly higher elastic modulus can be observed for the specimens cured at 210 °C, however, the standard deviations of both curing temperatures are overlapping. The opposite can be noticed regarding the elongation at break where the specimens cured at 140 °C show higher values. A significant difference can be seen in the strength that is also higher for the specimens cured at 140 °C. In this case, the standard deviations are smaller and not overlapping. A reason for this embrittlement could be a thermal degradation for the specimens cured at 210 °C, which is approximately 100 °C above the final glass transition temperature. Hence, 140 °C is the preferred final curing temperature with respect to the mechanical properties. In addition, the fracture surfaces of the bulk material cured at 140 °C in Fig. 4.21c do not show any unreacted particles. Therefore, this temperature seems to be high enough in combination with the accelerator to reach a sufficient solubility of the DCD in DGEBA.

Contrary, the fracture surfaces of the 3D printed specimens with the slower stepwise post-curing program show remaining DCD particles as explained in Section 4.3.5. To check whether a further heating step to 210 °C can lead to a full reaction of the DCD, this is examined for a 3D printed dog-bone specimen with a 90° infill. The specimen is prepared as described in Section 4.2.8. After the post-curing program it is further heated to a temperature of 210 °C with a rate of 1 K min<sup>-1</sup>. It is then held at that temperature for 10 min to ensure full conversion as predicted from the thermokinetic model in Appendix A.2.1. A uniaxial tensile test is performed with the same crosshead speed as in Section 4.2.10 and the fracture surface is analyzed by microscopy as presented in Section 4.2.11.

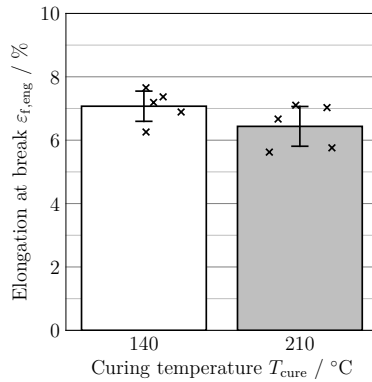
The fracture surface of the 3D printed dog-bone specimen with a 90° infill and post-cured at a temperature of 210 °C is shown in Fig. A.6. Similar to the 3D printed specimens with a maximum post-curing temperature of 140 °C, a large pore can be identified as the origin of the failure. Despite the higher curing temperature, the residual fracture surface is rough and small particles with a size less than 10 μm can be observed, which are assumed to be remaining DCD. Although the melting point of DCD is reached, there are no further reaction partners of the resin available as they were consumed at lower temperatures by the uron based accelerator. Thus, the DCD solidifies again in the form of particles during cooling. It seems that only curing directly at elevated temperatures yields full conversion of the DCD because then there is less opportunity for the uron based accelerator to consume epoxy groups itself. Since a curing temperature of 210 °C is not beneficial, 140 °C is chosen as the curing temperature for the bulk specimens and as the final step of the post-curing process for the 3D printed specimens presented in Section 4.2.8.



(a) Elastic modulus.



(b) Strength.



(c) Elongation at break.

**Figure A.5:** Comparison of the mechanical properties of casted and milled bulk specimens for the solid epoxy material formulation under different curing temperatures.

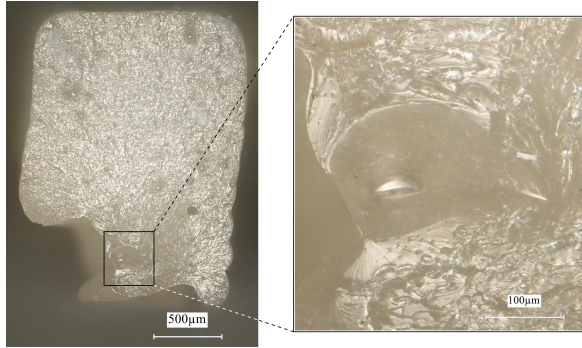


**Figure A.6:** Fracture surface of the 3D printed solid epoxy dog-bone specimen with a 90° infill and post-cured at a temperature of 210 °C.

### A.3 Photographs of 3D Printed Solid Epoxy Specimens

Figure A.7 depicts photographs of the 3D printed and post-cured dog-bones with different infill orientations to explore the mechanical anisotropy of the solid epoxy material for thermoset fused filament fabrication (FFF) printing. Photographs of the 3D printed and post-cured cubes with different single-walled carbon nanotube (SWCNT) filler contents for the analysis of the electrical properties of the functionalized solid epoxy material for thermoset FFF printing are shown in Fig. A.8. Figure A.9 presents a photograph of a 3D printed and post-cured functionalized dog-bone with an SWCNT content of 0.2 wt% that is utilized for the investigation of the thermo- and piezoresistive sensing capabilities of the solid epoxy material for thermoset FFF printing.

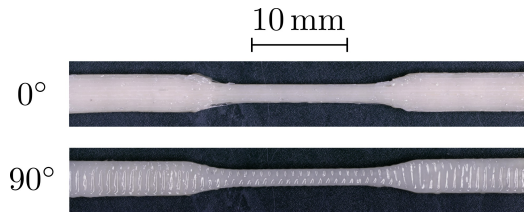


**Figure A.7:** Photographs of the 3D printed and post-cured dog-bones with different infill orientations to explore the mechanical anisotropy of the solid epoxy formulation.

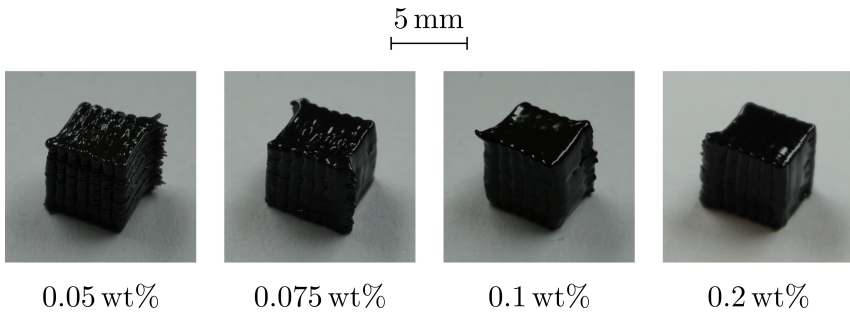


**Figure A.8:** Photographs of the 3D printed and post-cured cubes with different SWCNT filler contents for the analysis of the electrical properties of the functionalized solid epoxy formulation.

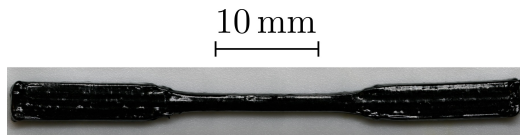


**Figure A.9:** Photograph of a 3D printed and post-cured functionalized dog-bone with an SWCNT content of 0.2 wt% to investigate the sensing capabilities of the solid epoxy formulation.



# Supervised Student Theses and Research Projects

## Bachelor Theses

T. Bilgin. “Mechanische Charakterisierung von Fused Deposition Modeling Materialien für energieabsorbierende Gitterstrukturen”, 2018.

S. Schibsdatt. “Reparatur und Fertigung von additiv gefertigten Hybrid-Bauteilen”. In cooperation with ZAL Zentrum für Angewandte Luftfahrtforschung GmbH, 2020.

N. Thordsen. “Micromechanical simulation of hygroscopic degradation of fiber-reinforced composites on the basis of a representative volume element”, 2020.

## Research Projects

S. Inman. “Simulation und Optimierung der Lasteinleitungsgeometrie bei additiv gefertigten Mikrostruktur Zugproben”, 2017.

K. Betz. “Charakterisierung der Streuung mechanischer Eigenschaften von Stereolithografie-Bauteilen”, 2017.

L. Bandegani. “Untersuchung des Einflusses von Pulveralterung und Wärmebehandlung bei durch selektives Laserschmelzen gefertigten Bauteilen aus TiAl6V4”, 2018.

K.-P. von Berg. “Realisierung eines Fused Filament Fabrication 3D-Druckprozesses mit hochmolekularem Epoxidharz”, 2018.

V. K. Wisniewski. “Filament development for a Fused Filament Fabrication 3D printing process based on a thermosetting polymer”, 2018.

E. Schröder. “Single Walled Carbon Nanotube / Epoxidharz Verarbeitung im Fused Filament Fabrication Process: Untersuchung der elektrischen Leitfähigkeit”, 2019.

M. Blecken. “Untersuchung der Festigkeitsstreuungen und Geometrieabweichungen additiv gefertigter Kunststoff-Gitterstrukturen”, 2019.

A. Adamanov. “Viscous short and long term behavior of a compressed plastic piston in automobile restraint device”. In cooperation with Autoliv B.V. & Co. KG, 2019.

A. Kurt. “Simulation der Streuung von mechanischen Eigenschaften und Geometrieabweichungen additiv gefertigter Kunststoff-Gitterstrukturen”, 2019.

H. Ipsen. “Simulation des Schadensverhaltens von additiv gefertigten Gitterstrukturen unter Zug- und Druckbelastung”, 2019.

O. Englert-Dudek. “Erstellung eines mechanischen Modells von Aerographit mit der Anwendung Ansys”, 2020.

M. W. H. Ahrens. “Materialformulierung für den Fused Deposition Modeling (FDM) 3D Druck mittels eines Duromeres”, 2020.

P. L. Holdorf. “Resorbierbare Polymere für den Einsatz als Darmstents”, 2020.

## Master Theses

M. Radek. “Charakterisierung der mechanischen Eigenschaften additiv gefertigter bionischer Mikrostrukturen”, 2017.

S. Inman. “Machbarkeitsstudie eines ergonomischen Verbundwerkstoff-Druckbehälters”. In cooperation with Drägerwerk AG & Co. KGaA, 2018.

O. Kaufmann. “Parameter study of 3D printed fiber reinforced parts using the coaxial extrusion process”. In cooperation with CTC GmbH, 2018.

M. Schulze. “Statische und zyklische mechanische Untersuchung von additiv gefertigten Titan-Gitterstrukturen”, 2019.

A. Holzschuh. “Finite Elemente Analyse Intestinaler Polymerstents”, 2021.

T. Tiedemann. “Untersuchung des Einflusses der mechanischen Eigenschaften eines beschichteten und unbeschichteten Elastomers auf das Reibungsverhalten mittels FEM Simulation”. In cooperation with Fraunhofer-Institut für Fertigungstechnik und Angewandte Materialforschung IFAM, 2021.

# Publications

## Journal Articles

X. Hu, M. Fassbender, **S. Drücker**, B. Fiedler, G. A. Luinstra, and I. Smirnova. “Intelligente Reaktoren: Kombination von Stimuli-responsiven Hydrogelen und 3D-Druck”. In: *Chemie Ingenieur Technik* 90.9 (2018), pp. 1211-1212.

X. Hu, J. Karnetzke, M. Fassbender, **S. Drücker**, S. Bettermann, B. Schroeter, W. Pauer, H.-U. Moritz, B. Fiedler, G. Luinstra, and I. Smirnova. “Smart reactors – Combining stimuli-responsive hydrogels and 3D printing”. In: *Chemical Engineering Journal* 387 (2020), p. 123413.

**S. Drücker**, M. Schulze, H. Ipsen, L. Bandegani, H. Hoch, M. Kluge, and B. Fiedler. “Experimental and numerical mechanical characterization of additively manufactured Ti6Al4V lattice structures considering progressive damage”. In: *International Journal of Mechanical Sciences* 189 (2021), p. 105986.

**S. Drücker**, J. K. Lüdeker, M. Blecken, A. Kurt, K. Betz, B. Kriegesmann, and B. Fiedler. “Probabilistic analysis of additively manufactured polymer lattice structures”. In: *Materials & Design* 213 (2022), p. 110300.

**S. Drücker**, H. Voormann, K.-P. von Berg, M. W. H. Ahrens, V. K. Wisniewski, E. Schröder, A. Kehne, S. Detjen, S. Kaysser, C.-A. Keun, and B. Fiedler. “Solid epoxy for functional 3D printing with isotropic mechanical properties by material extrusion”. In: *Additive Manufacturing* 55 (2022), p. 102797.

## Conferences

**S. Drücker**, S. Inman, and B. Fiedler. “Simulation and optimization of the load introduction geometry of additively manufactured lattice structure specimens”. In: *ECCM18 - 18th European Conference on Composite Materials*. Athens/Greece, June 25, 2018.

## Patents

C.-A. Keun, H. Meeuw, K. P. von Berg, **S. Drücker**, V. K. Wisniewski, and B. Fiedler. “Werkstoff, Werkstoffkomposition, Werkstoffherstellungsverfahren und Fertigungsverfahren”. Published patent application DE 10 2019 110 245 A1, Oct. 22, 2020.